Stratification in Drying Particle Suspensions

Yanfei Tang

Dissertation submitted to the Faculty of the
Virginia Polytechnic Institute and State University
in partial fulfillment of the requirements for the degree of

Doctor of Philosophy
in
Physics

Shengfeng Cheng, Chair
James A. Hanna
Mark L. Pitt
Uwe C. Täuber

November 16, 2018
Blacksburg, Virginia

Keywords: Evaporation, Stratification, Drying, Nanoparticle Suspension, Young-Laplace Equation.

Stratification in Drying Particle Suspensions

Yanfei Tang

(ABSTRACT)

This thesis is on molecular dynamics studies of drying suspensions of bidisperse nanoparticle mixtures. I first use an explicit solvent model to investigate how the structure of the dry film depends on the evaporation rate of the solvent and the initial volume fractions of the nanoparticles. My simulation results show that the particle mixtures stratify according to their sizes when the suspensions are quickly dried, consistent with the prediction of recent theories. I further show that stratification can be controlled using thermophoresis induced by a thermal gradient imposed on the drying suspension. To model larger systems on longer time scales, I explore implicit solvent models of drying particle suspensions in which the solvent is treated as a uniform viscous background and the liquid-vapor interface is replaced by a potential barrier that confines all the solutes in the solution. Drying is then modeled as a process in which the location of the confining potential is moved. In order to clarify the physical foundation of this moving interface method, I analyze the meniscus on the outside of a circular cylinder and apply the results to understand the capillary force experienced by a spherical particle at a liquid-vapor interface. My analyses show that the capillary force is approximately linear with the displacement of the particle from its equilibrium location at the interface. An analytical expression is derived for the corresponding spring constant that depends on the surface tension and lateral span of the interface and the particle radius. I further show that with a careful mapping, both explicit and implicit solvent models yield similar stratification behavior for drying suspensions of bidisperse particles. Finally, I apply

the moving interface method based on an implicit solvent to study the drying of various soft matter solutions, including a solution film of a mixture of polymers and nanoparticles, a suspension droplet of bidisperse nanoparticles, a solution droplet of a polymer blend, and a solution droplet of diblock copolymers.

Stratification in Drying Particle Suspensions

Yanfei Tang

(GENERAL AUDIENCE ABSTRACT)

Drying is a ubiquitous phenomenon. In this thesis, I use molecular dynamics methods to simulate the drying of a suspension of a bidisperse mixture of nanoparticles that have two different radii. First, I use a model in which the solvent is included explicitly as point particles and the nanoparticles are modeled as spheres with finite radii. Their trajectories are generated by numerically solving the Newtonian equations of motion for all the particles in the system. My simulations show that the bidisperse nanoparticle mixtures stratify according to their sizes after drying. For example, a "small-on-top" stratified film can be produced in which the smaller nanoparticles are distributed on top of the larger particles in the drying film. I further use a similar model to demonstrate that stratification can be controlled by imposing a thermal gradient on the drying suspension. I then map an explicit solvent system to an implicit one in which the solvent is treated as a uniform viscous background and only the nanoparticles are kept. The physical foundation of this mapping is clarified. I compare simulations using the explicit and implicit solvent models and show that similar stratification behavior emerge in both models. Therefore, the implicit solvent model can be applied to study much larger systems on longer time scales. Finally, I apply the implicit solvent model to study the drying of various soft matter solutions, including a solution film of a mixture of polymers and nanoparticles, a droplet of a bidisperse nanoparticle suspension, a solution droplet of a polymer blend, and a droplet of a diblock copolymer solution.

I dedicate this thesis to my beloved parents.

Acknowledgments

I am deeply grateful to my advisor, Prof. Shengfeng Cheng. This thesis could not have been finished without tremendous help from him. His support extends from my research to my life. My pursuit of a PhD in physics was not always smooth. I still remembered the first time I stepped into his office to consult him about my PhD career. Since the first meeting, he has treated me as a mentored student, a collaborator, and a friend in casual occasions. During my three years in his group, I am very lucky to work on many projects to sharpen my skills and broaden my vision in soft matter physics. I am greatly encouraged by him to materialize our thoughts into models, projects, and papers, which are scrutinized by him time after time. It is his diligence to make our collaboration fruitful. In all, I am proud to be his supervisee and collaborator.

I thank Dr. Gary Grest for providing us computing resources and inspiring ideas. Dr. Grest also generously shared his experiences on many research topics and helped us tremendously in the improvement of presentations of our papers. I also thank Chengyuan Wen from our group for helpful discussions about my research.

I express my gratitude to my PhD committee members: Prof. James Hanna, Prof. Mark Pitt, and Prof. Uwe Täuber. Among them, I particularly thank Prof. Täuber for his encouragement and insightful comments on my research.

I thank our graduate program coordinator, Betty Wilkins, and program support technician,

Katrina Loan. My thanks extend to our IT staff members including Roger Link and Travis Heath.

I thank my mentor, Prof. Thomas Maier, for his guidance and support during my stay at Oak Ridge National Laboratory (ORNL). I want to thank my other reliable collaborators: Prof. Vito Scarola, Dr. Feng Bao, Micheal Summers, Prof. Steven Johnston and Dr. Shaozhi Li. I sincerely thank Prof. Scarola and Prof. Maier for giving me the opportunity to study at ORNL.

I wish to thank all my friends in my study and in my life. My special thanks go to Yaxuan Zhang for her appreciation.

Finally, I am obliged to my parents for their endless love.

Contents

Chapter 1

Introduction

Evaporation is a ubiquitous process that plays an important role in many diverse fields including climate, environment, and industry [1]. It is also frequently used in material fabrications. For example, controlled evaporation is used to make polymer thin films [2, 3], polymeric particles [4], and nanocomposites [5, 6], and to assemble building blocks including particles into superstructures [7–12]. In a relatively simple case where a suspension containing particles undergoes drying, the structure of the final dry film is determined by three competing factors: the diffusion of the particles, their sedimentation due to gravity, and the receding motion of the liquid-vapor interface induced by solvent evaporation [13, 14]. For the systems concerned here the particles are small enough that the effects of gravity can be ignored. For example, for aqueous solutions, we can neglect gravity for particles with radius smaller than about 300 nm [15]. Furthermore, gravitational effects can also be suppressed by using a solvent with a density matching that of the particles. In these scenarios, sedimentation is not important and the competition between evaporation and particle diffusion

is quantified by a dimensionless Péclet number,

$$\mathrm{Pe} = \frac{H v_e}{D}, \tag{1.1}$$

where H is the thickness of the interfacial region affected by evaporation and can be taken as the film thickness for thin films, D is the diffusion constant of the particles, and v_e is the receding speed of the interface. The Péclet number is the ratio of two time scales: one is the diffusion time scale $\tau_D = H^2/D$ and the other is the time scale of drying $\tau_e = H/v_e$. Routh and Zimmerman derived the governing equation for the evolution of particle volume fractions, which is referred to as the RZ model hereafter, and obtained numerical solutions at various Péclet numbers [13]. Their analyses showed that when $\mathrm{Pe} \gg 1$, the particles are trapped and accumulated near the liquid-vapor interface, forming a skin layer since their diffusion is slow compared to the recession of the interface. However, when $\mathrm{Pe} \ll 1$, the diffusion of the particles is faster than the motion of the interface and the particles remain almost uniformly distributed in the drying film.

Since the diffusion constant of a particle depends on its size, the situation becomes particularly intriguing when the suspended particles are polydisperse. From the Einstein-Stokes relationship, $D = k_\mathrm{B}T/(3\pi\eta d)$, where k_B is the Boltzmann constant, T the temperature, η the solvent viscosity, and d the particle diameter. The Péclet number is thus proportional to d. The simplest polydisperse system is a suspension containing particles of two sizes d_l and d_s with a size ratio $\alpha = d_l/d_s > 1$. Trueman *et al.* extended the RZ model to such bidisperse suspensions and combined numerical simulations and experiments to show that the larger particles accumulate while the smaller ones are depleted near the interface when $\mathrm{Pe}_l > 1 > \mathrm{Pe}_s$ [16, 17]. This is called the "large-on-top" stratification. Using the extended RZ model, Atmuri *et al.* studied the effects of inter-particle interactions amongst the same species (i.e., the particles of the same size) on the particle distribution during drying of the

suspension [18]. They also investigated suspensions containing particles of the same size but some of them are neutral while the others are charged. Their numerical simulations showed that in this case the charged particles are depleted at the receding interface because of the repulsion between charged particles. As a result, neutral particles remain and accumulate near the interface. This finding is consistent with an earlier study of Nikiforow *et al.* [19], who studied a latex blend of charged and neutral particles of roughly the same size and found that stratification between the two species readily occurred after drying of the film with the neutral particles accumulating immediately below the film-air interface.

From these previous studies, it was believed that in bidisperse particle suspensions, stratification would likely be produced if the Péclet numbers of the two components were on different sides of unity (e.g., $\mathrm{Pe}_l > 1 > \mathrm{Pe}_s$) and the particles with a smaller diffusivity (e.g., the larger particles) would accumulate at the top of the dried film [16, 17]. However, Fortini *et al.* recently discovered the occurrence of a novel "small-on-top" stratifying scenario when $\mathrm{Pe}_l \gg \mathrm{Pe}_s \gg 1$ [20, 21]. Namely the smaller particles accumulate near the interface when the evaporation is very fast for both large and small particles, as shown in Fig. 1.1. They proposed that for very fast evaporation both large and small particles first accumulate just below the receding interface, creating gradients of their concentration distributions in the direction perpendicular to the film. The concentration gradients lead to gradients of the associated osmotic pressure, which cause the particles to drift. However, the drift velocity is asymmetric for the large and small particles. Fortini *et al.* argued that if the volume fraction of small particles is large enough to make them the majority phase just below the film-air interface, then the large particles will drift away from this region faster than the small particles roughly by a factor of $\alpha^2 - 1$. The net result is an accumulation of small particles at the top of the drying film. This mechanism leading to 'small-on-top" stratification is termed diffusiophoresis. The finding of Fortini *et al.* seems to be consistent with a phenomenon

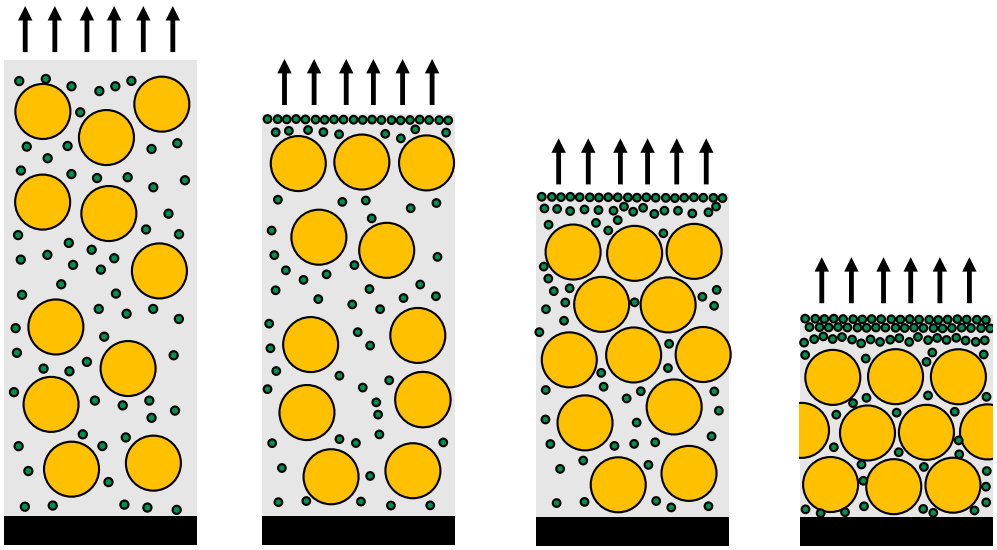

Figure 1.1: Schematic figure about process of "small-on-top" stratification in a drying thin film of a bidisperse mixture of colloidal particles. All the particles are uniformly distributed in the film prior to evaporation while after fast drying, the smaller particles are preferentially distributed on top of the larger particles.

observed earlier by Luo *et al.*, who studied drying aqueous dispersions containing a mixture of latex particles with a diameter $\sim$ 550 nm and much smaller ceramic nanoparticles and found an enrichment of nanoparticles in interstitial spaces among latex particles near the top surface of the drying film [22]. Howard *et al.* performed numerical simulations based on an implicit solvent model, similar to the one used by Fortini *et al.*, to systematically study the effects of particle size ratios and evaporation rates on stratification [23]. They found that "small-on-top" stratification can persist even when the Péclet numbers are of order 1 and noticed an unexpected accumulation of the larger particles near the substrate at small evaporation rates (i.e., small v_e).

To better understand stratifying phenomena, Zhou, Jiang, and Doi proposed a diffusion model, referred to as the ZJD model hereafter, for mixtures of hard spheres up to second virial coefficients [24]. The equations describing the time evolution of particle concentrations in the ZJD model are similar to those in the extended RZ model but the expressions for chemical

potential are different [16, 24]. Analyses and numerical solutions of the ZJD model revealed that the "small-on-top" structure is created by the cross-interactions between particles of different sizes, which affect the larger particles much more strongly than the smaller ones roughly by a factor of α^3 [24]. A state diagram in the Pe_s–ϕ_s plane was predicted where stratification occurs if $\alpha^2(1 + \mathrm{Pe}_s)\phi_s > 1$, with ϕ_s being the initial volume fraction of the smaller particles.

Makepeace *et al.* recently combined experiments and simulations to test the ZJD model [25]. They found that at low particle concentrations the ZJD model fit their measurements and modeling data reasonably well while for concentrated suspensions the ZJD model significantly over-predicts "small-on-top" stratification, i.e., actual stratification occurs at α, Pe_s, and ϕ_s much larger than those predicted by the ZJD model. Liu *et al.* performed experiments on the drying of suspensions containing a mixture of larger polystyrene nanoparticles and smaller silica nanoparticles and identified "small-on-top" states via atomic force microscopy (AFM) characterization of the film surface [26]. Their results seem to fit the ZJD model, though their measurements are in the $\mathrm{Pe}_l > 1 > \mathrm{Pe}_s$ regime. Martín-Fabiani *et al.* showed that stratification can be turned on and off on demand by mixing smaller particles, whose size can be varied by changing the pH of the suspension, and larger particles with a fixed size [27]. At low pH, $\alpha \approx 7$ and "small-on-top" stratification occurs while at high pH, α decreases to about 4 and stratification is suppressed. Their work demonstrated the effects of high particle concentrations and the associated jamming that prevents the particles to stratify.

From the reported studies we now understand that stratifying phenomena in a drying suspension containing a bidisperse mixture of neutral particles depend on several factors including the evaporation rate of the solvent, the initial volume fractions of the particles, the particle size ratio, and the interactions between the particles [18, 20, 23–25]. The ZJD model predicts

that for the initial volume fractions only that of the smaller particles matters [24]. However, in previous simulations [16–18, 20, 23, 25] and theory [24] the solvent was treated as an implicit, uniform viscous background. Very recently, Sear and Warren used the Asakura-Oosawa model to study the drift of a large particle in a solute (i.e., small particle) gradient [28, 29], taking into account the contribution from the solvent back-flow to the pressure gradient, and showed that the analyses of Fortini *et al.* and the ZJD model based on an implicit solvent overestimate the drift velocity of large particles roughly by a factor of α^2 [29]. With this correction, their prediction is that "small-on-top" stratification occurs only when $\mathrm{Pe}_s\phi_s \gtrsim 1$. Therefore, the threshold of Pe_s driving a system into the "small-on-top" regime at a given ϕ_s is higher than the ZJD prediction roughly by a factor of α^2, which may provide an explanation of the finding of Makepeace *et al.* that the ZJD model tends to over-predict stratification [25]. Hereafter we refer the work of Sear and Warren as the SW model. In another recent work [30], Sear applied a gelation model originally developed by Okuzono and Doi for the drying of a polymer film [31] to stratifying phenomena and considered the jamming of particles at high volume fractions and the resulting dynamic arrest of particle motion, which occur when the accumulation of particles near a receding liquid-vapor interface surpasses the jamming point. In the Sear model, "small-on-top" stratification only occurs for a finite range of ϕ_s: $0.64/\mathrm{Pe}_s < \phi_s < 0.2$. These studies thus point to the importance of including a solvent explicitly when studying the drying of a particle suspension. Furthermore, all the theoretical models developed so far are based on isothermal systems but a previous work revealed that temperature and density gradients can emerge in a fast evaporating liquid [32], whose roles in stratifying phenomena are unclear.

To fill the gap, in Chapter 2 we use large scale molecular dynamics simulations with an explicit solvent model to investigate the effects of the evaporation rate of the solvent and the volume fractions of the nanoparticles on the nanoparticle distribution in a drying film. We

examine the density profiles of the solvent and nanoparticles as a function of time. An order parameter is then defined to quantify the degree of stratification and three possible states, "small-on-top", "large-on-top", and "uniform", can be identified using the order parameter. A state diagram in the plane of Pe_s and ϕ_s is constructed and compared to the predictions of the ZJD model, the SW model, and the Sear model. Our results show that "small-on-top" stratification can occur when $\mathrm{Pe}_s\phi_s \gtrsim c$ with $c \sim 1$.

In the simulations discussed in Chapter 2, only a layer of the solvent adjacent to the bottom substrate is thermalized at a given temperature during solvent evaporation, mimicking a typical experimental situation in which the substrate is held at a constant temperature. For such systems, evaporative cooling at the surface of the suspension makes the temperature at the liquid-vapor interface lower than that in the bulk. As a result, a negative temperature gradient is generated from the bulk to the interface in the normal direction of the film. The diffusion of nanoparticles is affected by this thermal gradient, a process termed thermophoresis. In particular, we find that the larger the nanoparticles, the stronger their tendency to migrate toward a cooler region. Therefore, for the systems studied in Chapter 2, themophoresis has a net effect of pushing a larger fraction of larger nanoparticles toward the liquid-vapor interface during evaporation. Thermophoresis is thus at competition with diffusiophoresis that yields "small-on-top". This competition explains our observation that only weak "small-on-top" stratification was found in the systems studied in Chapter 2. At extremely high evaporation rates, evaporative cooling can be significant, resulting in large thermal gradients and strong thermophoresis that can dominate diffusiophoresis and drive the system into "larger-on-top" instead of "small-on-top" predicted by the diffusiophoretic models [20, 24, 29, 30].

The results in Chapter 2 indicate that if a positive thermal gradient, instead of a negative one induced by the evaporative cooling effect, is present in a drying suspension (i.e., if the

temperature at the liquid-vapor interface is higher than that in the bulk of the suspension), then the associated thermophoresis will push a larger fraction of larger nanoparticles away from the interface as the temperature there is higher. As a result, themophoresis and diffusiophoresis will work in synergy and lead to enhanced "small-on-top" stratification. However, if a negative thermal gradient is tuned such that thermophoresis and diffusiophoresis cancel out each other, then a dry film with a uniform distribution of nanoparticles can be obtained. In Chapter 3, we demonstrate this strategy and show that a thermal gradient imposed on a drying suspension can be used to control the distribution of nanoparticles in the dry film. "Larger-on-top", "small-on-top", and uniform distributions can be produced with an appropriate choice of the thermal gradient. We also discuss experimental approaches to achieve various thermal gradients in a drying particle suspension.

The explicit solvent models in Chapter 2 and Chapter 3 are powerful in terms of revealing the fundamental physics underlying the drying process of a particle suspension. However, simulations based on such models require a huge amount of computational resources, which limit the size and time of a system that can be modeled. To overcome these limitations, it is desirable to use alternative approaches to model a drying process. One possibility is to map an explicit solvent system to an implicit one by treating the solvent as a uniform viscous background. The liquid-vapor interface is then replaced by a potential barrier that confines all the particles in the suspension. As the physical foundation of this mapping, it is crucial to understand the capillary force experienced by a spherical particle when it is displaced out of its equilibrium position at a liquid-vapor interface. To this end, a complete theory is needed on a meniscus on the outside of a cylinder that is vertically aligned and penetrates a liquid-vapor interface. We fulfill these two tasks in Chapter 4 and Chapter 5, respectively. Our analyses show that a harmonic potential can be approximately used to describe the confining effect of a liquid-vapor interface on a spherical particle, with a spring

constant that depends on the particle radius, the interfacial tension, and the lateral span of the interface. Such a relationship was also discovered earlier by Joanny and de Gennes for a pinned contact line [33].

In Chapter 6, we map an explicit solvent system to an implicit one and compared the behavior of the two systems during drying. We find that comparable stratification occurs in both models when the suspensions are dried quickly. Our results thus justify the usage of implicit solvent models for particle suspensions. We also discuss the potential limitations and pitfalls of the implicit solvent approach. In Chapter 7, we apply an implicit solvent model to the drying of various soft matter solutions, including a solution film of a mixture of polymers and nanoparticles, a suspension droplet of bidisperse nanoparticles, a solution droplet of a polymer blend, and a solution droplet of diblock copolymers. A rich set of structures after drying is discovered.

In Chapter 8, we summarize all the studies presented in this thesis. A brief discussion about the limitations of our work is provided. An outlook is included on the future of possible research on drying particle suspensions.

Chapter 2

Stratification in drying bidisperse nanoparticle suspensions

This chapter is part of our publication [34]:

Yanfei Tang, Gary. S. Grest, and Shengfeng Cheng, "Stratification in drying films containing bidisperse mixtures of nanoparticles." Langmuir 34, 7161 (2018).

I designed and built all the models for molecular dynamics simulations. Dr. Grest ran all the simulations. I performed all the data analyses and prepared figures. All authors contributed to the writing of this paper. My contributions to this paper were under Dr. Cheng's supervision.

2.1 Introduction

In this chapter we report large-scale molecular dynamics (MD) simulations of the drying of bidisperse particle suspensions, with the solvent modeled explicitly. The model is built upon an earlier model of monodisperse nanoparticle suspensions developed by Cheng and Grest [35] to study the evaporation-induced self-assembly of nanoparticles. To span regimes from $\mathrm{Pe}_l \gg \mathrm{Pe}_s \gg 1$ to $\mathrm{Pe}_l \gg 1 \gtrsim \mathrm{Pe}_s$, we use nanoparticles with diameters 20 and 5 times of that of the solvent. In particular, we focus on the role of the evaporation rate (i.e., Pe_s) and the volume fraction of the smaller nanoparticles, ϕ_s, in controlling the distribution of nanoparticles in the resulting dry films.

2.2 Methods

The solvent is modeled by beads with a mass m interacting through a standard Lennard-Jones (LJ) potential, $U_{\mathrm{LJ}}(r) = 4\epsilon\left[(\sigma/r)^{12} - (\sigma/r)^6 - (\sigma/r_c)^{12} + (\sigma/r_c)^6\right]$, where r is the distance between the centers of two beads, ϵ the unit of energy, and σ the diameter of beads. The interaction is truncated at $r_c = 3.0\sigma$. The nanoparticles are modeled as a uniform distribution of LJ particles of a mass density $1.0m/\sigma^3$. The diameter of a large nanoparticle (LNP) is $d_l = 20\sigma$ and of a small nanoparticle (SNP) is $d_s = 5\sigma$. The mass is $m_l = 4188.8m$ and $m_s = 65.4m$, respectively, for LNPs and SNPs. The nanoparticle-nanoparticle interaction potential, Eqs. (7.12) and (7.13), can be determined analytically by integrating over all the interacting LJ particles within the two nanoparticles [36, 37]. The same Hamaker constant $A_{nn} = 39.48\epsilon$ sets the strength of interaction between all the nanoparticles. To avoid flocculation [38, 39], we set the nanoparticle-nanoparticle interactions to be purely repulsive by truncating the potential at 20.574σ, 13.086σ, and 5.595σ, respectively, for the

LNP/LNP, LNP/SNP, and SNP/SNP pairs. The interaction between a solvent bead and a nanoparticle, Eq. (7.11), can be described similarly with an integrated LJ potential. We set the interaction strength between the solvent and the nanoparticles as $A_{ns} = 100\epsilon$ and truncate the potential at $d/2 + 4\sigma$ where d is the nanoparticle diameter. As a result, both the LNPs and SNPs are fully solvated by the solvent [40].

All the solvent beads are placed in a rectangular simulation box with dimensions $L_x \times L_y \times L_z$, where $L_x = 201\sigma$, $L_y = 201\sigma$, and $L_z = 477\sigma$. These beads form a liquid film with a thickness $H \sim 300\sigma$ (see Table 2.1 for the value of H in each system), which serves as the solvent, and a vapor phase above it. Periodic boundary conditions are imposed in the x-y plane, in which the liquid-vapor interface is located. The nanoparticles are randomly dispersed in the liquid solvent and the system is equilibrated before evaporation is turned on. All the particles are confined between two flat walls at $z = 0$ and $z = L_z$ via a LJ 9-3 potential, $U_W(h) = \epsilon_W \left[(2/15)(D/h)^9 - (D/h)^3 - (2/15)(D/h_c)^9 + (D/h_c)^3\right]$, where $\epsilon_W = 2.0\epsilon$ is the interaction strength, D the characteristic length, h the distance between the center of the particle and the wall, and h_c the cutoff. We set $D = \sigma$ and $h_c = 3\sigma$ (0.8583σ) at the lower (upper) wall for the solvent/wall interactions; the upper wall is thus repulsive for the solvent. For the nanoparticle/wall interactions we set $D = d/2$ and $h_c = 0.8583D$ at both walls to make them purely repulsive for all the nanoparticles.

All simulations were performed with the Large-scale Atomic/Molecular Massively Parallel Simulator (LAMMPS) [41]. The equations of motion were integrated using a velocity-Verlet algorithm with a time step $\delta t = 0.01\tau$, where $\tau = \sigma(m/\epsilon)^{1/2}$ is the time unit. During the equilibration, Langevin dynamics were applied to all the particles with a damping constant $\Gamma = 0.1\tau^{-1}$ at a reduced temperature $T = 1.0\epsilon/k_B$. We equilibrated the system for at least $4 \times 10^5\tau$ so that all the nanoparticles were well dispersed in the solvent. In the evaporation runs, the Langevin thermostat was applied only for the solvent and the nanoparticles within

10σ of the lower wall [32]. The evaporation was implemented by removing the vapor beads in the deletion zone $[L_z - 100\sigma, L_z]$, which was about 70σ away from the equilibrium liquid-vapor interface. The evaporation rate was controlled by varying the rate at which the vapor beads in the deletion zone were removed from the system. As the initial thickness of the liquid film is about 300σ and we only focus on the range of drying where the film is still more than half of its initial thickness, the distance from the thermalized layer to the liquid-vapor interface is thus at least 140σ. This separation is more than sufficient to ensure that the evaporating behavior at the interface is not affected by the thermostat employed in our simulations [32, 42].

2.3 Results and discussion

Table 2.1: Parameters for the fifteen systems studied.

System	N_l	N_s	ϕ_l	ϕ_s	H/σ	ζ	$v\tau/\sigma$	Pe_l	Pe_s
$\phi_{0.011}R_{30}$	200	1920	0.072	0.011	289.2	30	1.14×10^{-3}	109.7	27.4
$\phi_{0.011}R_5$	200	1920	0.072	0.011	289.2	5	2.05×10^{-4}	19.7	4.9
$\phi_{0.034}R_{30}$	200	6400	0.068	0.034	304.4	30	1.13×10^{-3}	114.3	28.6
$\phi_{0.034}R_5$	200	6400	0.068	0.034	304.4	5	2.04×10^{-4}	20.7	5.2
$\phi_{0.034}R_1$	200	6400	0.068	0.034	304.4	1	4.33×10^{-5}	4.4	1.1
$\phi_{0.068}R_{30}$	200	12800	0.068	0.068	306.5	30	1.04×10^{-3}	105.9	26.5
$\phi_{0.068}R_5$	200	12800	0.068	0.068	306.5	5	2.03×10^{-4}	20.8	5.2
$\phi_{0.068}R_1$	200	12800	0.068	0.068	306.5	1	4.21×10^{-5}	4.3	1.1
$\phi_{0.10}R_{30}$	200	19200	0.067	0.10	309.7	30	8.69×10^{-4}	89.7	22.4
$\phi_{0.10}R_5$	200	19200	0.067	0.10	309.7	5	1.96×10^{-4}	20.2	5.1
$\phi_{0.10}R_1$	200	19200	0.067	0.10	309.7	1	4.15×10^{-5}	4.3	1.1
$\phi_{0.13}R_{30}$	200	25600	0.067	0.13	307.2	30	7.61×10^{-4}	78.0	19.5
$\phi_{0.13}R_5$	200	25600	0.067	0.13	307.2	5	1.91×10^{-4}	19.6	4.9
$\phi_{0.16}R_{20}$	200	32000	0.065	0.16	317.8	20	6.37×10^{-4}	67.5	16.9
$\phi_{0.16}R_5$	200	32000	0.065	0.16	317.8	5	1.85×10^{-4}	19.6	4.9

All of our simulations have $N_l = 200$ large nanoparticles (LNPs) of a diameter $d_l = 20\sigma$, where σ is the unit of length. The small nanoparticles (SNPs) have a diameter $d_s = 5\sigma$ and

their number, N_s, is varied from 1920 to 32000. Further details of the simulations are given in the Methods section 2.2. All the nanoparticles are initially dispersed in a liquid consisting of Lennard-Jones (LJ) particles of a size σ in equilibrium with its vapor in a rectangular box with dimensions $L_x \times L_y \times L_z$, where $L_x = 201\sigma$, $L_y = 201\sigma$, and $L_z = 477\sigma$. The number of LJ particles vary from about 7×10^6 for $N_s = 1920$ to about 5×10^6 for $N_s = 32000$. The initial volume fraction of nanoparticles is $\phi_i \equiv \pi N_i d_i^3/(6L_xL_yH)$, where $i \in \{l, s\}$ and H is the film thickness at equilibrium. Evaporation of the solvent is implemented by removing the LJ particles in the deletion zone $[L_z - 100\sigma, L_z]$ [32]. The evaporation rate is controlled by setting the number of particles, ζ, removed every τ, where τ is the LJ unit of time. When the solvent evaporates into a vacuum, the evaporation rate is initially very high ($\zeta \sim 600$), then decreases with time, and finally reaches a plateau value corresponding to $\zeta \sim 20$–30, which slightly depends on ϕ_s [32]. For the drying nanoparticle suspensions studied in this chapter, we set ζ constant and the values of ζ are varied to span very fast evaporation ($\zeta = 20$ or 30) to the slowest evaporation rate ($\zeta = 1$) accessible with current computational resources.[1] We label each system as $\phi_{\phi_s}R_\zeta$ using the values of ϕ_s and ζ. For each system we directly follow the location of the liquid-vapor interface during evaporation and compute v_e, which quantifies the speed of evaporation. For diffusion constants, we take $D_l = 3 \times 10^{-3}\sigma^2/\tau$ from our previous study [35] and assume $D_s = D_l d_l/d_s = \alpha D_l$. The values of Péclet numbers can then be estimated. In particular, $\mathrm{Pe}_s = \frac{Hv_e}{D_s} \approx \frac{v_e}{4\times10^{-5}\sigma/\tau}$. For the systems studied here, $v_e \approx 4\zeta \times 10^{-5}\sigma/\tau$. As a result, the values of ζ and Pe_s are close, the latter of which can thus be roughly read from the subscript of R in the system label $\phi_{\phi_s}R_\zeta$. Then $\mathrm{Pe}_l = \alpha\mathrm{Pe}_s = 4\mathrm{Pe}_s$. All the systems and parameters are listed in Table 2.1.

Snapshots of 4 nanoparticle suspensions under various evaporation rates are shown in Fig. 2.1. These 4 are picked as they are representative to demonstrate how the distribution of nanopar-

[1] The simulation results with $\zeta = 30$ or 20 are very close to those obtained with the solvent evaporating into a vacuum.

ticles in a drying film changes when the evaporation rate (i.e., Pe_s) and ϕ_s are varied. Snapshots of the other 11 systems can be found in the Appendix A. We first focus on the systems $\phi_{0.10}R_{30}$, $\phi_{0.10}R_5$, and $\phi_{0.10}R_1$ with $N_s = 19200$ [Figs. 2.1(a)-(c)] and investigate the role of evaporation rates. For the ultrafast evaporating system $\phi_{0.10}R_{30}$, the SNPs quickly accumulate and form a dense skin layer near the liquid-vapor interface, as shown in Fig. 2.1(a). However, the LNPs are also found to accumulate just below this interfacial layer of SNPs. When the evaporation rate is reduced by a factor of 6 in the system $\phi_{0.10}R_5$, the skin layer of SNPs becomes less distinct, though the SNPs still accumulate near the interface, as shown in Fig. 2.1(b). In this case the extent of accumulation for the LNPs just below the surface layer of SNPs diminishes significantly. As a result, the "small-on-top" stratification is enhanced in $\phi_{0.10}R_5$, in which the solvent evaporates more slowly than in $\phi_{0.10}R_{30}$. This trend is not predicted by the existing theories [20, 24], which anticipate that "small-on-top" stratification should be suppressed and become less distinct when the evaporation rate is reduced. Below we will show that this unexpected behavior results from the density gradients of the solvent that develop during evaporation. When the evaporation rate is further reduced by a factor of 5 in the system $\phi_{0.10}R_1$, the accumulation of nanoparticles near the interface almost disappears and the LNPs and SNPs are uniformly distributed in the drying film, as shown in Fig. 2.1(c).

Figure 2.1(d) shows the system $\phi_{0.034}R_5$, which has the same evaporation rate as $\phi_{0.10}R_5$ [Fig. 2.1(b)], but ϕ_s is smaller by a factor of 3. Compared to $\phi_{0.10}R_5$, the surface accumulation of SNPs during solvent evaporation is weaker and the enrichment of LNPs near the receding interface is much stronger in $\phi_{0.034}R_5$.

To further quantify how the distributions of the solvent, LNPs, and SNPs evolve during evaporation, we plot their density profiles in Fig. 2.2 at various times corresponding to the snapshots in Fig. 2.1. The density profiles for the remaining 11 systems can be found in the

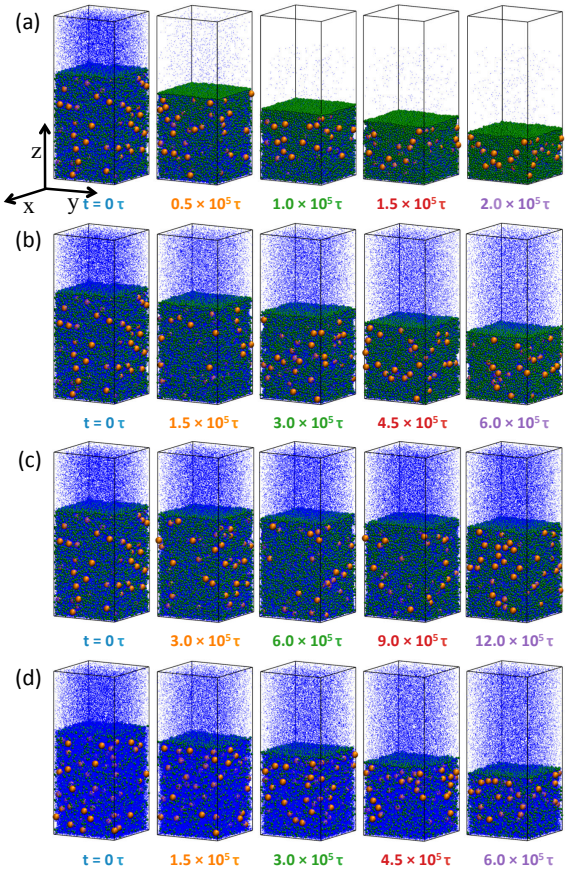

Figure 2.1: Snapshots of the systems during evaporation for (a) $\phi_{0.10}R_{30}$, (b) $\phi_{0.10}R_5$, (c) $\phi_{0.10}R_1$, and (d) $\phi_{0.034}R_5$. Time is indicated below each snapshot with $t = 0\tau$ for the equilibrium state prior to evaporation. Corresponding density profiles are plotted in Fig. 2.2. Color code: LNPs (orange), SNPs (green), and solvent (blue). For clarity, only 5% of the solvent beads are visualized. In the last frame the volume fractions of nanoparticles are: (a) $\phi_l = 0.15$, $\phi_s = 0.23$; (b) $\phi_l = 0.11$, $\phi_s = 0.16$; (c) $\phi_l = 0.080$, $\phi_s = 0.12$; (d) $\phi_l = 0.11$, $\phi_s = 0.057$.

Appendix A. The density is defined as $\rho_i(z) = n_i(z)m_i/(L_xL_y\delta z)$, where $n_i(z)$ represents the number of i-type particles in the spatial bin $[z-\delta z/2, z+\delta z/2]$ with the bin width $\delta z = 1.0\sigma$ and m_i is the mass of i-type particles. The unit of density is thus m/σ^3. For a nanoparticle occupying several bins, we partition the nanoparticle mass to bins based on the partial volume of the nanoparticle enclosed by each bin. For computing the solvent density, the solvent particles are treated as point masses and the excluded volume occupied by nanoparticles in each spatial bin is subtracted.[2] To understand the density profiles of the solvent, we also include in Fig. 2.2 (top row) the corresponding local temperature, $T(z)$, which is computed as the mean kinetic energy of solvent beads in the spacial bin $[z-2.5\sigma, z+2.5\sigma]$. The results clearly show evaporative cooling, especially for ultrafast evaporation rates, which leads to negative temperature gradients in the liquid solvent. The calculation of temperature in an evaporating system, which is out of equilibrium, as well as the fact that $T(z)$ has a minimum at the liquid-vapor interface, is discussed in detail in Ref. [32].

Figure 2.2 shows quantitatively the trends that are qualitatively identified from Fig. 2.1. It is noted that for all the systems at equilibrium there is always a slight density peak near the liquid-vapor interface for the SNPs since they are smaller and their centers can get closer to the interface. When the solvent evaporates very fast, both the LNPs and SNPs are found to accumulate near the interface, as shown in Figs. 2.2(c) and (d) for $\phi_{0.10}R_{30}$. When the evaporation rate is reduced, the SNPs still accumulate near the interface but the LNPs are almost uniformly distributed in the region below the surface layer where SNPs are concentrated [Figs. 2.2(g) and (h)]. As a result, the "small-on-top" stratification becomes more significant for $\phi_{0.10}R_5$. This change is accompanied by a change of the density profile of the solvent as the evaporation rate is reduced. As shown in Fig. 2.2(b) for $\phi_{0.10}R_{30}$ with a ultrafast evaporation rate, the solvent density increases significantly at the liquid-vapor

[2]The radius of the spherical excluded volume of a SNP (LNP) is determined to be 3.12σ (10.6σ) which is 0.62σ (0.6σ) larger than its nominal radius.

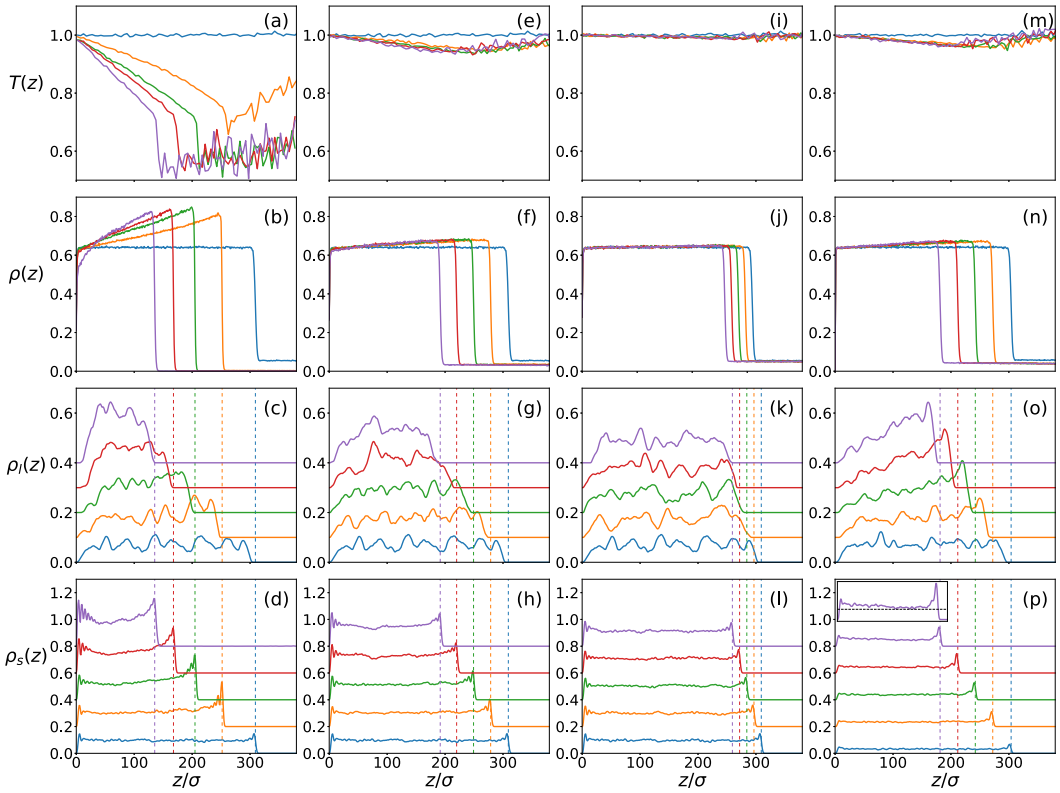

Figure 2.2: Temperature profile during evaporation (top row) and density profiles for the solvent (second row), LNPs (third row), and SNPs (bottom row) for $\phi_{0.10}R_{30}$: (a)–(d), $\phi_{0.10}R_5$: (e)–(h), $\phi_{0.10}R_1$: (i)–(l), and $\phi_{0.034}R_5$: (m)–(p). For each system, each set of curves of the same color corresponds to the snapshot with time indicated in the same color in Fig. 2.1. The vertical dashed lines indicate the location of the liquid-vapor interface. For clarity, the density profiles for LNPs (SNPs) are shifted upward by $0.1m/\sigma^3$ ($0.2m/\sigma^3$) successively. The inset in (p) shows a weakly negative gradient of SNP density for $\phi_{0.034}R_5$ at time $t = 6 \times 10^5\tau$ with a dashed horizontal reference line.

interface due to strong evaporative cooling [Fig. 2.2(a)], leading to a large positive gradient of the density profile. The gradients are much smaller for $\phi_{0.10}R_5$ with a smaller evaporation rate [Figs. 2.2(e) and (f)]. In the systems studied here, the nanoparticles are well solvated and form a uniform dispersion in equilibrium prior to solvent evaporation. A density gradient of the solvent that develops during evaporation induces a chemical potential gradient, which drives nanoparticles to regions with a higher solvent density. Our simulations thus indicate a phoretic effect on nanoparticle motion when the solvent evaporates ultrafast. Hereafter we

use the term "thermophoresis" to denote the drift of nanoparticles under a density gradient of the solvent, which is caused by the thermal gradient in the evaporating solvent [43]. A disscusion about thermophoresis of nanoparticles is in Appendices B. A similar effect associated with the density gradients of polymers was observed in our previous work where a polymer solution containing nanoparticles underwent drying [44].

As the solvent evaporates, the liquid-vapor interface recedes and the nanoparticles with Pe > 1 have a tendency to accumulate near the interface. When the SNPs are the major phase and their accumulation at the interface leads to a concentration gradient that is large enough, the LNPs are pushed away by an osmotic pressure induced by the gradient of SNP concentration. This diffusiophoretic mechanism is underlying the current physical models of "small-on-top" stratification [20, 24, 29, 30]. However, a positive gradient of solvent density can develop during evaporation because of evaporative cooling of the liquid-vapor interface and its magnitude is large when evaporation is ultrafast. This gradient of solvent density tends to drive all nanoparticles to the interface, but the thermophoretic effect is stronger for LNPs than for SNPs (see the Appendix B for direct evidence of this behavior). The net effect of the positive gradient of solvent density is thus to push more LNPs toward the interfacial region. The competition between thermophoresis favoring more LNPs near the interface and a fast receding interface, which leads to SNP concentration at the interface and pushes LNPs out of this region via diffusiophoresis, is the key to understand our results. For ultrafast evaporation ($\zeta = 30$), thermophoresis is significant and we observe an accumulation of LNPs just below the skin layer of SNPs, as in the system $\phi_{0.10}R_{30}$ [Figs. 2.2(c) and (d)]. When the evaporation rate is reduced to $\zeta = 5$ as in the system $\phi_{0.10}R_5$, the density gradient of the solvent, as well as the temperature gradient, is much smaller [Figs. 2.2(f) and (e)], which cannot overcome the concentration gradient of SNPs any more in terms of transporting LNPs. Therefore, thermophoresis is strongly suppressed and the LNPs do not accumulate

near the interface in $\phi_{0.10}R_5$, resulting in stronger "small-on-top" stratification [Figs. 2.2(g) and (h)].

That the solvent density develops a positive gradient in the interfacial region during ultrafast evaporation is due to strong evaporative cooling at the interface [32], as shown in Fig. 2.2 (top row). In this case the diffusion of the solvent toward the interface is driven by a temperature gradient. Evaporative cooling also makes nanoparticles to diffuse more slowly near the receding interface, which increases the Péclet numbers of those nanoparticles. This effect is stronger for higher evaporation rates which lead to stronger evaporative cooling. The Péclet numbers used in this chapter are defined with the diffusion constants in the solvent at the bulk temperature and are thus the lower bounds of actual values. However, this simplification does not affect the results and conclusions presented in this chapter, as discussed in more detail later.

When the evaporation rate is reduced, the degree of interfacial cooling decreases. More examples of the temperature profile at various evaporation rates are included in the Appendix A. For low evaporation rates, the thermal conduction in the suspension is fast enough to maintain a uniform temperature profile and the density profile of the solvent is almost flat. This situation is realized in the system $\phi_{0.10}R_1$ [Figs. 2.2(i)–(l)], where evaporation is not fast enough to enable SNPs to accumulate at the interface and there is no density gradient of the solvent to drive nanoparticles into the interfacial region either. As a result, the nanoparticles are almost uniformly distributed in the drying film for $\phi_{0.10}R_1$.

Comparison of $\phi_{0.10}R_5$ with $N_s = 19200$ and $\phi_{0.034}R_5$ with $N_s = 6400$ shows the effect of the initial volume fraction of SNPs, ϕ_s, on the evaporation-induced stratification. In both cases the evaporation rate is the same ($\zeta = 5$) and the density gradients of the solvent and the temperature gradients are similar [Figs. 2.2(e), (f), (m), and (n)]. However, the interfacial region in which SNPs are accumulated is wider for $\phi_{0.10}R_5$ which has a larger ϕ_s

[compare Figs. 2.2(h) and (p)]. In $\phi_{0.10}R_5$ the LNPs are almost uniformly distributed in the region below the SNP-rich skin layer [Fig. 2.2(g)], even though $\mathrm{Pe}_l \gg 1$. The underlying reason is that the diffusiophoretic force due to the gradient of SNP concentration, which drives the LNPs away from the interface, almost balances the thermophoretic force from the small positive gradient of solvent density, which pushes the LNPs toward the interface. For $\phi_{0.034}R_5$ which has a much smaller ϕ_s, however, there is a strong accumulation of LNPs near the interface [Fig. 2.2(o)], as ϕ_s is too small to yield a noticeable gradient of SNP concentration that is needed to balance the gradient of solvent density. In other words, ϕ_s is too small to enable diffusiophoresis to neutralize thermophoresis. In the late stage of drying, the distribution of SNPs in $\phi_{0.034}R_5$ even shows a negative gradient and $\rho_s(z)$ decreases slightly toward the interface [Fig. 2.2(p) and inset], indicating "large-on-top" stratification. This trend is qualitatively consistent with the prediction of the existing theories that a transition from "small-on-top" to "large-on-top" will occur when ϕ_s is reduced [24, 29, 30].

Presently, there is actually no universally adopted criterion on how to identify and quantify stratification. In experiments, especially in those using surface characterization such as AFM measurements, an excess of small particles at the top surface is taken as a signature of "small-on-top" stratification as it is difficult to probe depth profiles of particle concentrations [25, 26]. However, this criterion is not suitable for our simulations as an excess of SNPs at the surface of the film even occurs in equilibrium. In theory, a "small-on-top" state is usually defined as the one in which large particles have a negative concentration gradient going toward the surface of the film [24, 25]. Here, to obtain a quantitative measure of the degree of stratification, we use the full concentration profile of nanoparticles and compute the average positions of SNPs and LNPs along the z direction (i.e., normal to the film) as $\langle z_i \rangle = \frac{1}{N_i} \sum_{n=1}^{N_i} z_{in}$ with $i \in \{l, s\}$, as well as the average separation $\langle z_l \rangle - \langle z_s \rangle$. The results are shown in Figs. 2.3. At equilibrium, both $\langle z_l \rangle$ and $\langle z_s \rangle$ are very close to $H/2$, where $H \equiv H(0)$

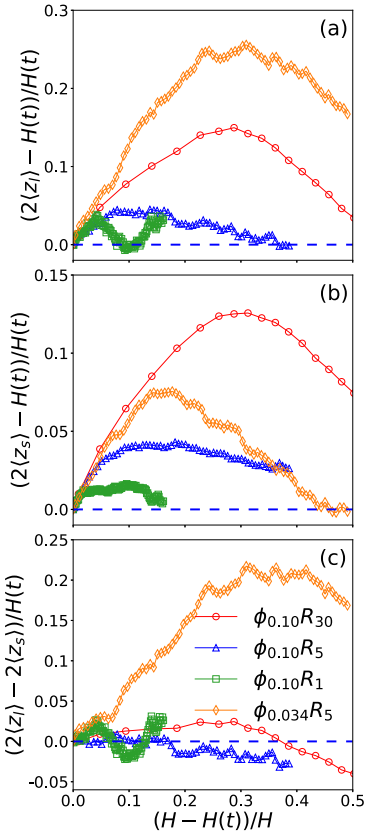

Figure 2.3: Average position in the z direction relative to the center of the film, normalized by $H(t)/2$, is plotted against the extent of drying, quantified as $(H - H(t))/H$, for (a) LNPs and (b) SNPs. Panel (c) shows the average separation between LNPs and SNPs, normalized by $H(t)/2$, as a function of the extent of drying. Data are for $\phi_{0.10}R_{30}$ (red circles), $\phi_{0.10}R_5$ (blue triangles), $\phi_{0.10}R_1$ (green squares), and $\phi_{0.034}R_5$ (orange diamonds).

is the equilibrium film thickness. If the i-type nanoparticles are accumulated (depleted) near the liquid-vapor interface during evaporation, then $\langle z_i \rangle$ becomes larger (smaller) than $H(t)/2$ with $H(t)$ as the film thickness at time t. In Figs. 2.3(a) and (b) we plot $\langle z_l \rangle - H(t)/2$ and $\langle z_s \rangle - H(t)/2$, all normalized by $H(t)/2$, against $(H - H(t))/H$, which quantifies the extent of drying. Fig. 2.3(a) clearly shows that the LNPs accumulate near the interface for $\phi_{0.10}R_{30}$ (faster evaporation) and $\phi_{0.034}R_5$ (smaller ϕ_s), while they are depleted near the interface in the late stage of drying for $\phi_{0.10}R_5$ (reduced evaporation rate, larger ϕ_s). Fig. 2.3(b) shows in the early stage of drying, the SNPs always accumulate near the receding interface, even for $\mathrm{Pe}_s \simeq 1$ as in $\phi_{0.10}R_1$.

In Fig. 2.3(c), we plot $\langle z_l \rangle - \langle z_s \rangle$, normalized by $H(t)/2$, as a function of $(H - H(t))/H$. A "small-on-top" stratifying state corresponds to $\langle z_l \rangle - \langle z_s \rangle < 0$ while a "large-on-top" case has $\langle z_l \rangle - \langle z_s \rangle > 0$. A larger negative (positive) value of $\langle z_l \rangle - \langle z_s \rangle$ indicates stronger small-on-top (large-on-top) stratification. If the distribution of nanoparticles in the film is uniform, then $\langle z_l \rangle - \langle z_s \rangle \simeq 0$. Our analyses show that the classification scheme adopted here yields results consistent with those based on concentration gradients of particles. To be consistent with the criteria used in the ZJD and SW models [24, 29], we focus on the range of drying up to $H(t) = H/2$ and regard the state at this stage as the stratification outcome. Fig. 2.3(c) shows that "small-on-top" only emerges at late times for $\phi_{0.10}R_{30}$ but occurs very quickly for $\phi_{0.10}R_5$. It is clear that "small-on-top" stratification is enhanced as Pe_s is reduced ($\phi_{0.10}R_{30} \to \phi_{0.10}R_5$). When Pe_s is reduced further, a "small-on-top" to "uniform" transition occurs ($\phi_{0.10}R_5 \to \phi_{0.10}R_1$). When ϕ_s is reduced at a given Pe_s, there is a transition from "small-on-top" to "large-on-top" ($\phi_{0.10}R_5 \to \phi_{0.034}R_{30}$: ϕ_s changes from 0.10 to 0.034).

In Fig. 2.4, all 15 systems studied here are included in the state diagram in the Pe_s–ϕ_s plane, and compared to the predictions of the ZJD model [24], the SW model [29], and the Sear model [30]. The 4 systems shown in Figs.2.1–2.3 are already classified. The identification

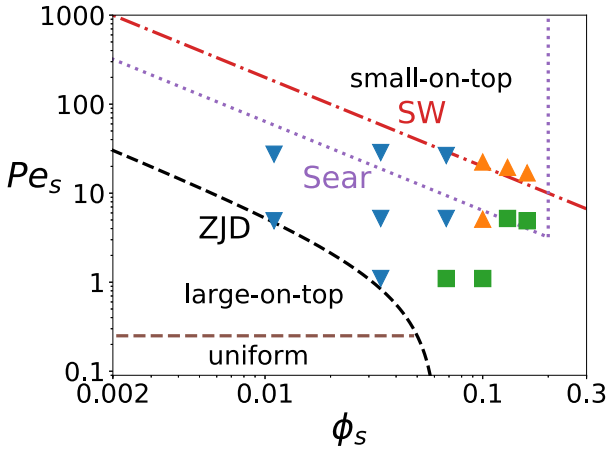

Figure 2.4: The state diagram for the 15 systems studied here with the predictions of the ZJD model [24], the SW model [29], and the Sear model [30]. The systems showing "small-on-top" or "large-on-top" stratification are indicated by upward or downward triangles, respectively. The systems that do not show stratified distributions of nanoparticles are designated as "uniform" and indicated with squares. The ZJD model predicts that "small-on-top" occurs when $\mathrm{Pe}_s \gtrsim 1/(\alpha^2\phi_s) - 1$ (black dashed line) and "uniform" occurs when $\mathrm{Pe}_s < 1/\alpha$ (brown dashed line). The SW model predicts that "small-on-top" occurs when $\mathrm{Pe}_s \gtrsim 2/\phi_s$ (red dash-dotted line). The Sear model predicts that "small-on-top" occurs only for a finite range of ϕ_s, corresponding to $0.64/\mathrm{Pe}_s < \phi_s < 0.20$ (purple dotted line).

of the stratifying outcome for the remaining 11 systems is included in the Appendix A. In our simulations, only 4 systems show "small-on-top" stratification, including $\phi_{0.10}R_{30}$, $\phi_{0.10}R_5$, $\phi_{0.13}R_{30}$, and $\phi_{0.16}R_{20}$. Other 4 systems have a uniform distribution of nanoparticles after drying, including $\phi_{0.068}R_1$, $\phi_{0.10}R_1$, $\phi_{0.13}R_5$, and $\phi_{0.16}R_5$. The remaining 7 exhibit "large-on-top" stratification. Note that all systems simulated here are in the "small-on-top" regime predicted by the ZJD model. However, the simulation data show that "small-on-top" stratification only occurs at Pe_s and ϕ_s much higher than the threshold value from the ZJD model that predicts $\alpha^2(\mathrm{Pe}_s + 1)\phi_s > 1$. The comparison thus indicates that the ZJD model significantly overestimates "small-on-top" stratification, in agreement with Makepeace *et al.* [25] and Sear and Warren [29].

As discussed before, the Péclet numbers used to construct Fig. 2.4 are the lower bounds. If the temperature dependence of the diffusion constants were accounted for, then the actual Péclet numbers might even be higher especially for high evaporation rates (i.e., for $\zeta = 30$ or 5), shifting the corresponding data points in Fig. 2.4 upward. Furthermore, the amount of shift is very small as the Péclet numbers enter Fig. 2.4 on a logarithmic scale. As a result, Fig. 2.4 and the discussion below are not affected by the simplification adopted here that the Péclet numbers are defined using the diffusion constants in the solvent thermalized at $T = 1.0\epsilon/k_B$ (see Methods section for more details) and ignoring their potential variation during evaporation because of evaporative cooling.

It is challenging to distinguish the SW model and the Sear model using our simulation results. The SW model predicts that the "small-on-top" regime roughly corresponds to $\mathrm{Pe}_s \gtrsim 2/\phi_s$ [29]. Our data fit to this prediction reasonably well with 3 systems exhibiting "small-on-top" as expected by the SW model. This agreement indicates that the explicit solvent model used here has successfully captured the back-flow of the solvent when nanoparticles drift, as emphasized in the SW model. This back-flow largely cancels out the osmotic pressure

on LNPs from the concentration gradient of SNPs. As a result, much larger Pe_s and ϕ_s are needed to drive a system into the "small-on-top" regime. However, our simulations also indicate that the solvent develops negative temperature and positive density gradients for ultrafast evaporation because of evaporative cooling at the interface. The presence of thermophoretic effects associated with these density gradients can explain the deviation of the simulation results from the prediction of the SW model. For example, the system $\phi_{0.10}R_5$ is predicted to be in the "large-on-top" regime but actually shows "small-on-top" stratification, which as discussed earlier is due to thermophoresis of nanoparticles from the density gradient of the solvent. As another example, the systems $\phi_{0.068}R_{30}$ is at the boundary of the "small-on-top" regime according to the SW model. However, for this ultrafast evaporating system the large positive gradient of solvent density pushes LNPs toward the interface much more strongly than SNPs, i.e., thermophoresis is significant. Consequently, $\phi_{0.068}R_{30}$ shows clear "large-on-top" stratification.

Our data also seem to be roughly consistent with the Sear model [30], which predicts that "small-on-top" stratification only occurs when $0.64/\mathrm{Pe}_s < \phi_s < 0.2$. Fig. 2.4 shows that the 4 "small-on-top" systems identified in our simulations are roughly consistent with this prediction. However, $\phi_{0.068}R_{30}$ and $\phi_{0.034}R_{30}$ are in the "small-on-top" regime predicted by the Sear model, but actually are identified as "large-on-top" in our simulations. In these systems where ϕ_s is small, the thermophoretic effects from the density gradients of the solvent dominate, which push LNPs toward the interface strongly and drive the systems into the "large-on-top" regime.

Both the SW and Sear models predict that the boundary of the "small-on-top" regime is roughly at $\mathrm{Pe}_s\phi_s \gtrsim c$ with c at the order of 1 [29, 30]. This prediction is supported by our simulation results. To test the Sear model further, one would need data for $\phi_s > 0.2$. However, with the present model, if ϕ_s is too large, some SNPs move into the vapor during

evaporation.[3] At present, the regime of very high volume fractions of SNPs remains an open problem.

Limitations of the computational model used here should be noted. The SNPs in this study have a diameter about 5 times of the size of the solvent particle. If we denote the Péclet number of the solvent as Pe_0, then $\mathrm{Pe}_0 \simeq \mathrm{Pe}_s/5$. In our simulations, Pe_s varies from about 1 to 30. As a result, Pe_0 is about 0.2 to 6. In most experiments, Pe_0 is much less than 0.1. This comparison indicates our simulations are all in the ultrafast evaporation regime from an experimental perspective.

Similar conclusions can be drawn if we examine the receding speed of the liquid-vapor interface, v_e. The lowest value of v in our simulations is $\sim 4 \times 10^{-5}\sigma/\tau$. With a typical value of σ/τ at 100 m/s, this speed is about 4 mm/s in simulations. For water evaporating under ambient conditions, v is typically about 0.1 μm/s. Recently, Utgenannt *et al.* used infrared radiation to speed up the evaporation of water and increased v to about 2 μm/s [10]. In the experiment of Luo *et al.*, v is about 2.5 μm/s [22]. Even so, the value of v in our simulations is still about 2×10^3 times larger than that in the experiments. This large factor can be understood as follows. In a typical experiment on the drying of particle suspensions, the thickness of films is usually around 0.1 to 1 mm. However, in our simulations, the film thickness is about 300σ, or 150 nm if we set $\sigma = 0.5$ nm. To achieve the same Péclet number, $\mathrm{Pe} \equiv vH/D$, the value of v in our simulations has to be larger than that in a typical experiment by a factor of about 10^3 to 10^4. However, if a drying experiment was performed on a liquid film with submicron thickness containing nanoparticles, the evaporation rates (i.e., the values of v) would have to be similar to those studied here in order to drive the system into the regime where "small-on-top" stratification might occur. Density/temperature gradients are expected to develop in such liquid films that undergo ultrafast drying and the

[3] We have observed that some SNPs (~ 500) moved into the vapor during solvent evaporation for $\phi_s = 0.13$ and 0.16. These SNPs are exlcuded from the analyses presented here.

thermophoretic effects found in our simulations may become experimentally relevant.

The solvent in this study is modeled as a LJ liquid at temperature $T = 1.0\epsilon/k_{\mathrm{B}}$, where ϵ is the unit of energy (see the Methods section). This temperature is about $0.9T_c$, where T_c is the critical temperature of a LJ liquid. At this temperature the solvent can evaporate extremely fast, which leads to strong evaporative cooling and large density gradients near the interface. For water with $T_c = 647$ K, this condition would correspond to a temperature around 600 K and a pressure around 120 atm to maintain a liquid-vapor coexistence at this temperature. If water evaporates at 600 K into a vacuum, then the evaporation rate and the corresponding receding speed of the interface will be comparable to those in our simulations. The density gradients of the liquid are also expected to emerge in such systems.

In order to design MD simulations of the drying of nanoparticle suspensions that are more comparable to typical experiments, one would need to decrease v, but keep $\mathrm{Pe}_s \sim 1$. One viable possibility is to decrease the diffusion constant of nanoparticles. For example, larger particles can be used but they would require more solvent particles to form suspensions, rendering very big systems that may be inaccessible with current computational resources. Another way is to make the solvent more viscous with regard to the diffusion of nanoparticles but to maintain the liquid-vapor coexistence, which is needed for the evaporation process to be fast enough to be modeled via MD. Several options include tuning the nanoparticle-solvent interactions to slow down the diffusion of nanoparticles or adding other solutes such as polymer chains into the suspension to increase its viscosity. The nanoparticle-nanoparticle interactions are another factor that may be explored. In this chapter to be consistent with most theoretical models based on hard spheres, we set the direct nanoparticle-nanoparticle interactions to be purely repulsive, though there exist weak solvent-mediated attractions between nanoparticles. It is interesting to see how the outcome of drying changes when nanoparticles strongly attract each other. All these remain potential directions for future

studies.

2.4 Conclusion

MD simulations with an explicit solvent are reported on the drying of bidisperse nanoparticle suspensions and indicate that "small-on-top" stratification occurs when the evaporation rate (quantified by the Péclet numbers of the nanoparticles: Pe_l and Pe_s) and the volume fraction of the smaller particles (ϕ_s) are large enough. Boundary of the "small-on-top" regime is found to be roughly $\mathrm{Pe}_s\phi_s \gtrsim c$ with $c \sim 1$, consistent with the SW model ($c = 2$) [29] and the Sear model ($c = 0.64$) [30]. In the Pe_s–ϕ_s plane, this boundary is to the right of and above the boundary, roughly $\mathrm{Pe}_s\phi_s \gtrsim \alpha^{-2}$ for small ϕ_s, predicted by the ZJD model that treats the solvent as an implicit viscous background [24]. The two predictions differ roughly by a factor of α^2, which can be quite large if the particle size ratio $\alpha \gg 1$. As pointed out by Sear and Warren [29], this is due to the fact that the implicit solvent model neglects the back-flow of the solvent when particles drift, which largely cancels out the diffusiophoretic drift of LNPs induced by the concentration gradient of SNPs. As a result, the drift velocity of LNPs in a drying film is overestimated by a factor of α^2 by the implicit solvent model [20, 24]. Our results are consist with the SW and Sear models, confirming that it is important to include the solvent explicitly in a physical model of stratification, or generally the drift of particles, in a suspension.

Our simulations further reveal that the solvent can develop positive density gradients in ultrafast evaporating suspensions because of evaporative cooling of the interface, which leads to thermophoretic effects on particle motion. For a bidisperse nanoparticle suspension undergoing quick drying ($\mathrm{Pe}_l > \mathrm{Pe}_s \gg 1$), the net thermophoretic effect is to push more LNPs toward the interfacial region. This effect can lead to "large-on-top" stratification at high Pe_s

even when "small-on-top" stratification is expected. This deviation is due to thermophoresis which favors "large-on-top" and competes with a fast receding interface that drives "small-on-top" as emphasized in the diffusiophoretic models [20, 24, 29, 30]. Similar effect can also make "small-on-top" stratification stronger as the evaporation rate is reduced, since the thermophoretic driving which favors LNPs on top is mitigated. Our results confirm the necessity of considering solvent explicitly in theory and modeling. In the presence of gravity, a convective flow can form to balance the solvent gradient from ultrafast evaporation. This points to the potential need of considering convective flow in next-generation physical models of stratifying phenomena.

Because of thermophoresis that drives more LNPs toward the receding interface, the simulations reported here only show weak "small-on-top" stratification when it actually occurs. In other cases thermophoresis is strong enough that the stratification of large and small particles is reversed to "large-on-top" even when "small-on-top" is predicted by the diffusiophoretic models [29, 30]. In order to promote "small-on-top" stratification, thermophoresis needs to be suppressed. Indeed, we have observed stronger "small-on-top" stratification if all the liquid and vapor are thermalized at a constant temperature during evaporation, where thermal and density gradients and associated thermophoretic transport are removed. However, thermophoresis can also be exploited to produce "large-on-top" stratification under circumstances where it is not expected. Our results thus indicate that phoretic effects can be used as a knob to control the outcome of stratification. Work along this line is discussed in the next chapter.

Chapter 3

Control of stratification via thermophoresis

This chapter is part of a paper that is currently under review at *Langmuir*:

Yanfei Tang, Gary. S. Grest, and Shengfeng Cheng, "Control of stratification in drying particle suspensions via temperature gradients," submitted to Langmuir.

I designed and built all the models for molecular dynamics simulations. Dr. Grest ran most of the simulations. I ran the simulations to demonstrate the thermophoresis of the nanoparticles and to compute their diffusion coefficients. I performed all the data analyses and prepared figures. All authors contributed to the writing of this paper. My contributions to this paper were under Dr. Cheng's supervision.

3.1 Introduction

In the previous chapter, we demonstrated the occurrence of counterintuitive "small-on-top" stratification when a suspension of a bidisperse mixture of nanoparticles is dried extremely fast. At present, the idea of diffusiophoresis being responsible for "small-on-top" stratification is widely supported [20, 23, 24, 29, 30, 34]. In this picture, when the Péclet number of the smaller particles, Pe_s, is much larger than 1 and the volume fraction of the smaller particles, ϕ_s, is above certain threshold that depends on Pe_s, the smaller particles congregate near the receding interface during evaporation and their distribution develops a gradient that decays into the drying film. This gradient tends to push the larger particles out of the interfacial region and consequently the larger particles are depleted near the interface, resulting in "small-on-top" stratification.

The key ingredient of the diffusiophoretic model is that the cross-interaction between the large and small particles has asymmetric effects on the phoretic drift of particles and drives the larger ones away from the interfacial region faster than the smaller ones [24, 29]. Therefore, the size asymmetry, quantified as $\alpha = d_l/d_s$, is a crucial parameter that controls the outcome of stratification, with larger α favoring "small-on-top" stratification. Martín-Fabiani *et al.* studied a system with the smaller particles coated with hydrophilic shells and explored the effect of changing the pH of the initial dispersion [27]. In a dispersion with low pH, α is large enough to lead to "small-on-top" stratification. When the pH is raised, α is reduced as the hydrophilic shells swell substantially, and stratification is switched off.

The approach of Martín-Fabiani *et al.* can be used for systems where the particle size can be tuned with external stimuli [27]. However, other possible approaches of controlling stratification for systems with fixed particle sizes have rarely been explored. In a previous work [34], we used molecular dynamics (MD) modeling to study drying suspensions of a binary

mixture of nanoparticles and found that for fast evaporation rates, the solvent can develop a negative temperature gradient toward the interface because of evaporative cooling effect. This temperature gradient induces thermophoresis, in which the larger particles are pushed more strongly into the interfacial region where the temperature is lower and the solvent density is higher. The competition between thermophoresis generated by evaporative cooling and diffusiophoresis can thus suppress "small-on-top" stratification at ultra fast drying rates or even turn the stratification into "large-on-top". This discovery further indicates that thermophoresis, with a controlled thermal gradient other than the naturally occurring evaporative cooling, may be used to control stratification. In this chapter, we employ MD modeling to test this idea in detail and demonstrate that stratification in a drying suspension can be controlled on demand with a temperature gradient imposed on the system, i.e., via controlled thermophoresis.

3.2 Methods

We performed MD simulations on a suspension of a bidisperse mixture of nanoparticles [34]. The solvent is modeled explicitly as beads of mass m and interacting with each other via a Lennard-Jones (LJ) potential, $U_{\rm LJ}(r) = 4\epsilon\left[(\sigma/r)^{12} - (\sigma/r)^6 - (\sigma/r_c)^{12} + (\sigma/r_c)^6\right]$, where r is the center-to-center distance between beads, ϵ is an energy scale, σ is a length scale, and the potential is truncated at $r_c = 3\sigma$. The nanoparticles are modeled as spheres with a uniform distribution of LJ beads at a mass density $1.0m/\sigma$ [36, 37]. The large nanoparticles (LNPs) have diameter $d_l = 20\sigma$ and mass $m_l = 4188.8m$, while the small nanoparticles (SNPs) have diameter $d_s = 5\sigma$ and mass $m_s = 65.4m$. The size ratio is $\alpha = 4$. The nanoparticle-nanoparticle interactions, Eqs. (7.12) and (7.13), are given by integrated forms of a LJ potential for spheres with a Hamaker constant, $A_{\rm nn}$, characterizing the interaction strength

[36, 37]. In this study, $A_{\mathrm{nn}} = 39.48\epsilon$. To ensure that nanoparticles are well dispersed in the initial suspension, the nanoparticle-nanoparticle interactions are rendered purely repulsive by truncating them at 20.574σ, 13.085σ, and 5.595σ for the LNP-LNP, LNP-SNP, and SNP-SNP pairs, respectively. The nanoparticle-solvent interactions, Eq. (7.11), are described by similar integrated forms of a LJ potential with a Hamaker constant $A_{\mathrm{ns}} = 100\epsilon$ and a cutoff length $d/2 + 4\sigma$, where d is the nanoparticle diameter [40].

The entire system consists of $\sim 7 \times 10^6$ LJ beads, 200 LNPs, and 6400 SNPs. The system is placed in a rectangular simulation cell of dimensions $L_x \times L_y \times L_z$, where $L_x = L_y = 201\sigma$, and $L_z = 477\sigma$. The liquid-vapor interface is in the x-y plane, in which periodic boundary conditions are imposed. In the initial suspension, the thickness of the liquid film is about 304σ. The volume fractions of LNPs and SNPs in the initial dispersion are $\phi_l = 0.068$ and $\phi_s = 0.034$, respectively. Along the z-axis, all the particles are confined in the simulation cell by two walls at $z = 0$ and $z = L_z$. The particle-wall interaction is given by a LJ-like 9-3 potential, $U_W(h) = \epsilon_W \left[(2/15)(D_W/h)^9 - (D_W/h)^3 - (2/15)(D_W/h_c)^9 + (D_W/h_c)^3\right]$, where the interaction strength $\epsilon_W = 2.0\epsilon$, h is the distance between the particle center and the wall, and h_c is the cutoff length of the potential. For the solvent beads, $D_W = 1\sigma$ and $h_c = 3\sigma$ (0.8583σ) at the lower (upper) wall. With these parameters, the liquid solvent completely wets the lower wall while the upper wall is purely repulsive. For the nanoparticles, both walls are repulsive with $D_W = d/2$ and $h_c = 0.8583 D_W$, where d is the nanoparticle diameter.

To model evaporation of the solvent, a rectangular box of dimensions $L_x \times L_y \times 20\sigma$ at the top of the simulation cell was designated as a deletion zone and a certain number (ζ) of vapor beads of the solvent in this zone were removed every τ, where τ is the reduced unit of time. In this chapter, two evaporation rates $\zeta = 30$ and $\zeta = 5$ are adopted. At these rates, the liquid-vapor interface retreats during evaporation at almost a constant speed, v_e. The value of v_e is determined for each evaporating suspension by directly computing the

location of the interface as a function of time. The diffusion coefficients of nanoparticles are calculated with direct, independent simulations and the results are $D_l = 1.76 \times 10^{-3}\sigma^2/\tau$ for LNPs and $D_s = 1.55 \times 10^{-2}\sigma^2/\tau$ for SNPs at the initial volume fractions of nanoparticles prior to evaporation (see the Appendix C). The ratio $D_s/D_l = 8.8$ is higher than $\alpha = 4$, the value expected from the Stokes-Einstein relation because of the finite concentrations of nanoparticles [38]. With values of D_l, D_s, v_e, and H determined, the Péclet numbers for LNPs and SNPs, Pe_l and Pe_s, are computed for each evaporating system.

The Large-scale Atomic/Molecular Massively Parallel Simulator (LAMMPS) [41] was employed for all the simulations reported here. A velocity-Verlet algorithm with a time step $\delta t = 0.01\tau$ was used to integrate the equation of motion, where $\tau = \sigma(m/\epsilon)^{1/2}$ is the LJ unit of time. In the thermalized zone(s) specified for each system, a Langevin thermostat with a small damping rate $\Gamma = 0.01\tau^{-1}$ was used for the solvent beads.

3.3 Results and discussion

Our goal is to demonstrate that a temperature gradient and the associated thermophoretic effect can be used to control stratification in a drying suspension of a polydisperse mixture of nanoparticles. We have previously shown that particles of different sizes have different thermophoretic responses to a thermal gradient [34]. In our previous work, only a thin layer of the liquid solvent adjacent to the bottom wall is thermalized at T_l during evaporation, as shown in Fig. 3.1(a). Because of evaporative cooling at the liquid-vapor interface, a negative temperature gradient develops and its magnitude is larger for faster evaporation rates. The negative thermal gradient induces a positive gradient of the solvent density toward the interface, which generates a driving force to transport nanoparticles into the interfacial region [43, 45]. The thermophoretic driving force is stronger for larger particles.

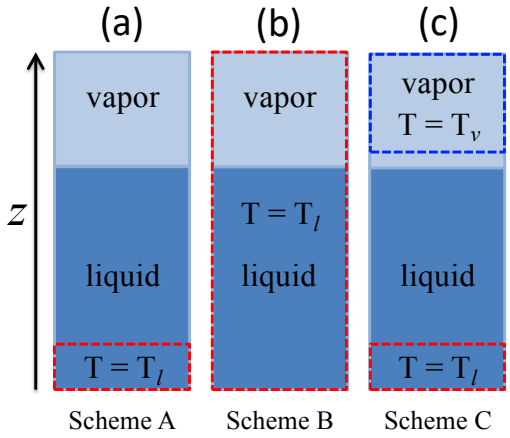

Figure 3.1: Schematics of three types of thermalizations during solvent evaporation: (a) Only a thin layer of the liquid solvent adjacent to the bottom wall is thermalized at T_l; (b) All the liquid and vapor are thermalized at T_l; (c) A thin layer of the liquid solvent adjacent to the bottom wall is thermalized at T_l while the vapor zone at some distance away from the equilibrium liquid-vapor interface is thermalized at T_v. We set $T_l = 1.0\epsilon/k_{\mathrm{B}}$ while T_v can be higher or lower than T_l to create a thermal gradient.

For $A_{\mathrm{ns}} = 100\epsilon$, SNPs show very weak or even no thermophoretic response (see Appendix B). As a result, for very fast evaporation more LNPs than SNPs are driven toward the interface in a drying bidisperse suspension [34]. The thermphoresis caused by evaporative cooling competes with the diffusiophoresis that leads to "small-on-top" stratification at fast drying rates, which is why only weak "small-on-top" stratification was observed in our previous simulations [34]. In certain cases the "small-on-top" stratification expected by the existing theory [29] was even converted to "large-on-top" in the presence of strong thermophoresis [34].

Based on the physical picture depicted above, it is natural to investigate the effects of a controlled thermal gradient on stratification in a drying suspension. In this chapter, we explore this idea by comparing three types of thermalization schemes as sketched in Fig. 3.1. The Scheme A is the same as in our previous work in which only a 10σ thick layer of the liquid solvent at the bottom of the suspension is thermalized at T_l [Fig. 3.1(a)]. Evaporative cooling leads to a negative temperature gradient in the suspension toward the interface. In

Scheme B, all the solvent beads in the simulation cell are thermalized at T_l [Fig. 3.1(b)] and thus there are no thermal gradients during evaporation. In Scheme C, in addition to a liquid layer of thickness 10σ thermalized at T_l near the bottom wall, the vapor beads with z-coordinates between $L_z - 150\sigma$ and L_z are thermalized at T_v [Fig. 3.1(c)]. In this way, a positive (negative) thermal gradient is imposed if $T_v > T_l$ (if $T_v < T_l$), and the magnitude of the gradient is controlled by $|T_v - T_l|$ and the thickness of the film. For all the systems studied in this chapter, $T_l = 1.0\epsilon/k_\mathrm{B}$. For Scheme C, T_v is varied from $0.75\epsilon/k_\mathrm{B}$ to $1.2\epsilon/k_\mathrm{B}$.

Table 3.1: Parameters for all the systems studied. Refer to Fig. 3.1 for the thermalization schemes.

System	ζ	$v_e\tau/\sigma$	Pe_l	Pe_s	Thermalization Scheme
$T^l_{1.0}\zeta_{30}$	30	1.13×10^{-3}	195.4	22.2	A
$T^l_{1.0}\zeta_5$	5	2.04×10^{-4}	35.3	4.0	A
$T_{1.0}\zeta_{30}$	30	1.18×10^{-3}	204.4	23.2	B
$T_{1.0}\zeta_5$	5	2.11×10^{-4}	36.6	4.1	B
$T^l_{1.0}T^v_{1.2}\zeta_5$	5	2.04×10^{-4}	35.3	4.0	C, $T_v = 1.2\epsilon/k_\mathrm{B}$
$T^l_{1.0}T^v_{1.1}\zeta_5$	5	1.99×10^{-4}	34.4	3.9	C, $T_v = 1.1\epsilon/k_\mathrm{B}$
$T^l_{1.0}T^v_{1.05}\zeta_5$	5	2.04×10^{-4}	35.3	4.0	C, $T_v = 1.05\epsilon/k_\mathrm{B}$
$T^l_{1.0}T^v_{0.9}\zeta_5$	5	6.93×10^{-4}	119.7	13.6	C, $T_v = 0.9\epsilon/k_\mathrm{B}$
$T^l_{1.0}T^v_{0.85}\zeta_5$	5	9.90×10^{-4}	171.0	19.4	C, $T_v = 0.85\epsilon/k_\mathrm{B}$
$T^l_{1.0}T^v_{0.75}\zeta_5$	5	1.03×10^{-3}	177.2	20.2	C, $T_v = 0.75\epsilon/k_\mathrm{B}$

For Scheme A, the systems are labeled as $T^l_{1.0}\zeta_y$ where the subscript y denotes the value of ζ. For Scheme B, $T_{1.0}\zeta_y$ is used to emphasize that the entire system is maintained at $1.0\epsilon/k_\mathrm{B}$ during evaporation. For Scheme C, the systems are labeled as $T^l_{1.0}T^v_x\zeta_y$, where x indicates the value of T_v. All the systems studied are listed in Table 3.1. $T^l_{1.0}T^v_{1.1}\zeta_5$ and $T^l_{1.0}T^v_{1.05}\zeta_5$ have results in line with $T^l_{1.0}T^v_{1.2}\zeta_5$. We also studied systems with $\zeta = 5$ and $T_v < T_l$, which show negative thermal gradients in the suspension and thermophoresis similar to those in $T^l_{1.0}\zeta_{30}$ and $T^l_{1.0}\zeta_5$ where evaporative cooling occurs. However, we observed condensation of droplets in the vapor phase if T_v is made lower than the temperature at the liquid-vapor interface in Scheme A with the same ζ. Despite this unwanted effect, cooling the vapor at a temperature

lower than that of the suspension could be one experimental approach to apply a negative thermal gradient for systems which evaporate slowly or for which the effect of evaporative cooling is not as strong as that of the model LJ liquid employed in our simulations. The last five systems in Table 3.1 with T_v varying from $0.75\epsilon/k_\mathrm{B}$ to $1.1\epsilon/k_\mathrm{B}$ are included in the Appendix D. In the main text we focus on the first five systems in Table 3.1.

Snapshots of the first five nanoparticle suspensions in Table 3.1 during solvent evaporation are shown in Fig. 3.2. For $T^l_{1.0}\zeta_{30}$ and $T^l_{1.0}\zeta_5$ [Figs. 3.2(a) and (b)], the evaporative cooling of the liquid-vapor interface leads to a negative thermal gradient along the normal direction toward the interface. Although for both systems "small-on-top" stratification is expected by the model of Zhou *et al.* since $\mathrm{Pe}_l \gg \mathrm{Pe}_s > 1$ [24], thermophoresis associated with the negative temperature gradient works against diffusiophoresis and transports more LNPs into the interfacial region. As a result, the two systems exhibit "large-on-top" stratification.

When all the solvent beads in the simulation cell are thermalized during evaporation, the temperature in the entire system is constant and no thermal gradients are produced. Thermophoresis is thus suppressed and only diffusiophoresis remains. The expected outcome is "small-on-top" stratification for $\mathrm{Pe}_l \gg \mathrm{Pe}_s > 1$. The results from $T_{1.0}\zeta_{30}$ and $T_{1.0}\zeta_5$ confirm this prediction, as shown in Figs. 3.2(c) and (d). For example, comparing the last snapshot for $T^l_{1.0}\zeta_5$ (the second row of Fig. 3.2) and that for $T_{1.0}\zeta_5$ (the fourth row of Fig. 3.2), the transition from "large-on-top" to "small-on-top" is clearly visible after the thermal gradients and the associated thermophoresis are inhibited.

The last row of Fig. 3.2 shows the snapshots for $T^l_{1.0}T^v_{1.2}\zeta_5$. In this system, the vapor beads of the solvent at $\sim 23\sigma$ above the initial liquid-vapor interface prior to evaporation are thermalized at $T_v = 1.2\epsilon/k_\mathrm{B} > T_l$ during evaporation. The top region of the drying suspension is thus heated. Consequently, there is a positive temperature gradient in the liquid solvent along the normal direction toward the interface. The solvent density develops a negative

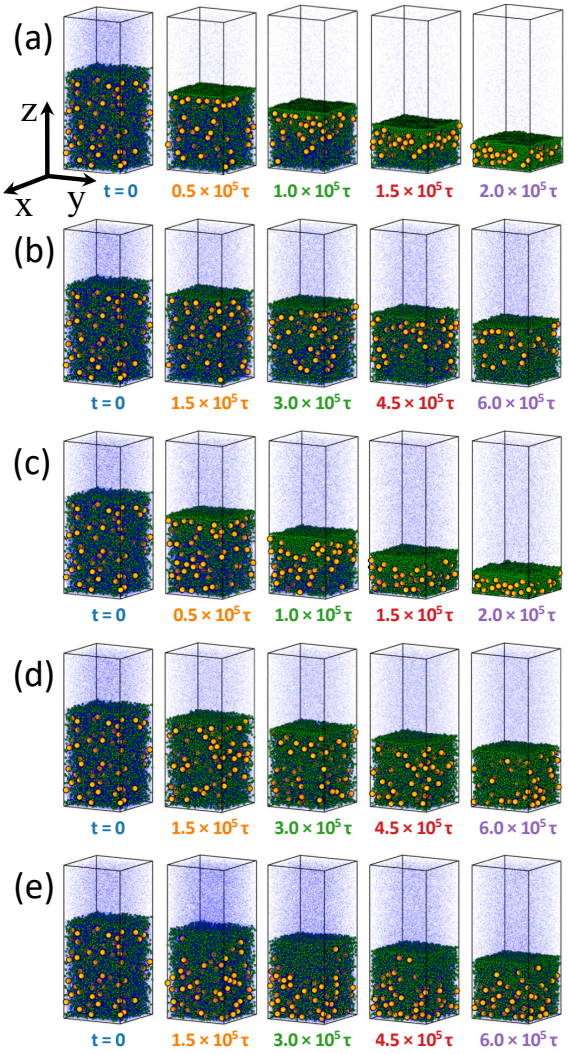

Figure 3.2: Snapshots during solvent evaporation for (a) $T^l_{1.0}\zeta_{30}$, (b) $T^l_{1.0}\zeta_5$, (c) $T_{1.0}\zeta_{30}$, (4) $T_{1.0}\zeta_5$, and (5) $T^l_{1.0}T^v_{1.2}\zeta_5$. Elapsed time since evaporation was initiated at $t = 0$ is listed under each snapshot. Temperature and density profiles of the five systems are shown in Fig. 3.3. Color code: SNPs (green), LNPs (orange), and solvent (blue). Only 5% of the solvent beads are visualized to improve clarity.

gradient and the accompanied thermophoresis drives LNPs toward the substrate. As a result, thermophoretic and diffusiophoretic effects are in synergy and strong "small-on-top" stratification is generated, which is apparent in Fig. 3.2(e).

To understand quantitatively the stratifying phenomena in drying particle suspensions, we plot the temperature and density profiles in Fig. 3.3. The local temperature $T(z)$ at height z is computed from the average kinetic energy of the solvent beads in the spatial bin $[z - 2.5\sigma, z + 2.5\sigma]$ [32]. The temperature profiles in the top row of Fig. 3.3 clearly show the negative thermal gradients induced by evaporative cooling for $T^l_{1.0}\zeta_{30}$ and $T^l_{1.0}\zeta_5$, with the effect stronger at larger evaporation rates. $T_{1.0}\zeta_{30}$ and $T_{1.0}\zeta_5$ do not exhibit thermal gradients as all the solvent is thermalized at T_l, as shown in Figs. 3.3(i) and (m). $T^l_{1.0}T^v_{1.2}\zeta_5$ with $T_v > T_l$ exhibits an externally imposed positive thermal gradient [Fig. 3.3(q)].

The local density of solvent or nanoparticles is computed as $\rho_i(z) = n_i(z)m_i/(L_xL_y\sigma)$, where $n_i(z)$ represents the number of particles in the spatial bin $[z - 0.5\sigma, z + 0.5\sigma]$ and m_i is the particle mass. A nanoparticles straddling several bins is partitioned based on its partial volume in each bin. When computing the solvent density, the volume occupied by the nanoparticles is subtracted. The second row of Fig. 3.3 shows the solvent density as a function of height and the profiles exhibit gradients in accordance with the thermal gradients. Particularly, a positive (negative) thermal gradient generates a negative (positive) density gradient for the solvent and the stronger the thermal gradient, the stronger the density gradient. This correlation results from the fact that local thermal equilibrium is always maintained even at the fastest evaporation rates adopted in our simulations [32].

The density profiles for LNPs and SNPs are shown in the bottom two rows of Fig. 3.3, respectively. These profiles demonstrate the phoretic response of the nanoparticles to the thermal gradients (or the density gradients of the solvent induced by the thermal gradients) as well as the effects of the evaporation rate. For all the simulations discussed here, the

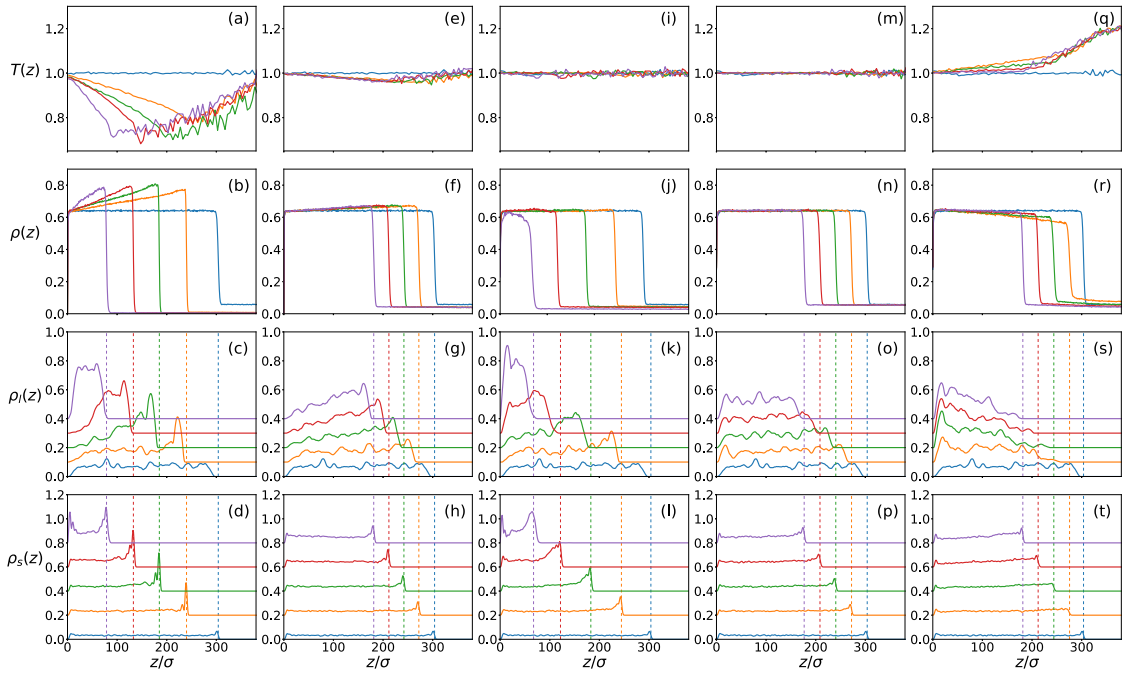

Figure 3.3: Temperature profiles (top row) and density profiles for the solvent (second row), LNPs (third row), and SNPs (bottom row) for $T^l_{1.0}\zeta_{30}$ (a-d), $T^l_{1.0}\zeta_5$ (e-h), $T_{1.0}\zeta_{30}$ (i-l), $T_{1.0}\zeta_5$ (m-p), and $T^l_{1.0}T^v_{1.2}\zeta_5$ (q-t), respectively. The curves follow the same order as the snapshots shown Fig. 3.2. The vertical dashed lines indicate the location of the liquid-vapor interface. For clarity, the density profiles for LNPs (SNPs) are shifted upward by $0.1m/\sigma^3$ ($0.2m/\sigma^3$) successively.

evaporation rates are high enough such that $\mathrm{Pe}_l \gg \mathrm{Pe}_s > 1$. The corresponding fast receding liquid-vapor interface tends to trap both LNPs and SNPs just below the interface. If no other factors are at play, this effect combined with a large enough ϕ_s is expected to yield "small-on-top" stratification via the diffusiophoresis mechanism as suggested by Sear and collaborators [20, 29] and Zhou *et al.* [24]. This scenario is indeed the case for $T_{1.0}\zeta_{30}$ and $T_{1.0}\zeta_5$, as shown in the third and fourth columns of Fig. 3.3 where there are no thermal gradients. The diffusiophoresis model also implies that the degree of "small-on-top" stratification is enhanced when the evaporation rate is increased [20, 24]. However, as shown later, $T_{1.0}\zeta_5$ actually exhibits stronger "small-on-top" stratification than $T_{1.0}\zeta_{30}$, even though the evaporation rate is increased six fold in the latter system. This discrepancy may be due to the small thickness of the suspension film studied in our simulations, which is limited by the available computational resources. The effect of film thickness on stratification will be explored in the future.

When only a thin layer of solvent beads at the bottom wall is thermalized, the temperature in the vicinity of the liquid-vapor interface decreases because of evaporative cooling effect. The resulting enhancement of the solvent density at the interface leads to thermophoretic drift of nanoparticles with the effect more significant for larger particles. This physical picture explains the observations for $T^l_{1.0}\zeta_{30}$ and $T^l_{1.0}\zeta_5$. In these two systems, the SNPs are found to accumulate at the surface of the evaporating suspension as $\mathrm{Pe}_l \gg \mathrm{Pe}_s > 1$ [Figs. 3.3(d) and (h)]. However, a significant accumulation of LNPs is found just below the enriched surface layer of SNPs, as shown in Figs. 3.3(c) and (g). The net outcome is actually "large-on-top" stratification, which will be confirmed later with an order parameter quantifying stratification (see Fig. 3.4). Furthermore, the degree of "large-on-top" stratification is stronger for $T^l_{1.0}\zeta_5$ than for $T^l_{1.0}\zeta_{30}$, indicating a delicate competition between diffusiophoresis and thermophoresis. The lower evaporation rate in $T^l_{1.0}\zeta_5$ suppresses both processes but it appears

that diffusiophoresis is mitigated slightly more, creating stronger "large-on-top" for $T^l_{1.0}\zeta_5$.

In our previous work [34], we obtained a state diagram of stratification with systems all thermalized with Scheme A (i.e., a thin layer of liquid solvent contacting the substrate is thermalized at $T_l = 1.0\epsilon/k_\mathrm{B}$) and only observed weak "small-on-top" stratification at values of Pe_s and ϕ_s far exceeding the critical values predicted the diffusiophoretic model of Zhou *et al.* [24]. The presence of thermophoresis at fast evaporation rates may help understand the discrepancy between the simulations and the theory [34]. Indeed, when thermophoresis is suppressed, systems that are driven into the "large-on-top" regime by thermophoresis can be turned into (usually weak) "small-on-top". Examples are the transition from $T^l_{1.0}\zeta_{30}$ to $T_{1.0}\zeta_{30}$ and that from $T^l_{1.0}\zeta_5$ to $T_{1.0}\zeta_5$.

To achieve strong "small-on-top" stratification, a natural idea is to enable thermophoresis that works in conjunction with diffusiophoresis. This cooperation requires a thermal gradient during evaporation that is opposite to the one induced by evaporative cooling. To realize this, we thermalize the vapor zone from $L_z - 150\sigma$ to L_z at a temperature $T_v > T_l$. The data in the fifth column of Fig. 3.3 are for $T^l_{1.0}T^v_{1.2}\zeta_5$ where $T_v = 1.2\epsilon/k_\mathrm{B}$. A positive thermal gradient and a negative density gradient of the solvent can be seen clearly in Figs. 3.3(q) and (r), respectively. Since the gradients are reversed, the LNPs are now driven toward the substrate via thermophoresis [Fig. 3.3(s)] while the SNPs are much less affected [Fig. 3.3(t)]. The final result is strong "small-on-top" stratification where the LNPs are accumulated near the substrate and depleted in the interfacial region while the SNPs exhibit a positive density gradient (i.e., accumulation) toward the interface.

It is expected that for systems thermalized with Scheme C and $T_v < T_l$, a negative thermal gradient develops in the liquid solvent, similar to the evaporative cooling case in Scheme A. Consequently, systems under Scheme C with $T_v < T_l$ could display "large-on-top" stratification as long as the thermal gradient is large enough. These cases are in fact observed

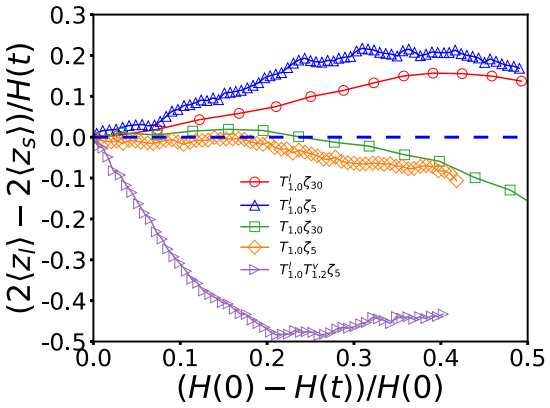

Figure 3.4: Mean separation between LNPs and SNPs normalized by $H(t)/2$, *vs* extent of drying, $(H(0) - H(t))/H(0)$, for $T^l_{1.0}\zeta_{30}$ (red circle), $T^l_{1.0}\zeta_5$ (blue upward triangle), $T_{1.0}\zeta_{30}$ (green square), $T_{1.0}\zeta_5$ (yellow diamond), and $T^l_{1.0}T^v_{1.2}\zeta_5$ (purple right-pointing triangle).

and discussed in detail in the Appendix D, where some complications are noted related to droplet condensation in a vapor that is thermalized at low temperatures.

To quantify stratification, we define an order parameter using the full density profiles of nanoparticles [34]. The mean heights of LNPs and SNPs are computed as $\langle z_i\rangle = \frac{1}{N_i}\sum_{n=1}^{N_i} z_{in}$ with $i \in \{l, s\}$. The order parameter of stratification is then computed as $(2\langle z_l\rangle - 2\langle z_s\rangle)/H(t)$, i.e., the mean separation between LNPs and SNPs normalized by $H(t)/2$, where $H(t)$ is the instantaneous thickness of the suspension. In the equilibrium suspension prior to evaporation, both $\langle z_l\rangle$ and $\langle z_s\rangle$ are very close to $H(0)/2$, where $H(0)$ is the initial film thickness. During evaporation, $\langle z_l\rangle - \langle z_s\rangle < 0$ indicates "small-on-top" stratification while $\langle z_l\rangle - \langle z_s\rangle > 0$ signifies "large-on-top".

In Fig. 3.4 the order parameter of stratification is plotted against the extent of drying, quantified as $(H(0) - H(t))/H(0)$, for the first five systems listed in Table 3.1. It is clear that $T_{1.0}\zeta_{30}$ and $T_{1.0}\zeta_5$ exhibit "small-on-top" stratification when diffusiophoresis dominates while thermal gradients and thermophoresis are absent. The extent of stratification is slightly stronger for $T_{1.0}\zeta_5$, though it dries more slowly. "Large-on-top" is observed for $T^l_{1.0}\zeta_{30}$ and

$T^l_{1.0}\zeta_5$ and is again stronger for $T^l_{1.0}\zeta_5$ that has a smaller evaporation rate. Although thermophoresis is much weaker for $T^l_{1.0}\zeta_5$ because of the reduced evaporation rate, diffusiophoresis favoring "small-on-top" is suppressed even more when evaporation is slowed down and the delicate interplay of the two phoretic processes leads to stronger "large-on-top" stratification for $T^l_{1.0}\zeta_5$.

A dramatic "small-on-top" state is clearly demonstrated in Fig. 3.4 for $T^l_{1.0}T^v_{1.2}\zeta_5$. Note that in the equilibrium suspension, $\phi_l = 2\phi_s$. If in the final dry film all the SNPs were on top of all the LNPs (i.e., a complete stratification) but each group is uniformly distributed in its region, then $\langle z_l \rangle = H(t)/3$ and $\langle z_s \rangle = 5H(t)/6$, yielding $(2\langle z_l \rangle - 2\langle z_s \rangle)/H(t) = -1$. As shown in Fig. 3.4, the order parameter of stratification reaches a minimal value around -0.5 for $T^l_{1.0}T^v_{1.2}\zeta_5$, indicating that the vertical distribution of the binary mixture of nanoparticles is substantially segregated in the drying film with SNPs on top of LNPs. This outcome is clearly visible in Fig. 3.2(e) as well.

Evaporative cooling is a natural effect in a fast drying liquid. If a particle suspension is placed on a substrate that is kept at a constant temperature and the suspension undergoes very fast solvent evaporation, then a temperature lower than that of the substrate is expected at the evaporating interface, resulting in a negative thermal gradient in the suspension. $T^l_{1.0}\zeta_{30}$ and $T^l_{1.0}\zeta_5$ studied here are set up to mimic such situations. However, it is challenging to maintain a constant temperature or induce a positive thermal gradient along the normal direction toward the interface in a drying suspension, especially when the evaporation rate is high. One possible approach is to dissolve a gas (e.g., N_2, Ar, He, or CO_2) into the solvent (e.g., water). Beaglehole showed that heating a water film with a dissolved gas from above or below produces very different temperature distributions within the liquid [46, 47]. When heated from below, a fairly uniform temperature is found throughout the liquid. However, when the liquid is heated from above, a temperature gradient develops in it with

the temperature higher at the liquid-vapor interface. Then it may be possible to study the effect of solvent evaporation on the particle distribution in a drying film under isothermal conditions and positive thermal gradients, similar to Scheme B and C.

3.4 Conclusion

In this chapter we have focused on how stratification can be controlled in a drying suspension of a bidisperse mixture of nanoparticles via MD simulations with an explicit solvent model. We demonstrated that a thermal gradient and the induced thermophoresis can be used to alter stratification from "large-on-top" all the way to strong "small-on-top". This strategy is based on the observation that particles of different sizes in a suspension have different responses to a thermal gradient. In particular, larger particles experience a larger driving force that transports them into cooler regions where the solvent density is higher. For $A_{\mathrm{ns}} = 100\epsilon$ adopted here, the smaller nanoparticles show little or even no response to a thermal gradient. When a suspension undergoes fast drying and only a thin layer of the solvent adjacent to the substrate is thermalized at T_l, mimicking an experimental situation where the substrate supporting the suspension is maintained at a constant temperature during solvent evaporation, a negative temperature gradient develops in the suspension because of the evaporative cooling effect that makes the temperature at the evaporating interface to drop below T_l. A larger fraction of the larger nanoparticles are driven into the interfacial region via the thermophoresis induced by this thermal gradient. As a result, the fast drying suspensions display "large-on-top" stratification instead of "small-on-top" expected by the diffusiophoresis model in which the suspension is assumed to be isothermal during evaporation.

Interestingly, when the entire suspension is maintained at T_l during drying by thermalizing

all the solvent beads in the simulation cell, they do exhibit "small-on-top" stratification at fast evaporation rates, consistent with the prediction of the diffusiophoresis model [20, 24, 29]. However, the degree of stratification is found to be weak, probably due to the fact that ϕ_s is small and the liquid film is thin for the simulations reported here. When a positive thermal gradient is induced in the suspension by thermalizing the vapor at a temperature higher than T_l, all the larger nanoparticles are propelled toward the substrate. In this case, the synergy between thermophoresis and diffusiophoresis is underlying the observation of strong "small-on-top" stratification. Our results thus reveal a potentially useful strategy of controlling stratification via a regulated thermal gradient in a drying suspension of polydisperse particles.

Chapter 4

Meniscus on the outside of a small cylinder

This chapter is based on our publication [48]:

Yanfei Tang and Shengfeng Cheng, "The meniscus on the outside of a circular cylinder from microscopic to macroscopic scales," J. Colloid Interface Sci. 533, 401 (2019).

I performed all the analytical and numerical work under Dr. Cheng's supervision. All authors contributed to the writing of this paper.

4.1 Introduction

In the previous two chapters, we described the moleculary dynamics simulations of bidisperse nanoparticle suspensions that underwent drying with the solvent modeled explicitly. Such explicit solvent models have the advantage to capture potentially important factors such as

hydrodynamic interactions between nanoparticles and evaporation-induced flow in the drying suspensions. However, these simulations are computationally expensive. It is thus desirable to develop other methods that enable us to study larger particle suspensions over longer times and to quickly scan parameter spaces that are of interest to theories and experiments. In one such attempt, an explicit solvent system is mapped to an implicit one in which the solvent is treated as a uniform viscous background [20, 21]. In the implicit solvent model, only suspended particles are included explicitly and therefore much larger systems can be handled with available computational resources. One key ingredient of an implicit solvent system is a potential barrier that serves as the role of a liquid-vapor interface in an explicit solvent system and confines all the particles in the suspension [20, 21]. A portion of a harmonic potential was frequently used as the potential barrier [49]. To understand this approximation, we found out that it is important to understand the capillary force exerted on a spherical particle when it is displaced out of its equilibrium location at a liquid-vapor interface. After a careful analysis, we realized that to fulfill this task, it is necessary to understand the meniscus on the outside of a circular cylinder vertically penetrating a liquid-vapor interface. In this chapter, we present a complete solution to this problem. In the next chapter, we apply the solution to obtain the capillary force on a spherical particle at a liquid-vapor interface.

A liquid meniscus as a manifestation of capillary action is ubiquitous in nature and our daily life. For example, its formation and motion play critical roles in water uptake in plants [50]. Capillary adhesion due to the formation of menisci between solid surfaces makes wet hair stick together and allows kids to build sandcastles [51]. Menisci are also involved in many technologies and industrial processes [52] such as meniscus lithography [53], dip-pen nanolithography [54], dip-coating (Langmuir-Blodgett) assembly of nanomaterials [55–57], meniscus-mediated surface assembly of particles [58], meniscus-assisted solution printing [59],

etc.

A meniscus system frequently discussed in the literature is the one formed on the outside of a circular cylinder that is vertically immersed in a liquid bath. One application of this geometry is the fabrication of fiber probes by chemical etching [60]. A cylinder with radius at the nanometer scale has also been attached to the tip of an atomic force microscope to perform nano-/micro-Whilhemy and related liquid property measurements [61]. The shape of the meniscus is governed by the Young-Laplace equation [62]. Extensive studies have been reported for the scenario where the liquid bath is unbound and the lateral span of the liquid-vapor interface is much larger than the capillary length of the liquid [63–68]. Different methods have been applied in these studies, including numerical integration [64, 65] and analytical approaches such as matched asymptotic expansions [66–68] and hodograph transformations for cylinders with complex shapes [68]. An approximate formula has been derived for the meniscus height, which depends on the radius of the cylinder and the contact angle of the liquid on the cylinder surface [63, 66]. The meniscus exerts a force that either drags the cylinder into or expels it from the liquid depending on if the contact angle is acute or obtuse. A recent study of the meniscus rise on a nanofiber showed that the force on the nanofiber highly depends on the lateral size of the liquid-vapor interface if this size is smaller than the capillary length [69].

In this chapter we consider a geometry as sketched in Fig. 4.1 where a small circular cylinder vertically penetrating a liquid bath that is confined by a cylindrical container. With the cylinder and the container being coaxial, the system has axisymmetry that enables certain analytical treatments. By fixing the contact angle on the surface of the container to be $\pi/2$, we have a meniscus that systematically transits from being laterally confined to unbound, when the size of the container is increased. For such a system, the meniscus profile is governed by the general Young-Laplace equation that was first studied by Bashforth and

Adams more than a century ago [70]. This equation has been discussed in various systems including liquid in a tube [71], sessile and pendant droplets [72, 73] and a capillary bridge between two spheres [74].

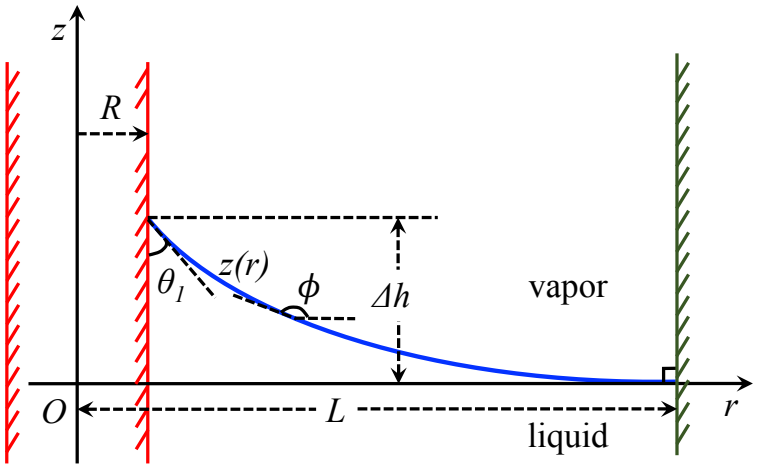

Figure 4.1: A rising meniscus on the outside of a circular cylinder vertically immersed in a liquid bath confined in a cylindrical container that is coaxial with the cylinder.

In the limit where the size of the cylindrical container is much smaller than the capillary length, the gravitational term in the Young-Laplace equation can be neglected and the equation becomes analytically solvable. Solutions have been reported for various capillary bridges between solid surfaces [75–77] and tested with molecular dynamics simulations [78, 79]. We have obtained a solution for the meniscus in Fig. 4.1 based on elliptic integrals when the lateral size of the meniscus is small and found that the meniscus height depends on the container size logarithmically. We further numerically solve the full Young-Laplace equation for an arbitrary container size and find that the meniscus height approaches an upper limit found in some early work when the lateral span of the interface is much larger than the capillary length [63, 65, 66]. Finally, we find an approximate expression of the meniscus height on the cylinder that is applicable to any lateral size of the liquid-vapor interface. This work is the basis of a related work on the wetting behavior of particles at a liquid-vapor interface [80], where the theoretical results presented here are applied to study

the detachment of a spherical particle from a liquid bath.

4.2 Theoretical considerations

4.2.1 General equation of the meniscus shape

The geometry of the system considered in this chapter is sketched in Fig. 4.1. A circular cylinder with radius R is immersed in a liquid bath confined in a cylindrical wall with radius $L > R$. The cylinder and the wall are coaxial and the system is thus axisymmetric. The shape of the meniscus in this ring-shaped tube is determined by the surface tension of the liquid, the contact angles on the two surfaces, and possibly gravity. Our interest is to examine the crossover from the case where $L-R$ is small to the case where the cylinder is immersed in a liquid bath with an infinite lateral span. Since in the latter limit the liquid-vapor interface is flat at locations far away from the cylinder, we will set the contact angle on the wall to be $\pi/2$. Then a meniscus will rise (depress) on the outside of the cylinder if the contact angle on its surface, θ_1, is smaller (larger) than $\pi/2$. The case where $\theta_1 = \pi/2$ is trivial with the liquid-vapor interface being flat everywhere. Here we focus on the case with $\theta_1 < \pi/2$, where a meniscus rises on the cylinder and generates a force to pull the cylinder into the liquid bath. However, the final results on predicting the meniscus height also apply to the case where $\theta_1 > \pi/2$.

The equilibrium shape of the meniscus is governed by a form of the Young-Laplace equation studied by Bashforth and Adams before [70],

$$\frac{z''}{(1+z'^2)^{3/2}} + \frac{z'}{r(1+z'^2)^{1/2}} = \frac{\Delta p}{\gamma} + \frac{\Delta \rho g z}{\gamma} \ , \tag{4.1}$$

where $z(r)$ is the meniscus height at distance r from the central axis of the cylinder, $z' \equiv \frac{\mathrm{d}z}{\mathrm{d}r}$, $z'' \equiv \frac{\mathrm{d}^2z}{\mathrm{d}r^2}$, Δp is the pressure jump from the vapor to the liquid phase at $r = L$ and $z = 0$, γ is the surface tension of the liquid, $\Delta\rho \equiv \rho_l - \rho_v$ is the difference of the liquid and vapor densities, and g is the gravitational constant. A brief derivation of this equation is provided in Appendix E.1. In the following discussion, we use a water-air liquid interface at 25°C as an example, for which $\gamma \approx 0.072\,\mathrm{N/m}$ and $\Delta\rho \approx 10^3\,\mathrm{kg/m^3}$.

To facilitate discussion, we define $2\tilde{H} \equiv \frac{\Delta p}{\gamma}$ and $\kappa^2 \equiv \frac{\Delta\rho g}{\gamma}$, i.e., $\kappa^{-1} = \sqrt{\frac{\gamma}{\Delta\rho g}}$ is the so-called capillary length, which is a characteristic length scale of the problem. For water at 25°C, $\kappa^{-1} \approx 2.7$ mm. Eq. (4.1) can then be made dimensionless via a variable change

$$x \equiv \kappa r \ , \quad y \equiv \kappa z \ . \tag{4.2}$$

The result is the following nonlinear differential equation

$$\frac{y''}{(1+y'^2)^{3/2}} + \frac{y'}{x(1+y'^2)^{1/2}} = \frac{2\tilde{H}}{\kappa} + y \ , \tag{4.3}$$

with boundary conditions

$$y' = -\cot\theta_1 \quad \text{at} \quad x = \kappa R \ , \tag{4.4a}$$

$$y' = 0 \quad \text{at} \quad x = \kappa L \quad \text{and} \quad y = 0 \ . \tag{4.4b}$$

As pointed out in Ref. [71], Eq. (4.3) is invariant under the transformation $y \to -y$, $\theta_1 \to \pi - \theta_1$, and $\tilde{H} \to -\tilde{H}$, indicating the symmetry between a rising and a depressing meniscus. This second-order nonlinear differential equation can be rewritten in terms of the local titled angle of the liquid-vapor interface, ϕ, as defined in Fig. 4.1. Since $y' \equiv \frac{\mathrm{d}y}{\mathrm{d}x} = \frac{\mathrm{d}z}{\mathrm{d}r} = \tan\phi$, Eq.

(4.3) then becomes

$$\frac{\mathrm{d}\sin\phi}{\mathrm{d}x} + \frac{\sin\phi}{x} = -\frac{2\tilde{H}}{\kappa} - y \ . \tag{4.5}$$

Eq. (4.5) and $\frac{\mathrm{d}y}{\mathrm{d}x} = \tan\phi$ can be further rewritten into a pair of coupled first-order nonlinear differential equations in terms of $x(\phi)$ and $y(\phi)$,

$$\frac{\mathrm{d}x}{\mathrm{d}\phi} = -\left(\frac{2\tilde{H}}{\kappa} + y + \frac{\sin\phi}{x}\right)^{-1} \cos\phi \ , \tag{4.6a}$$

$$\frac{\mathrm{d}y}{\mathrm{d}\phi} = -\left(\frac{2\tilde{H}}{\kappa} + y + \frac{\sin\phi}{x}\right)^{-1} \sin\phi \ . \tag{4.6b}$$

with boundary conditions

$$\phi = \phi_1 \quad \text{at} \quad x = \kappa R \ , \tag{4.7a}$$

$$\phi = \phi_2 \quad \text{at} \quad x = \kappa L \quad \text{and} \quad y = 0 \ , \tag{4.7b}$$

where $\phi_1 = \theta_1 + \pi/2$ and $\phi_2 = \pi$ for the system sketched in Fig. 4.1. Here θ_2 is the contact angle on the wall and is fixed at $\pi/2$ in this chapter. Generally, $\phi_2 = \frac{3\pi}{2} - \theta_2$ for $0 \le \theta_2 \le \pi$.

In a general case, Eq. (4.6) can be numerically solved by the shooting method [81]. For the case where contact angle θ_1 is close to $\pi/2$, a zero-order solution is provided in Appendix E.2. For a general contact angle θ_1, analytical solutions of the meniscus can be found when $L \ll \kappa^{-1}$, where the terms on the right sides of Eqs (4.1), (4.3), and (4.6) due to gravity are negligible [Sec. 4.2.2]. In the opposite limit where $L \gg \kappa^{-1}$, the Δp term is negligible and an approximate solution of the capillary rise on the outside of a small cylinder with $R \ll \kappa^{-1}$ was found before by James using the method of asymptotic matching expansions [Sec. 4.2.3]. Below we discuss these limits and numerical solutions of Eq. (4.6) for $R \ll \kappa^{-1}$

and an arbitrary L (which is of course larger than R). The results naturally show the crossover from one limit ($R \ll L \ll \kappa^{-1}$) to the other ($R \ll \kappa^{-1} \ll L$).

4.2.2 Analytical solution in the $L \ll \kappa^{-1}$ limit

When the radius of the cylindrical wall is small, i.e., $L \ll \kappa^{-1}$, the Bond number $gL^2\Delta\rho/\gamma \ll 1$. As a result, the gravity's effect can be ignored and Eq. (4.1) reduces to

$$\frac{z''}{(1+z'^2)^{3/2}} + \frac{z'}{r(1+z'^2)^{1/2}} = 2\tilde{H} \ , \tag{4.8}$$

with $\tilde{H}$ being the local mean curvature of the liquid-vapor interface. This equation has been solved analytically before for a capillary bridge between a sphere and a flat surface [76, 82]. Here we use the same strategy to solve it for the meniscus in a ring-shaped container as depicted in Fig. 4.1.

It is convenient to introduce reduced variables $X = r/R$, $Y = z/R$ and a parameter $u = \sin\phi$. Eq. (4.8) is then simplified as

$$-2H = \frac{\mathrm{d}u}{\mathrm{d}X} + \frac{u}{X} \ , \tag{4.9}$$

where H is the dimensionless mean curvature defined as $H \equiv R\tilde{H}$. The boundary conditions are

$$\phi = \phi_1 \quad \text{at} \quad X = 1 \ , \tag{4.10a}$$

$$\phi = \phi_2 \quad \text{at} \quad X = l \quad \text{and} \quad Y = 0 \ , \tag{4.10b}$$

where $\phi_1 = \theta_1 + \pi/2$, $\phi_2 = \pi$, and $l = L/R$ is the scaled radius of the cylindrical container.

The solution for Eq. (4.9) is

$$u = \frac{c}{4HX} - HX \ . \tag{4.11}$$

The boundary condition in Eq. (4.10b) yields $c = 4H^2l^2$. The other boundary condition in Eq. (4.10a) can then be used to determine the dimensionless mean curvature as

$$H = \frac{\sin\phi_1}{l^2 - 1} \ . \tag{4.12}$$

From Eq. (4.11) and $\mathrm{d}Y/\mathrm{d}X = \tan\phi$, we obtain the analytic solution of the meniscus profile,

$$X(\phi) = \frac{1}{2H}\left(-\sin\phi + \sqrt{\sin^2\phi + c}\right) \ , \tag{4.13}$$

$$Y(\phi) = \frac{1}{2H}\int_{\phi_2}^{\phi}\left(-\sin t + \frac{\sin^2 t}{\sqrt{\sin^2 t + c}}\right)\mathrm{d}t \ . \tag{4.14}$$

The solution for $Y(\phi)$ in Eq. (4.14) can be written in terms of elliptic integrals,

$$Y(\phi) = \frac{1}{2H}(\cos\phi - \cos\phi_2) + \frac{\sqrt{c}}{2H}\Big[E(\phi, j) - E(\phi_2, j) - F(\phi, j) + F(\phi_2, j)\Big] \ , \tag{4.15}$$

where $j^2 \equiv -\frac{1}{c}$. $F(\phi, j)$ and $E(\phi, j)$ are the incomplete elliptic integrals of the first kind and second kind, respectively,

$$F(\phi, j) = \int_0^{\phi} \frac{1}{\sqrt{1 - j^2\sin^2 t}}\,\mathrm{d}t \ , \tag{4.16}$$

$$E(\phi, j) = \int_0^{\phi} \sqrt{1 - j^2\sin^2 t}\,\mathrm{d}t. \tag{4.17}$$

The meniscus rise can be easily computed as $\Delta h = RY(\phi_1)$, or explicitly,

$$\Delta h = \frac{R}{2H}(1-\sin\theta_1) + \frac{R\sqrt{c}}{2H}\Big[F(\pi/2-\theta_1, j) - E(\pi/2-\theta_1, j)\Big] \ . \tag{4.18}$$

Some examples of the meniscus profile are shown in Fig. 4.2 for $L/R = 5$ and $\theta_1 = 0°$, $30°$, and $60°$, respectively.

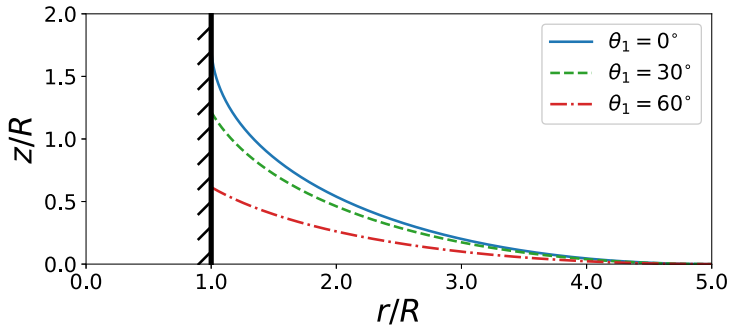

Figure 4.2: Meniscus profiles from the analytic solution in Eqs. (4.13) and (4.14) for $L/R = 5$ and $\theta_1 = 0°$ (blue solid line), $30°$ (green dashed line), and $60°$ (red dash-dotted line).

The analytical prediction in Eq. (4.18) actually indicates that $\Delta h \sim R\ln(L/R)$ when $\kappa^{-1} \gg L > R$. To see this scaling behavior transparently, we examine the limit where $\kappa^{-1} \gg L \gg R$, i.e., the cylinder is much smaller than the cylindrical container and both are much smaller than the capillary length. In this limit we can take $l \gg 1$ and $j^2 \to -\infty$, and approximate the elliptic integrals in Eq. (4.18) by series expansions. The mathematical derivation is provided in Appendix E.3. The final result on the meniscus height is

$$\Delta h = R\cos\theta_1\Big[\ln\frac{2L}{R(1+\sin\theta_1)} - \frac{1}{2}\Big] \ . \tag{4.19}$$

A more intuitive way to see the logarithmic behavior is to note that in the limit of $l \gg 1$, the

dimensionless mean curvature H approaches zero and Eq. (4.1) can be rewritten as [62, 69],

$$\frac{r}{(1+r'^2)^{1/2}} = R\cos\theta_1 \ , \tag{4.20}$$

where $r' \equiv \frac{\mathrm{d}r}{\mathrm{d}z}$. The solution of this equation is known as a catenary curve [62]. The meniscus is thus a catenoid with its generatrix given by

$$z(r) = R\cos\theta_1 \ln\left[\frac{L+(L^2-R^2\cos^2\theta_1)^{1/2}}{r+(r^2-R^2\cos^2\theta_1)^{1/2}}\right] . \tag{4.21}$$

The meniscus height can be computed as $\Delta h = z(R)$ and an approximate expression is

$$\Delta h = R\cos\theta_1 \ln\left[\frac{2L}{R(1+\sin\theta_1)}\right] , \tag{4.22}$$

where the condition $L/R \gg 1 \geq \cos\theta_1$ is used. In both Eqs. (4.19) and (4.22) the scaling dependence of Δh on $R\ln(L/R)$ is obvious. However, the expression in Eq. (4.19) for Δh is smaller than Eq. (4.22) by $(R\cos\theta_1)/2$. This difference stems from the different boundary conditions at the wall. Eq. (4.19) is based on Eq. (4.14) which describes a meniscus that meets the wall with a contact angle $\pi/2$. However, Eq. (4.22) is based on a catenary curve, for which the contact angle at the wall is close to but not exactly $\pi/2$.

4.2.3 Approximate solution in the $L \gg \kappa^{-1}$ limit

In the literature, the meniscus on the outside of a circular cylinder vertically penetrating a liquid bath was mostly investigated for the case where the lateral span of the liquid bath is much larger than the capillary length [63–68], i.e., $L \gg \kappa^{-1}$. In this limit, $\tilde{H} \to 0$ and the

Young-Laplace equation that needs to be solved reads

$$\frac{y''}{(1+y'^2)^{3/2}} + \frac{y'}{x(1+y'^2)^{1/2}} = y \ . \tag{4.23}$$

The boundary condition Eq. (4.4a) remains the same but Eq. (4.4b) is replaced by

$$y' = 0 \quad \text{at} \quad x \to \infty \quad \text{and} \quad y = 0 \ . \tag{4.24}$$

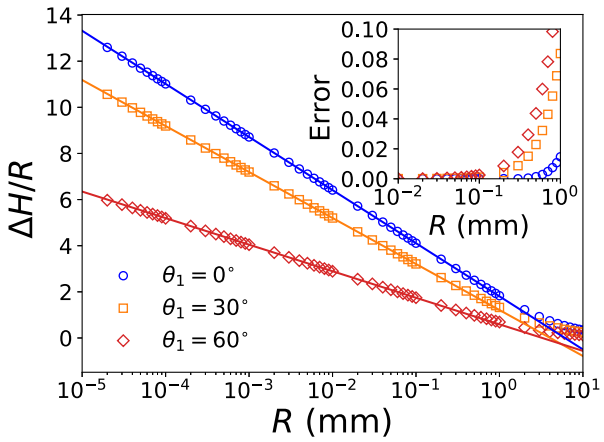

Figure 4.3: Comparison of the meniscus height (Δh) between the Derjaguin-James formula (Eq. (4.25), solid lines) and numerical results (symbols) using Huh-Scriven's integration scheme [65] as a function of the radius of the cylinder, R, for different contact angles: $\theta_1 = 0°$ (blue line and ○), 30° (orange line and □), and 60° (red line and ◇). The lateral span of the liquid bath is treated as infinite by using Eq. (4.24) as a boundary condition. Inset: the relative deviation of the numerical results on Δh from the prediction using the Derjaguin-James formula is plotted against R.

Eq. (4.23) has been studied with methods of numerical integration [64, 65] and matched asymptotic expansions [66, 67]. The meniscus height is approximately given by the Derjaguin-James formula [63, 66],

$$\Delta h = R\cos\theta_1 \Big[\ln \frac{4\kappa^{-1}}{R\,(1+\sin\theta_1)} - E \Big] \ , \tag{4.25}$$

where $E = 0.57721...$ is the Euler-Mascheroni constant. Eq. (4.25) is expected to predict the meniscus height accurately when the radius of the cylinder is much smaller than the capillary length that is in turn much smaller than the lateral span of the liquid bath, namely $R \ll \kappa^{-1} \ll L$. A comparison between the Derjaguin-James formula and numerical results has been fully discussed in Ref. [66] for $L \to \infty$. This comparison is revisited in Fig. 4.3. Practically, for water at room temperature it is legitimate to use the Derjaguin-James formula to estimate the meniscus height on a cylinder when its radius is less than about 0.1 mm.

4.3 Numerical results and discussion

As discussed in Sec. 4.2.1, the general Young-Laplace equation [Eq. (4.3)] can only be solved numerically. We rewrite Eq. (4.3) into a pair of coupled firs-order differential equations [Eq. (4.6)] and adopt the shooting method to obtain their numerical solutions for a given R that is much smaller than κ^{-1} and an arbitrary L that varies from $2R$ to a value much larger than κ^{-1}.

Figure 4.4 shows numerical solutions of the meniscus height on a circular cylinder immersed vertically in water when L is varied. Cylinders with radii R from 100 nm to 10 μm and contact angles θ_1 from 0 to 60° are used as examples. The data show the following trends. When L is smaller than 1 mm, i.e., $L/R < 10^2$ for $R = 10\,\mu$m, $L/R < 10^3$ for $R = 1\,\mu$m, and $L/R < 10^4$ for $R = 100\,$nm, the meniscus height Δh is well predicted by Eq. (4.18), which is derived with gravity ignored. In this limit, Δh grows with L logarithmically. In the other limit where L is larger than 10 mm, i.e., $L/R > 10^3$ for $R = 10\,\mu$m, $L/R > 10^4$ for $R = 1\,\mu$m, and $L/R > 10^5$ for $R = 100\,$nm, the meniscus height fits to the Derjaguin-James formula in Eq. (4.25), which is derived assuming $R \ll \kappa^{-1}$ and $L \to \infty$. For L with an intermediate value between 1 mm and 10 mm, the numerical data on the meniscus rise show clearly the

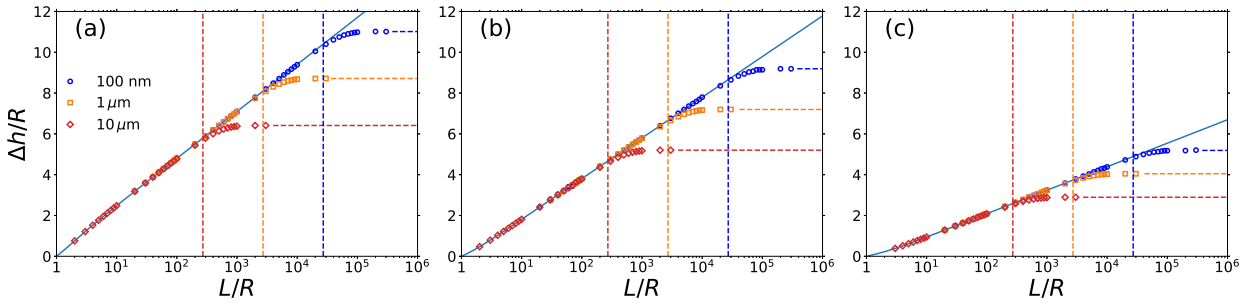

Figure 4.4: The meniscus height, Δh, for different contact angles on the surface of the cylinder: (a) $\theta_1 = 0°$, (b) 30°, and (c) 60° as a function of the lateral span of the liquid bath, L. The solid line is the analytical expression of Δh for $L \ll \kappa^{-1}$ [Eq. (4.18)]. The horizontal dashed lines are the predictions of the Derjaguin-James formula for $L \gg \kappa^{-1}$ [Eq. (4.25)]. The vertical horizontal lines indicate where $L = \kappa^{-1}$. The symbols are numerical solutions of Eq. (4.6) for an arbitrary L using the shooting method. Data are for cylinders with different radii: $R = 100\,\text{nm}$ (red ○), $1\,\mu\text{m}$ (orange □), and $10\,\mu\text{m}$ (blue ◇). Both Δh and L are normalized by R.

crossover between the logarithmic regime [Eq. (4.18)] and the saturation regime described by the Derjaguin-James formula. The latter thus provides an upper bound of the meniscus rise on the outside of a circular cylinder with a radius much smaller than the capillary length.

The results in Fig. 4.4 indicates that for a cylinder with $R \ll \kappa^{-1}$, the Young-Laplace equation without gravity as shown in Eq. (4.8) can be used to describe the meniscus on the outside of the cylinder when $L \lesssim 0.4\kappa^{-1}$, while the liquid bath can be considered as unbounded and the Derjaguin-James formula applies when $L \gtrsim 4\kappa^{-1}$. The range $0.4\kappa^{-1} \lesssim L \lesssim 4\kappa^{-1}$ is the crossover region in which the full Young-Laplace equation [Eqs. (4.1), (4.3), (4.5), or (4.6)] needs to be employed. This conclusion seems to hold for other liquids with different capillary lengths. For example, we have solved Eq. (4.6) numerically for a hexadecane-water mixture at 25 °C, for which $\kappa^{-1} = 4.824$ mm, and found roughly the same crossover zone.

An interesting finding is that the intersection between the solid line from Eq. (4.18) and the corresponding dashed line from the Derjaguin-James formula in Eq. (4.25) occurs at

$L \approx 1.85\kappa^{-1}$ for all the systems considered here. The relationship can be understood if we compare Eq. (4.19), which is an approximate form of Eq. (4.18) on the meniscus height in the limit of $\kappa^{-1} \gg L \gg R$, to the Derjaguin-James formula in Eq. (4.25). At $L = 2e^{1/2-E}\kappa^{-1} \approx 1.85\kappa^{-1}$, the two predictions are equal. This estimate is in perfect alignment with the discovery that at $L \approx 1.85\kappa^{-1}$, the meniscus height from Eq. (4.18) matches that predicted by the Derjaguin-James formula. In a related work, we find that $L \approx 1.85\kappa^{-1}$ is also the saturation length of the lateral span of a liquid-vapor interface when discussing how the effective spring constant experienced by a detaching particle depends on the lateral size of the interface [80]. Note that Eq. (4.18) holds for $\kappa^{-1} \gg L > R$ and is thus more general than Eq. (4.19), which requires $\kappa^{-1} \gg L \gg R$. Our numerical results indicate that Eq. (4.18) provides a good estimate of Δh for L up to about $0.4\kappa^{-1}$.

Based on this observation and the finding that the crossover zone, $0.4\kappa^{-1} \lesssim L \lesssim 4\kappa^{-1}$, is relatively small, we propose that for a cylinder with radius $R \ll \kappa^{-1}$ and vertically immersed in a liquid bath with lateral span designated as L, the meniscus height on the outside of the cylinder can be computed using Eq. (4.18) with the parameter l given as follows,

$$l = \begin{cases} L/R & \text{if } L \leq 1.85\kappa^{-1} \ , \\ 1.85\kappa^{-1}/R & \text{if } L > 1.85\kappa^{-1} \ . \end{cases} \tag{4.26}$$

Note that the parameter l, in addition to θ_1 and R, enters in the computation of the parameters H, c, and j in Eq. (4.18). For $L \leq 1.85\kappa^{-1}$, the meniscus height Δh depends on L logarithmically while it saturates to the upper bound expressed in the Derjaguin-James formula when $L > 1.85\kappa^{-1}$. Our numerical data indicate that Eq. (4.18) with l from Eq. (4.26) is quite accurate for the meniscus height. Even within the crossover region $0.4\kappa^{-1} \lesssim L \lesssim 4\kappa^{-1}$, the relative deviation of the actual meniscus height from the prediction based on Eqs. (4.18) and (4.26) is less than 5%, as shown in Fig. E.1 in Appendix E.4.

By carefully examining the relative error of using Eqs. (4.18) and (4.26) to compute the meniscus height Δh and how the error depends on L, R, and θ_1 [see Appendix E.4 for detail], we arrive at an approximate analytical expression of Δh for an arbitrary L that reads

$$\Delta h = \Delta h(\text{elliptic}) \times \{1 - m(\kappa L)[\kappa R(1+\sin\theta_1)]^{0.12}\} \ , \tag{4.27}$$

where Δh(elliptic) is the meniscus height from Eq. (4.18) based on elliptic integrals with the parameter l given in Eq. (4.26) and $m(\kappa L)$ is a universal function given as follows,

$$m(x) = \begin{cases} 0.085 \exp\left[(x-1.85)^{1.83}/0.74\right] & \text{if } x \le 1.85 \ , \\ 0.085 \exp\left[(1.85-x)/0.875\right] & \text{if } x > 1.85 \ . \end{cases} \tag{4.28}$$

Note that $m(\kappa L)$ is independent of the contact angle, θ_1, and the cylinder radius, R. The dependence of Δh on R and θ_1 enters through Δh(elliptic) and the $\kappa R(1+\sin\theta_1)^{0.12}$ term in Eq. (4.27).

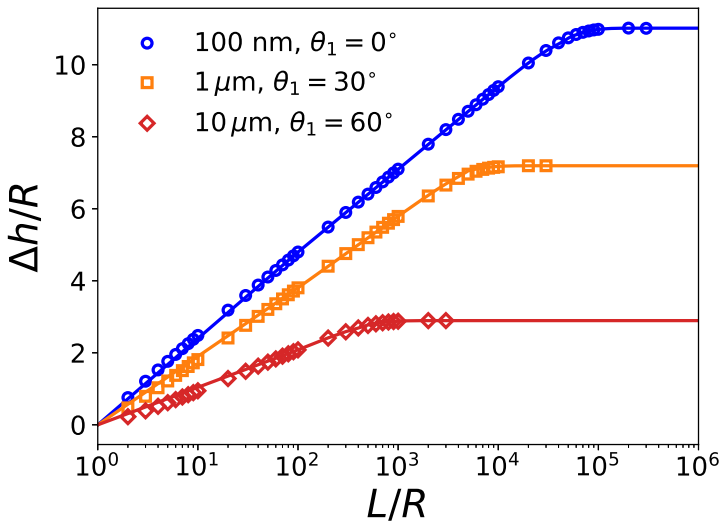

Figure 4.5: The numerical solutions of the meniscus height (symbols) at various combinations of R and θ_1 as a function of L are compared to the analytical expression in Eq. (4.22).

In Fig. 4.5, the analytical result on the meniscus height Δh in Eq. (4.22) is compared with numerical solutions of the full Young-Laplace equation rewritten as Eq. (4.6). A very good agreement has been found between the two, indicating that Eq. (4.22) can be used to accurately predict the meniscus height on the outside of a circular cylinder with $R \ll \kappa^{-1}$ for a meniscus with an arbitrary lateral span, including the crossover zone $0.4\kappa^{-1} \lesssim L \lesssim 4\kappa^{-1}$. However, Eq. (4.22) is a result obtained by comparing the analytical expression of the meniscus height in the limit of $\kappa L \ll 1$ and the numerical results for a full range of κL. It remains an open question if the universal expression of Δh in Eq. (4.22) for arbitrary L, R (as long as it is less than κ^{-1}), and θ_1 can be derived with an analytical approach.

The results presented in Figs. 4.4 and 4.5 are for L changing from $2R$ to a value much larger than κ^{-1} and for R changing from 100 nm to 10 μm, i.e., $R \ll \kappa^{-1}$. There are several limits that are of interest but not explored in detail in this chapter. In one, if R is made much larger than κ^{-1}, then the system depicted in Fig. 4.1 can be regarded as a meniscus between two flat walls (or even be reduced to a meniscus on one flat wall if $L - R \gg \kappa^{-1}$) [83]. There is a crossover from the $R \ll \kappa^{-1}$ limit, the focus of this chapter, and the $R \gg \kappa^{-1}$ limit. In the crossover, R is comparable to κ^{-1} and the numerical procedure of dealing with the Young-Laplace equation rewritten as Eq. (4.6) can be applied. In the limit of R being reduced to nanometer scales, the line-tension effect associated with the large curvature (R^{-1}) of the contact line on the surface of the cylinder may become important [84]. In the case where $L-R$ is small enough, factors including disjoining pressure will kick in [78]. If $L-R$ is further reduced such that the molecular nature of a liquid has to be taken into account, the continuum theory of capillarity may break down [78]. These limits are intriguing directions for future studies.

4.4 Conclusions

The problem of a small circular cylinder immersed in a liquid bath has been studied for many years. The focus was mainly on the limit where the liquid bath is much larger than the capillary length (i.e., $L \gg \kappa^{-1} \gg R$) [63–68] or on the case where gravity is negligible and the liquid-vapor interface can be described as a catenary (i.e., $\kappa^{-1} \gg L \gg R$) [62, 69]. In this chapter, we provide a comprehensive discussion of the meniscus on the outside of a circular cylinder with $R \ll \kappa^{-1}$ vertically positioned in a liquid bath with lateral span L ranging from microscopic to macroscopic scales. We obtain an analytical solution of the meniscus profile based on elliptic integrals when $\kappa^{-1} \gg L > R$ and the solution reduces to a catenary when $\kappa^{-1} \gg L \gg R$. In these solutions, the meniscus height $\Delta h \sim R\ln(L/R)$. Our numerical solutions of the full Young-Laplace equation for an arbitrary L indicate that Δh indeed scales with $R\ln(L/R)$ up to about $L \lesssim 0.4\kappa^{-1}$. In the opposite limit where $L \gtrsim 4\kappa^{-1}$, the meniscus height agrees well with the prediction of the Derjaguin-James formula and scales with $R\ln(\kappa^{-1}/R)$. The range $0.4\kappa^{-1} \lesssim L \lesssim 4\kappa^{-1}$ is the crossover region where the actual value of Δh deviates from the prediction of either the analytical solution based on elliptic integrals or the Derjaguin-James formula.

Our analyses reveal a universal behavior that the analytical solution [Eq. (4.18)], which predicts $\Delta h \sim R\ln(L/R)$, always reaches the upper bound set by the Derjaguin-James formula at $L \approx 1.85\kappa^{-1}$. Therefore, the analytical solution with its parameter $l = L/R$ when $L \leq 1.85\kappa^{-1}$ and capped at $l = 1.85\kappa^{-1}/R$ when $L > 1.85\kappa^{-1}$ can be used to estimate the meniscus height Δh. The relative deviation of the actual value of Δh determined via numerical solutions from this estimate is found to be only noticeable in the crossover region but still less than 5%. We further find that the relative errors at different R and contact angles at the surface of the cylinder, if properly scaled, as a function of κL all collapse to a master curve. With a fitting function to this master curve, we obtain an analytical

expression [Eq. (4.22)] that can be used for accurate prediction of Δh for the whole range of L from microscopic to macroscopic scales including the crossover zone. Although in this chapter we only consider cases with the contact angle on the wall being fixed at $\pi/2$, the theoretical analyses and numerical treatments of the general Young-Laplace equation can also be extended to more general cases with other contact angles at the wall surface.

Chapter 5

Small particle at a liquid-vapor interface

This chapter is based on our publication [80]:

Yanfei Tang and Shengfeng Cheng, "Capillary forces on a small particle at a liquid-vapor interface: theory and simulation," Phys. Rev. E 98, 032802 (2018). Copyright (2018) by American Physical Society.

I performed all the analytical and numerical work under Dr. Cheng's supervision. All authors contributed to the writing of this paper.

5.1 Introduction

Recently, the drying of colloidal suspensions has attracted great attention as it provides a facile procedure to generate dry colloidal films and superstructures with controlled arrangements of particles [85]. To understand the structural formation in colloidal suspensions

induced by solvent evaporation, much effort has been made to model such systems using molecular dynamics (MD) simulations [11, 20, 21, 23, 34, 86]. In these simulations, one key aspect is the representation of the solvent. In a few works, the solvent is modeled explicitly as Lennard-Jones liquids [34, 86]. However, such simulations are extremely expensive and the parameter space that can be explored is rather limited [34]. In others, an implicit solvent model is adopted and a liquid-vapor interface is modeled as a confining potential for all the solutes in the solution [11, 20, 21, 23]. Usually, a harmonic potential is used with the potential minimum indicating a particle's equilibrium position relative to the interface [49]. The evaporation process of the solvent is mimicked by moving the interface in a controlled manner. In this moving interface method of modeling the evaporation process of a suspension, a spring constant has to be assumed in the harmonic potential to capture the confining effect of the interface on the particles in the liquid solvent. Though a harmonic potential for a particle adsorbed at an interface is intuitively sensible and has been widely used [49, 87], there lacks a systematic physical interpretation of the associated spring constant. A deeper understanding is thus needed on the effective potential experienced by a particle when it is displaced out of its equilibrium position at a liquid-vapor interface.

Understanding the behavior of a particle at a liquid-vapor interface (or more generally, a fluid-fluid interface) is also important in many fields such as interfacial self-assembly of particles [88–91], emulsion and foam stabilization [92–94], fabrication of colloidal gels [95], interfacial particle adsorption [87, 96], flotation processing of minerals [97], and granular materials [98]. A comprehensive review of this topic can be found in Ref. [99]. Because of its practical importance, the detachment of a particle from a planar liquid surface has been studied for a long time [97, 100–110]. The problem of the quasistatic removal of a sphere from a liquid surface has a strong connection with the meniscus on the outside of a cylinder in a liquid bath, which is governed by the Young-Laplace equation [62]. White and

Tallmadge [64], and Huh and Scriven [65] numerically studied the meniscus on a cylinder vertically penetrating an unbound liquid surface. A formula for the meniscus height was proposed by James for this case [66], which was actually suggested earlier by Derjaguin [63] (see the note at the end of Ref. [66]). We call this result the Derjaguin-James formula, which is very accurate for small cylinders. A similar formula for the meniscus height on a sphere at the surface of a large liquid bath has been widely used in later research [97]. Pitois and Chateau studied the work of detachment of removing a small particle from an interface both experimentally and analytically using a theory based on the Derjaguin-James formula [105, 106]. Anachkov *et al.* recently refined Pitois and Chateau's theory by correcting the filling angle at which a capillary bridge ruptures and compared the theory with experimental data collected with a colloidal-probe atomic force microscope (AFM) [108]. Experimental efforts have been reported where the capillary force and meniscus shape were examined by a laser scanning confocal microscope for a microparticle detaching from a liquid surface [111].

Pulling a small sphere from a liquid surface can be used as a technique known as sphere tensiometry to measure the surface tension of the liquid and its contact angle on the surface of the sphere [100, 103]. This method is based on the fact that surface tension is the physical origin of the capillary force on a particle that controls its detachment behavior. Depending on the size of the particle, gravity and buoyancy force may also come into play [101, 102]. To the best of our knowledge, in most studies reported so far on particle detachment from a liquid surface, the surface was assumed to be unbound laterally [97, 100–106, 108, 110, 112]. This assumption is valid when the lateral size of the liquid bath L is much lager than the capillary length κ^{-1} of the interface. However, in recent AFM experiments the size of the particle is at the scale of micrometers and the lateral span of the meniscus can be comparable or even smaller than κ^{-1} [108]. De Baubigny *et al.* showed that the lateral size of a liquid bath can affect the capillary force and meniscus rise on a nanofiber [69]. Recently, we studied

the meniscus on a small cylinder located at the center of a liquid-vapor interface that is confined in a cylindrical container of a finite radius L [48]. Our results show the crossover from nanometer/micrometer scales where the meniscus rise grows with L logarithmically to macroscopic scales where the meniscus rise saturates to a value predicted by the Derjaguin-James formula. Similar crossover is expected to occur for a small sphere at a liquid-vapor interface as well.

In a seminal work on contact angle hysteresis, Joanny and de Gennes showed that the capillary force associated with contact line pinning on a defect exhibits a linear dependence on the deformation of the contact line, and the resulting spring constant has a logarithmic dependence on a length scale, which can be interpreted as the average distance between the defects [33]. An experiment by Nadkarni and Garoff on the contact line pinning on a single defect confirmed the theoretical prediction of Joanny and de Gennes and revealed a relation between the pinning of a contact line and the removal of a particle from a liquid surface [113]. A similar connection was discussed by O'Brien as well [104]. Later works by Preuss and Butt [114], and by Ettelaie and Lishchuk [115, 116] showed that a linear force-displacement curve emerges not only for a particle detaching from a planar liquid surface but also in the case of a surface with an overall curvature. A similar behavior was observed for spheroidal particles by Davies *et al.* [117].

In this chapter our goal is to study the force-displacement curve for a particle at a liquid-vapor interface with a finite lateral extent ranging from nanometer to macroscopic scales. To achieve this goal, we study a small particle with radius R at a liquid-vapor interface with both the macroscopic theory of capillarity and MD simulations, the latter of which has been widely used recently to study capillary phenomena at nanometer scales [78, 79, 118–120]. In particular, we place the liquid in a cylindrical container with radius L ($> R$) and the particle along the central axis of the container. The meniscus around the particle and the

capillary force on it are computed when it is placed at different height across the liquid-vapor interface. This geometry allows us to systematically explore the crossover from a region where $L \ll \kappa^{-1}$, and thus gravity can be ignored, to a region where $L \gtrsim \kappa^{-1}$ and gravity starts to play a role. We systematically study this crossover with the macroscopic theory of capillarity based on the Young-Laplace equation. At nanometer scales, we perform MD simulations and compare the simulation results on the meniscus profile and capillary force with the predictions of the macroscopic theory. A good agreement is found between the two. At micrometer to macroscopic scales, we compare the theory with the experimental data by courtesy of Anachkov [108] and show that the finite extent of the menisci involved in the experiments needs to be considered in order to understand the experimental results.

This chapter is organized as follows. In Sec. 5.2 we present a complete theory of a meniscus on the outside of a sphere with the lateral span of the meniscus varying from nanometer to macroscopic scales. The MD simulation methods are introduced in Sec. 5.3. In Sec. 5.4 we discuss and compare the results from the theory, simulations, and experiments. We conclude this chapter in Sec. 5.5 by summarizing the results on the effective confining potential on a particle from a liquid-vapor interface, which provide a physical foundation of the moving interface method of modeling solvent evaporation.

5.2 Macroscopic theory of capillarity

5.2.1 General theory

The geometry of the systems studied in this chapter, as well as a snapshot from MD simulations, is sketched in Fig. 5.1, where a particle of radius R straddles a liquid-vapor interface. The liquid bath is placed in a cylindrical container with radius L. The central axis of the

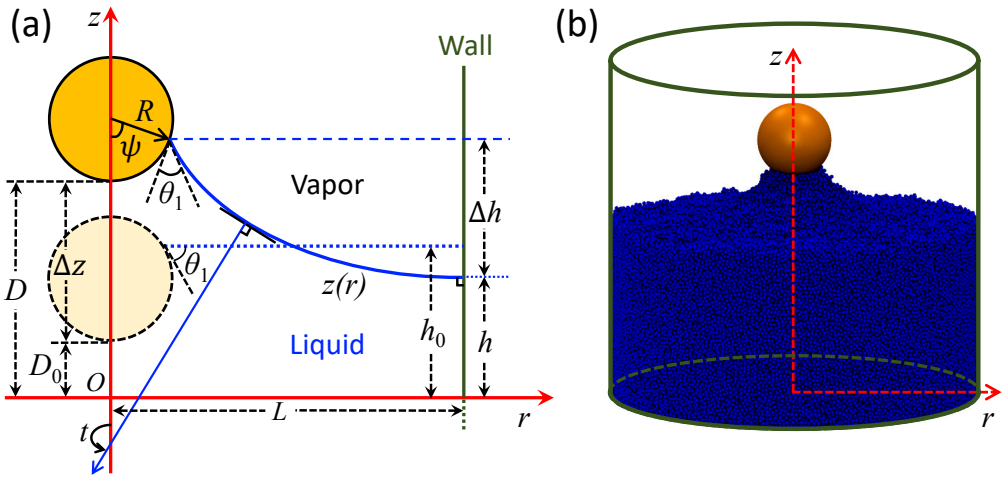

Figure 5.1: (a) Sketch of a spherical particle at the center of the surface of a liquid bath in a cylindrical container: particle at an equilibrium height (dashed light yellow sphere) and being pulled upward (solid orange sphere). (b) Snapshot from MD simulations of a system with a spherical particle pulled from a liquid-vapor interface.

container is taken as the z axis, along which the particle's center is located. A bottom wall at $z = 0$ is used to confine the liquid from below. To study the crossover from a system where L is larger than but comparable to R to a system where the meniscus is unbound (i.e., $L \to \infty$), we set the contact angle of the liquid on the container surface to be $\pi/2$. First, this choice guarantees the flatness of the liquid-vapor interface far away from the particle when $L \to \infty$, which is expected for an unbound meniscus [64, 65]. Second, with this choice the analytical solution of the Young-Laplace equation is greatly simplified for $L \ll \kappa^{-1}$ and the numerical treatment of the equation at $L \simeq \kappa^{-1}$, where the gravitational contribution to the local pressure jump across the liquid-vapor interface has to be taken into account, is much easier to implement [48].

The contact angle of the liquid on the particle surface is denoted as θ_1. Here we do not consider any pinning effect of a contact line on the surface of either the particle or the container. When the particle is in its equilibrium location, the liquid-vapor interface is flat and intersects with the particle surface at a filling angle $\psi = \pi - \theta_1$, as shown in Fig. 5.1(a).

We denote the height of this flat interface in equilibrium as h_0. The equilibrium position of the particle center is then at $h_0 - R\cos\theta_1$ [121].

When the particle is pulled upward or pressed downward vertically (i.e., along the central axis of the cylindrical container), the liquid-vapor interface will bend and form a meniscus, as shown in Fig. 5.1 for pulling. If we denote the distance from the bottom of the particle to the bottom wall as D, then its value for a particle in the equilibrium location is $D_0 = h_0 - R(1+\cos\theta_1)$ and $\Delta z \equiv D - D_0 = D - h_0 + R(1+\cos\theta_1)$ is the displacement of the particle from its equilibrium height. In this chapter, our main goal is to understand how the capillary force on the particle depends on Δz. For this purpose, we must solve the meniscus profile $z(r)$. For simplicity, we define $z_0(r) \equiv z(r) - h$, where h is the height at which the meniscus meets the container surface. The range of z_0 is then $[0, \Delta h]$ (or $[\Delta h, 0]$), where Δh denotes the meniscus rise (or depression).

Considering that a meniscus can develop a neck where $|\frac{\mathrm{d}z_0}{\mathrm{d}r}|$ is infinite, the function $z_0(r)$ becomes double-valued for a range of r near the neck. It is therefore more convenient to represent the meniscus as $r(z_0)$, which is always a single-valued function of $z_0 \in [0, \Delta h]$ for a rising meniscus (or $z_0 \in [\Delta h, 0]$ for a depressed meniscus). The function $r(z_0)$ is the solution of a form of the Young-Laplace equation studied by Bashforth and Adams before [70],

$$\frac{r''}{(1+r'^2)^{3/2}} - \frac{1}{r(1+r'^2)^{1/2}} = \frac{\Delta p}{\gamma} + \frac{\Delta\rho g z_0}{\gamma} \ , \tag{5.1}$$

where $r' \equiv \frac{\mathrm{d}r}{\mathrm{d}z_0}$, $r'' \equiv \frac{\mathrm{d}^2 r}{\mathrm{d}z_0^2}$, Δp is the pressure jump from the vapor to the liquid phase at $r = L$ (i.e., the pressure on the vapor side minus that on the liquid side across the liquid-vapor interface at $r = L$), γ is the surface tension of the liquid, $\Delta\rho \equiv \rho_l - \rho_v$ is the difference of the liquid and vapor densities, and g is the gravitational constant. Equation. (5.1) is for a rising meniscus that may have a neck. To describe a depressed meniscus, the left hand side

of Eq. (5.1) should be multiplied with -1.

A physical solution of Eq. (5.1) for a given D needs to satisfy the constraint that the volume of the liquid bath,

$$V = \pi \int_0^{\Delta h} r^2(z_0)\,\mathrm{d}z_0 + \pi L^2 h - \frac{\pi R^3}{3}\left(2 - 3\cos\psi + \cos^3\psi\right) \ , \tag{5.2}$$

is fixed at a constant set by parameters h_0, L, R, and θ_1, which set up the physical problem at hand. Since for the particle in its equilibrium location, $\Delta h = 0$, $h = h_0$, and $\psi = \pi - \theta_1$, the fixed volume is

$$V = \pi L^2 h_0 - \frac{\pi R^3}{3}\left(2 + 3\cos\theta_1 - \cos^3\theta_1\right) \ . \tag{5.3}$$

Equations (5.1)–(5.3) actually provide an implicit relation for the filling angle ψ, which in turn determines the meniscus profile on the outside of the particle. For a given Δz, we have

$$D = \Delta z + h_0 - R(1 + \cos\theta_1) \ . \tag{5.4}$$

The procedure of solving the meniscus profile for the given Δz starts with an assumed filling angle ψ. Then Eq. (5.1) is solved either analytically or numerically to obtain the meniscus profile, $r(z_0)$, including the meniscus height, Δh. The height of the liquid-vapor interface at $r = L$ is furthermore given by

$$h = D + R(1 - \cos\psi) - \Delta h \ . \tag{5.5}$$

With $r(z_0)$, Δh, and h determined, the volume of the liquid bath can be computed with

Eq. (5.2) and compared to Eq. (5.3) until for the given Δz, a filling angle ψ is found to satisfy the volume constraint.

After the meniscus profile is determined at a given Δz, i.e., after the filling angle ψ is found for the given Δz using the self-consistent procedure described above, the total capillary force on the particle can be computed as

$$\begin{aligned} F = & 2\pi\gamma R \sin\psi \sin(\theta_1 + \psi) \\ & - (\Delta p + \Delta\rho g \Delta h)\, \pi R^2 \sin^2\psi \\ & - \Delta\rho g \frac{\pi R^3}{3} \left(2 - 3\cos\psi + \cos^3\psi\right) \ , \end{aligned} \tag{5.6}$$

where the first term is a direct contribution from the surface tension of the liquid at the contact line on the particle surface, the second term captures the contribution of the Laplace pressure with the gravitational effect included, and the last term is a buoyancy force.

The full Eq. (5.1) is hard to solve analytically. The main difficulty is the presence of the gravitational term, the importance of which is captured by a capillary length defined as,

$$\kappa^{-1} = \sqrt{\frac{\gamma}{\Delta\rho g}}.$$

For water at room temperature, $\kappa^{-1} \approx 2.7$ mm. In this chapter, we are mainly concerned about a small particle with size ranging from nanometer to micrometer scales. Therefore, it is always the case that $R \ll \kappa^{-1}$. In the limit of $R < L \ll \kappa^{-1}$, the gravitational term in Eq. (5.1) is negligible and the equation can be solved analytically with the elliptic integrals. In the opposite limit where $R \ll \kappa^{-1} \ll L$, the approximate Derjaguin-James formula can be used to estimate Δh [63, 66]. In the crossover region where $L \sim \kappa^{-1}$, we recently found another approximate formula [48], based on numerical solutions of Eq. (5.1), to predict Δh.

In the following we first discuss a way to transform Eq. (5.1) that allows numerical treatments in general and then analyze the different regions in detail.

Equation (5.1) can be made dimensionless via a change of variables,

$$x \equiv \kappa r \ , \quad y \equiv \kappa z_0 \ . \tag{5.7}$$

The result is the following nonlinear differential equation for a rising meniscus,

$$\frac{x''}{(1+x'^2)^{3/2}} - \frac{1}{x(1+x'^2)^{1/2}} = \frac{2\tilde{H}}{\kappa} + y \ , \tag{5.8}$$

where $x' \equiv \frac{\mathrm{d}x}{\mathrm{d}y}$, $x'' \equiv \frac{\mathrm{d}^2x}{\mathrm{d}y^2}$, and $2\tilde{H} \equiv \Delta p/\gamma$. Again, the two terms on the left hand side need to flip signs for a depressed meniscus. This second-order differential equation can be rewritten into two coupled first-order differential equations for which numerical treatments are much easier. To this end, we take the local normal vector of the liquid-vapor interface pointing toward the liquid phase and introduce an angle parameter t, which is the angle of rotating the z axis *counterclockwise* to the local normal vector, as shown in Fig. 5.1. It is easy to show that t always changes from π at the surface of the container to $\theta_1 + \psi$ on the particle surface. For a rising meniscus, $\theta_1 + \psi < \pi$ while for a depressed one, $\theta_1 + \psi > \pi$.

Equation (5.8) can be rewritten in terms of t as

$$\frac{\mathrm{d}\sin t}{\mathrm{d}x} + \frac{\sin t}{x} = -\frac{2\tilde{H}}{\kappa} - y \ . \tag{5.9}$$

Equation (5.9) is actually more general than Eq. (5.8) as Eq. (5.9) applies no matter whether the meniscus is rising or depressed while Eq. (5.8) only describes a rising meniscus, though both can deal with a meniscus with a neck. It is thus advantageous to use Eq. (5.9) to describe an (axisymmetric) meniscus on the outside of a spherical particle at a liquid-vapor

interface.

Rewriting Eq. (5.9) for $\frac{\mathrm{d}x}{\mathrm{d}t}$ and using $\frac{\mathrm{d}y}{\mathrm{d}x} = \tan t$, we obtain a pair of coupled first-order nonlinear differential equations,

$$\frac{\mathrm{d}x}{\mathrm{d}t} = -\left(\frac{2\tilde{H}}{\kappa} + y + \frac{\sin t}{x}\right)^{-1} \cos t \ , \tag{5.10a}$$

$$\frac{\mathrm{d}y}{\mathrm{d}t} = -\left(\frac{2\tilde{H}}{\kappa} + y + \frac{\sin t}{x}\right)^{-1} \sin t \ , \tag{5.10b}$$

with the following boundary conditions,

$$t = \theta_1 + \psi \quad \text{at} \quad x = \kappa R \sin\psi \ , \tag{5.11a}$$

$$t = \pi \quad \text{at} \quad x = \kappa L \quad \text{and} \quad y = 0 \ . \tag{5.11b}$$

Generally, numerical solutions of Eq. (5.10) can be obtained by the shooting method [81]. It should be emphasized that Eq. (5.10) provides a unified description for a rising or depressed meniscus with or without a neck. The difference only shows up in the boundary condition in Eq. (5.11a). For a meniscus rising on the particle surface, $\theta_1 + \psi < \pi$ while for a depressed one, $\theta_1 + \psi > \pi$. Moreover, if $\theta_1 + \psi < \pi/2$ or $\theta_1 + \psi > 3\pi/2$, then the meniscus has a neck.

5.2.2 $L \ll \kappa^{-1}$ limit

In the limit of $R < L \ll \kappa^{-1}$, the Bond number $\mathrm{Bo} \equiv gL^2\Delta\rho/\gamma = \kappa^2 L^2$ is much smaller than 1, indicating that gravity can be ignored in the treatment of the meniscus. Equation (5.1) for a rising meniscus can be simplified as

$$\frac{r''}{(1+r'^2)^{3/2}} - \frac{1}{r(1+r'^2)^{1/2}} = 2\tilde{H} \tag{5.12}$$

with $2\tilde{H} \equiv \Delta p/\gamma$. For a depressed meniscus, the right hand side of Eq. (5.12) should be $-2\tilde{H}$. Equation. (5.12) can be solved analytically for the boundary condition sketched in Fig. 5.1. The derivation below benefits from a seminal paper of Orr *et al.* on the theory of pendular rings [76] and a recent work by Rubinstein and Fel [82].

We first make Eq. (5.12) dimensionless by introducing new variables $X = r/R$ and $Y = z_0/R$. Defining $u = \sin t$ with the angle parameter t introduced previously, we can rewrite Eq. (5.12) as

$$-2H = \frac{\mathrm{d}u}{\mathrm{d}X} + \frac{u}{X} \ , \tag{5.13}$$

where $H \equiv R\tilde{H}$ is the dimensionless mean curvature of the meniscus. The boundary conditions are

$$t = t_1 \quad \text{at} \quad X_1 = \sin\psi \ , \tag{5.14a}$$

$$t = t_2 \quad \text{and} \quad Y_2 = 0 \quad \text{at} \quad X_2 = l \ , \tag{5.14b}$$

where $t_1 = \theta_1 + \psi$, $t_2 = \pi$, and $l = L/R > 1$ is the scaled radius of the bucket. Like Eq. (5.9), Eq. (5.13) applies to both rising and depressed menisci and is more general than Eq. (5.12).

The solution for Eq. (5.13) is

$$u = \frac{c}{4HX} - HX \ . \tag{5.15}$$

The boundary condition Eq.(5.14a) indicates that

$$c = 4H \sin\psi \left[H \sin\psi + \sin(\theta_1 + \psi)\right] \ . \tag{5.16}$$

The other boundary condition Eq.(5.14b) yields

$$c = 4H^2 l^2 \ . \tag{5.17}$$

As a result, H is given by

$$H = \frac{\sin\psi \sin(\theta_1 + \psi)}{l^2 - \sin^2\psi} \ . \tag{5.18}$$

Note that $l \equiv L/R > 1$ and therefore the denominator in Eq. (5.18), $l^2 - \sin^2\psi$, is always positive. For a rising meniscus, $H > 0$ as $0 < \theta_1 + \psi < \pi$ while for a depressed one, $H < 0$ as $\pi < \theta_1 + \psi < 2\pi$. When the particle is in its equilibrium location, $\theta_1 + \psi = \pi$ and $H = 0$, which is expected for a flat liquid-vapor interface. Generally, H asymptotically approaches 0 when $l \equiv L/R \to \infty$.

Equation (5.15) yields a parametric relation, $X(t)$, which must be positive definite. Then the solution of the meniscus profile $Y(t)$ can be determined by noting that $\mathrm{d}Y/\mathrm{d}X = \tan t$. The results are

$$X(t) = \frac{1}{2H}\left(-\sin t \pm \sqrt{\sin^2 t + c}\ \right), \tag{5.19}$$

$$Y(t) = \frac{1}{2H}\int_{t_2}^{t}\left(-\sin\phi \pm \frac{\sin^2\phi}{\sqrt{\sin^2\phi + c}}\right)\mathrm{d}\phi \ , \tag{5.20}$$

where the + (−) sign is for a rising (depressed) meniscus. Hereafter, when the sign $\pm$ or $\mp$ appears in an equation, the upper sign is always for a rising meniscus while the lower sign is for a depressed one. In general, $t_2 = 3\pi/2 - \theta_2$ where θ_2 is the contact angle of the liquid on the container surface. For the systems considered here, $\theta_2 = \pi/2$ and therefore $t_2 = \pi$.

Equation (5.20) can be evaluated by the elliptic integrals and the result is

$$\begin{aligned} Y(t) &= \frac{1}{2H}(\cos t - \cos t_2) \\ &\pm \frac{\sqrt{c}}{2H}\Big[E(t,j) - E(t_2,j) - F(t,j) + F(t_2,j)\Big] \ , \end{aligned} \tag{5.21}$$

where $j^2 \equiv -\frac{1}{c}$. $F(t,j)$ and $E(t,j)$ are the incomplete elliptic integrals of the first kind and second kind, respectively,

$$E(t,j) \equiv \int_0^t \sqrt{1 - j^2 \sin^2\phi}\, \mathrm{d}\phi, \tag{5.22}$$

$$F(t,j) \equiv \int_0^t \frac{1}{\sqrt{1 - j^2 \sin^2\phi}}\, \mathrm{d}\phi. \tag{5.23}$$

The meniscus height, Δh, is given by $Y(t_1)$ with $t_1 = \theta_1 + \psi$ and the result is

$$\begin{aligned} \Delta h &= \frac{R}{2H}\Big[\cos(\theta_1 + \psi) + 1\Big] \\ &\pm \frac{R\sqrt{c}}{2H}\Big[E(\theta_1 + \psi - \pi, j) - F(\theta_1 + \psi - \pi, j)\Big] \ . \end{aligned} \tag{5.24}$$

Equation (5.24) holds as long as $\kappa^{-1} \gg L > R$. An approximate formula can be derived for Δh in the limit of $\kappa^{-1} \gg L \gg R$ using the series expansions of the elliptic integrals and the asymptotic behavior,

$$H = \frac{\sin\psi \sin(\theta_1 + \psi)}{l^2 - \sin^2\psi} \simeq \frac{\sin\psi \sin(\theta_1 + \psi)}{l^2} \to 0. \tag{5.25}$$

The result is

$$\Delta h \simeq R\sin\psi\sin(\theta_1+\psi) \times\left\{\ln\frac{2L}{R\sin\psi[1-\cos(\theta_1+\psi)]}-\frac{1}{2}\right\}, \tag{5.26}$$

which indicates that $\Delta h \sim R\ln(L/R)$ for $\kappa^{-1} \gg L \gg R$. Our numerical results indicate that this scaling relationship holds up to about $L \lesssim 0.4\kappa^{-1}$ [48]. Equation. (5.26) is very close to the result for a catenoid for which $H = 0$, except for the $-1/2$ term in the curly braces [48].

Again, a self-consistent procedure using the constraint that the volume of the liquid bath is fixed needs to be employed to determine the filling angle ψ for a given displacement, Δz. This procedure can be facilitated if we note that for the solution of the meniscus profile given in Eqs. (5.19) and (5.21), the volume of the liquid bath can be expressed analytically as

$$\frac{V}{R^3}=\frac{\pi}{8H^3}J_s+\pi l^2\frac{h}{R}-\frac{1}{3}\pi(2-3\cos\psi+\cos^3\psi), \tag{5.27}$$

where

$$\begin{aligned} J_s &= (4+c)(\cos t_1-\cos t_2) \\ &\quad -\frac{4}{3}\left(\cos^3 t_1-\cos^3 t_2\right) \\ &\quad \pm\sqrt{c}\left\{\frac{8+c}{3}\Big[E(t_1,k)-E(t_2,k)\Big]\right. \\ &\quad \left.-\frac{4+c}{3}\Big[F(t_1,k)-F(t_2,k)\Big]\right\} \\ &\quad \mp\frac{2}{3}\left[\sin(2t_1)\sqrt{\sin^2 t_1+c}-\sin(2t_2)\sqrt{\sin^2 t_2+c}\,\right]. \end{aligned} \tag{5.28}$$

After ψ is determined for a given Δz, the capillary force in the limit of $\kappa^{-1} \gg L > R$ can

be computed as

$$F = 2\pi\gamma R\Big[\sin\psi\sin(\theta_1+\psi) - H\sin^2\psi\Big] \tag{5.29}$$

with H given in Eq. (5.18).

Since for $l = L/R \gg 1$, the dimensionless mean curvature $H \to 0$, the capillary force is dominated by the surface tension term,

$$F \simeq 2\pi\gamma R\sin\psi\sin(\theta_1+\psi)\ , \tag{5.30}$$

and the meniscus height can be approximated as

$$\Delta h \simeq R\sin\psi\sin(\theta_1+\psi)\ln\frac{2L}{R}\ . \tag{5.31}$$

From Eqs. (5.4) and (5.5), we have

$$\Delta z = \Delta h + h - h_0 + R(\cos\theta_1 + \cos\psi)\ . \tag{5.32}$$

For $l = L/R \gg 1$, the meniscus height satisfies $\Delta h \gg R(\cos\theta_1+\cos\psi)$ and the displacement of the liquid-vapor interface far away from the particle becomes negligible, i.e., $h = h_0$. Therefore, we have approximately

$$\Delta z \simeq \Delta h\ . \tag{5.33}$$

Combining Eqs. (5.30), (5.31), and (5.33), we finally arrive at the Joanny-de Gennes' Hookean

law [33],

$$F \simeq \frac{2\pi\gamma}{\ln(2L/R)}\Delta z \ , \tag{5.34}$$

which yields an effective spring constant for a particle at a liquid-vapor interface that softens with the lateral span of the interface as $\ln^{-1}(2L/R)$. The denominator $\ln(2L/R)$ in Eq. (5.34) was absent in the form derived by Pieranski [49], which was used in many papers including the recent ones on modeling solvent evaporation with the moving interface method [11, 20, 21, 23]. This omission is easy to understand since in Pieranski's model, the liquid-vapor interface is always flat even for a particle out of its equilibrium location at the interface [49]. However, in the model discussed here the meniscus height on the outside of the particle scales with $\ln(2L/R)$.

5.2.3 Region with $L \gtrsim \kappa^{-1}$

Our previous work indicated that the theory presented in Sec. 5.2.2 can be used to describe a meniscus on the outside of a small circular cylinder pretty accurately for L up to $\sim 0.4\kappa^{-1}$ [48]. For $L \gtrsim 4\kappa^{-1}$, the interface can be treated as unbound and the meniscus height is given by the Derjaguin-James formula

$$\begin{aligned}\Delta h = {} & R\sin\psi\sin(\theta_1+\psi) \\ & \times\left\{\ln\frac{4\kappa^{-1}}{R\sin\psi[1-\cos(\theta_1+\psi)]} - E\right\} \ ,\end{aligned} \tag{5.35}$$

where $E = 0.57721...$ is the Euler-Mascheroni constant.

In the crossover region $0.4\kappa^{-1} \lesssim L \lesssim 4\kappa^{-1}$, our previous work revealed an approximate

expression of Δh as [48]

$$\begin{aligned}\Delta h &= \Delta h(\text{elliptic}) \\ &\times \left\{1 - m(\kappa L)\Big(\kappa R \sin\psi[1-\cos(\theta_1+\psi)]\Big)^{0.12}\right\} ,\end{aligned} \tag{5.36}$$

where $\Delta h(\text{elliptic})$ is the expression of the meniscus height in Eq. (5.24) based on the elliptic integrals and $m(x)$ is a kink function that reads

$$m(x) = \begin{cases} 0.085\exp\left[(x-1.85)^{1.83}/0.74\right] & \text{if } x \le 1.85 , \\ 0.085\exp\left[(1.85-x)/0.875\right] & \text{if } x > 1.85 . \end{cases} \tag{5.37}$$

Note that $l \equiv L/R$ is a key parameter entering the expression of $\Delta h(\text{elliptic})$ in Eq. (5.24). In the Derjaguin-James formula [Eq. (5.35)] the term L/R is replaced by κ^{-1}/R. We can therefore make Eq. (5.36) applicable for an arbitrary L (as long as it is larger than R) by using the following definition of l for $\Delta h(\text{elliptic})$,

$$l = \begin{cases} L/R & \text{if } L \le 1.85\kappa^{-1} , \\ 1.85\kappa^{-1}/R & \text{if } L > 1.85\kappa^{-1} . \end{cases} \tag{5.38}$$

The particular choice of the cutoff $1.85\kappa^{-1}$ can be understood by equating Δh in Eq. (5.26), which is a close approximation of Eq. (5.24), to that in the Derjaguin-James formula in Eq. (5.35). At $L = 2e^{1/2-E}\kappa^{-1} \approx 1.85\kappa^{-1}$, the two expressions are equal. With l defined in Eq. (5.38), the meniscus height Δh in Eq. (5.36) reduces to the expression in Eq. (5.24) for $L \ll \kappa^{-1}$, while it reduces to the Derjaguin-James formula in Eq. (5.35) for $L \gg \kappa^{-1}$. It also agrees well with the numerical solutions of Δh in the crossover region where $L \sim \kappa^{-1}$ [48].

It should be clarified that the analytical results in Sec. 5.2.2 for $L \ll \kappa^{-1}$ and the empirical

results [Eqs. (5.36), (5.37), (5.38)] for a full range of L are obtained with the assumption that the contact angle on the container surface θ_2 is fixed at $\pi/2$. When $L \gg \kappa^{-1}$, the meniscus can be treated as unbound and the meniscus profile around the central sphere is independent of θ_2. In this limit the meniscus rise is given by the Derjaguin-James formula. In the opposite limit where $L \lesssim \kappa^{-1}$, the meniscus profile depends on θ_2. However, all different results on the meniscus rise for different values of θ_2 at $L \lesssim \kappa^{-1}$ will converge to the same limit set by the θ_2-independent Derjaguin-James formula, when L is increased to be much lager than κ^{-1}. The transition to an unbound meniscus at a general θ_2 is an interesting problem for future research. Here we only consider the case $\theta_2 = \pi/2$.

For $L \gtrsim \kappa^{-1}$, the displacement of the liquid-vapor interface (i.e., $h - h_0$) induced by the particle displacement is negligible and thus $h \simeq h_0$. As a result, the particle displacement

$$\Delta z \approx \Delta h + R(\cos\theta_1 + \cos\psi) \ . \tag{5.39}$$

Equation (5.39) and (5.36) together provide an expression of Δz with the filling angle ψ as a parameter for $L \gtrsim \kappa^{-1}$ (other physical quantities, L, R, and θ_1 are already known when the problem is set up). In this limit, there is no need to use the volume constraint of the liquid bath to connect ψ to Δz.

The capillary force in the region with $L \gtrsim \kappa^{-1}$ becomes

$$\begin{aligned} F = 2\pi\gamma R\Big[&\sin\psi\sin(\theta_1+\psi) - \frac{1}{2}\kappa^2\Delta h R\sin^2\psi \\ &- \frac{1}{6}\kappa^2 R^2(2 - 3\cos\psi + \cos^3\psi)\Big] \ . \end{aligned} \tag{5.40}$$

The Laplace pressure term drops out because $H \simeq 0$ in this limit. In this chapter we are concerned about particles with $R \ll \kappa^{-1}$ and then the buoyancy force and the gravitational

contribution in Eq. (5.40) are negligible compared to the surface tension contribution. As a result, the capillary force is dominated by the surface tension term. Equation (5.40) provides an expression of the capillary force with ψ as a parameter. Combining Eqs. (5.40), (5.39), and (5.36), we obtain a force-displacement curve parameterized by ψ for $L \gtrsim \kappa^{-1}$.

5.3 Simulation methods

A snapshot from MD simulations of a particle at a liquid-vapor interface is shown in Fig. 5.1(b). In order to address generic behavior, we consider a molecular liquid consisting of short linear chains of four spherical beads. This tetramer model captures many aspects of the behavior of short hydrocarbon chains [78, 79]. All the beads interact with a Lennard-Jones (LJ) potential,

$$V_{\mathrm{LJ}}(a) = 4\epsilon \left[\left(\frac{\sigma}{a}\right)^{12} - \left(\frac{\sigma}{a}\right)^{6} - \left(\frac{\sigma}{a_c}\right)^{12} + \left(\frac{\sigma}{a_c}\right)^{6} \right] , \tag{5.41}$$

where a is the distance between the centers of beads, σ represents an effective bead diameter, and ϵ is an energy scale. The LJ potential is truncated at $a_c = 2.5\sigma$. Two neighboring beads on a chain are connected by a bond described by a finitely extensible nonlinear elastic (FENE) potential [122],

$$V_{\mathrm{FENE}}(a) = -\frac{1}{2} K R_0^2 \ln\left(1 - \frac{a^2}{R_0^2}\right) , \tag{5.42}$$

where the canonical values are adopted with $R_0 = 1.5\sigma$ and $K = 30\epsilon/\sigma^2$.

A spherical particle is modeled as a uniform distribution of LJ mass points. The interaction between the particle and a LJ bead is determined by integrating the LJ potential between

the bead and all the mass points on the particle [36, 37]. The resulting potential is

$$U_{\rm ns}(a) = \frac{2}{9}\frac{R_{\rm n}^3\sigma^3 A_{\rm ns}}{(R_{\rm n}^2-a^2)^3} \times\left[1-\frac{(5R_{\rm n}^6+45R_{\rm n}^4a^2+63R_{\rm n}^2a^4+15a^6)\sigma^6}{15(R_{\rm n}-a)^6(R_{\rm n}+a)^6}\right] , \tag{5.43}$$

where a is the center-to-center distance between the bead and particle and the radius of the particle is $R_{\rm n}$. In our simulations $R_{\rm n} = 10\sigma$. If we take $\sigma \simeq 0.5$ nm, then $R_{\rm n}$ is about 5 nm. The particle-bead potential is truncated at $a_c = 14\sigma$. The Hamaker constant $A_{\rm ns}$ controls the wetting behavior of the liquid on the particle surface.

The liquid bath is placed in a cylindrical container of nominal radius $L_{\rm n}$. Two values, $L_{\rm n} = 50\sigma$ and 75σ, are used in our simulations. The central axis of the container is along the z axis. Without the particle, the free liquid-vapor interface is parallel to the horizontal x-y plane. Two horizontal walls are used at $z = 0$ and $z = 100\sigma$ to confine the liquid and vapor. The interaction between a LJ bead and the top, bottom, or side wall is governed by a LJ 9-3 potential

$$U_{\rm w}(a) = \epsilon_{\rm w}\left[\frac{2}{15}\left(\frac{\sigma}{a}\right)^9-\left(\frac{\sigma}{a}\right)^3-\frac{2}{15}\left(\frac{\sigma}{a_{\rm c}}\right)^9+\left(\frac{\sigma}{a_{\rm c}}\right)^3\right] , \tag{5.44}$$

where a is the distance from the bead center to the wall and $a_{\rm c} = 2.5\sigma$, 0.8583σ, and 3.0σ are the cutoff distances at the side, top, and bottom wall, respectively. The interaction strength is set with $\epsilon_{\rm w} = 2.1\epsilon$ to yield a 90° contact angle on the side wall, as confirmed with independent simulations.

The whole system is thermalized at a constant temperature $T = 0.7\epsilon/k_{\rm B}$, where $k_{\rm B}$ is the Boltzmann constant. At this temperature, the tetramer LJ liquid has a density $\rho_l = 0.927m/\sigma^3$ and the vapor density $\rho_v = 0$. Our motivation to pick this nonvolatile liquid is to

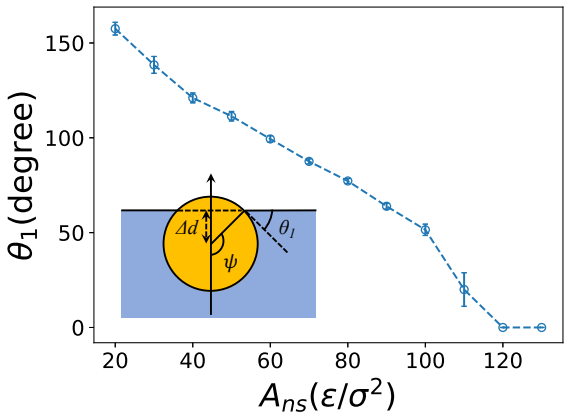

Figure 5.2: Contact angle θ_1 vs. Hamaker constant $A_{\rm ns}$ for a particle with $R_{\rm n} = 10\sigma$ at the surface of the tetramer liquid. The inset shows the equilibrium configuration of the particle straddling the liquid-vapor interface, where $\psi = \pi - \theta_1$.

generate a liquid-vapor interface that is sharp and can equilibrate quickly. To determine the surface tension of the tetramer liquid, we simulated a liquid film in a cubic simulation cell with a liquid-vapor interface in the x-y plane, in which the periodic boundary conditions are used. The liquid film is in contact with a bottom wall at $z = 0$ and confined by a top wall at $z = 100\sigma$. The liquid-vapor interface is located at about $z = 51\sigma$. The surface tension was computed with the Kirkwood-Buff formula [123],

$$\gamma = \frac{1}{2}\int \left[p_{zz}(z) - \frac{p_{xx}(z) + p_{yy}(z)}{2} \right] \mathrm{d}z \ , \tag{5.45}$$

where $p_{xx}(z)$, $p_{yy}(z)$, and $p_{zz}(z)$ are the three diagonal components of the stress tensor. The result is $\gamma = 1.018\epsilon/\sigma^2$ in the LJ units. A rough mapping between LJ and real units can be found in a previous study [78].

The wetting behavior of the tetramer liquid on the particle surface depends on the Hamaker constant $A_{\rm ns}$. Considering the finite radius of the particle, we identified the contact angle of the liquid on the particle surface directly by placing the particle at the surface of the liquid film that was used in the calculation of surface tension. When the particle settles into its

equilibrium location, the liquid-vapor interface is flat and intersects with the particle surface with a filling angle $\psi = \pi - \theta_1$. The particle center is then at distance $\Delta d = R\cos\theta_1$ from the liquid-vapor interface. By computing Δd in MD simulations, we can determine the contact angle as

$$\theta_1 = \arccos(\Delta d/R) \ . \tag{5.46}$$

To determine Δd, we need to obtain the location of the liquid-vapor interface, which was achieved by fitting the density profile of the liquid far away from the particle to the following functional form,

$$\rho(z) = \frac{1}{2}(\rho_l + \rho_v) - \frac{1}{2}(\rho_l - \rho_v)\tanh\left[\frac{2(z - z_i)}{d_s}\right] \ , \tag{5.47}$$

where z_i is the location and d_s is the width of the interface, respectively.

The results for θ_1 as a function of $A_{\rm ns}$ are shown in Fig. 5.2. The contact angle decreases when the Hamaker constant between the particle and liquid increases [40, 124]. This trend is expected as stronger interactions between a solid surface and a liquid favor the wetting of the solid by the liquid. The contact angle θ_1 and surface tension γ are used as material properties when the simulation results of the meniscus on the outside of a particle are compared to the predictions of the macroscopic theory of capillarity.

We used a pulling process to place the particle at various locations along the vertical z axis across the liquid-vapor interface. The particle was first fully immersed in the liquid bath. Then the particle was pulled upward with a constant speed $v_e = 0.02\sigma/\tau \sim 4$ m/s along the z direction. This speed is about six orders of magnitude larger than typical velocities of displacing particles (~ 1 μm/s) in AFM experiments [108]. To get rid of the inertial effects [78], we allowed the meniscus to relax for at least 5000τ when the particle was pulled to and

Table 5.1: Parameters of all five systems studied in this chapter.

$A_{\rm ns}$	θ_1	$R_{\rm n}/\sigma$	$L_{\rm n}/\sigma$	h_0/σ	No. of tetramers
100	48.5°	10	50	51.4	90000
80	76.5°	10	50	51.3	90000
60	98.2°	10	50	51.1	90000
40	120.5°	10	50	51.0	90000
100	48.5°	10	75	51.1	202612

then fixed at a certain location. After relaxation the meniscus profile was determined from the density profile of the liquid and the capillary force on the particle was computed. The procedure was repeated when the particle was pulled to its next location until the meniscus broke up. The parameters of all five systems studied with MD simulations are summarized in Table 5.1.

The Large-scale Atomic/Molecular Massively Parallel Simulator (LAMMPS) developed at Sandia National Laboratories [41] was adopted to perform all the MD simulations reported here. A velocity-Verlet algorithm was used to integrate the equation of motion with a time step $\delta t = 0.005\tau$, where $\tau = \sigma(m/\epsilon)^{1/2}$ is the LJ unit of time and m is the mass of a LJ bead. The particle has a mass $M = \frac{4\pi R^3 m}{3\sigma^3} = 4188.79m$. In all the simulations, the liquid was held at $T = 0.7\epsilon/k_{\rm B}$ via a Langevin thermostat with a damping rate $\Gamma = 0.1\tau^{-1}$.

5.4 Results and discussion

5.4.1 Theoretical procedure to determine filling angle

With the theory in Sec. 5.2.2, the meniscus profile can be predicted in the region with $L \ll \kappa^{-1}$ when the contact angle θ_1 and the filling angle ψ on the particle surface are given. Some examples for $\theta_1 = \pi/4$, $L/R = 5$, $D = 4R$ (i.e., with the particle center fixed at $z = 5R$), and various values of ψ are given in Fig. 5.3(a). The corresponding volume under

the meniscus profile (V) and the height of the meniscus rise or depression (Δh) are shown in Fig. 5.3(b). It should be pointed out that the meniscus profile, $r(z_0)$, depends on R, L, θ_1, and ψ, but not on D. However, as discussed in Sec. 5.2.2 for the system sketched in Fig. 5.1, the volume of the liquid bath is conserved. When the particle is pulled or pushed vertically to a certain height, the filling angle of the meniscus that is physically realized needs to satisfy the volume constraint. This fact is easy to understand as D, which sets the vertical location of the particle, is the parameter controlled in both simulations and experiments. The filling angle ψ is then a parameter set by the fixed volume of the liquid bath.

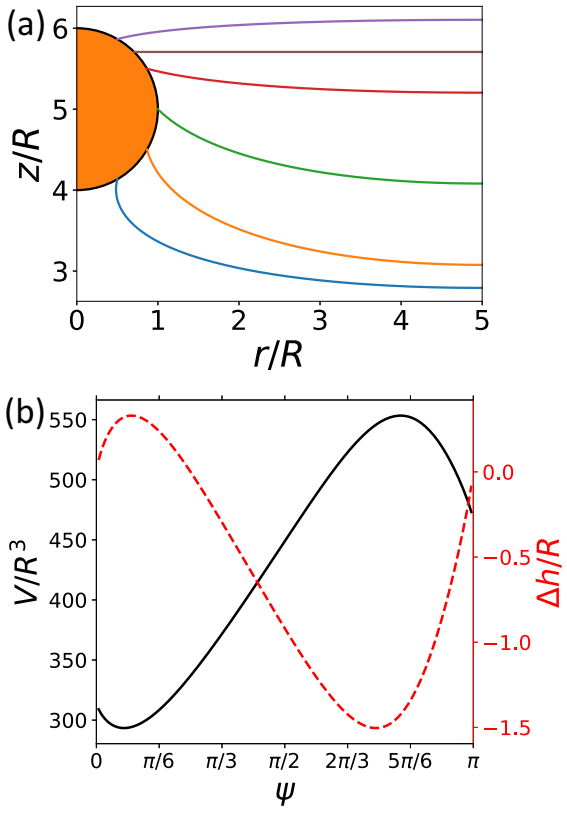

Figure 5.3: (a) Meniscus profiles for $\theta_1 = \pi/4$ and different filling angles: $\psi = \pi/6$, $\pi/3$, $\pi/2$, $2\pi/3$, $3\pi/4$, $5\pi/6$ (from bottom to top). The ratio $L/R = 5$ is used here and the center of the particle is fixed at $z = 5R$ (i.e., $D = 4R$ in Fig. 5.1). (b) The volume under the meniscus profile (solid black line) measured from the bottom wall at $z = 0$ and the height of the meniscus (dashed red line) measured from the contact line on the container surface as a function of ψ for the parameters in (a).

As shown in Fig. 5.3(b), V and Δh are anticorrelated but nonmonotonic when ψ varies. This behavior indicates that for a certain range of initial volumes of the liquid bath, there could be two possible values of ψ fulfilling the volume constraint. To determine which ψ is the physical solution, we will only consider filling angles $\psi \in [\psi_{\min}, \psi_{\max}]$ with $\psi_{\min}$ and $\psi_{\max}$ being the solutions of $\frac{\mathrm{d}V}{\mathrm{d}\psi} = 0$. In particular, V has a minimal value $V_{\min}$ at $\psi = \psi_{\min}$ and a maximal value $V_{\max}$ at $\psi = \psi_{\max}$. Clearly, V is a monotonically increasing function of $\psi \in [\psi_{\min}, \psi_{\max}]$. Then the initial volume of the liquid bath, which is set by R, L, θ_1, and D_0 or h_0 through Eq. (5.3), can be used to determine the filling angle ψ for the given D, which sets the displacement of the particle, Δz, through Eq. (5.4). With ψ determined, the meniscus profile and the capillary force on the particle can be readily computed. If the initial volume of the liquid bath is smaller than $V_{\min}$ at the given D, then the meniscus is assumed to be ruptured and the particle is completely in the vapor. On the contrary, if the initial volume is larger than $V_{\max}$ at the given D, then the particle is fully immersed in the liquid bath.

We can use intuitive arguments to justify the criterion adopted here of only picking $\psi \in [\psi_{\min}, \psi_{\max}]$ for a given D. For a particle in its equilibrium location at a liquid-vapor interface, the interface is flat and the filling angle $\psi = \pi - \theta_1$. When the particle is pulled upward, the filling angle starts to decrease from $\pi - \theta_1$ as the contact line is free to slide. It is natural to assume that the filling angle changes continuously when the particle is pulled higher and higher until at a critical filling angle the meniscus ruptures and detaches from the particle surface. On the contrary, if the particle is pushed downward from its equilibrium height, then the filling angle increases continuously from $\pi - \theta_1$ until at another critical filling angle the meniscus collapses and the particle submerges into the liquid. In any case, a filling angle further away from 0 (for the case of the particle being pulled upward from its equilibrium location) or π (for the case of being pushing downward) is more physically possible than

the other one when there are two possible filling angles that satisfy the volume constraint. Therefore, it is physically sensible to exclude filling angles less than $\psi_{\min}$ and those larger than $\psi_{\max}$.

A complete understanding of the rupture and collapse of a meniscus requires an analysis of the stability of the meniscus under perturbations and fluctuations, which is beyond the scope of this thesis. Interestingly, it can be shown rigorously that $\psi_{\min}$ and $\psi_{\min}$ are actually independent of D and V. This fact is easy to understand as both D and V can be changed arbitrarily by moving the location of the bottom confining wall in Fig. 5.1 while at the same time the meniscus profile does not change at all. Below we further demonstrate this fact mathematically.

We first consider the case where D is fixed as in Fig. 5.3. Note that h and Δh are still functions of ψ. Using $\mathrm{d}D = 0$ and Eq. (5.5), we obtain

$$\frac{\mathrm{d}h}{\mathrm{d}\psi} + \frac{\mathrm{d}\Delta h}{\mathrm{d}\psi} - R\sin\psi = 0 \ , \tag{5.48}$$

which is a constraint that the derivatives of h and Δh have to satisfy. In this case, V is a function of ψ through Eq. (5.2), from which we get

$$\frac{\mathrm{d}V}{\mathrm{d}\psi} = \pi[r(\Delta h)]^2\frac{\mathrm{d}\Delta h}{\mathrm{d}\psi} + \pi L^2\frac{\mathrm{d}h}{\mathrm{d}\psi} - \pi R^3\sin^3\psi \ . \tag{5.49}$$

Using $r(\Delta h) = R\sin\psi$ and Eq. (5.48), we can rewrite $\frac{\mathrm{d}V}{\mathrm{d}\psi}$ as

$$\frac{\mathrm{d}V}{\mathrm{d}\psi} = \pi\left(R^2\sin^2\psi - L^2\right)\left(\frac{\mathrm{d}\Delta h}{\mathrm{d}\psi} - R\sin\psi\right) \ . \tag{5.50}$$

Since $R\sin\psi < L$, the condition $\frac{\mathrm{d}V}{\mathrm{d}\psi} = 0$ when D is fixed is equivalent to

$$\frac{\mathrm{d}\Delta h}{\mathrm{d}\psi} - R\sin\psi = 0 \ . \tag{5.51}$$

The boundary values of the filling angle, $\psi_{\min}$ and $\psi_{\max}$, can be determined using Eq. (5.51). Since the meniscus profile, $r(z_0)$, does not depend on D, Eq. (5.51) is independent of D, indicating that $\psi_{\min}$ and $\psi_{\max}$ are D-independent as well. The approximate reflection symmetry between V and Δh as functions of ψ, as shown in Fig. 5.3, can also be understood on the basis of Eq. (5.50). From this equation, $\frac{\mathrm{d}V}{\mathrm{d}\psi}$ and $\frac{\mathrm{d}\Delta h}{\mathrm{d}\psi}$ have opposite signs for a wide range of ψ since $R\sin\psi < L$. This anticorrelation is particularly true for ψ close to the filling angle for a flat liquid-vapor interface (i.e., when the particle is in its equilibrium location). However, the reflection symmetry between V and Δh is only approximate as the condition $\frac{\mathrm{d}V}{\mathrm{d}\psi} = 0$ is equivalent to Eq. (5.51), not $\frac{\mathrm{d}\Delta h}{\mathrm{d}\psi} = 0$.

Equation (5.51) can also be understood from a different perspective based on the intuitive arguments discussed previously. Now we consider a liquid bath with a fixed volume V. When the particle is in its equilibrium location at the surface of the liquid bath, the filling angle is $\pi - \theta_1$. When the particle is pulled upward (or pushed downward), the filling angle decreases (increases) from $\pi - \theta_1$ until the meniscus collapses and the particle is detached from (enclosed by) the interface. In this perspective, D can be regarded as a function of ψ under the constraint that V is fixed. From Eq. (5.5), we get

$$\frac{\mathrm{d}D}{\mathrm{d}\psi} = \frac{\mathrm{d}h}{\mathrm{d}\psi} + \frac{\mathrm{d}\Delta h}{\mathrm{d}\psi} - R\sin\psi \ . \tag{5.52}$$

Since V is now a constant, $\mathrm{d}V = 0$, which together with Eq. (5.2) yield

$$\pi R^2 \sin^2\psi \frac{\mathrm{d}\Delta h}{\mathrm{d}\psi} + \pi L^2 \frac{\mathrm{d}h}{\mathrm{d}\psi} - \pi R^3 \sin^3\psi = 0 \ . \tag{5.53}$$

Combining Eqs. (5.52) and (5.53), we obtain

$$\frac{\mathrm{d}D}{\mathrm{d}\psi} = -L^{-2}\left(R^2\sin^2\psi - L^2\right)\left(\frac{\mathrm{d}\Delta h}{\mathrm{d}\psi} - R\sin\psi\right) \ . \tag{5.54}$$

As a result, the condition $\frac{\mathrm{d}D}{\mathrm{d}\psi} = 0$ when V is fixed is also equivalent to Eq. (5.51). Since for a meniscus with a constant V, there is an identity $\frac{\mathrm{d}D}{\mathrm{d}\psi} = \frac{\mathrm{d}\Delta z}{\mathrm{d}\psi}$. The implication is then that the particle displacement, Δz, reaches the minimal (maximal) value at $\psi = \psi_{\max}$ ($\psi_{\min}$) for a fixed-volume meniscus.

The meniscus profile given by $r(z_0)$ and the meniscus height, Δh, only depend on θ_1, R, L, and ψ. Furthermore, Δh can be written as $R \times f(\theta_1, \psi, L/R)$ as shown in Eq. (5.24). Therefore, the solutions to Eq. (5.51), $\psi_{\min}$ and $\psi_{\max}$, only depend on θ_1 and L/R, not on D or V. As a matter of fact, $\psi_{\min}$ and $\psi_{\max}$ can be taken approximately as the filling angles at which the meniscus ruptures and collapses, respectively [108]. When a particle is pulled or pushed at a liquid-vapor interface with different h_0 (i.e, different V and D) but the same θ_1, R, and L, exactly the same force-displacement curve is expected, as well as the same $\psi_{\min}$ and $\psi_{\max}$. The condition $\frac{\mathrm{d}D}{\mathrm{d}\psi} = 0$ was also used previously by Anachkov *et al.* to find the critical angle at which a meniscus breaks [108].

The results of the critical filling angles $\psi_{\min}$ and $\psi_{\max}$ as functions of θ_1, determined using Eq. (5.51), are shown in Fig. 5.4 for $L/R = 5$ and 50, respectively. Some interesting behaviors are observed. When $\theta_1 \to 0$, $\psi_{\max} \to \pi$ independent of L/R. When $\theta_1 \to \pi$, $\psi_{\min} \to 0$. A further analysis shows that $\psi_{\min}$ and $\psi_{\max}$ as functions of θ_1 satisfy the following relationship,

$$\psi_{\min}(\theta_1) + \psi_{\max}(\pi - \theta_1) = \pi \ . \tag{5.55}$$

This identity originates from the invariance of the Young-Laplace equation [Eq. (5.1)] under the transformation $z_0 \to -z_0$, $\theta_1 \to \pi - \theta_1$, and $\Delta p \to -\Delta p$ [71].

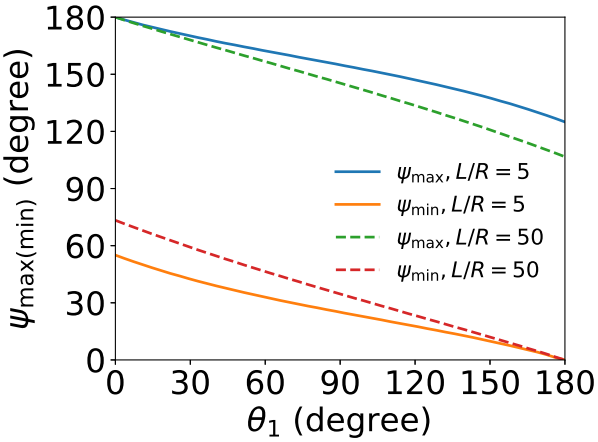

Figure 5.4: Critical filling angles $\psi_{\min}$ (bottom two lines) and $\psi_{\max}$ (top two lines) vs. θ_1 for $L/R = 5$ (solid lines) and 50 (dashed lines).

5.4.2 Meniscus profiles for $L \ll \kappa^{-1}$

With the procedure described in Sec. 5.4.1 to determine the filling angle ψ, we can theoretically predict the meniscus profile for any given set of R, L, θ_1, h_0, and D (or Δz) in the limit of $L \ll \kappa^{-1}$. Some examples are shown in Fig. 5.5 for a solvophilic and a solvophobic sphere, respectively. The results indicate that the theory and the procedure presented here can be used to determine the meniscus profile accurately and efficiently for a wide range of parameters and configurations. Below we directly compare the theoretical predictions of the meniscus profile to those obtained from MD simulations and discuss the force-displacement curves in detail.

To make a fair comparison between simulations and the macroscopic theory of capillarity, care must be taken in defining the radii of the particle and the cylindrical container in the simulations. Repulsive hard-cores of LJ potentials and their integrated forms lead to an excluded zone on any solid surface in which no liquid resides and make the effective radii larger than the nominal radii set in the simulations. We found that the effective radii are $R = 10.35\sigma$ for the particle with $R_{\rm n} = 10\sigma$ and $L = 49.7\sigma$ (74.7σ) for the cylindrical

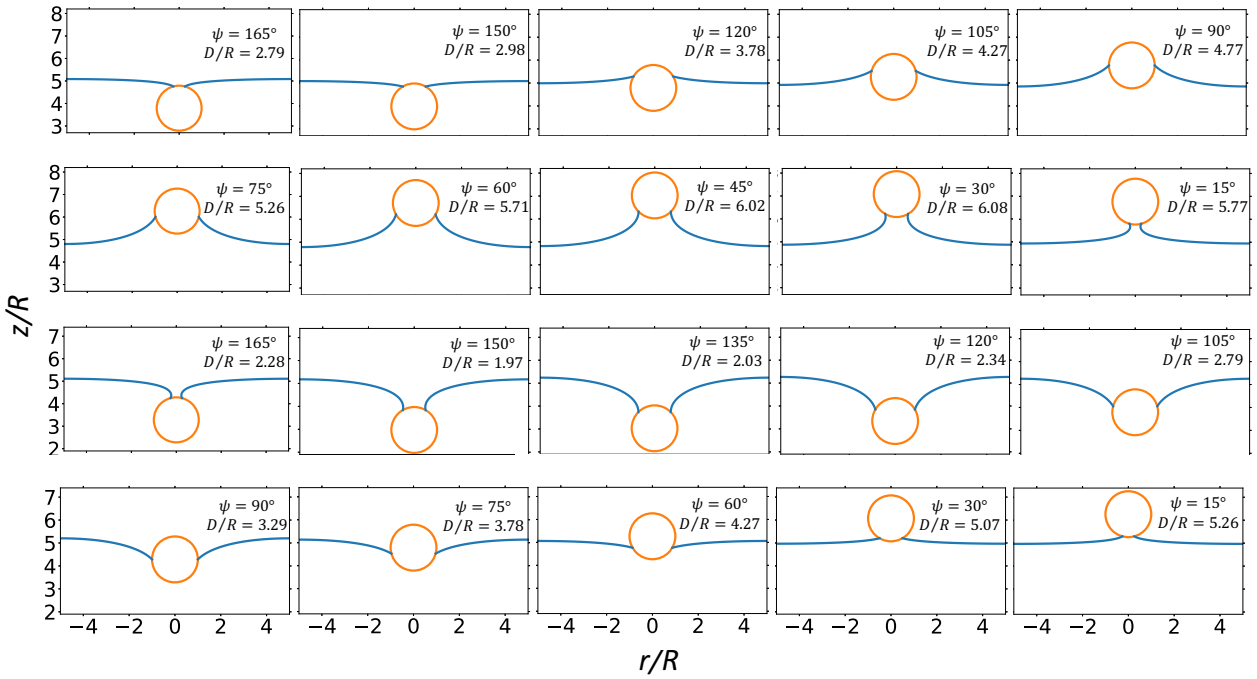

Figure 5.5: Meniscus profiles predicted by the theory in Sec. 5.2.2 for $L/R = 5$ and $V/R^3 = 125\pi$. The first and second rows are for a solvophilic sphere with $\theta_1 = 45°$ and $D_0/R = 3.34$. The third and fourth rows are for a solvophobic sphere with $\theta_1 = 135°$ and $D_0/R = 4.71$. The values of ψ and D are indicated in each plot.

container with $L_n = 50\sigma$ (75σ). These effective radii are used in the theoretical analyses of the systems simulated with MD.

In simulations the liquid-vapor interface can be located directly from the density distribution of the liquid. Statistical fluctuations of the interface can be reduced numerically by noting the axisymmetry of the systems simulated. Using color-scale plots, Fig. 5.6 shows the angle-averaged density profile $\rho(r, z)$ of the liquid as a function of height z and radial distance r from the central axis of the container. The density profiles were averaged over 51 snapshots from MD simulations. We computed the location of the interface at a given r by fitting $\rho(r, z)$ to Eq. (5.47). The results are shown in Fig. 5.6 as circles. The red lines are the predictions based on Eqs. (5.19) and (5.21). In all cases with different θ_1 and L_n, an excellent agreement is found between the simulation and theory, no matter whether the meniscus is

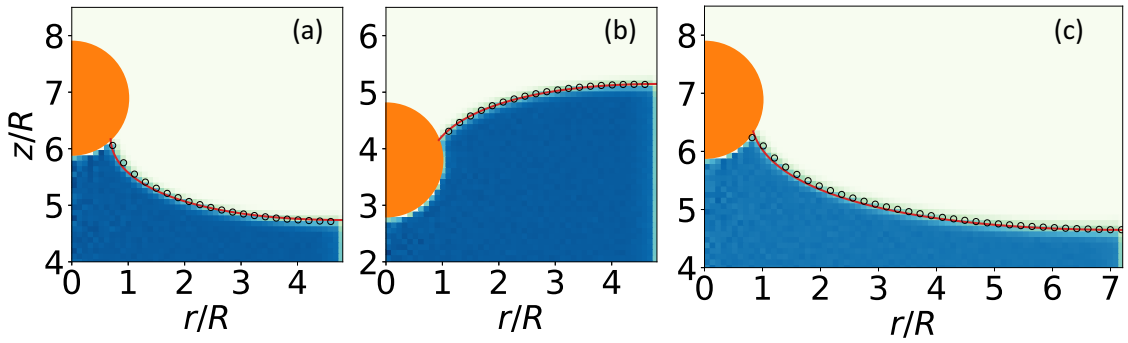

Figure 5.6: Comparison of the meniscus profile between the theory in Sec. 5.2.2 and MD simulations for (a) $\theta_1 = 48.5°$, $D = 61\sigma$, $L_n = 50\sigma$, and $h_0 = 51.4\sigma$; (b) $\theta_1 = 120.5°$, $D = 29\sigma$, $L_n = 50\sigma$, and $h_0 = 51\sigma$; (c) $\theta_1 = 48.5°$, $D = 61\sigma$, $L_n = 75\sigma$, and $h_0 = 51.1\sigma$. The angular averaged density of the liquid is represented by a color-scale plot. The black circles indicate the location of the liquid-vapor interface from simulations. The solid red line indicates the theoretical prediction of the meniscus profile.

rising [Figs. 5.6(a) and (c)] or depressed [Fig. 5.6(b)]. The good agreement indicates that the particle size is large enough that possible effects associated with line tensions are negligible and the macroscopic theory of capillarity is applicable for menisci at nanometer scales.

5.4.3 Force-displacement curves for $L \ll \kappa^{-1}$

Our main goal in this chapter is to understand the effective potential confining a particle to its equilibrium location at a liquid-vapor interface. In Fig. 5.7, the force-displacement curves are shown for the systems with $R_n = 10\sigma$ ($R = 10.35\sigma$), $L_n = 50\sigma$ ($L = 49.7\sigma$), and various values of θ_1. The symbols represent the capillary force computed in MD simulations using the pulling protocol described in Sec. 5.3. To quantify the uncertainty of MD calculations, we partitioned the total simulation time (5000τ) during which the force was computed into ten blocks. An average force was computed for each block. Then the average over all ten blocks was taken as the final mean force and the standard deviation of the ten block averages was plotted as error bars in Fig. 5.7.

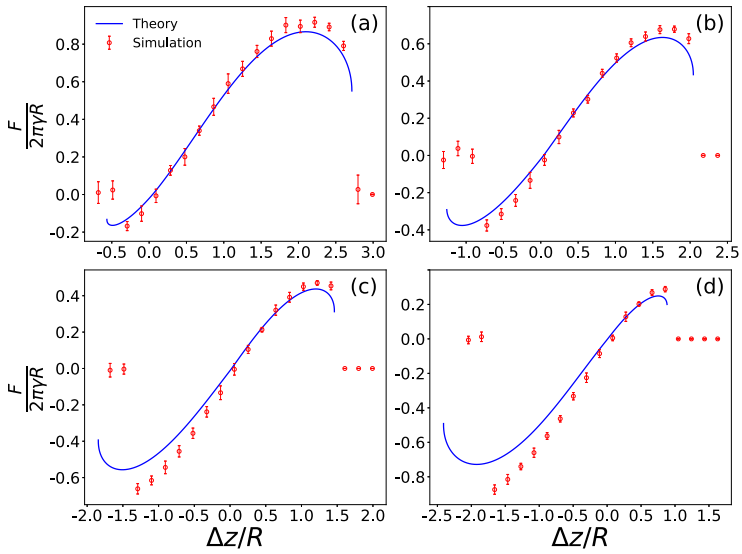

Figure 5.7: Capillary force (F) vs. vertical displacement of the particle (Δz) from its equilibrium location at a liquid-vapor interface for $L_n = 50\sigma$ and various values of θ_1: (a) 48.5°, (b) 76.5°, (c) 98.2°, and (d) 120.5°. The red circles are results from MD simulations and the blue lines are the corresponding theoretical predictions.

The solid lines in Fig. 5.7 are the predictions of the macroscopic theory of capillarity described in Sec. 5.2.2. Since the simulations are in the limit of $R < L \ll \kappa^{-1}$, Eq. (5.29) is used for the capillary force in the theory. In all cases, the theoretical predictions agree reasonably with the MD results, especially in the region of $0 \lesssim \Delta z \lesssim R$. However, the theoretical values tend to be systematically lower than those computed in simulations in terms of magnitude. Clear deviation is observed when the capillary force is close to its extremal values before the meniscus breaks up or the particle submerges into the liquid bath. In particular, the theory seems to work well for solvophilic particles with $\theta_1 < \pi/2$ [Figs. 5.7(a) and (b)] but less so for solvophobic particles with $\theta_1 > \pi/2$ [Figs. 5.7(c) and (d)]. For the latter systems, the theoretical predictions of the capillary force are significantly lower than the MD results for the $F < 0$ branch with regard to magnitude, up to about 30% right before particle immersion. At this point there is no physical explanation of the observed discrepancy between the theory and simulations on capillary forces, though the two agree very well when meniscus profiles are

concerned. One possibility might be when a solvophobic particle is close to its submerging or detaching point, the meniscus strongly bends and the interfacial tension of such a bent interface starts to deviate from the value computed for a flat interface without any curvature [125].

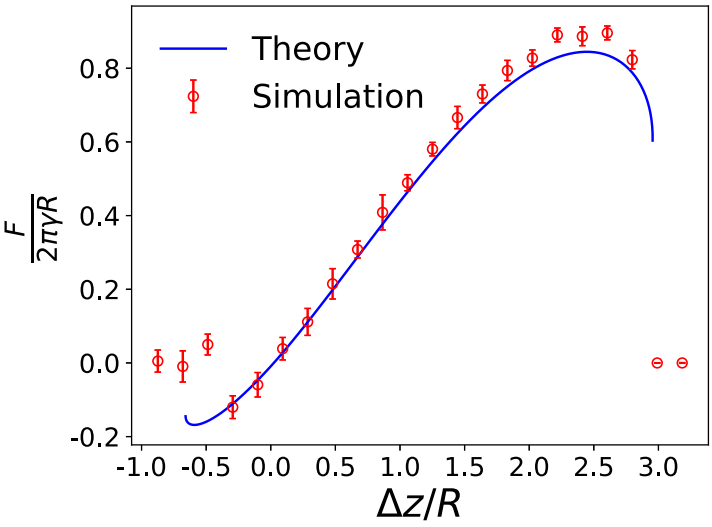

Figure 5.8: Capillary force (F) vs. vertical displacement of the particle (Δz) from its equilibrium location at a liquid-vapor interface for $L_{\rm n} = 75\sigma$ and $\theta_1 = 48.5°$. The red circles are results from MD simulations and the blue line is the corresponding theoretical prediction.

Figure 5.8 shows the force-displacement curve for a system with $R_{\rm n} = 10\sigma$ ($R = 10.35\sigma$), $L_{\rm n} = 75\sigma$ ($L = 74.7\sigma$) and $\theta_1 = 48.5°$. In this case, the macroscopic theory fits well the $F < 0$ branch (i.e., the region with an upward pushing force on the particle). However, for the region where $F > 0$ and the capillary force is pulling the particle downward into the liquid bath, the theoretical predictions are again lower than the simulation results. The largest deviation occurs when the capillary force is near its maximum value at $\Delta z \simeq 2.3R$. The corresponding rising meniscus breaks up when the particle is pulled up further.

When the ratio $l \equiv L/R$ gets larger, the dimensionless mean curvature of the interface becomes smaller roughly as l^{-2} [see Eq. (5.18)]. Eventually the meniscus profile reduces to

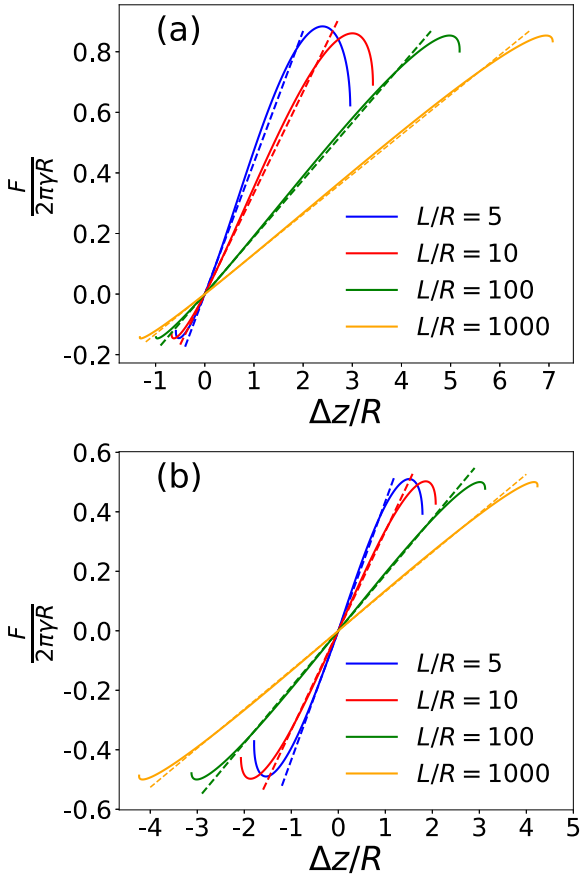

Figure 5.9: Capillary force (F) vs. vertical displacement of the particle (Δz) from its equilibrium location at a liquid-vapor interface: theory (solid lines) vs. the Joanny-de Gennes' Hookean form in Eq. (5.34) (dashed lines) for (a) $\theta_1 = 45°$ and (b) $\theta_1 = 90°$ with $L/R = 5$ (blue), 10 (red), 100 (green), and 1000 (yellow) from the most to least tilted from horizontal in each plot, respectively.

a catenary curve with zero mean curvature [48, 62]. The meniscus height for a catenoid is very similar to the expression in Eq. (5.26) but without the -1/2 term in the curly braces. In the limit of $L \gg R$, the force-displacement curve reduces to the Joanny-de Gennes' law in Eq. (5.34) with an effective spring constant $k_s = 2\pi\gamma/\ln(2L/R)$ [33]. In Fig. 5.9 this linear force-displacement relationship is compared to the theoretical solutions using the elliptic integrals for $\theta_1 = 45°$. Even for $L/R = 5$, the theoretical results fit reasonably to the Joanny-de Gennes' law with a linear behavior apparent for $|\Delta z/R| \ll 1$, though deviations can be

seen at lager displacements or when the particle is close to detaching from or submerging into the liquid. The agreement is improved and the linear region of the force-displacement curve is widened when L/R becomes larger. For $L/R = 1000$, the linear force-displacement curve from the Joanny-de Gennes' law overlaps with the theoretical solution based on the elliptic integrals for a wide range of Δz, except very close to the extrema at which the capillary force bends and deviates from the linear dependence on Δz.

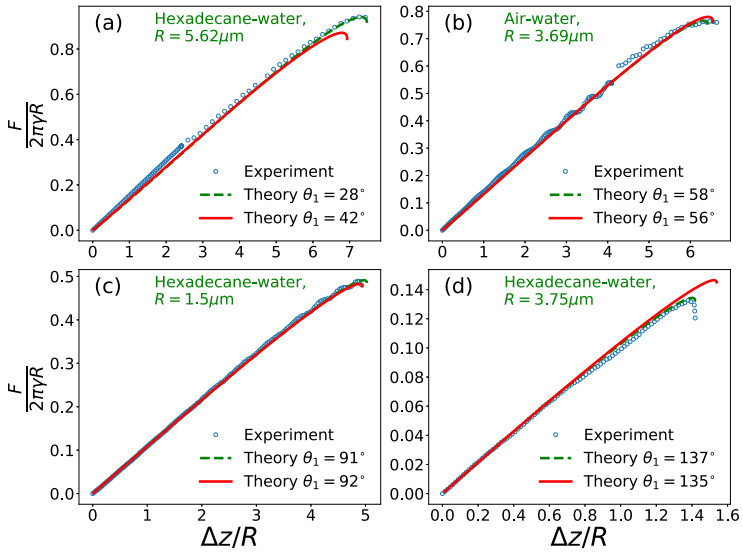

Figure 5.10: Capillary force (F) vs. vertical displacement of the particle (Δz) from its equilibrium location at a liquid-vapor interface: theory (lines) vs. experimental data (circles, by courtesy of Anachkov [108]). Panels (a), (c), and (d) are for particles with various radii at a hexadecane-water interface; panel (b) is for a water-air interface. The solid and dashed lines are from the theory in Sec. 5.2.2 with different values of θ_1 and (a) $L = 4$ mm, (b) $L = 4$ mm, (c) $L = 9$ mm, and (d) $L = 17$ mm, respectively.

The approximate linear dependence of the capillary force (F) on the particle displacement (Δz) has been confirmed experimentally. For example, Fig. 5.10 includes some experimental data from the group of Anachkov for microparticles at water-air and water-oil interfaces, where a linear relationship between F and Δz is apparent unless the meniscus is close to breaking up [108]. In the experimental setup to measure F, the liquid (water) was filled in a cone-shaped container in the middle of a much larger vessel. Water and air or oil met at

the opening of the cone, the radius of which was about 1 mm. Therefore, the lateral span of the water-air (oil) interface was about 1 mm.

The interfacial tension of a water-hexadecane interface is 52.5 ± 0.5 mN/m and of a water-air interface is 72 mN/m at 25 °C. The density of hexadecane is 770 kg/m^3 and that of water is 1000 kg/m^3. As a result, the capillary length (κ^{-1}) is about 4.82 mm and 2.7 mm for a water-hexadecane and a water-air interface, respectively. In the experiments, the radius of the particle was varied from 1.5 to 5.62 μm, much smaller than κ^{-1}. Our previous work showed that the theory presented in Sec. 5.2.2 and the solutions of the Young-Laplace equation based on the elliptic integrals apply for $L \lesssim 0.4\kappa^{-1}$, which is about 1.9 mm for the water-hexadecane and 1.1 mm for the water-air system, respectively. Therefore, the interface involved in the experiments can be assumed to have a constant mean curvature and gravity can be ignored. However, the contact angle of the interface at the edge of the cone, θ_2, is unknown. The theory presented in this chapter is based on $\theta_2 = \pi/2$. In order to use the theory in Sec. 5.2.2 to fit the experimental data, we will treat L as a fitting parameter in the theory. This treatment is based on the assumption that a meniscus emerging in the experiments with $L = 1$ mm and $\theta_2 \neq \pi/2$ is only a portion of a meniscus with a different L but $\theta_2 = \pi/2$. A more rigorous treatment may be using a fixed $L \simeq 1$ mm as in the experiments but allowing θ_2 to vary, which requires extending the theory in Sec. 5.2.2 to the case $\theta_2 \neq \pi/2$. Such analyses will be reported in the future.

The lines in Fig. 5.10 are the theoretical fits using Eqs. (5.24), (5.29), and (5.32) with L as a fitting parameter. An excellent agreement is found between the theory and experimental results for all the cases. The two lines are for two contact angles that were reported in Ref. [108] for each case using different measurement techniques. It should be noted that almost identical fits can be obtained using Eqs. (5.26), (5.30), and (5.33). This fact is not a coincidence and can be understood as follows. In the experiments $L \gg R$ and the mean

curvature of the meniscus is thus close to 0. In this limit, the meniscus is essentially a catenoid, to which Eqs. (5.26), (5.30), and (5.33) apply.

In Ref. [108], the same experimental data included in Fig. 5.10 were fit using the Derjaguin-James formula [Eq. (5.35)] for the meniscus rise. Some deviations were noted. The Derjaguin-James formula was derived for a meniscus with an unbound lateral span. Our previous work showed that it applies when $L \gtrsim 4\kappa^{-1}$ for $\theta_2 = \pi/2$ [48]. These conditions were not met in the experiments in Ref. [108], which may explain the observed difference between the fits using the Derjaguin-James formula and the experimental data [108].

5.4.4 Effects of gravity for $L \gtrsim \kappa^{-1}$

In Sec. 5.2.2, it is found that a meniscus on the outside of a particle with $R \ll L \ll \kappa^{-1}$ is a surface of revolution with a constant mean curvature. In this case, the meniscus height (Δh) grows with L logarithmically, as shown in Eq. (5.26). When L becomes comparable to or larger than κ^{-1}, gravity comes into effect and the logarithmic growth ceases with Δh saturating to a value predicted by the Derjaguin-James formula [Eq. (5.35)]. The logarithmic dependence of Δh on L is the origin of the Joanny-de Gennes' law in Eq. (5.34) for $R \ll L \ll \kappa^{-1}$, which states that the effective spring constant associated with a liquid-vapor interface for a particle straddling the interface can be written as $k_s \simeq 2\pi\gamma/\ln(2L/R)$. According to this expression, k_s gradually decreases as L increases. However, as Δh eventually saturates and becomes L-independent when $L \gg \kappa^{-1}$, the spring constant is expected to saturate in the same limit.

From our previous work on the wetting of a cylinder vertically penetrating a liquid-vapor interface, we know that Eq. (5.24) is accurate for the meniscus height for L up to about $0.4\kappa^{-1}$ with the parameter $l \equiv L/R$. When $L > 1.85\kappa^{-1}$, Eq. (5.24) can still be used for

Δh with the parameter l replaced by $1.85\kappa^{-1}/R$. This finding leads to a re-definition of l in Eq. (5.38), which can be combined with Eq. (5.24) and an error correcting function [Eq. (5.37)] to yield an approximate formula of Δh. The resulting formula is shown in Eq. (5.36) and works for an arbitrary L including the crossover zone $0.4\kappa^{-1} \lesssim L \lesssim 4\kappa^{-1}$.

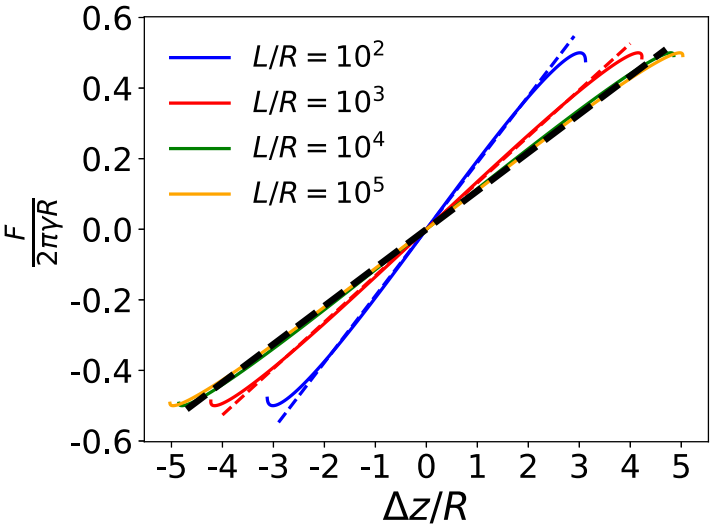

Figure 5.11: Capillary force (F) vs. vertical displacement of the particle (Δz) from its equilibrium location at a water-air interface: theory (solid lines) vs. the Hookean form with the effective spring constant in Eq. (5.56) (dashed lines) for $\theta_1 = 90°$, $R = 1$ μm, and $L/R = 10^2$ (blue), 10^3 (red), 10^4 (green), and 10^5 (yellow) from the most to least tilted from horizontal, respectively. In particular, the black dashed line corresponds to $k_s = 2\pi\gamma/\ln(3.7\kappa^{-1}/R)$, which is the saturated value of k_s for large L.

Similar to Δh, the spring constant k_s also exhibits crossover and saturation when the lateral span of the liquid-vapor interface is increased. As result, we can generalize the expression of k_s as

$$k_s \simeq \frac{2\pi\gamma}{\ln(2l)} \,, \tag{5.56}$$

with the parameter l given in Eq. (5.38) instead of being always L/R. This expression of k_s is expected to work for an arbitrary value of the ratio L/R. In Fig. 5.11 we plot the

force-displacement curves for a particle at a water-air interface computed using Eqs. (5.36), (5.39), and (5.40) for $\theta_1 = \pi/2$, $R = 1$ μm and various values of L ranging from 100 μm to 100 mm. The capillary length is $\kappa^{-1} = 2.7$ mm. The linear region of each curve has a slope that agrees well with the effective spring constant from Eq. (5.56), i.e., $k_s = 2\pi\gamma/\ln(2l)$ with $l = L/R$ for $L \leq 1.85\kappa^{-1}$ while $l = 1.85\kappa^{-1}/R$ for $L > 1.85\kappa^{-1}$. It is clear that when $L \to \infty$, the spring constant k_s saturates to $2\pi\gamma/\ln(3.7\kappa^{-1}/R)$.

5.5 Conclusions

In this chapter, we presented a comprehensive theory of the meniscus on the outside of a small particle (i.e., $R \ll \kappa^{-1}$ with κ^{-1} being the capillary length of the interface involved) at a liquid-vapor interface confined in a cylindrical container with radius L ($> R$). By placing the particle along the central axis of the container, we computed the capillary force on the particle when it was displaced out of its equilibrium height relative to the interface. With the contact angle of the liquid on the container surface being fixed at $\pi/2$, the setup allowed us to systematically study the crossover from a meniscus with a constant Laplace pressure to an unbound one governed by gravity, when L is increased from $L \ll \kappa^{-1}$ to $L \gg \kappa^{-1}$. In the limit of $R < L \ll \kappa^{-1}$, an analytic solution based on the elliptic integrals was found for the Young-Laplace equation, resulting in a meniscus of a constant mean curvature and with a height that grows logarithmically with L. In the limit of $R \ll \kappa^{-1} \ll L$, the meniscus height saturates to a value given by the Derjaguin-James formula. In the crossover region, which is roughly $0.4\kappa^{-1} \lesssim L \lesssim 4\kappa^{-1}$, an approximate formula was proposed for the meniscus height based on our previous work on the wetting of a cylinder.

Via MD simulations we showed that the meniscus shape at nanometer scales matches well the prediction of the macroscopic theory of capillarity based on the Young-Laplace equation.

The capillary force is reasonably predicted by the theory as well, especially the branch where the force is attractive and pulling the particle toward the liquid phase. However, for the repulsive branch where the force is pushing the particle out of the liquid, the theory always predicts a force with a magnitude smaller than that computed in MD simulations. The origin of this discrepancy is not understood at present.

The simulation and theoretical results show that the capillary force on a small particle at a liquid-vapor interface can be reasonably approximated as a linear function of the displacement of the particle out of its equilibrium location, especially for small deviations. This approximation holds from nanometer to macroscopic scales and the associated effective spring constant can be written as $k_s = 2\pi\gamma/\ln(2l)$. For $L \leq 1.85\kappa^{-1}$, the parameter $l = L/R$, indicating that k_s decreases as the reciprocal of $\ln L$ as L increases. For $L > 1.85\kappa^{-1}$, the spring constant k_s saturates to $2\pi\gamma/\ln(3.7\kappa^{-1}/R)$.

Our result for k_s differs from the result of Pieranski [49], who predicted $k_s = 2\pi\gamma$, by the factor $\ln^{-1}(2l)$ associated with the lateral span of the meniscus. In Pieranski's analyses, the liquid-vapor interface was always flat regardless of the location of the particle's center relative to the interface. In other words, the deformation of the meniscus was not considered when the particle was displaced out of its equilibrium location. The analyses were based on free energies but not self-consistent as the force exerted on the particle by the liquid-vapor interface was always 0. In this chapter, we fully account for the evolution of the meniscus on the outside of a particle moving across a liquid-vapor interface. Our results thus provide a rigorous theoretical foundation of the moving interface method in which a liquid-vapor interface is modeled as a harmonic potential with regard to its confining effect on small particles at the interface or in the liquid phase. A physical interpretation is found for the associated spring constant in terms of the surface tension of the interface (γ), the particle size (R), the lateral span of the interface (L), and possibly the capillary length (κ^{-1}) of

the interface when L is large. We expect this approach of modeling a liquid-vapor interface as a confining potential for particles will find wide applications in simulating evaporation of particle suspensions, interfacial adsorption and assembly of particles, and many other processes involving particles at interfaces.

We derived k_s using a single particle at a liquid-vapor interface. When multiple particles are adsorbed at an interface, capillary interactions mediated by menisci can occur. In this case, it is nontrivial to model the interface as a confining potential for each particle. However, if we interpret L as the average interfacial distance between the particles, similar to the treatment of Joanny and de Gennes of a contact line pinned by multiple defects [33], then a harmonic potential with $k_s = 2\pi\gamma/\ln(2l)$ for each particle at the interface will at least partially capture the capillary interactions.

Chapter 6

Comparison between implicit and explicit solvent models

This chapter is based on a paper that is currently under review at *The Journal of Chemical Physics*:

Yanfei Tang, Gary. S. Grest, and Shengfeng Cheng, " Stratification of drying particle suspensions: Comparison of implicit and explicit solvent simulations", submitted to The Journal of Chemical Physics.

I designed and built all the models for molecular dynamics simulations. Dr. Grest ran the explicit solvent simulations. I implemented the implicit solvent model in LAMMPS and ran the implicit solvent simulations. I performed all the data analyses and prepared figures. All authors contributed to the writing of this paper. My contributions to this paper were under Dr. Cheng's supervision.

6.1 Introduction

The results in the previous two chapters provide a physical foundation of an implicit solvent model for a particle suspension. However, it is still important to compare results from an implicit solvent model directly with those from an explicit one and to examine if consistent results are obtained from the two. In this chapter, we undertake this task and compare the stratification behavior during the drying of a bidisperse particle suspension when the solvent is treated either explicitly or implicitly.

The field of drying-induced stratification was recently reviewed by Schulz and Keddie [126]. Molecular modeling has played an important role in the process of discovering and revealing the fundamental physics of stratification [20, 23, 25, 27, 34, 86, 127, 128]. Fortini *et al.* conducted Langevin dynamics simulations to unequivocally establish the occurrence of "small-on-top" stratification during fast drying of bidisperse particle suspensions [20, 25, 27]. Howard *et al.* adopted a similar method and combined it with a dynamical density functional theory to show that "small-on-top" stratification is enhanced when the particle size ratio α is increased [23, 127]. Tatsumi *et al.* performed Langevin dynamics simulations for $\alpha = 1.5$, 2, and 4 with particle-particle interactions described by the Hertzian theory of a nonadhesive elastic contact and showed that segregation is most enhanced at an intermediate value of Pe_l [128]. In all these modeling studies, the solvent was treated as a continuous, viscous, and isothermal background with hydrodynamic flow ignored, which is consistent with the assumption usually made in phenomenological theories of stratification [20, 24]. However, the recent analyses of Sear and Warren showed that the solvent backflow around a migrating particle may be important and theories neglecting it may substantially overestimate stratification [29]. The implication is that results based on implicit solvent models may not be realistic [126].

Statt *et al.* used molecular dynamics (MD) simulations to investigate stratification in drying mixtures of long and short polymer chains and compared the results from an implicit and an explicit solvent model [86]. They carefully matched the sizes of polymer chains and their diffusion coefficients in the two models. With the implicit solvent, stratification was observed while no stratification occurred in the explicit solvent under the same drying conditions. They concluded that hydrodynamic interactions, which are not included in the implicit solvent model, are responsible for the different outcomes. The work by Statt *et al.* thus presents a serious challenge to the modeling of drying particle suspensions as it raises a question whether one can trust the results from simulations based on implicit solvent models. It should be noted that these simulations are for polymer solutions and it is unclear if the results can be generalized to colloidal suspensions, though Statt *et al.* suggested that they should apply to particle mixtures [86].

In our previous work [34], we have employed MD simulations with an explicit solvent modeled as a Lennard-Jones liquid to study the drying process of suspensions of bidisperse mixtures of nanoparticles. Though thermophoresis caused by evaporative cooling competed with diffusiophoresis and complicated the distribution of nanoparticles during drying, "small-on-top" stratification was observed, underscoring the discovery of Fortini *et al.*. In this chapter, we use a similar model but suppress thermophoresis by thermalizing the entire solvent and thus keeping the system isothermal during evaporation. Then we map the explicit solvent model to an implicit one by matching the diffusion coefficients of nanoparticles via tuning the frictional damping in the corresponding Langevin equation. We compare the results from the explicit and implicit solvent models and find comparable "small-on-top" stratification in both. Our results thus corroborate the usage of an implicit solvent model for drying particle suspensions. Furthermore, we use the implicit solvent model to study the effect of initial thickness of a suspension film of nanoparticles on their final distribution in the dry film when

either the Péclet number or the receding speed of the film's free surface is fixed.

6.2 Model and methodology

We performed MD simulations with both an explicit and an implicit solvent model to study the drying process of suspensions of a bidisperse mixture of nanoparticles. The explicit solvent model is described in detail in our previous study [34] and is summarized below. The implicit solvent model is based on the method of Fortini *et al.* [20] to mimic the process of solvent evaporation. We carefully matched the two models such that the particles have the same, purely repulsive interactions with each other and exhibit almost the same diffusive behavior in the explicit and implicit solvents. By comparing the results from these two models, we study the role of a solvent during drying. In particular, the possible effects of hydrodynamic interactions in drying particle suspensions, which are not captured by the implicit solvent model, will be clarified.

6.2.1 Explicit solvent model

The explicit solvent is modeled as a fluid consisting of Lennard-Jones (LJ) beads of mass m that interact with each other via a LJ potential

$$U_{\mathrm{LJ}}(r) = 4\epsilon \left[(\sigma/r)^{12} - (\sigma/r)^{6} - (\sigma/r_c)^{12} + (\sigma/r_c)^{6} \right] , \tag{6.1}$$

where r is the center-to-center separation between beads, ϵ is an energy unit, and σ is a length unit. The potential is truncated at $r_c = 3\sigma$ for the solvent. The nanoparticles are modeled as spheres with a uniform distribution of LJ mass points at density $1.0m/\sigma^3$ [36, 37]. The large nanoparticles (LNPs) have diameter $d_l = 20\sigma$ and mass $m_l = 4188.8m$. The small

nanoparticles (SNPs) have diameter $d_s = 5\sigma$ and mass $m_s = 65.4m$. The size ratio is $\alpha = d_l/d_s = 4$. The nanoparticles interact with each other via an integrated LJ potential with a Hamaker constant $A_{\rm nn} = 39.48\epsilon$ [36, 37]. To avoid aggregation, the nanoparticle-nanoparticle interactions are made purely repulsive by truncating the potentials at their minima, which are 20.574σ for LNP-LNP, 13.085σ for LNP-SNP, and 5.595σ for SNP-SNP pairs, respectively. The nanoparticle-solvent interaction is also modeled as an integrated LJ potential with a Hamaker constant $A_{\rm ns} = 100\epsilon$ and a cutoff $d/2 + 4\sigma$ with d being the nanoparticle diameter [36, 37]. The nanoparticle-solvent interaction adopted here is attractive at large separations and strong enough to guarantee that both LNPs and SNPs are well dispersed in the solvent but not too strong to lead to a solvent layer bound to the nanoparticles [40].

A rectangular box with dimensions $L_x \times L_y \times L_z$ is used as the simulation cell, where $L_x = L_y = 201\sigma$ and L_z is varied for each system. The liquid-vapor interface is in the x-y plane, in which periodic boundary conditions are imposed. Two walls at $z = 0$ and $z = L_z$ are used to confine all the particles in the cell. The particle-wall interaction is given by a LJ 9-3 potential,

$$U_W(h) = \epsilon_W \left[(2/15)(D_W/h)^9 - (D_W/h)^3 - (2/15)(D_W/h_c)^9 + (D_W/h_c)^3\right] \ , \qquad (6.2)$$

where $\epsilon_W = 2.0\epsilon$ is the interaction strength, D_W is a characteristic length, h is the distance between the center of a particle and the wall, and h_c is the cutoff of the potential. For the solvent, we set $D_W = 1\sigma$ and $h_c = 3\sigma$ (0.8583σ) at the lower (upper) wall. The lower wall is thus wetted by the solvent while the upper wall is nonwetted. For the nanoparticles, both walls are nonadsorptive with $D_W = d/2$ and $h_c = 0.8583D_W$, where d is the nanoparticle diameter.

Prior to evaporation, the explicit solvent system contains 200 LNPs, 6400 SNPs, and 7.1×10^6 solvent beads. The system is well equilibrated with a liquid-vapor interface located at height $H(0) = 304\sigma$. The volume fractions are $\phi_l = 0.068$ for LNPs and $\phi_s = 0.034$ for SNPs. The diffusion coefficients of the nanoparticles in the equilibrium suspension are determined as $D_l = 1.76 \times 10^{-3}\sigma^2/\tau$ for LNPs and $D_s = 1.55 \times 10^{-2}\sigma^2/\tau$ for SNPs [129]. The ratio $D_l/D_s = 8.8$, which is more than twice the size ratio α. The deviation from the Stokes-Einstein relation is due to the finite concentrations of nanoparticles [37, 38]. To implement evaporation, a rectangular box with dimensions $L_x \times L_y \times 20\sigma$ at the top of the simulation cell is designated as the deletion zone and ζ solvent beads are removed every τ from this zone. For this chapter, $\zeta = 30$ to yield a very fast evaporation rate. At this rate, the liquid-vapor interface recedes at an almost constant speed $v_e = (H(0) - H(t)))/t$, where $H(t)$ is the film thickness at time t clocked since the start of evaporation. With D_l, D_s, $H(0)$, and v_e known, the Péclet numbers for LNPs and SNPs are computed. All the parameters are listed in Table 6.1.

All the simulations were conducted with Large-scale Atomic/Molecular Massively Parallel Simulator (LAMMPS) [41]. The equation of motion is integrated by a velocity-Verlet algorithm with a time step $\delta t = 0.01\tau$. A Langevin thermostat with a damping time $\Gamma = 100\tau$ is used for the entire solvent including the vapor to fix its temperature at $1.0\epsilon/k_{\mathrm{B}}$. Therefore, the system is isothermal and thermophoresis is suppressed [34], as typically assumed in an implicit solvent model.

6.2.2 Implicit solvent model

An implicit solvent system is prepared by removing all the solvent from an equilibrated suspension in the explicit solvent model. The nanoparticle-nanoparticle and nanoparticle-

wall interactions remain unchanged. The role of the liquid solvent in the explicit model, in which the nanoparticles are suspended, is replaced by a potential barrier that confines all the nanoparticles in the suspension. For each nanoparticle, the confining potential has the form of the right half of a harmonic potential and its minimum is always located at $d/2$ below the location of the liquid-vapor interface, where d is the diameter of the nanoparticle. In other words, the contact angle of the solvent on the nanoparticle is set to 0 [80]. A nanoparticle experiences a Hookean restoring force that pushes it back into the suspension when the particle is near the interface. To mimic evaporation, the location of the liquid-vapor interface is moved downward along the z-axis, i.e., the instantaneous film thickness $H(t)$ is decreased at a given speed, v_e. Therefore, $H(t) = H(0) - v_e t$ with t being the time elapsed after the evaporation is initiated. Mathematically, the force exerted on the nanoparticle by the liquid-vapor interface is given by

$$F_z^i = \begin{cases} k_s \left[z_n - H(t) + d/2 \right] & \text{for } |z_n - H(t)| \leq d/2, \\ 0 & \text{otherwise,} \end{cases} \tag{6.3}$$

where k_s is a spring constant characterizing the strength of the confining potential, and z_n is the nanoparticle position along the z axis. In a previous work [80], we have analyzed the capillary force experienced by a spherical particle adsorbed at a liquid-vapor interface, which depends on the contact angle of the liquid on the particle surface. Our results show that the Hookean form in Eq. (6.3) is a reasonable approximation, though caution needs to be taken in the physical interpretation of k_s [80]. In this chapter, we use $k_s = 0.3\epsilon/\sigma^2$.

For all the implicit solvent simulations, the times step $\delta t = 0.005\tau$. A Langevin thermostat is applied to all the nanoparticles in order to maintain the temperature of the system at $1.0\epsilon/k_{\mathrm{B}}$. To compare the two solvent models, we matched the diffusion coefficients of the nanoparticles in the implicit solvent model to those in the explicit solvent. To this end, we tuned the

damping time, Γ, of the Langevin thermostat applied to LNPs and SNPs in the implicit solvent. With $\Gamma = 11\tau$ for LNPs and 1.3τ for SNPs, the resulting diffusion coefficients of LNPs and SNPs in the implicit solvent are $D_l = 1.70 \times 10^{-3}\sigma^2/\tau$ and $D_s = 1.59 \times 10^{-2}\sigma^2/\tau$, which are in very good agreement with those in the explicit solvent at the initial volume fractions.

Since an implicit solvent system only contains nanoparticles and is computationally much more efficient, we were able to study thicker suspension films and explore the effect on stratification of the initial film thickness, $H(0)$, with the initial volume fractions of LNPs and SNPs fixed. The value of the receding speed of the liquid-vapor interface, v_e, is either fixed, where the Péclet numbers increase proportionally with the initial thickness of a film, or varied to yield similar Péclet numbers as in the system with $H(0) = 304\sigma$ and $v_e = 1.18 \times 10^{-3}\sigma/\tau$.

All the systems studied in this chapter are summarized in Table 6.1. We use H_e to denote the explicit solvent system, which has $H(0) = 304\sigma$ and $v_e = 1.18 \times 10^{-3}\sigma/\tau$. The implicit solvent system with the same initial film thickness and evaporation rate is denoted as H_1v_1. For other implicit solvent systems, H_qv_f is used to indicate that the initial film thickness is $q \times H(0)$ and the receding speed of the interface is $v_e = f \times 1.18 \times 10^{-3}\sigma/\tau$. In this chapter, we vary q from 1 to 8 and f from 1 to 1/8.

Table 6.1: Parameters for all the systems studied.

System	$H(0)/\sigma$	N_l	N_s	ϕ_l	ϕ_s	$v_e\tau/\sigma$	Pe_l	Pe_s
H_e	304	200	6400	0.068	0.034	1.18×10^{-3}	203.8	23.3
H_1v_1	304	200	6400	0.068	0.034	1.18×10^{-3}	211.0	22.7
$H_2v_{1/2}$	626.5	400	12800	0.066	0.033	5.91×10^{-4}	217.8	23.3
$H_4v_{1/4}$	1246.5	800	25600	0.067	0.033	2.96×10^{-4}	217.0	23.2
$H_8v_{1/8}$	2476.5	1600	51200	0.067	0.033	1.50×10^{-4}	218.5	23.4
H_2v_1	626.5	400	12800	0.066	0.033	1.18×10^{-3}	434.9	46.6
H_4v_1	1246.5	800	25600	0.067	0.033	1.18×10^{-3}	865.2	92.8
H_8v_1	2476.5	1600	51200	0.067	0.033	1.18×10^{-3}	1719.0	187.2

6.3 Results and discussion

In Fig. 6.1 we show snapshots of five suspensions before and after drying, including H_e, H_1v_1, $H_2v_{1/2}$, $H_4v_{1/4}$, and $H_8v_{1/8}$ that all have similar Péclet numbers. After the film thickness is reduced to $H(t) \simeq 0.3H(0)$, all the systems exhibit "small-on-top" stratification. The "small-on-top" state is more visually prominent for thicker films such as $H_2v_{1/2}$, $H_4v_{1/4}$, and $H_8v_{1/8}$, though quantitative analyses show that the degree of stratification in these thick films is close to that in H_e. Furthermore, H_e and H_1v_1 have identical distributions of nanoparticles prior to evaporation and are dried at very similar rates. At $H(t) \simeq 0.3H(0)$ when the simulations were stopped, H_e exhibits slightly stronger "small-on-top" stratification than H_1v_1, which may be due to the fact in the explicit solvent, the diffusion coefficients of the nanoparticles decrease as their concentration increases during solvent evaporation. This observation is in discordance with the theoretical analysis of Sear and Warren [29] and the simulation study of Statt *et al.* [86]. Sear and Warren showed that back-flow around a drifting particle in an explicit solvent suppresses the diffusiophoretic driving on the larger particles from a concentration gradient of the smaller particles [29]. As a result, "small-on-top" stratification is expect to be significantly promoted in an implicit solvent model where back-flow is missing [29]. Statt *et al.* used MD to simulate a mixture of long and short polymer chains in an explicit and an implicit solvent and found that the implicit solvent system exhibits "small-on-top" stratification while the explicit one does not [86]. However, the analysis of Sear and Warren [29] is based on the Asakura-Oosawa model [28], which is about the diffusion of a very large particle in a polymer solution with concentration gradients. The simulations of Statt *et al.* are for polymer mixtures [86]. We suspect that colloidal suspensions and polymer solutions behave quite differently in terms of diffusiophoresis and stratification. It is interesting to explore if the Asakura-Oosawa model can be extended to a particle with size comparable to the size of polymer chains in the solution, where the curvature of the particle

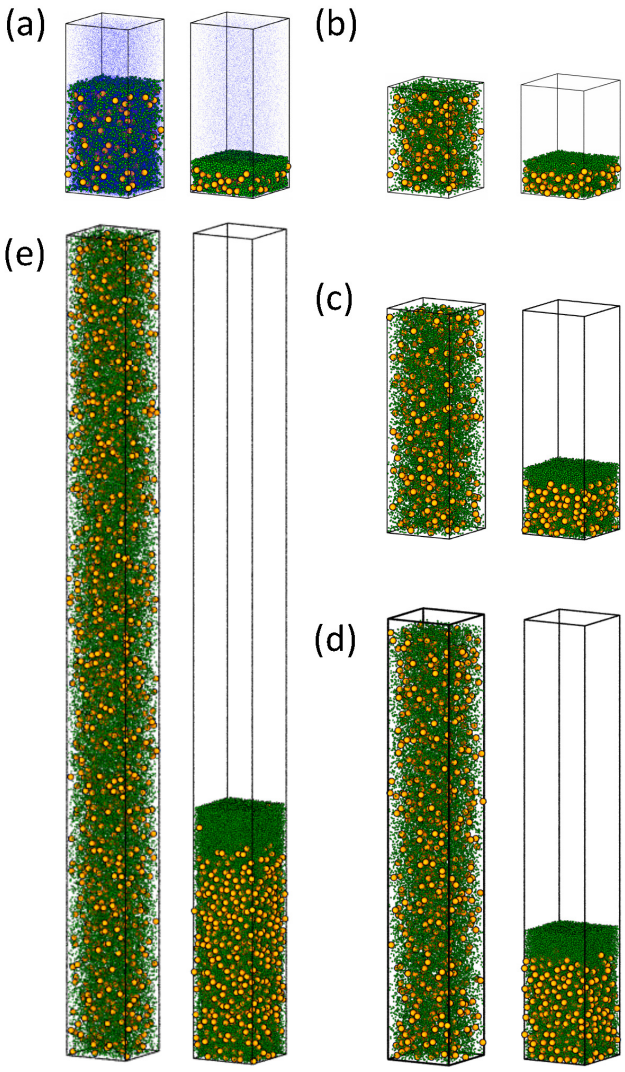

Figure 6.1: Snapshots of drying suspensions: (a) the explicit solvent system H_e; the implicit solvent systems (b) H_1v_1, (c) $H_2v_{1/2}$, (d) $H_4v_{1/4}$, and (e) $H_8v_{1/8}$. For each system, the left snapshot is for the equilibrium suspension prior to evaporation while the right is for the state with $H(t) \simeq 0.3H(0)$. Color code: LNPs (orange), SNPs (green), and solvent (blue).

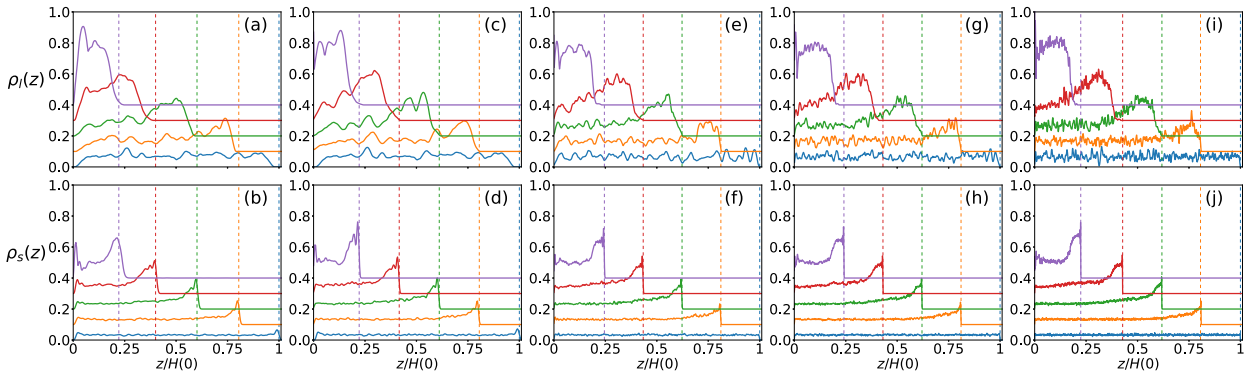

Figure 6.2: Evolution of density profiles for LNPs (top row) and SNPs (bottom row) for H_e [(a) and (b)], H_1v_1 [(c) and (d)], $H_2v_{1/2}$ [(e) and (f)], $H_4v_{1/4}$ [(g) and (h)], and $H_8v_{1/8}$ [(i) and (j)]. The vertical dashed lines indicate the location of the liquid-vapor interface. For clarity, each profile is shifted vertically by $0.1m/\sigma^3$ from the previous one.

comes into play.

For quantitative analyses, in Fig. 6.2 we plot the density profiles of LNPs and SNPs along the normal direction of the film, which are computed as $\rho_i(z) = n_i(z)m_i/(\sigma L_x L_y)$ with $i \in \{l, s\}$. Specifically, $n_i(z)$ is the number of i-type particles in a spatial bin of thickness σ centered on z and m_i is the mass of one i-type particle. For a nanoparticle straddling several bins, its contribution to $n_i(z)$ is a fraction equal to the ratio between its volume enclosed by each bin and the entire volume of the nanoparticle. To compare different films, in Fig. 6.2 we normalize z by the initial film thickness, $H(0)$, for each suspension film.

Several features can be easily identified from these density profiles. During drying, both LNPs and SNPs are enriched near the receding liquid-vapor interface since $\mathrm{Pe}_l \gg \mathrm{Pe}_s \gg 1$ and all the five systems exhibit qualitatively similar density profiles. However, the enrichment of SNPs in the interfacial region is stronger in its degree than that of LNPs. For all the implicit solvent systems, the density profiles at the same stage of drying (i.e., at the same $H(t)/H(0)$) are all similar. In the final state with $H(t) \simeq 0.3H(0)$, the density profile of LNPs along the z-axis has a slight negative gradient for H_e, is almost flat for H_1v_1, while

exhibits a very weak positive gradient for $H_2v_{1/2}$, $H_4v_{1/4}$, and $H_8v_{1/8}$. Therefore, H_e with an explicit solvent is expected to display stronger "small-on-top" stratification than all the implicit solvent systems, while stratification of similar amplitudes is expected for $H_2v_{1/2}$, $H_4v_{1/4}$, and $H_8v_{1/8}$.

The state of stratification can be characterized by examining the mean heights of LNPs and SNPs as a function of time, which are computed as $\langle z_i \rangle = \frac{1}{N_i} \sum_{n=1}^{N_i} z_{in}$ with $i \in \{l, s\}$ for LNPs and SNPs, respectively. Here z_{in} is the z coordinate of the n-th nanoparticle of type i. An order parameter of stratification can then be defined as $(2\langle z_l \rangle - 2\langle z_s \rangle)/H(t)$, i.e., as the difference in average height of LNPs and SNPs normalized by a half of the instantaneous thickness of the drying film [34]. In the equilibrium suspension before evaporation, $\langle z_l \rangle \simeq \langle z_s \rangle \simeq H(0)/2$ and therefore $\langle z_l \rangle - \langle z_s \rangle \simeq 0$. After drying is initiated, $\langle z_l \rangle - \langle z_s \rangle > 0$ indicates "large-on-top" stratification while "small-on-top" corresponds to $\langle z_l \rangle - \langle z_s \rangle < 0$.

In Fig. 6.3 we plot $(2\langle z_l \rangle - H(t))/H(t)$, $(2\langle z_s \rangle - H(t))/H(t)$, and $(2\langle z_l \rangle - 2\langle z_s \rangle)/H(t)$ against $1 - H(t)/H(0)$ that quantifies the extent of drying. As shown in Fig. 6.3(a), the data on $\langle z_l \rangle$ collapse for all the implicit solvent systems H_1v_1, $H_2v_{1/2}$, $H_4v_{1/4}$, and $H_8v_{1/8}$ with similar Péclet numbers. For most of the drying process, $\langle z_l \rangle$ is larger than $H(t)/2$, indicating that the LNPs are enriched in the top half of the drying film. Only in the very late stage of drying, i.e., for $H(t)/H(0) \lesssim 0.35$, the LNPs become more concentrated in the bottom half of the drying film. For H_e, in the initial stage of drying, the LNPs show similar behavior as those in the implicit solvent systems and are enriched in the top half of the drying film. However, in the late stage of drying, the LNPs start to diffuse out of the top half of the drying suspension and their average height becomes smaller than $H(t)/2$. The transition from an enrichment of LNPs in the top half to a concentration in the lower half of the drying film occurs in H_e around $H(t)/H(0) \simeq 0.45$, which is earlier than the transition in the implicit solvent systems.

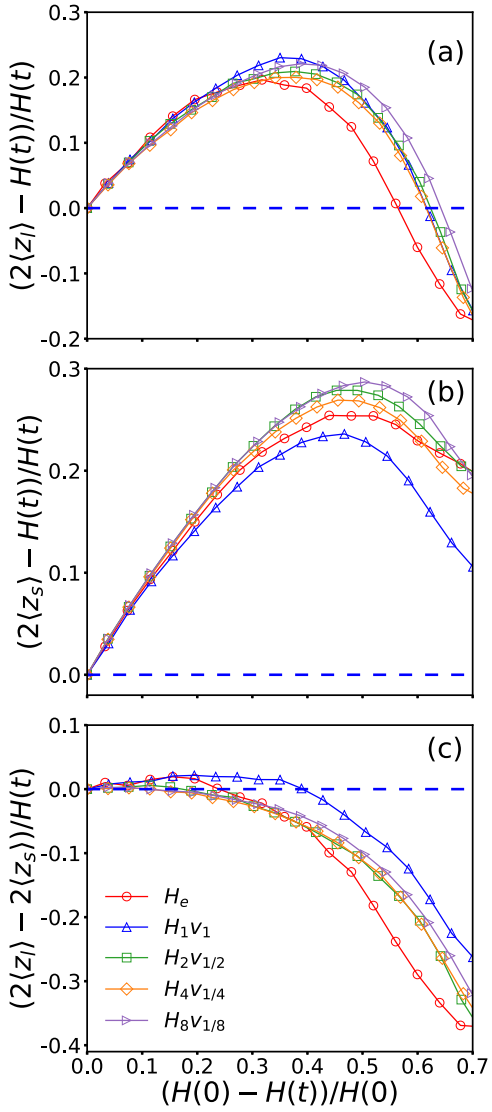

Figure 6.3: Mean height relative to the center of a drying film of (a) LNPs and (b) SNPs and (c) the difference in average height of LNPs and SNPs, all normalized by $H(t)/2$, are plotted against the extent of drying, $(H(0) - H(t))/H(0)$, for H_e (red circle), H_1v_1 (blue upward triangle), $H_2v_{1/2}$ (green square), $H_4v_{1/4}$ (yellow diamond), and $H_8v_{1/8}$ (purple right-pointing triangle).

As shown in Fig. 6.3(b), the SNPs are always accumulated in the top half of the drying film for both explicit and implicit solvent models. When $H(t)/H(0) \lesssim 0.8$, $\langle z_s \rangle$ shows larger variations among the implicit solvent systems with different $H(0)$. The accumulation of SNPs in the top half of the drying film is weaker in H_1v_1 and is enhanced when the initial film gets thicker. For $H_2v_{1/2}$, $H_4v_{1/4}$, and $H_8v_{1/8}$, the results of $(2\langle z_s \rangle - H(t))/H(t)$ *vs* $1 - H(t)/H(0)$ are close to each other and the shift from one curve to another is nonmonotonic when $H(0)$ is increased (i.e., for $H_2v_{1/2} \rightarrow H_4v_{1/4} \rightarrow H_8v_{1/8}$), indicating that the initial films are thick enough to lead to a convergence in the behavior of SNPs. From Fig. 6.3(b), we also note that the accumulation of SNPs in the top half of the drying film is always stronger in H_e than in H_1v_1.

From $\langle z_l \rangle$ and $\langle z_s \rangle$, we expect that H_e should yield the strongest "small-on-top" stratification while H_1v_1 should lead to the weakest. Furthermore, $H_2v_{1/2}$, $H_4v_{1/4}$, and $H_8v_{1/8}$ are expected to be very similar in terms of the degree of stratification. The order parameter plots in Fig. 6.3(c), $(2\langle z_l \rangle - 2\langle z_s \rangle)/H(t)$ *vs* $1 - H(t)/H(0)$, confirm all these predictions. Our results clearly demonstrate the emergence of "small-on-top" stratification in both explicit and implicit solvent models.

In contrast to the previous report of Statt *et al.* on polymer solutions where "small-on-top" stratification only occurs in the implicit solvent system [86], "small-on-top" occurs in both models here, with the degree of stratification slightly stronger in the explicit solvent. Our results indicate that the physics of drying may have some differences in colloidal suspensions and polymer solutions. To map a polymer solution in an explicit solvent to a system with an implicit solvent, both the monomer-monomer interactions and the viscous damping on the monomers have to be adjusted to match the size (i.e., the radius of gyration) and diffusion of polymer chains. However, for a colloidal suspension in which the particles are well dispersed, only the damping needs to be tuned to match the diffusion coefficient as a particle has the

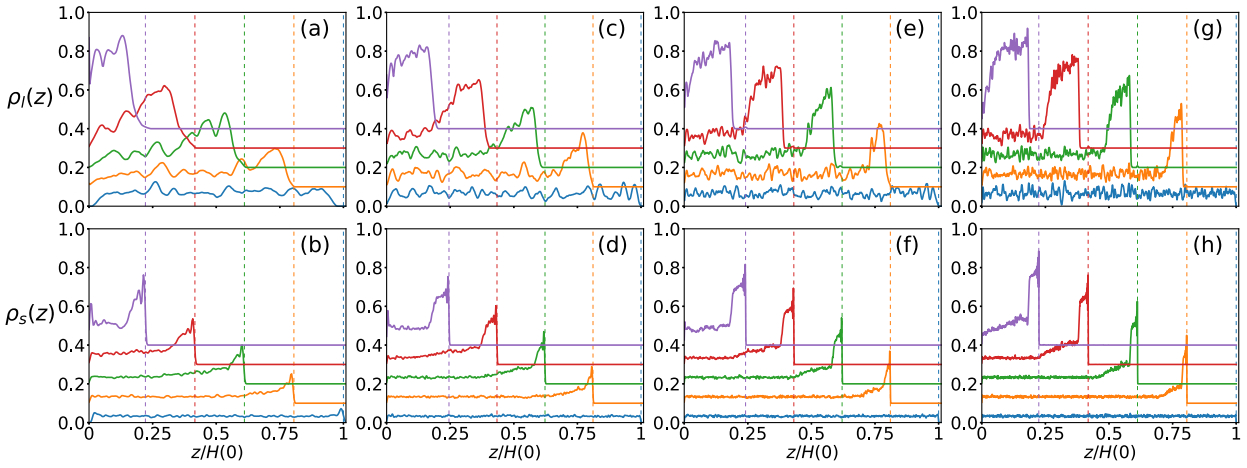

Figure 6.4: Evolution of density profiles for LNPs (top row) and SNPs (bottom row) for H_1v_1 [(a) and (b)], H_2v_1 [(c) and (d)], H_4v_1 [(e) and (f)], and H_8v_1 [(g) and (h)]. The vertical dashed lines indicate the location of the liquid-vapor interface. For clarity, in each plot a profile is shifted upward by $0.1m/\sigma^3$ from the previous one.

same size in both models. Statt *et al.* concluded that hydrodynamic interactions are not captured by the implicit solvent model and their missing leads to the occurrence of "small-on-top" stratification in their polymer solutions with the implicit solvent [86]. In nanoparticle suspensions studied here, hydrodynamic interactions seem to play a much weaker role but more work is needed to elucidate their possible effects.

Using the implicit solvent model, we have also studied the effect of increasing the initial film thickness at a fixed evaporation rate. We compare four systems, H_1v_1, H_2v_1, H_4v_1, and H_8v_1, where $H(0)$ is increased from 304σ to 2476.5σ but v_e is fixed at $1.18 \times 10^{-3}\sigma/\tau$. As results, the Péclet numbers increase proportionally with $H(0)$ and Pe_l increases from 211.0 to 1719.0. As shown in the bottom row of Fig. 6.4, the density profiles of SNPs plotted against $z/H(0)$ are qualitatively similar for the four systems. The main difference is that the peak value of $\rho_s(z)$ at the evaporating interface becomes slightly larger for larger $H(0)$. Another difference is the appearance of a plateau of $\rho_s(z)$ just right below the highly SNP-enriched skin layer at the evaporating liquid-vapor interface when the film is thick enough,

as in H_2v_1, H_4v_1, and H_8v_1. The absolute thickness of this plateau zone increases as $H(0)$ is increased, possibly indicating a jammed state of SNPs in this zone. Below this plateau, $\rho_s(z)$ first decreases substantially in a very narrow region and then gradually decreases as z gets smaller. Eventually, $\rho_s(z)$ reaches another plateau corresponding to the density of SNPs in the equilibrium suspension prior to evaporation. Fig. 6.4 also shows that the density profiles of LNPs remain qualitatively unchanged when $H(0)$ is increased (especially when $H(0)$ is large as in H_4v_1 and H_8v_1) but the evaporation rate is fixed. Going from the evaporating interface to the bulk of the drying suspension, $\rho_l(z)$ first decreases gradually and then decays rapidly to its value in the equilibrium suspension before evaporation. As $H(0)$ is increased, the peak value of $\rho_l(z)$ also becomes slightly larger [see the top row of Fig. 6.4].

The average height of LNPs and SNPs plotted in Fig. 6.5(a) and (b) shows interesting systematic changes as $H(0)$ is increased. First, $\langle z_s\rangle/H(t)$ shifts upward more considerably than $\langle z_l\rangle/H(t)$ with increasing $H(0)$. The data indicate that for a film with a larger initial thickness, the accumulation of both SNPs and LNPs near the receding interface and in the top half of the drying film is enhanced. For example, for H_1v_1 with $H(0) = 304\sigma$, the LNPs actually are at deficit in the top half of the film at the late stage of drying. However, for H_4v_1 with $H(0) = 1246.5\sigma$ and H_8v_1 with 2476.5σ, the LNPs are always enriched in the top half of the film during the entire drying process, as shown in Fig. 6.5(a). For all the systems, Fig. 6.5(b) shows that the SNPs are always accumulated in the top half of the drying film. As $H(0)$ increases, the SNPs form a thicker jammed layer below the receding interface and the LNPs are trapped in this layer, though they are expected to be pushed out of the region close to the interface via the diffusiophoretic mechanism. As a result, the enrichment of both SNPs and LNPs is enhanced near the evaporating interface when $H(0)$ is larger.

Fig. 6.5(c) shows that all the four systems display "small-on-top" stratification, which emerges almost instantaneously for H_2v_1, H_4v_1, and H_8v_1 once the solvent evaporation

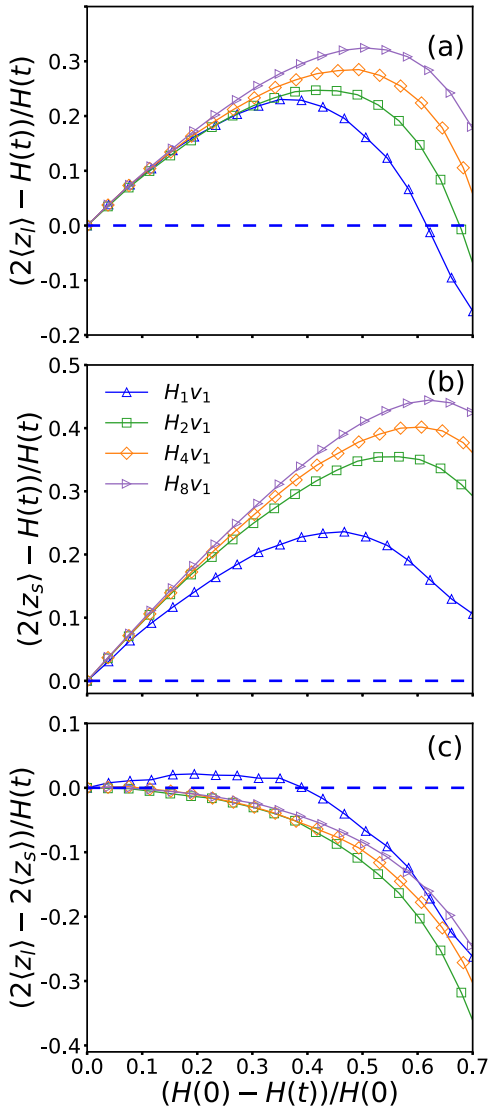

Figure 6.5: Mean height relative to the center of a drying film of (a) LNPs and (b) SNPs and (c) the difference in average height of LNPs and SNPs, all normalized by $H(t)/2$, are plotted against the extent of drying, $(H(0) - H(t))/H(0)$, for H_1v_1 (blue upward triangle), H_2v_1 (green square), H_4v_1 (yellow diamond), and H_8v_1 (purple right-pointing triangle).

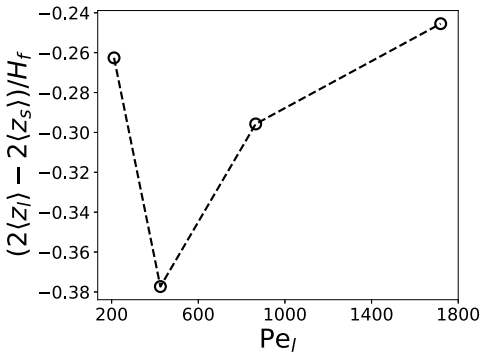

Figure 6.6: Difference in average height of LNPs and SNPs, normalized by $H_f/2$, is plotted against Pe_l for H_1v_1, H_2v_1, H_4v_1, and H_8v_1 from left to right. The data are extracted from Fig. 6.5(c) at $H(t) = H_f \simeq 0.3H(0)$.

is initiated. However, in the early stage of drying, H_1v_1 shows very weak "large-on-top" stratification. For H_1v_1, a transition to "small-on-top" occurs at $H(t)/H(0) \simeq 0.45$.

When v_e is fixed, the Péclet numbers become larger from H_1v_1 to H_8v_1 as $H(0)$ is increased. In Fig. 6.6 we plot the amplitude of stratification $(2\langle z_l\rangle - 2\langle z_s\rangle)/H(t)$ at $H(t) = H_f \simeq 0.3H(0)$ as a function of Pe_l. The four data points are for H_1v_1, H_2v_1, H_4v_1, and H_8v_1, respectively. Note that a more negative value of $(2\langle z_l\rangle - 2\langle z_s\rangle)/H(t)$ indicates stronger "small-on-top" stratification. Fig. 6.6 shows that stratification is most pronounced for an intermediate value of Pe_l, which is around 435 for the systems studied here. This nonmonotonic behavior of the degree of stratification was also found in the simulations of Tatsumi *et al.*, where the Péclet numbers were increased by increasing v_e while fixing $H(0)$.

6.4 Conclusions

In this chapter, we employed MD simulations to compare an explicit solvent model to an implicit model in studying the drying process of bidisperse particle suspensions. In the explicit model, the solvent is modeled as a Lennard-Jones liquid. In the implicit model, the

solvent is treated as a viscous, uniform, isothermal background. In contrast to a previous report on polymer solutions where "small-on-top" stratification does not occur in the explicit solvent but occurs in the implicit one [86], we have observed the occurrence of "small-on-top" in both models. Our results indicate that the implicit solvent model can be used effectively for modeling the drying of thin film suspensions, for which the evaporative flow of the solvent is essentially one-dimensional. However, it remains unclear why the back-flow of the solvent around a migrating particle and the hydrodynamic interactions between the particles seem to be unimportant in the systems studied here [29, 86].

With the implicit solvent model, we further study the effect of the initial film thickness on the drying of a suspension film of a bidisperse mixture of nanoparticles. Our results indicate that for films that are initially thick enough, the Péclet number is a valid dimensionless number capturing the competition between solvent evaporation and nanoparticle diffusion. For fast drying, the accumulation of either large or small nanoparticles near the receding interface is similar when the receding speed of the liquid-vapor interface is decreased in proportion to the increase of the initial film thickness, which results in similar Péclet numbers. For these systems, the degree of stratification is also similar. However, if the receding speed of the interface is fixed, then the accumulation near the interface is more significant for both large and small nanoparticles when the film gets thicker. The degree of stratification varies nonmonotonically and is most enhanced at a Péclet number that is not too large.

In the systems studied here, the direct nanoparticle-nanoparticle interactions are purely repulsive and the same in both solvent models to ensure that the nanoparticles are well dispersed in the suspension, though there might be solvent-mediated weak attractions between the nanoparticles in the explicit solvent. If there are direct attractions between the nanoparticles or strong nanoparticle-solvent attractions leading to a layer of solvent bound to each particle, then mapping an explicit solvent system to an implicit one requires a careful

tuning of the nanoparticle-nanoparticle potentials to mimic the effect of the solvent. This mapping can be achieved by following the procedure outlined by Grest *et al.* to derive an effective potential between nanoparticles in an implicit solvent [39]. For such systems, it is an interesting question whether similar stratification can be observed in drying polydisperse particle suspensions with explicit and implicit solvents.

Chapter 7

Applications of moving interface method

This chapter is based on a paper that is currently in preparation:

Yanfei Tang, Gary. S. Grest, and Shengfeng Cheng, "Modeling Solution Drying by Moving a Liquid-Vapor Interface: Method and Applications", to be submitted.

I designed and built all the models for molecular dynamics simulations and ran all the simulations. I performed all the data analyses and prepared figures. Dr. Grest contributed to the overall design of this project. All authors contributed to the writing of this paper. My contributions to this paper were under Dr. Cheng's supervision.

7.1 Introduction

The comparison in the previous chapter demonstrated that when carefully implemented, an implicit solvent model can be used to study the drying of certain particle suspensions. In this

chapter we apply this method to various soft matter solutions including a solution film of a mixture of polymers and nanoparticles, a droplet of a bidisperse nanoparticle suspension, a solution droplet of a polymer blend, and a droplet of diblock copolymer solution.

Drying is a phenomenon we witness everyday [130]. It is also a useful tool for material fabrications [85, 131]. In a typical process, raw materials are dissolved or dispersed in an appropriate solvent and the resulting solution is dried to yield desired materials with certain structures. For example, drying is also frequently used to produce paint coatings [22, 132–134], polymer films [3, 135], polymeric particles [136], and polymer nanocomposites [5, 44, 137, 138]. Because of its practical importance and rich nonequilibrium physics [14, 132], many efforts have been devoted to elucidate the fundamental processes and mechanisms of the drying of soft matter solutions [85, 126], including modeling based on molecular dynamics methods [11, 12, 20, 21, 23, 34, 35, 44, 86, 127–129, 139–142].

To model the drying of soft matter solutions, a key challenge is the treatment of the solvent. To capture factors that may be important in an evaporation process, such as hydrodynamic interactions between solutes [86], evaporation-induced flow in the solution (e.g., capillary flow in an evaporating sessile droplet showing the coffee-ring effect) [143], and instabilities during drying including Rayleigh-Bénard and Bénard-Marangoni instabilities [3, 144, 145], it is ideal to include the solvent explicitly in a computational model [11, 12, 34, 35, 44, 86, 129, 139, 140, 142]. However, such models are computationally extremely expensive as the number of solvent particles is usually much larger than that of the solutes at realistic volume fractions. For example, systems containing several million solvent particles or more have to be considered for several hundred to several thousand nanoparticles [34, 35]. Because of the large system size, only fast evaporation rates can be modeled in this approach [11, 12, 34, 35, 44, 86, 129, 139, 140, 142]. Considering the limitations of explicit solvent models, it is natural to explore alternative approaches that are computationally more efficient and able

to quickly yield results that are at least qualitatively correct. One such effort is to model the solvent as an uniform viscous medium in which the solutes are dispersed and moving around. This approach is termed the implicit solvent modeling of soft matter solutions [39, 86, 142].

In the past few years, implicit solvent models have been applied to study the evaporation process of particle suspensions and polymer solutions and reveal many interesting phenomena induced by drying [20, 21, 23, 86, 127, 128, 139, 141, 142]. Fortini *et al.* used Langevin dynamics simulations based on such a model to study the drying of a bidisperse colloidal suspension film and demonstrated the counterintuitive "small-on-top" stratification in which the smaller particles are predominately distributed on top of the larger particles after drying [20, 21]. Tatsumi *et al.* used a similar model to investigate the role of evaporation rates on stratification. Howard *et al.* and Statt *et al.* employed this approach to simulate the drying of colloidal mixtures, polymer-colloid mixtures, and polydisperse polymer mixtures and observed various stratifying phenomena as well [23, 86, 127, 141]. We recently demonstrated that comparable stratification could be observed in both explicit and implicit solvent models for which the diffusion coefficients of the particles are matched [142].

In the implicit solvent approach toward drying modeling, all the solutes or particles are confined in the solution by a potential barrier, which plays the role of the liquid-vapor interface in a solution with an explicit solvent. One simple form of the confining potential is a harmonic potential. In a previous work, we analyzed the capillary force experience by a small spherical particle at a liquid-vapor interface and showed that this approximation is reasonable for many situations and the corresponding spring constant is related to the particle size, the interfacial tension, and the lateral span of the liquid-vapor interface [80]. A rigorous physical foundation was thus established for the implicit solvent models. In this chapter, we describe the general method of using the implicit solvent approach to study the drying process of a soft matter solution and apply this method to various systems including

solution films and droplets. The chapter is organized as follows. In Sec. 7.2 the model and simulation method are introduced. The applications of the method to various systems are presented in Sec. 7.3. In Sec. 7.4 we briefly summarize the method and discuss its limitation.

7.2 Model and simulation methodology

In an implicit solvent model, the solvent is treated as a uniform, viscous, isothermal, and isobaric background [142]. The motion of particles in this background is typically described by a Langevin equation that includes the Stokes drag force as a damping term. The damping rate can be chosen to tune the diffusion coefficient of the particles. For a system with a liquid-vapor interface, a potential barrier is used to restrict all the particles in the liquid phase. As shown previously [80], a harmonic potential can be employed as the barrier. The evaporation process of the solvent can be implemented by moving the location of the confining potential's minimum to mimic the receding motion of the liquid-vapor interface in the corresponding explicit solvent systems. Below we discuss these two main ingredients of an implicit solvent model for a particle suspension.

7.2.1 Langevin dynamics

In an implicit solvent, the equation of motion of particles is given by the following Langevin equation,

$$m\frac{d^2\mathbf{r}_i}{dt^2} = \sum_{j\neq i}\mathbf{f}_{ij} + \mathbf{F}_i^D + \mathbf{F}_i^R, \tag{7.1}$$

where m is the mass of the i-th particle, r_i is its position vector, $\mathbf{f}_{ij}$ is the force on the particle from its interaction with other particles in the system, $\mathbf{F}_i^D$ is the Stokes drag force, and $\mathbf{F}_i^R$

is a random force. The Stokes drag force can be expressed as

$$\mathbf{F}_i^D = -\xi \frac{d\mathbf{r}_i}{dt}, \tag{7.2}$$

where ξ is the friction (drag) coefficient of the particle. To maintain the system at a constant temperature T, the random force needs to follow the constraint set by the fluctuation-dissipation theorem,

$$\begin{aligned} \langle \mathbf{F}_i^R(t) \rangle &= 0, \\ \langle \mathbf{F}_i^R(t) \cdot \mathbf{F}_j^R(t') \rangle &= 6k_B T \xi \delta_{ij} \delta(t - t'), \end{aligned} \tag{7.3}$$

where $\langle \cdot \rangle$ stands for ensemble average, k_B is the Boltzmann constant, t is time, and $\delta(t)$ is the Dirac delta function.

For a particle in the dilute limit, the diffusion coefficient D is related to the friction coefficient ξ through

$$D = \frac{k_B T}{\xi}, \tag{7.4}$$

which is known as the Einstein relation. For a small particle with radius R in a fluid with a low Reynolds number flow and the no-slip condition of the fluid velocity is satisfied at the particle surface, the Stokes law states that $\xi = 6\pi\eta R$, where η is the viscosity of the fluid. This yields the Einstein-Stokes relation,

$$D = \frac{k_B T}{6\pi\eta R}. \tag{7.5}$$

The friction coefficient ξ is usually written in terms of a damping time Γ through $\xi \equiv \frac{m}{\Gamma}$. As a result, the Stokes drag becomes

$$\mathbf{F}_i^D = -\frac{m}{\Gamma} \frac{d\mathbf{r}_i}{dt}. \tag{7.6}$$

If the Stokes law holds, then $\Gamma = m/(6\pi\eta R)$. If we assume the particle has a uniform mass density ρ, then $m = \frac{4}{3}\pi R^3\rho$ and the damping time Γ becomes

$$\Gamma = \frac{2\rho}{9\eta}R^2. \tag{7.7}$$

The implication of this relationship is that for a bidisperse mixture of particles of two different radii, R_l for the larger and R_s for the smaller particles, the damping time of the larger particles needs to be α^2 times of that of the smaller ones in order for the Stokes-Einstein relation to hold, where $\alpha \equiv R_l/R_s$ is the size ratio.

7.2.2 Moving interface method of modeling drying

When the solvent evaporates from a solution, the liquid-vapor interface recedes. To mimic this process, the location of the minimum of the potential barrier that is used to confine all the particles (in general, solutes) in the liquid solvent is moved toward the solution phase at speed v_e. For evaporation at a constant rate v_e is time independent and the position of the liquid-vapor interface at time t is given by $H(t) = H(0) - v_e t$, where $H(0)$ is the initial thickness for a suspension film or the initial radius for a spherical droplet. Similarly, $H(t)$ is the thickness of a drying film or the radius of a drying droplet at time t. For a particle within distance R from the liquid-vapor interface, where R is the particle's radius, the particle experiences a force normal to the interface with a magnitude

$$F_n = \begin{cases} k_s\left(\Delta z_n + R\cos\theta\right) & \text{for } |\Delta z_n| \le R \\ 0 & \text{otherwise,} \end{cases} \tag{7.8}$$

where k_s is a spring constant, Δz_n is the shortest distance from the center of the particle to the instantaneous location of the liquid-vapor interface (which is flat for a film but curved

for a droplet), and θ is the contact angle of the liquid solvent on the surface of the particle. Mathematically, $\Delta z_n = z_n - H(t)$, where z_n is the particle's coordinate along the z-axis for a flat interface in the $x-y$ plane and with the bottom of the film located at $z = 0$ or along the radial direction for a spherical interface with the center of the droplet located at $z = 0$. The minimum of the confining potential is thus at $H(t) - R\cos\theta$. In Eq. (7.8), a positive (or negative) value indicates that the force is pointing toward the liquid solvent (or vapor phase).

Some ambiguities exist in the literature regarding the physical interpretation of k_s. Pieranski proposed that $k_s = 2\pi\gamma$ with γ being the interfacial tension of the liquid-vapor interface [49]. However, this expression completely neglects the capillary effect. Recently we analyzed the capillary force exerted on a spherical particle of radius R at a liquid-vapor interface when the particle is displaced out of its equilibrium location and showed that the linear approximation in Eq. (7.8) generally works well but the spring constant should be understood as $k_s = \frac{2\pi\gamma}{\ln(2L/R)}$, where L is the lateral span of the liquid-vapor interface [33, 80]. In the simulations reported here, we simply set $k_s = 3.0\epsilon/\sigma^2$, which is a reasonable value for the systems considered. We also typically set $\theta = 0$ and in this case the potential barrier representing the liquid-vapor interface becomes the right half of a harmonic potential, which ensures that all the solutes are confined in the solution. The contact angle θ can also be adjusted to tune the interaction between the solute and the liquid-vapor interface. For example, a finite θ can be used for systems with attractions between the solute and the interface [7].

7.3 Applications of moving interface method

7.3.1 Drying of polymer and nanoparticle hybrid solutions

Evaporation of a hybrid solution of polymers and nanoparticles has been studied via molecular dynamics simulations with an explicit [44] and an implicit solvent model [23]. Here we apply the moving interface method to study a mixture of 3200 linear polymer chains and 171 nanoparticles. Each chain consists of 100 beads of mass m and diameter σ. All the beads interact through a Lennard-Jones (LJ) potential,

$$U_{\mathrm{LJ}}(r) = 4\epsilon \left[(\sigma/r)^{12} - (\sigma/r)^{6} - (\sigma/r_c)^{12} + (\sigma/r_c)^{6} \right], \tag{7.9}$$

where r is the center-to-center separation of two beads, ϵ is the strength of the interaction, σ is a length scale, and r_c is the cutoff of the potential. In this section, $r_c = 2^{1/6}\sigma$, rendering the potential to be purely repulsive. Additionally, adjacent beads on a chain are connected by a spring described by a finitely extensible nonlinear elastic (FENE) potential [122],

$$U_{\mathrm{FENE}}(r) = -\frac{1}{2} k R_0^2 \ln\left(1 - \frac{r^2}{R_0^2}\right), \tag{7.10}$$

where $R_0 = 1.5\sigma$ and $k = 30\epsilon/\sigma^2$. The LJ interaction between a pair of beads bonded together is always truncated at $2^{1/6}\sigma$. With these parameters, the model describes polymer chains in a good solvent.

A nanoparticle is modeled as a sphere uniformly filled with LJ beads at mass density $1.0m/\sigma^3$ [36, 37]. The interaction between a nanoparticle and a monomer bead on a polymer is given

by an integrated LJ potential [36],

$$U_{\rm np}(r) = \frac{2}{9}\frac{R^3\sigma^3 A_{\rm np}}{(R^2-r^2)^3}\left[1 - \frac{(5R^6+45R^4r^2+63R^2r^4+15r^6)\sigma^6}{15(R-r)^6(R+r)^6}\right], \tag{7.11}$$

where R is the nanoparticle radius, r is the center-to-center distance between the nanoparticle and the monomer, and $A_{\rm np}$ is a Hamaker constant setting the interaction strength. Here we use $R = 10\sigma$ and $A_{\rm np} = 80\epsilon/\sigma^2$. The nanoparticle-polymer interaction is also made purely repulsive by truncating the potential at 10.8587σ.

The nanoparticle-nanoparticle interaction is given by an integrated LJ potential for two spheres [36],

$$U_{\rm nn}(r) = U_A(r) + U_R(r), \tag{7.12}$$

with

$$U_A(r) = -\frac{A_{\rm nn}}{6}\left[\frac{2R_1R_2}{r^2-(R_1+R_2)^2} + \frac{2R_1R_2}{r^2-(R_1-R_2)^2} + \ln\left(\frac{r^2-(R_1+R_2)^2}{r^2-(R_1-R_2)^2}\right)\right], \tag{7.13}$$

$$\begin{aligned} U_R(r) = \frac{A_{\rm nn}}{37800}\frac{\sigma^6}{r}\Bigg[&\frac{r^2-7r(R_1+R_2)+6(R_1^2+7R_1R_2+R_2^2)}{(r-R_1-R_2)^7} \\ &+ \frac{r^2+7r(R_1+R_2)+6(R_1^2+7R_1R_2+R_2^2)}{(r+R_1+R_2)^7} \\ &- \frac{r^2+7r(R_1-R_2)+6(R_1^2-7R_1R_2+R_2^2)}{(r+R_1-R_2)^7} \\ &- \frac{r^2-7r(R_1+R_2)+6(R_1^2-7R_1R_2+R_2^2)}{(r-R_1+R_2)^7}\Bigg], \end{aligned} \tag{7.14}$$

where R_1 and R_2 are the radii of the nanoparticles, r is the distance between their centers, and $A_{\rm nn}$ is a Hamaker constant. Here we use $A_{\rm nn} = 39.48\epsilon$ and $R_1 = R_2 = 10\sigma$. The nanoparticle-nanoparticle interaction is also purely repulsive with a cutoff 20.574σ for the potential. In this manner, the nanoparticles and polymer chains are guaranteed to be well

disperse in the implicit solvent prior to evaporation.

The hybrid solution of the nanoparticles and polymer chains is placed in a rectangular simulation cell with dimensions $L_x \times L_y \times L_z$, where $L_x = L_y = 200\sigma$ and $L_z = 800\sigma$. The liquid-vapor interface is modeled as a potential barrier as in Eq. (7.8) with $H(0) = 800\sigma$. The contact angle $\theta = 0$ is used for both polymer beads and nanoparticles. All the particles in the system are thermalized at a temperature $T = 1.0\epsilon/k_B$ with a Langevin thermostat. The damping time Γ is set equal to 1τ for the polymer beads and 100τ for the nanoparticles, respectively. The drying process is modeled by moving the liquid-vapor interface downward to $H(t) = 200\sigma$ at a constant speed $v_e = 0.024\sigma/\tau$. The entire drying process thus lasts for 25000τ.

All the simulations reported here were performed with Large-scale Atomic/Molecular Massively Parallel Simulator (LAMMPS) [41]. A velocity-Verlet algorithm with a time step $dt = 0.005\tau$ is used to integrate the equation of motion.

The initial volume fractions of the polymers and nanoparticles are $\phi_p = 0.0052$ and $\phi_n = 0.022$. The snapshots of the hybrid solution undergoing drying are shown in Fig. 7.1 for various times after the evaporation is initiated. Prior to evaporation, all the polymers and nanoparticles are uniformly distributed in the solution. After drying, the polymers are enriched near the descending interface. Because of the repulsion with the polymer chains, the nanoparticles are expelled from this skin layer of polymers and become accumulated just below the skin layer. As a result, a stratified state is created, similar to the results previously obtained with an explicit solvent model [44]. In the implicit solvent simulation of Howard *et al.*, similar stratification is also observed with nanoparticles concentrated below a concentrated layer of polymer chains [23]. However, a layer of nanoparticles is also found on top of the polymer skin layer in those simulations (see Figs. 6 and 7 of Ref. [23]). This is an effect of the potential barrier used in Ref. [23] to represent the liquid-vapor interface, where

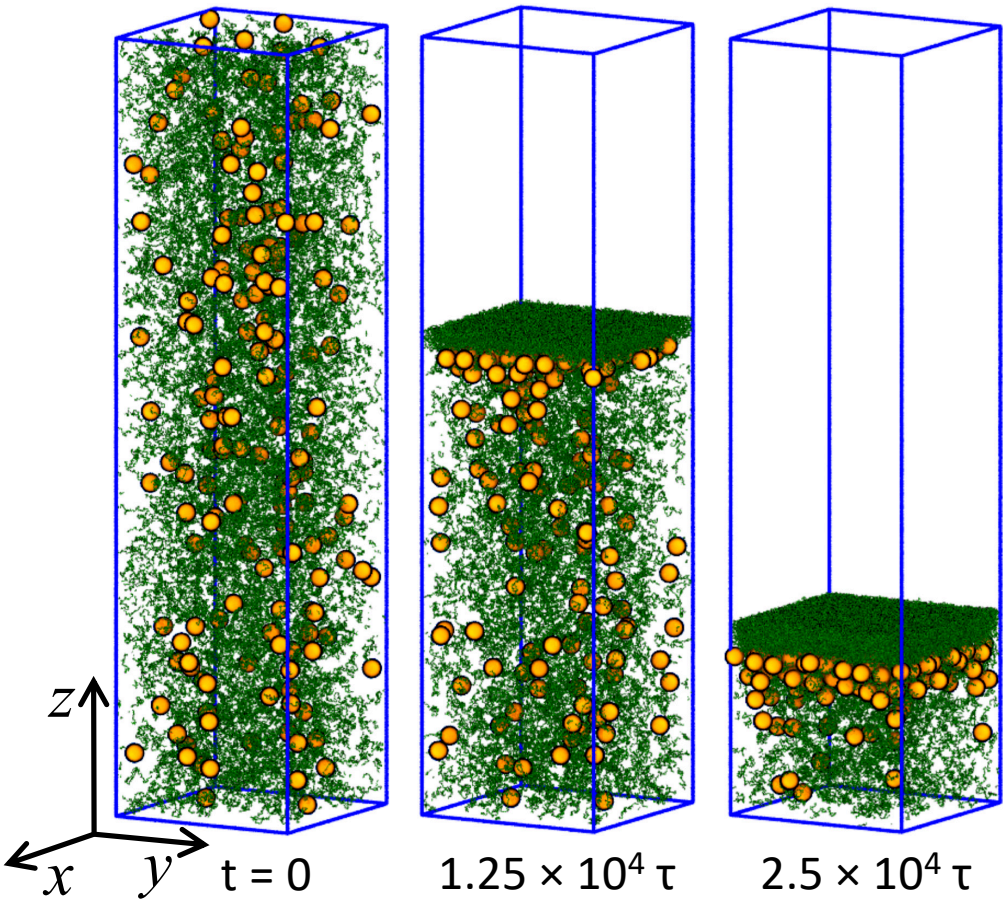

Figure 7.1: Snapshots of a hybrid solution of nanoparticles (orange) and polymers (green) at various time elapsed since the drying process is initiated.

the contact angle θ in Eq. (7.8) was set to be 90° for both nanoparticles and polymers. The resulting potential is thus attractive for both species and the attraction can be quite strong for nanoparticles, leading to their adsorption at the interface. Since here we use $\theta = 0$ in Eq. (7.8) for all the dispersed particles, this side effect is removed, as evident in Fig. 7.1

7.3.2 Drying of suspension droplets of a bidisperse mixture of nanoparticles

Stratification has mostly been discussed in the context of drying films [20, 21, 23, 25, 34, 86, 127, 128]. However, stratification can also occur in drying droplets under appropriate conditions, which may lead to fast procedures of making core-shell structures. In industry, spray drying processes are frequently practiced, where droplet drying is a critical step [146]. In one such process, a particle suspension is injected from a nozzle or an injector into a flowing gas. The liquid jet of the suspension then breaks into droplets, which further dry in the hot gas into clusters of particles (i.e., solutes). The drying of a single droplet was recently studied using the Leidenfrost effect: a droplet levitated on a hot substrate by its own vapor and then let dry [147]. Here we use the moving interface method to study the drying of a suspension droplet of a mixture of nanoparticles of two different radii, motivated by the possibility of creating a core-shell cluster with one type of nanoparticles in the outside shell while the other type in the inner core. In other words, a bidisperse nanoparticle mixture stratifies radially into either "small-on-outside" or "large-on-outside".

The droplet contains 200 large nanoparticles (LNPs) of radius $R_l = 10\sigma$ and 12800 small nanoparticles (SNPs) of radius $R_s = 2.5\sigma$, which are initially confined by a spherical potential barrier inside a sphere with radius $H(0) = 1000\sigma$, as shown in Fig. 7.2. Their initial volume fractions are $\phi_l = \phi_s = 0.0002$. Although the liquid-vapor interface of a droplet is curved,

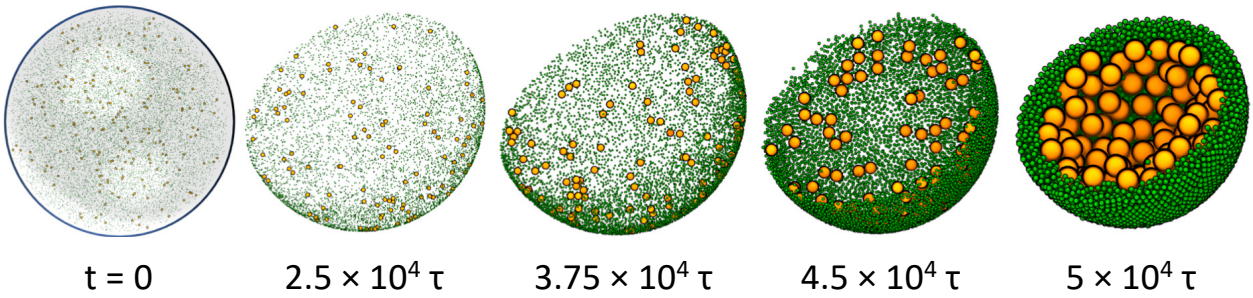

Figure 7.2: Snapshots of a droplet of a bidisperse mixture of LNPs (orange) and SNPs (green). The elapsed time since the start of evaporation is indicated below each snapshot. Only a half of each droplet is shown for clarity. The radius of the droplet is 1000σ, 550σ, 825σ, 990σ, and 100σ from left to right. All the droplets are scaled appropriately for better visualization. A "small-on-outside" structure is clear in the final snapshot.

we still adopt Eq. (7.8) for the particle-interface interaction [116]. We set the contact angle $\theta = 0$ for both LNPs and SNPs. The evaporation process is mimicked by decreasing the radius of the droplet at a constant speed, v_e. The instantaneous radius of the droplet at time t since the start of the evaporation is thus $H(t) = H(0) - v_e t$ and the minimum of the potential barrier is at $H(t) - R$. The nanoparticle-nanoparticle interactions are given by the potential in Eq. (7.12) with $A_{\mathrm{nn}} = 39.48\epsilon$. All these interactions are rendered purely repulsive with cutoff 20.574σ, 13.086σ, and 5.596σ for the LNP-LNP, LNP-SNP, and SNP-SNP pairs, respectively. A Langevin thermostat is used to maintain the temperature of the system at $T = 1.0\epsilon/k_B$. To conserve the Stokes-Einstein relation, the damping time is set to be 16τ for LNPs and 1τ for SNPs according to Eq. (7.7). During evaporation, the radius of the droplet is reduced to 100σ during 50000τ. The receding speed of the interface is $v_e = 1.8 \times 10^{-2}\sigma/\tau$.

Prior to drying, the nanoparticles are uniformly distributed in the droplet. During evaporation, the nanoparticles are enriched near the liquid-vapor interface. Because of the similar physical mechanism leading to "small-on-top" stratification in drying films of bidisperse particles, the SNPs form a concentrated shell near the interface while the LNPs are pushed out of this region and into the interior of the droplet via diffusiophoresis [24, 29]. In the final

state, a "small-on-outside" cluster is clearly observed as shown in Fig. 7.2. The simple model discussed here thus points to the possibility of creating core-shell clusters of particles using suspension droplets that undergo fast drying. Real spray drying processes are of course more complicated with many factors that are not captured by our simple model, such as air invasion, cracking, and buckling [147, 148]. Despite these limitations, our results indicate that increasing drying rates may lead to new strategies of controlling the structure of the resulting clusters or creating new structures that are otherwise difficult to produce.

7.3.3 Drying of solution droplets of a polymer blend

The moving interface method can also be used to study the drying of droplets of polymer solutoins. Here we focus on a solution of a polymer blend, which is a symmetric mixture of polymer A and polymer B, with 2048 chains of each type. Each chain is linear and consists of 12 beads of mass m that are bonded by the FENE potential in Eq. (7.10) [122]. In addition to the bonded interaction, all the nonbonded pairs of beads interact via a LJ potential with a cutoff 3.0σ. To model an incompatible polymer blend, the strength of the interaction is set to be $\epsilon_{AA} = \epsilon_{BB} = \epsilon$ while the cross interaction is weaker with $\epsilon_{AB} = 0.7\epsilon$. The entire systems is kept at $T = 1.0\epsilon/k_{\mathrm{B}}$ via a Langevin thermostat with damping time $\Gamma = 10\tau$.

In the initial state prior to drying, all the polymers are uniformly dispersed in a sphere with radius 100σ, as shown in Fig. 7.3(a). All the polymer beads are confined in this sphere with a spherical potential barrier as described in Sec. 7.3.2 with $H(0) = 100\sigma$. During drying, the radius of the droplet is reduced to $H_f = 24\sigma$ at rate $v_e = 1.52 \times 10^{-2}\sigma/\tau$. The entire drying process thus lasts 5000τ.

Figures 7.3(b) and (c) show that the morphology of the dry polymeric particle depends on drying conditions and the polymer-interface interaction controlled by the contact angle θ

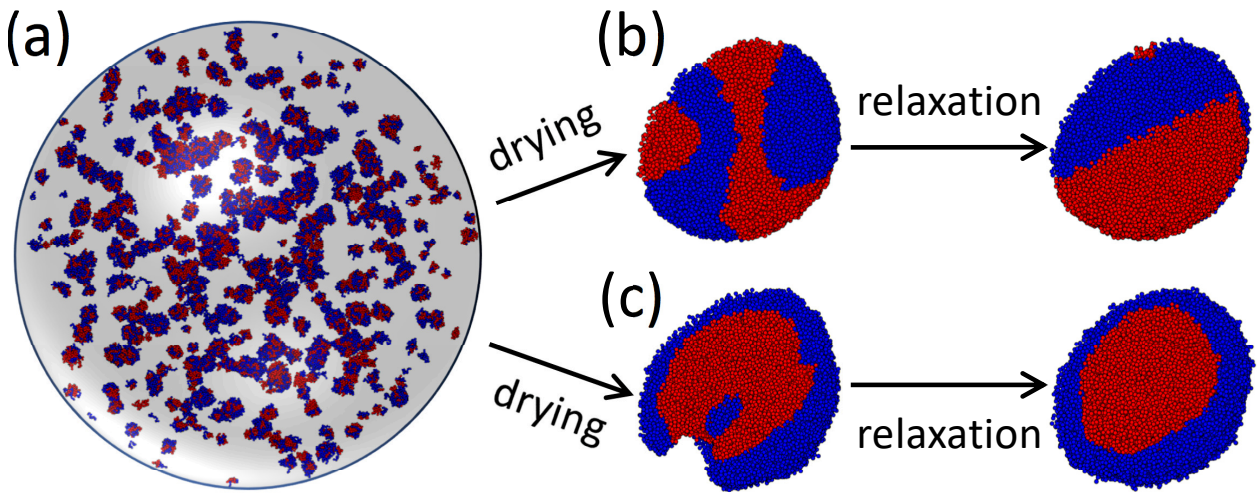

Figure 7.3: (a) Equilibrium solution droplet of a polymer blend prior to drying. Depending on the interaction with the receding liquid-vapor interface, polymeric particle with different morphologies are obtained after drying: (b) A Janus particle is produced with $\theta = 0$ for both polymer A (red) and B (blue) after drying for $5 \times 10^3\tau$ followed by a relaxation process for $5 \times 10^4\tau$; (c) A core-shell particle is produced with $\theta = 0$ for polymer A (red) and $\theta = \pi/2$ for polymer B (blue) after drying for $5 \times 10^3\tau$ followed by a relaxation process for $5 \times 10^4\tau$. For clarity, only a half of the particle is shown in (b) and (c).

in Eq. (7.8). In Fig. 7.3(b), $\theta = 0$ for both polymer A and B. The two polymers phase separate after fast drying as the cross attraction (A-B) is weaker than the self attraction (A-A or B-B) in the two components. Stripes of each component are clearly visible in the resulting polymeric particle. After relaxation, a Janus particle is produced with each component occupying half a sphere. In Fig. 7.3(c), $\theta = 0$ for polymer A while $\theta = \pi/2$ for polymer B, indicating that the liquid-vapor interface is repulsive for polymer A while there is an attraction between polymer B and the interface. Polymer B thus has a tendency to be adsorbed at the liquid-vapor interface. During fast drying, the B-type chains are enriched at the particle surface while all the A-type chains are pushed into the interior of the sphere though they have the same chain length. In the final particle with radius 24σ, a core-shell structure can be identified, but an island of polymer B in the domain of polymer A can also be seen. After relaxation, the island disappears and the phase separation is complete, leading to a polymeric particle with a well-define core-shell structure.

7.3.4 Drying of solution droplets of diblock copolymers

Block copolymers can also be employed to produce structured polymeric nanoparticles [149]. For a bulk system of block copolymers with incompatible blocks, there are well-known phase-separated structures such as lamellar, cylindrical, and spherical phases. In this section, we use a geometry almost identical to the one in Sec. 7.3.3 to study the drying of a solution droplet of diblock copolymer chains with monomers bonded by the FENE potential. We denote the chain length as N and vary N from 12 to 64. The number ratio between monomers in block A and those in block B is 1:1 in a diblock copolymer chain. The total number of monomers is fixed at 49152 and the number of chains is thus $49152/N$. For example, for $N = 12$, there are 4096 chains while for $N = 64$, the number of chains is 768. All the monomers interact with each other via a LJ potential as in Eq. (7.9). The cutoff of the monomer-monomer interaction is 3.0σ for nonbonded pairs. The interaction strength in the LJ potential is ϵ for A-A and B-B interactions and 0.7ϵ for A-B interactions. A Langevin thermostat with damping time $\Gamma = 10\tau$ is used to control the temperature of the system at $1.0\epsilon/k_{\mathrm{B}}$. In the initial state shown in Fig. 7.4(a), all the polymer chains are confined in a sphere with radius 100σ by a spherical potential barrier described by Eq. (7.8). During a drying period that lasts 5000τ, the radius of the droplet is shrunk to 24σ at a constant speed $v_e = 1.52 \times 10^{-2}\sigma/\tau$.

Similar to the case of droplets of a polymer blend, Fig. 7.4 shows that the structure of the resulting polymeric particle of diblock copolymers depends on the interaction between the two blocks and the liquid-vapor interface. This interaction is determined by the contact angle θ in Eq. (7.8). In Fig. 7.4(b), $\theta = 0$ for both blocks and the interface therefore appears neutral for all the monomers. After fast drying, stripes formed by each type of blocks are clearly visible because of the incompatibility of the blocks, resembling the lamellar phase in a bulk system of diblock copolymers. In Fig. 7.4(c), $\theta = 0$ for block A while $\theta = \pi/2$ for

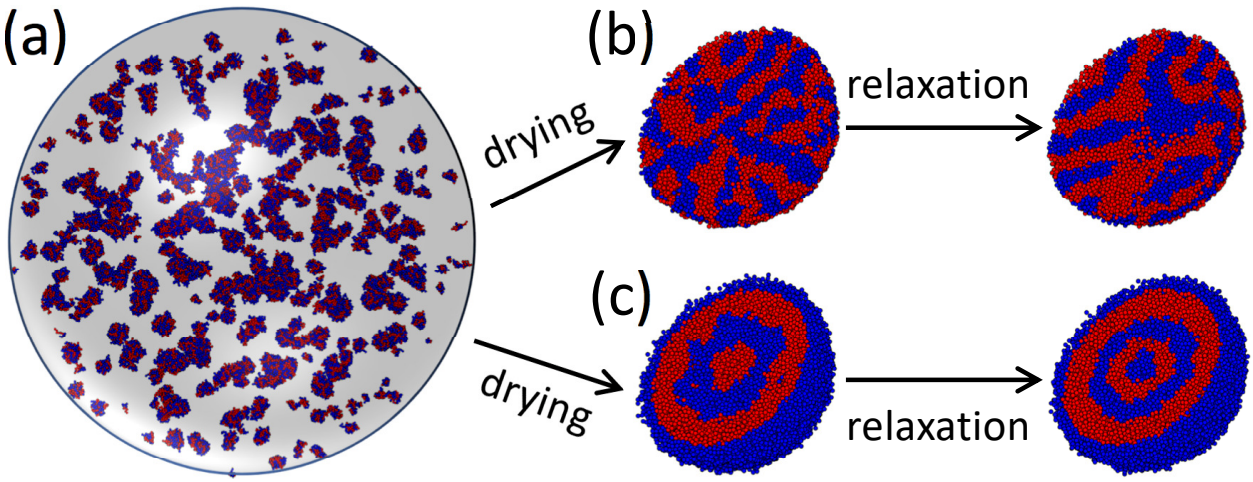

Figure 7.4: (a) Equilibrium solution droplet of a diblock copolymer with $N = 12$ prior to drying. Depending on the interaction with the receding liquid-vapor interface, polymeric particle with different morphologies are obtained after drying: (b) A patchy particle is produced with $\theta = 0$ for both block A (red) and B (blue) after drying for $5 \times 10^3\tau$ followed by a relaxation process for $5 \times 10^4\tau$; (c) An onion-like particle is produced with $\theta = 0$ for block A (red) and $\theta = \pi/2$ for block B (blue) after drying for $5\times10^3\tau$ followed by a relaxation process for $5 \times 10^4\tau$. For clarity, only a half of the particle is shown in (b) and (c).

block B. As a result, monomers in B blocks have a tendency to be adsorbed at the liquid-vapor interface while A blocks are repelled by the interface. After drying, an onion-like morphology emerges with a layer of B-type blocks at the surface of the particle, followed by alternating layers of A blocks and B blocks. The onion structure is more prominent after relaxation with the interfaces between neighboring shells smoothed. It is also interesting to notice that before relaxation, the domain at the particle's center is formed by A blocks while after relaxation, B blocks occupy the central domain. This transition indicates that the equilibrium morphology of a polymeric particle formed by incompatible diblock copolymers is determined by the delicate competition between the block lengths and the particle radius. This relationship remains an interesting direction of future research.

Figure 7.5 shows the effect of chain length N on the particle morphology, while keeping the length ratio of two blocks as 1:1 for each chain. For all these systems, $\theta = 0$ for both block

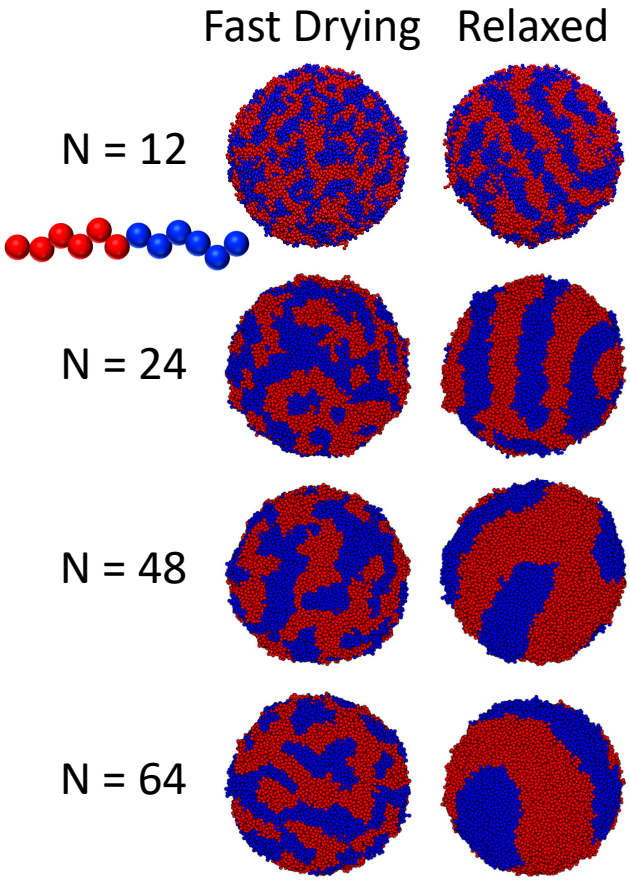

Figure 7.5: Effect of chain length N on particle morphology in drying droplets of diblock copolymers. For all the systems, $\theta = 0$ for both block A (red) and B (blue). The drying process lasts $5\times10^3\tau$, leading to particles in the left column. A relaxation process for $5\times10^4\tau$ yields particles in the right column.

A and B, indicating that the interface is neutral and repulsive for both components. After fast drying, phase separation occurs, resulting in patchy polymeric articles. After a following relaxation process in which the radius of the confining spherical potential is fixed, stripe-like domains are formed with each domain dominated by one-type of blocks. Each domain can be regarded as a patch. The number of patches is thus reduced in the relaxation process. Furthermore, the number of patches decreases as N is increased, as shown in Fig. 7.5. This can be understood by noticing that the domain are more coarse and the average size is larger when the block length is longer. For $N = 64$, the final polymeric nanoparticle after relaxation has a surface pattern similar to that of a baseball. Our results indicate that the chain length is a useful parameter to tune in order to control the surface pattern, including the number of patches, of a polymeric particle produced via drying a solution droplet of diblock copolymers.

Experimentally, the drying of solution droplets discussed above can be realized if a solution is broken into droplets that are suspended and dried in air. This process was realized in some experiments and industrial procedures such spray drying and superhearted steam drying [150, 151]. Another technique that can be used to produce polymeric particles or nanoparticle clusters from solution droplets is flash nanoprecipitation (FNP) invented by Johnson and Prud'homme [152, 153], in which a solute or a mixture of solutes (e.g., drug molecules, nanoparticles, polymers, etc.) is first dissolved in a solvent and then the solution is rapidly mixed with a non-solvent for the solute(s). In this process, the solution is broken into small droplets, which are dispersed in the non-solvent. As the solvent and non-solvent are miscible, the solvent is quickly extracted from the droplets, which shrink rapidly, and the solutes are compressed into particles or clusters by the surrounding non-solvent. This process is quite similar to the drying of a solution droplet. During drying, the solvent leaves the droplet via an evaporation process. In FNP, the solvent leaves the droplets via diffusion into

the non-solvent. In both cases, the surface of the droplet recedes, which is either a liquid-vapor interface or an interface between the droplet and the non-solvent. It is not surprising that polymeric particles with morphologies similar to those in Figs. 7.3 and 7.4 can also be produced using FNP [149]. The moving interface method discussed in this chapter can thus be applied to droplets undergoing FNP and to explore issues such as how the mixing rate of the solvent and non-solvent affects the structure of the resulting particles.

7.4 Conclusions

In this chapter, we review the method of modeling particle suspensions, polymer solutions, and their mixtures using an implicit solvent with the liquid-vapor interface mimicked by a potential barrier confining all the solutes (referring generally to molecular solutes including polymers as well as dispersed materials such as nanoparticles and colloids, or their mixtures) in the solvent. Their drying process can be studied with the moving interface method, in which the location of the liquid-vapor interface, i.e., the location of the confining potential barrier's minimum, is moved in a prescribed manner. The evaporation rate can be tuned by varying the speed at which the interface is moved. Various evaporation patterns, including drying films and droplets, can be realized with an appropriate choice of the way in which the interface (i.e, the equipotential surface of the confining potential) is moved. For example, the interface is flat and is translated along its normal direction when a film is dried while it is spherical and is shrunk radially for a drying droplet.

With the moving interface method, we have studied the drying of a hybrid solution of polymers and nanoparticles, a suspension droplet of a bidisperse mixture of nanoparticles, a solution droplet of a polymer blend, and a solution droplet of diblock copolymers. A rich set of structures are formed after drying, including stratified films, core-shell clusters (i.e.,

radially stratified clusters) of nanoparticles, Janus polymeric particles, core-shell particles, onion-like particles, and patchy particles. These structures are consistent with those observed previously in explicit solvent simulations and experiments, indicating that the moving interface method with an implicit solvent model can be used in certain situations to yield realistic results. Since the solvent is not treated explicitly, such method has the advantage of reducing the number of particles needed to describe a physical system and thus allows the modeling of very larger systems over longer time scales and at slow evaporation rates that may be directly comparable with typical experimental conditions.

Caution needs to be taken where the moving interface method can be applied. In this method, the solvent is treated as a uniform, viscous, isothermal, and isobaric medium. Therefore, there is no solvent flow. For drying films, spherical droplets, and cylindrical droplets, this condition can be satisfied and the systems can be modeled with the moving interface method. However, for systems in which the solvent develops flow patterns during drying, the moving interface method cannot be directly employed. One example is the drying of a sessile droplet on a substrate, in which a capillary flow emerges during evaporation, transporting solutes to the edge of the droplet, and leads to the famous coffee-ring effect if the peripheral of the droplet is pinned. Since the capillary flow is not captured by an implicit solvent model, it is impossible to produce the coffee-ring deposits with the simplest moving interface method. However, in these situations the moving interface method can be combined with other techniques such as lattice-Boltzmann method that is able to describe a flow field to study the drying process. Despite this limitation, there are still many scenarios in which the flow field of the solvent is not an dominant factor and the moving interface method can be useful because of its computational efficiency.

Chapter 8

Summary

Drying a multicomponent soft matter solution into a stratified film may lead to a facile, efficient technique of fabricating multilayered, multifunctional materials [126]. In this thesis, we used molecular dynamics (MD) simulations to investigate the drying process of a suspension of a bidisperse mixture of nanoparticles. With an explicit solvent model, we demonstrated that stratification occurs in a fast drying suspension (Chapter 2) and the outcome of stratification can be controlled with a thermal gradient imposed on the suspension and the induced thermophoresis (Chapter 3). In order to study larger systems over longer times, we then explored implicit solvent models of particle suspensions in which the particles are suspended in a uniform viscous background. A potential is used to represent the liquid-vapor interface and confine all the particles in the suspension. Evaporation can then be modeled by moving the location of the confining potential. In Chapter 4 and Chapter 5, we clarified the physical foundation of mapping a liquid-vapor interface into a confining potential. Then in Chapter 6 we used this method to map an explicit solvent system of a bidisperse nanoparticle suspension into an implicit solvent system. The comparison showed that similar stratification behavior was observed in both models. Finally, in Chapter 7 we applied the implicit solvent

model to study the drying of various soft matter solutions ranging from a suspension film of a mixture of nanoparticles and polymers to a solution droplet of diblock copolymers.

Because of the limitation of computational resources, MD simulations we have performed are limited to systems of a few million particles and time scales up to a few hundred nanoseconds. With the explicit solvent models, only a few hundred nanoparticles can be included in a system while with the implicit solvent models, more nanoparticles can be simulated. As a result, only ultra fast evaporation rates can be studied at present with the MD methods when the solvent is treated explicitly. The receding speed of the liquid-vapor interface during evaporation, v_e, is larger than about 10^{-3} m/s and 3 to 4 orders of magnitudes higher than a typical experimental value ($\sim 10^{-6}$ m/s). In the MD approach, the temperature of an equilibrium suspension before evaporation is about 70 $\sim$ 90% of the critical temperature of the solvent. For an aqueous solution, this indicates that the temperature range studied here is roughly from about 450 K to about 600 K. In order to model the drying of soft matter solutions at lower temperatures and slower evaporation rates, alternative approaches, typically more coarse-grained models, have to be adopted. Some examples include phase field models [154], Lattice Boltzmann methods [155], and Monte Carlo simulations [156].

MD simulations based on an implicit solvent model can be used to alleviate some of the limitations faced by the explicit solvent models. The implicit solvent models can be used for larger systems, longer times, slower drying rates, and lower temperatures. However, these models have their own issues. For example, hydrodynamic interactions may not be captured [86]. Evaporation-induced gradients and flows in a drying solution are not included as well [32]. As a result, the implicit solvent models can only be used for the drying of soft matter solutions with certain geometries including a planar film, a suspended spherical droplet, and a circular cylinder. For example, the models in their current forms cannot be used for the drying of sessile droplets where capillary flow induced by solvent evaporation can lead

to the formation of coffee rings [143]. The current implicit solvent models cannot capture various instabilities (e.g., Rayleigh-Bernard and Benard-Marangoni instabilities [157, 158]) that might emerge in drying solutions.

The drying of soft matter solutions is an emerging field in soft matter physics. Many problems are still open and many interesting systems and methods are under investigation. The methods and results presented in this thesis are focused on the stratification phenomenon in a drying suspension film containing a bidisperse mixture of nanoparticles. We hope this work will motivate more research on the drying of suspensions with other shapes, larger particles, aspherical particles, other types of solutes and suspended materials or their mixtures, a mixture of solvents, and other features that are not imagined at the moment.

Appendices

Appendix A

Additional results for Chapter 2

1920-SNP Systems: Figure A.1 shows snapshots of $\phi_{0.011}R_{30}$ and $\phi_{0.011}R_5$ with $N_s = 1920$ at various times during evaporation. The corresponding density profiles are shown in Fig. A.2. For these two systems, the initial volume fraction of the smaller nanoparticles (SNPs) is $\phi_s = 0.011 \simeq \phi_l/6$. During solvent evaporation, a skin layer of SNPs forms in both systems but is denser in $\phi_{0.011}R_{30}$, which has a higher evaporation rate. The accumulation of larger nanoparticles (LNPs) below the skin layer of SNPs is obvious for both systems and more significant for $\phi_{0.011}R_{30}$. Fig. A.3 shows the average positions of LNPs and SNPs ($\langle z_l \rangle$ and $\langle z_s \rangle$) and their mean separation ($\langle z_l \rangle - \langle z_s \rangle$) against $(H - H(t))/H$, where $H(t)$ is the film thickness at time t and $H \equiv H(0)$ is the equilibrium film thickness prior to evaporation. The quantity $(H - H(t))/H$ defines the extent of drying. The mean separation, $\langle z_l \rangle - \langle z_s \rangle$, characterizes the state of stratification with $\langle z_l \rangle - \langle z_s \rangle > 0$ signals "large-on-top" while $\langle z_l \rangle - \langle z_s \rangle < 0$ indicates "small-on-top". From Fig. A.3, it is clear that both $\phi_{0.011}R_{30}$ and $\phi_{0.011}R_5$ show the "large-on-top" stratification. This classification is consistent with the density profiles of nanoparticles shown in Fig. A.2, where the density profile of LNPs exhibits a positive gradient approaching the interfacial region. Though there is a surface

accumulation of SNPs, the density profile of SNPs shows a negative gradient in the central region of the film.

6400-SNP Systems: Figure A.4 shows snapshots of $\phi_{0.034}R_{30}$, $\phi_{0.034}R_5$, $\phi_{0.034}R_1$ with $N_s = 6400$ at various times during evaporation. The corresponding density profiles are shown in Fig. A.5 and the average positions of NPs and their mean separation are shown in Fig. A.6. All these 3 systems behave qualitatively similar as the 2 systems with $N_s = 1920$. This is expected as for the 3 systems, $\phi_s = 0.034$, which is still only about 1/2 of ϕ_l. Based on the density profiles and the order parameters, we classify these 3 systems as "large-on-top" as well.

12800-SNP Systems: Figure A.7 shows snapshots of $\phi_{0.068}R_{30}$, $\phi_{0.068}R_5$, and $\phi_{0.068}R_1$ with $N_s = 12800$ at various times during evaporation. The corresponding density profiles are shown in Fig. A.8 and the average positions of NPs and their mean separation are shown in Fig. A.9. For these systems, $\phi_s = \phi_l = 0.068$. The systems $\phi_{0.068}R_{30}$ and $\phi_{0.068}R_5$ behave similarly as the systems with $N_s = 1920$ and 6400 and show the "large-on-top" stratification. However, the thickness of the interfacial region, in which the SNPs are accumulated and form a skin layer, becomes wider than those in the systems with $N_s = 1920$ and 6400. Furthermore, the positive gradient of the density profile of LNPs below this skin layer of SNPs is smaller for $\phi_{0.068}R_{30}$ and $\phi_{0.068}R_5$ than for the systems with $N_s = 1920$ ($\phi_{0.011}R_{30}$ and $\phi_{0.011}R_5$) and $N_s = 6400$ ($\phi_{0.034}R_{30}$ and $\phi_{0.034}R_5$) at the same evaporation rate (i.e., the same ζ as in the subscript of R in the system label). For $\phi_{0.068}R_1$, the density profiles of LNPs and SNPs are almost flat, except for the slight density peak of SNPs at the interface which exists even in equilibrium. We classify this system as "uniform". This classification is corroborated by the order parameter shown in Fig. A.9(c) for $\phi_{0.068}R_1$, which oscillates around 0.

In general at the same evaporation rate, the surface accumulation of SNPs becomes more significant and the accumulation of LNPs below the skin layer of SNPs becomes less significant

when ϕ_s is increased. Eventually, the system is driven into the "small-on-top" regime when $\phi_s > c/\mathrm{Pe}_s$, where $c \sim 1$ and Pe_s is the Péclet number of SNPs. This transition is observed for the systems with $N_s = 19200$ ($\phi_{0.10}R_{30}$, $\phi_{0.10}R_5$, and $\phi_{0.10}R_1$), which are discussed in detail in the main text.

25600-SNP and 32000-SNP Systems: Figure A.10 shows snapshots of $\phi_{0.13}R_{30}$ and $\phi_{0.13}R_5$ with $N_s = 25600$ at various times during evaporation. The corresponding density profiles are shown in Fig. A.11 and the average positions of nanoparticles and their mean separation are shown in Fig. A.12. For $\phi_{0.13}R_{30}$, the order parameter $\langle z_l \rangle - \langle z_s \rangle$ first has a small positive value and then becomes negative. As shown in Figs. A.11(b), the density profiles of LNPs at early times have a small positive gradient, indicating that the LNPs accumulate slightly below the surface layer of SNPs. At late times, the density profiles of LNPs are almost flat. Figs. A.11(c) shows that when the interfacial region is approached, a positive gradient develops during evaporation for the density of SNPs. Combining the density profiles of LNPs and SNPs and the results on the order parameter, we classify $\phi_{0.13}R_{30}$ as "small-on-top". For $\phi_{0.13}R_5$, the density profiles of LNPs and SNPs during evaporation are almost always flat. We classify $\phi_{0.13}R_5$ as "uniform", though its order parameter has a small positive value.

Figure A.13 shows snapshots of $\phi_{0.16}R_{30}$ and $\phi_{0.16}R_5$ with $N_s = 32000$ at various times during evaporation. The corresponding density profiles are shown in Fig. A.14 and the average positions of nanoparticles and their mean separation are shown in Fig. A.15. These 2 systems behave similarly as the 2 systems with $N_s = 25600$. We classify $\phi_{0.16}R_{30}$ as "small-on-top" and $\phi_{0.16}R_5$ as "uniform", though the oder parameter in the latter system has a small negative value.

For the systems with $N_s = 25600$ and 32000, some (~ 500) SNPs move into the vapor during solvent evaporation. This undesirable behavior prevented us from running systems

with more SNPs. Exploring the regime with high volume fractions of SNPs remains an interesting direction for the future.

Temperature Profiles during Evaporation: The gradient of the solvent density is induced by a temperature gradient in the solvent, which is caused by the evaporative cooling at the interface. Examples of the temperature profiles are shown in Fig. A.16 for $\phi_{0.034}R_{30}$ at $t = 1 \times 10^5\tau$, for $\phi_{0.034}R_5$ at $t = 3 \times 10^5\tau$, and for $\phi_{0.034}R_1$ at $t = 4 \times 10^5\tau$, respectively. The trend is clear: the higher the evaporation rate, the stronger the evaporative cooling and the associated temperature gradient in the liquid solvent. It should also be pointed out that there is no pressure gradient along the z-direction in the evaporating suspensions studied here as mechanical equilibrium is established very quickly. Detailed discussion of temperature and pressure profiles in an evaporating liquid can also be found in Ref. [32].

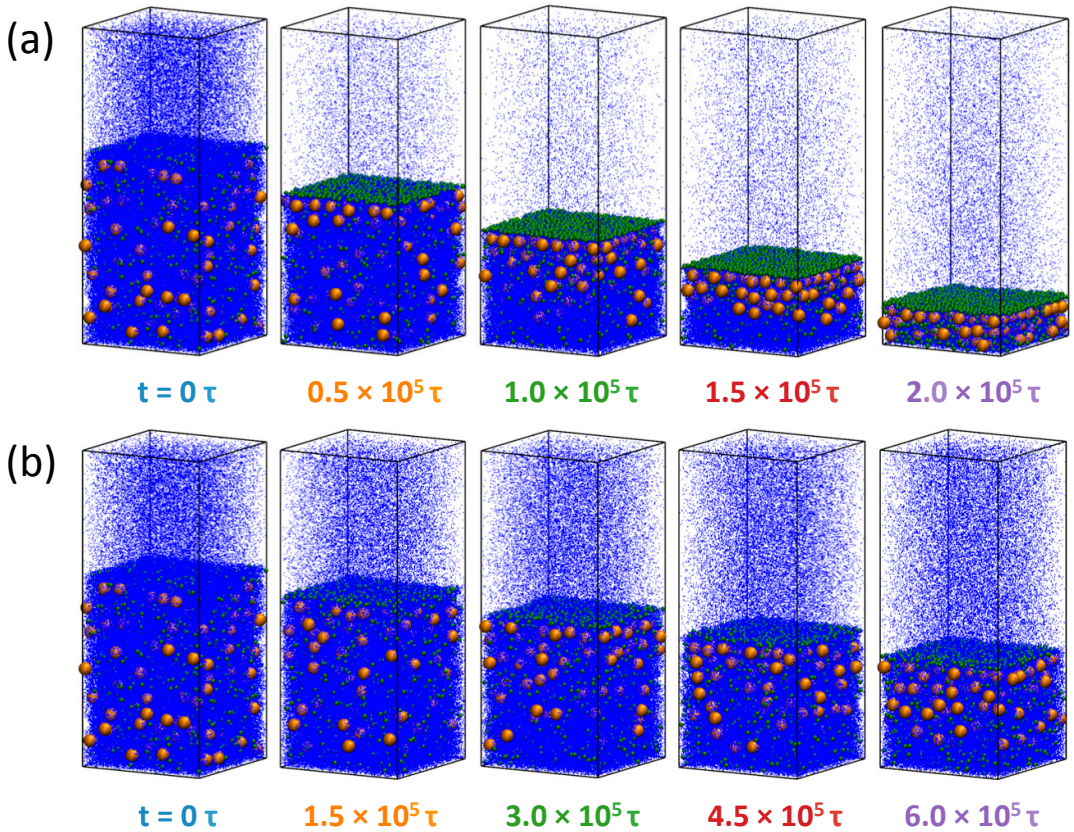

Figure A.1: Snapshots of (a) $\phi_{0.011}R_{30}$ and (b) $\phi_{0.011}R_5$ with $N_s = 1920$. Color code: LNPs (orange), SNPs (green), and solvent (blue). For clarity, only 5% of the solvent beads are visualized.

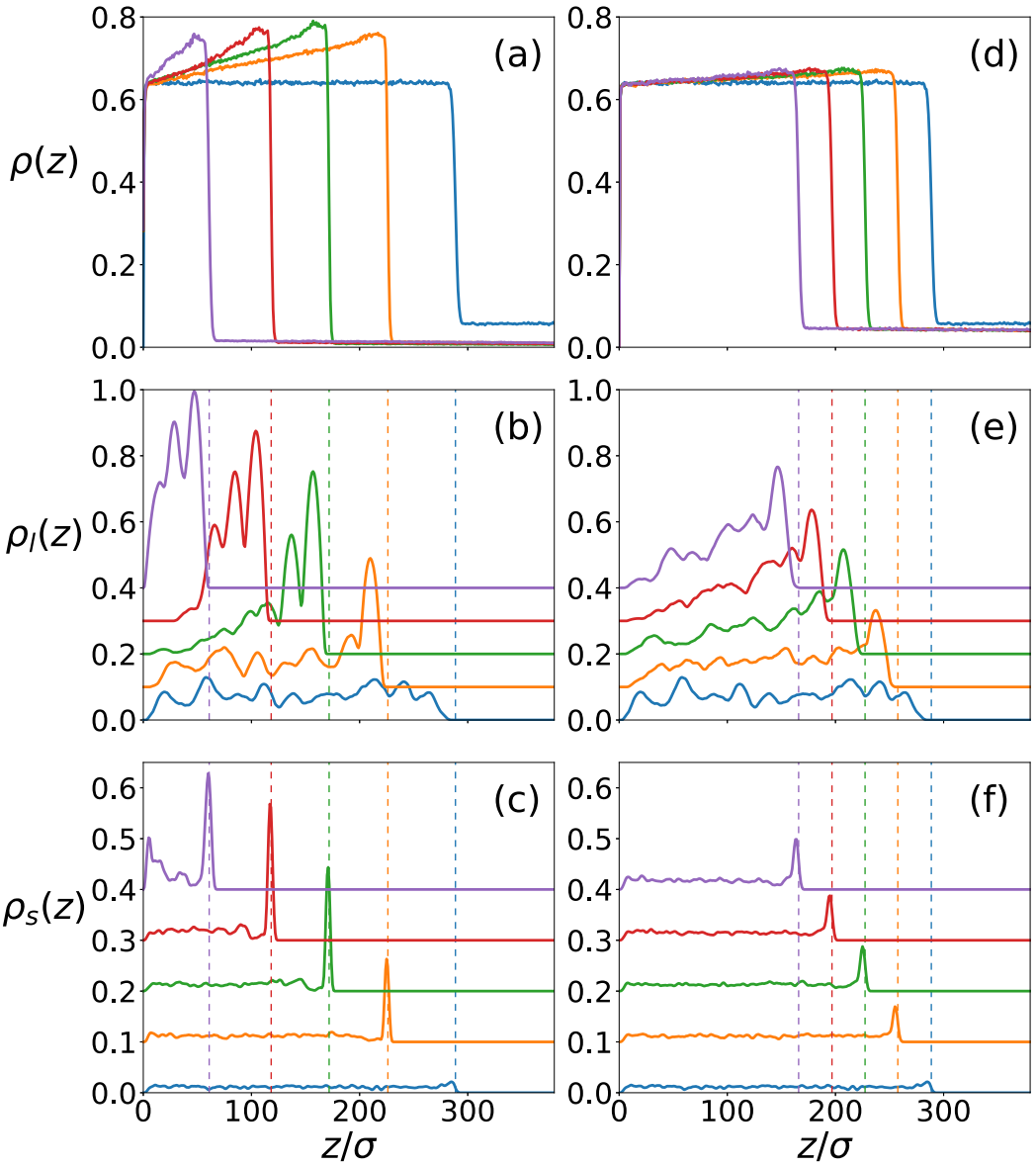

Figure A.2: Density profiles for $\phi_{0.011}R_{30}$ (left column) and $\phi_{0.011}R_5$ (right column): (a) and (d) solvent; (b) and (e) LNPs; (c) and (f) SNPs. The vertical dashed lines indicate the location of the liquid-vapor interface. For clarity, the density profiles for NPs are shifted upward successively by $0.1m/\sigma^3$.

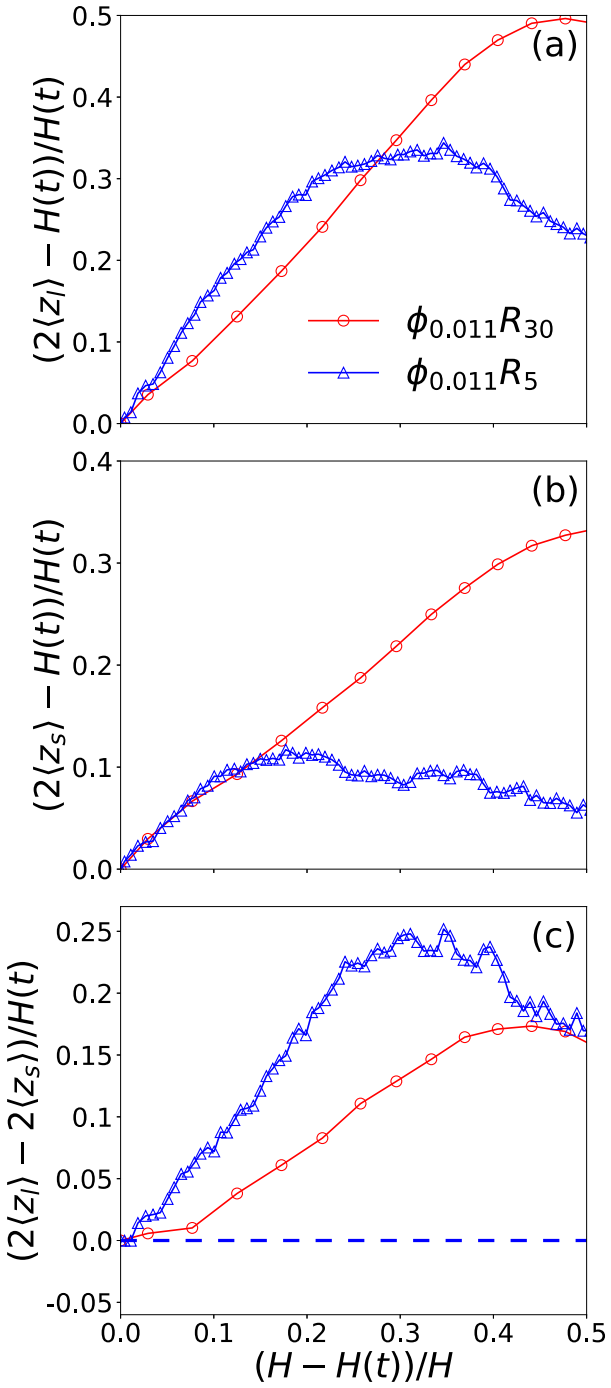

Figure A.3: Average position in the z direction relative to the center of the film, normalized by $H(t)/2$, is plotted against time $(H - H(t))/H$ for (a) LNPs and (b) SNPs. Panel (c) shows the average separation between LNPs and SNPs, normalized by $H(t)/2$, as a function of $(H - H(t))/H$. Data are for system $\phi_{0.011}R_{30}$ (red circles) and $\phi_{0.011}R_5$ (blue triangles).

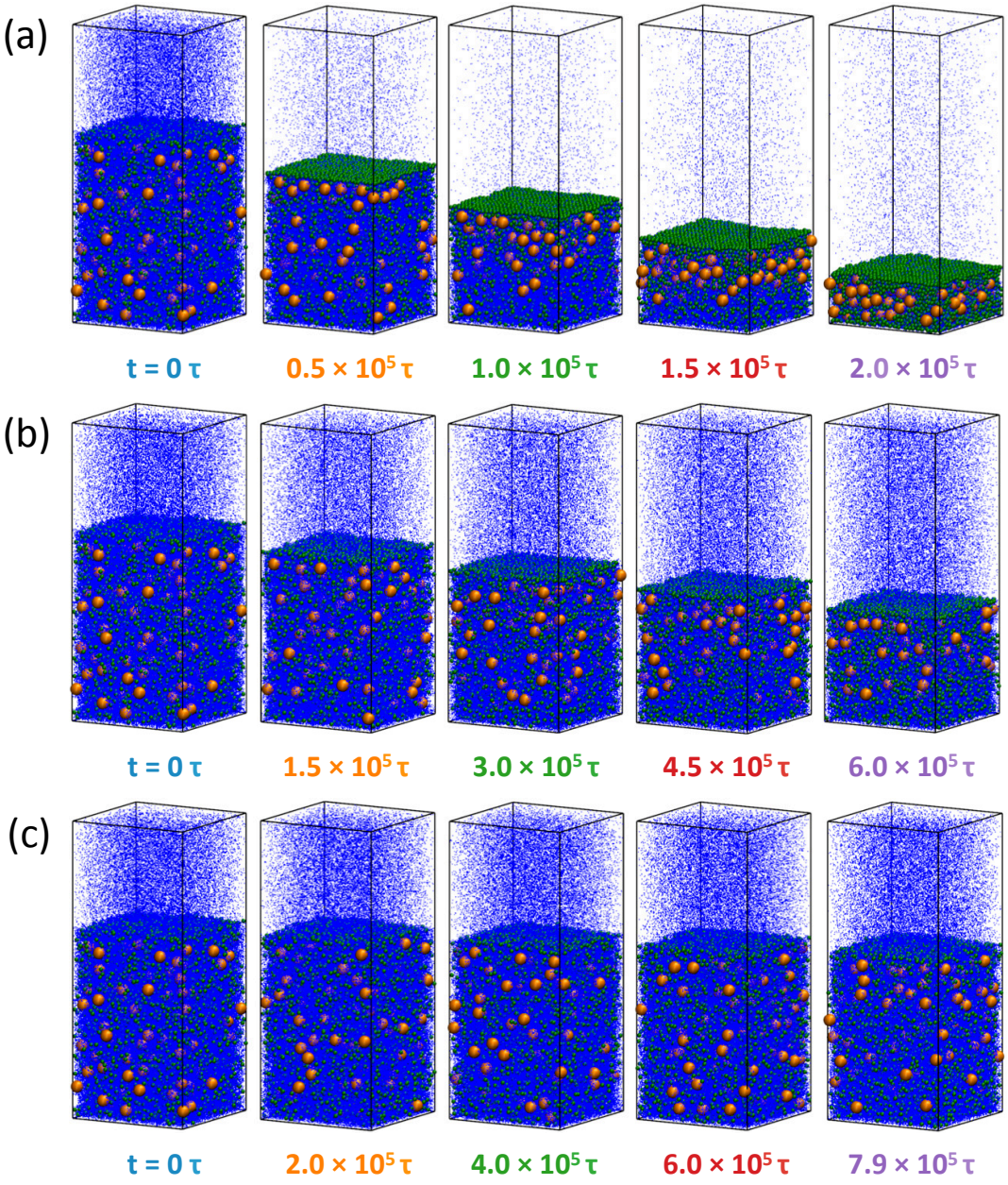

Figure A.4: Snapshots of (a) $\phi_{0.034}R_{30}$, (b) $\phi_{0.034}R_5$, and (c) $\phi_{0.034}R_1$ with $N_s = 6400$. Color code: LNPs (orange), SNPs (green), and solvent (blue). For clarity, only 5% of the solvent beads are visualized.

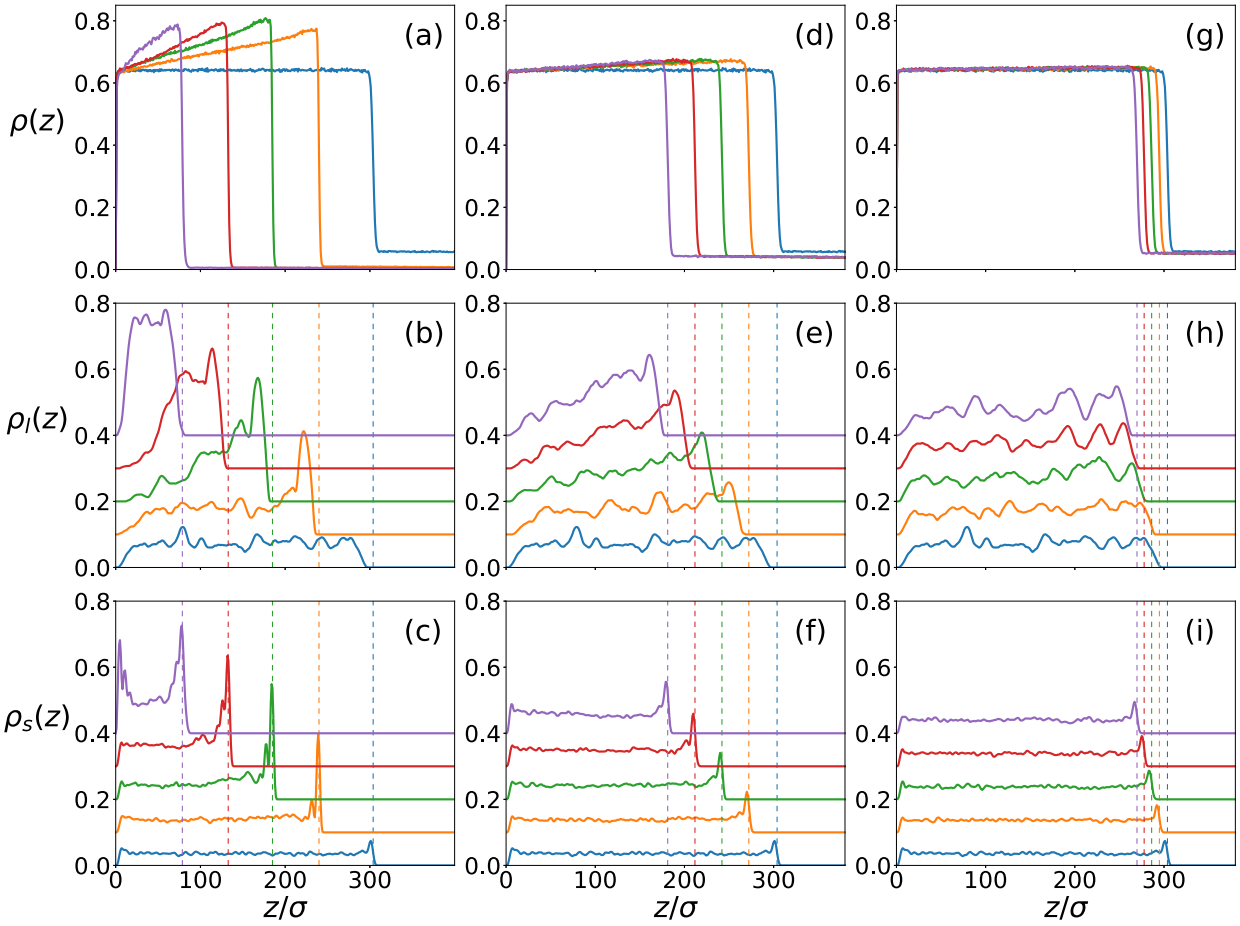

Figure A.5: Density profiles for $\phi_{0.034}R_{30}$ (left column), $\phi_{0.034}R_5$ (middle column), and $\phi_{0.034}R_1$ (right column): solvent (top row); LNPs (middle row); SNPs (bottom row). The vertical dashed lines indicate the location of the liquid-vapor interface. For clarity, the density profiles for nanoparticles are shifted upward successively by $0.1m/\sigma^3$.

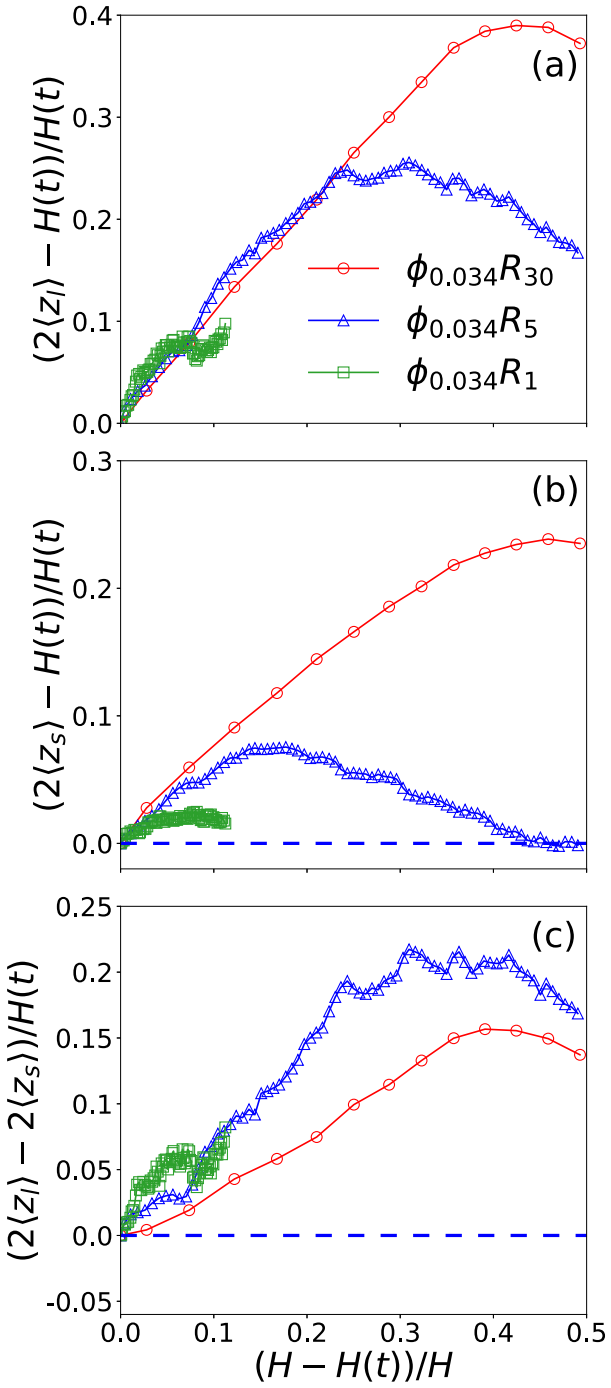

Figure A.6: Average position in the z direction relative to the center of the film, normalized by $H(t)/2$, is plotted against time $(H - H(t))/H$ for (a) LNPs and (b) SNPs. Panel (c) shows the average separation between LNPs and SNPs, normalized by $H(t)/2$, as a function of $(H - H(t))/H$. Data are for system $\phi_{0.034}R_{30}$ (red circles), $\phi_{0.034}R_5$ (blue triangles) and $\phi_{0.034}R_1$ (green squares).

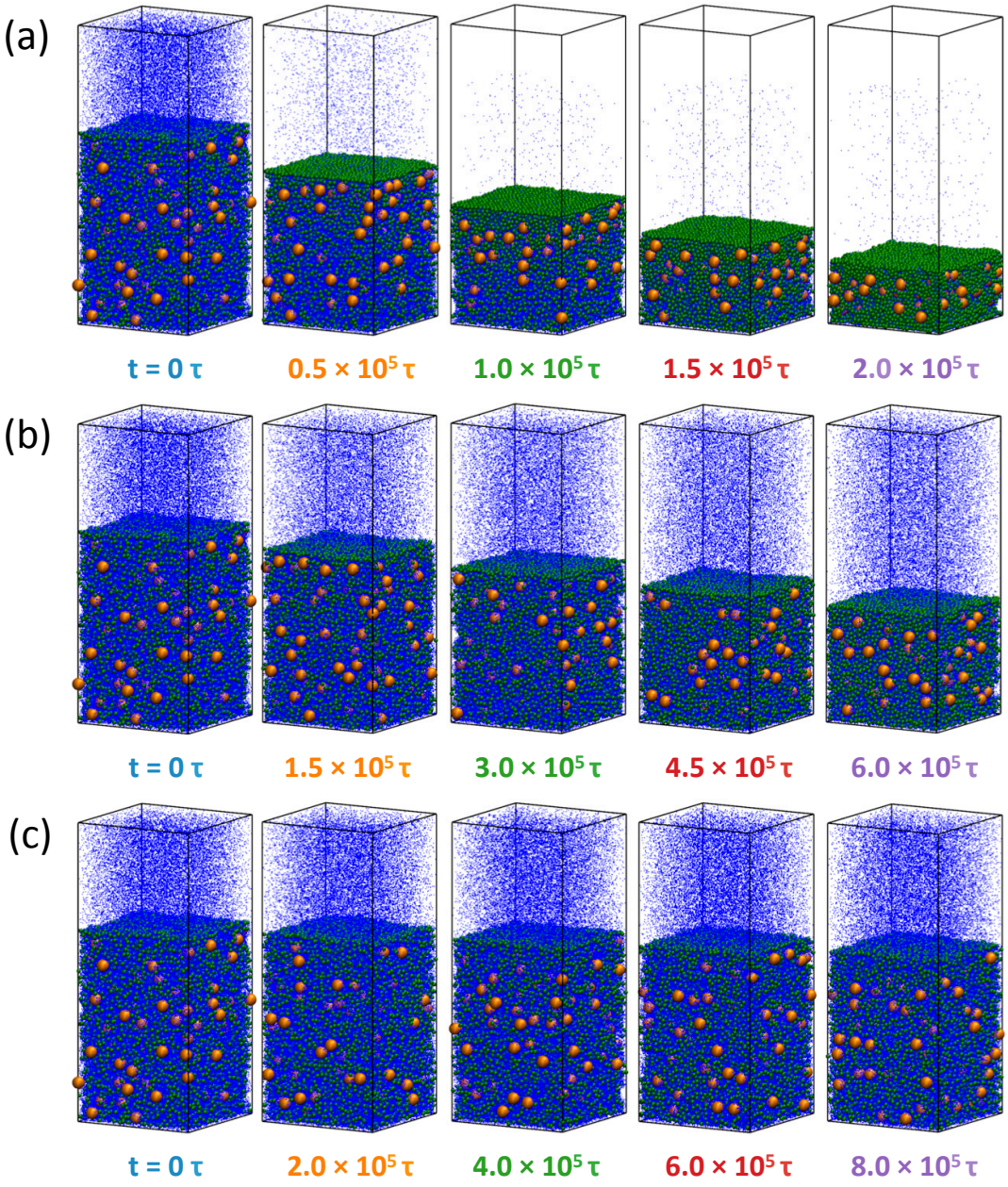

Figure A.7: Snapshots of (a) $\phi_{0.068}R_{30}$, (b) $\phi_{0.068}R_5$, and (c) $\phi_{0.068}R_1$ with $N_s = 12800$. Color code: LNPs (orange), SNPs (green), and solvent (blue). For clarity, only 5% of the solvent beads are visualized.

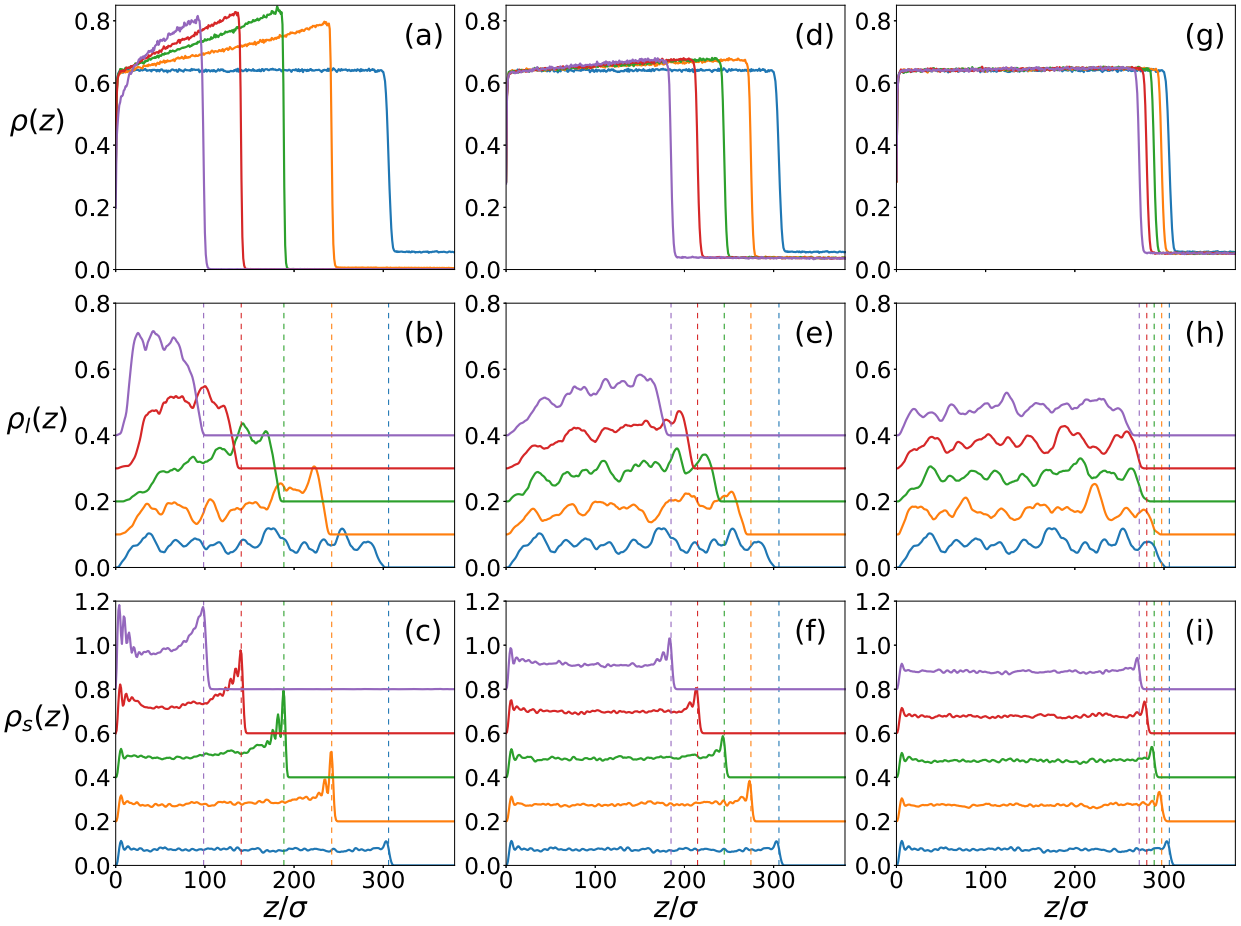

Figure A.8: Density profiles for $\phi_{0.068}R_{30}$ (left column), $\phi_{0.068}R_5$ (middle column), and $\phi_{0.068}R_1$ (right column): solvent (top row); LNPs (middle row); SNPs (bottom row). The vertical dashed lines indicate the location of the liquid-vapor interface. For clarity, the density profiles for LNPs (SNPs) are shifted upward successively by $0.1m/\sigma^3$ ($0.2m/\sigma^3$).

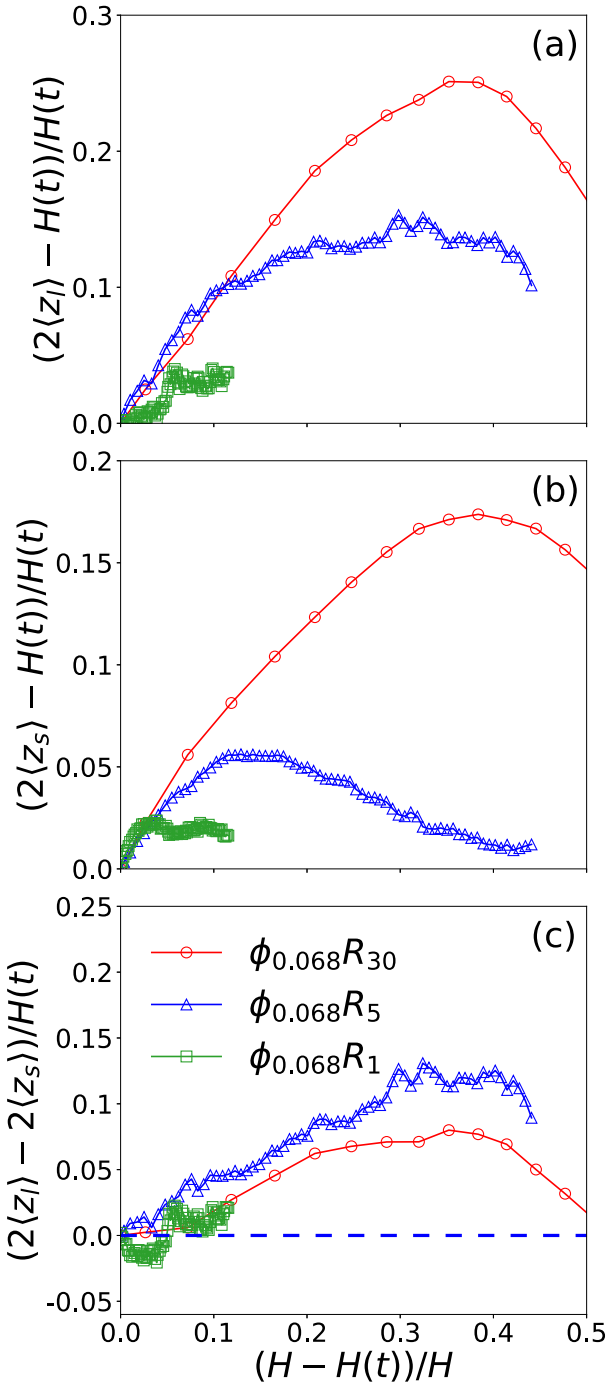

Figure A.9: Average position in the z direction relative to the center of the film, normalized by $H(t)/2$, is plotted against time $(H - H(t))/H$ for (a) LNPs and (b) SNPs. Panel (c) shows the average separation between LNPs and SNPs, normalized by $H(t)/2$, as a function of $(H - H(t))/H$. Data are for system $\phi_{0.068}R_{30}$ (red circles), $\phi_{0.068}R_5$ (blue triangles) and $\phi_{0.068}R_1$ (green squares).

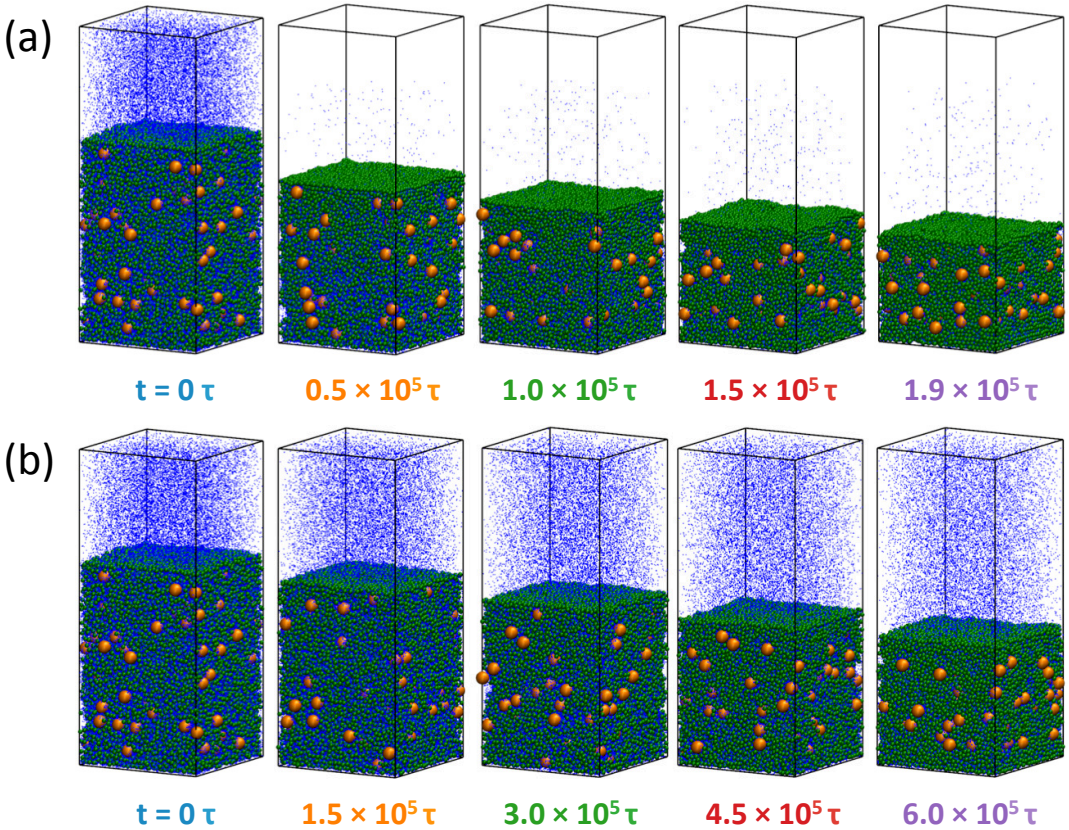

Figure A.10: Snapshots of (a) $\phi_{0.13}R_{30}$ and (b) $\phi_{0.13}R_5$ with $N_s = 25600$. Color code: LNPs (orange), SNPs (green), and solvent (blue). For clarity, only 5% of the solvent beads are visualized.

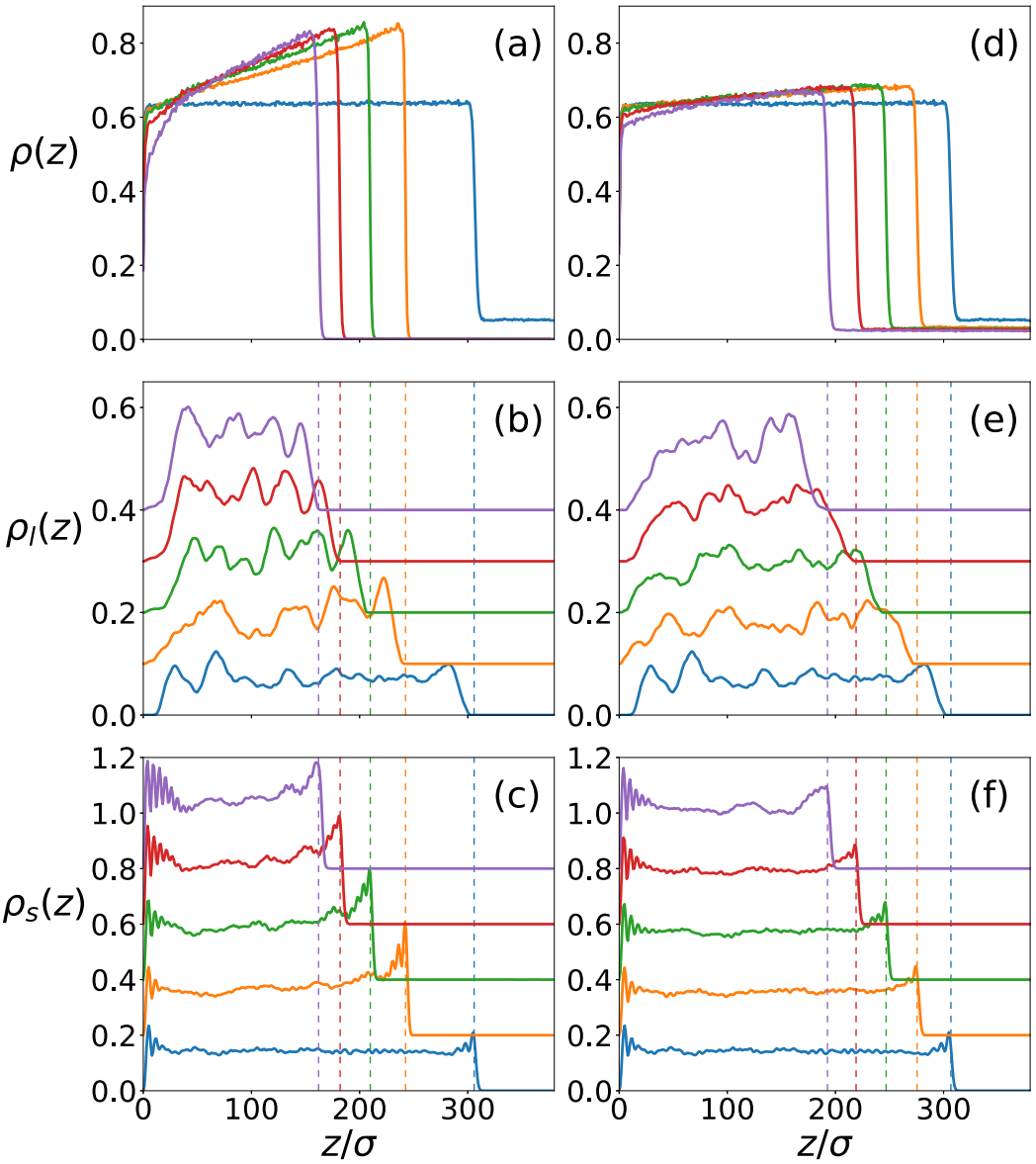

Figure A.11: Density profiles for $\phi_{0.13}R_{30}$ (left column) and $\phi_{0.13}R_5$ (right column): (a) and (d) solvent; (b) and (e) LNPs; (c) and (f) SNPs. The vertical dashed lines indicate the location of the liquid-vapor interface. For clarity, the density profiles for LNPs (SNPs) are shifted upward successively by $0.1m/\sigma^3$ ($0.2m/\sigma^3$).

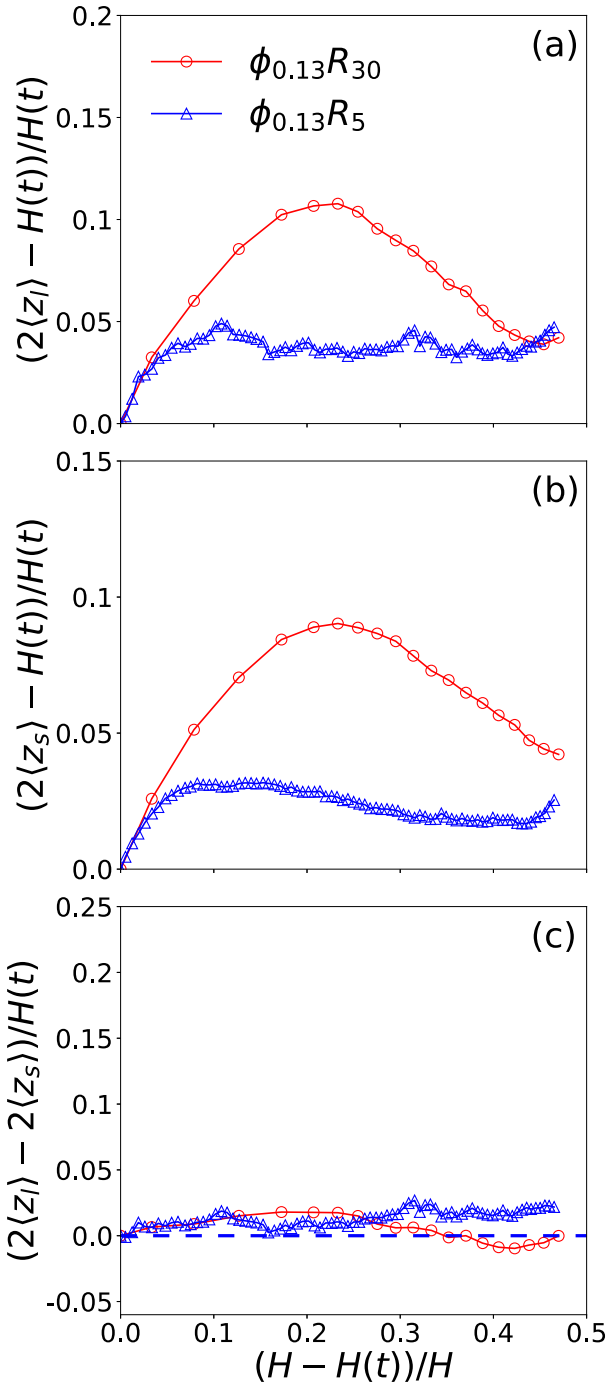

Figure A.12: Average position in the z direction relative to the center of the film, normalized by $H(t)/2$, is plotted against time $(H - H(t))/H$ for (a) LNPs and (b) SNPs. Panel (c) shows the average separation between LNPs and SNPs, normalized by $H(t)/2$, as a function of $(H - H(t))/H$. Data are for system $\phi_{0.13}R_{30}$ (red circles) and $\phi_{0.13}R_5$ (blue triangles).

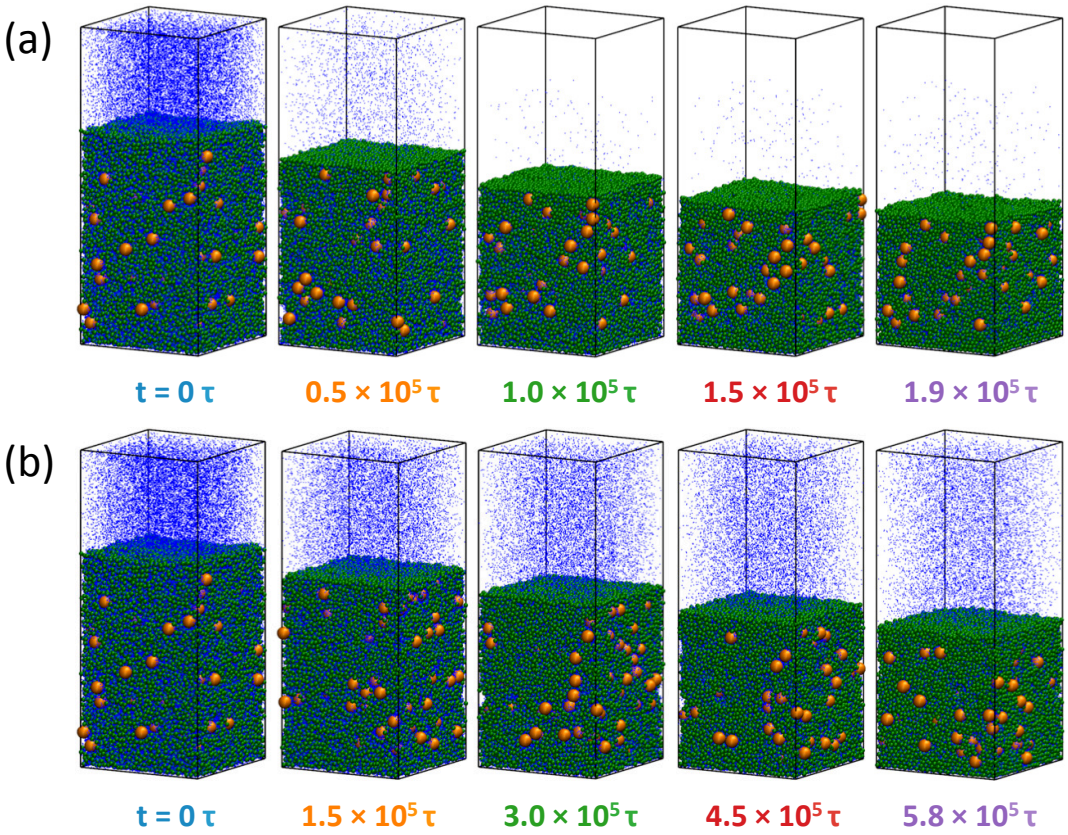

Figure A.13: Snapshots of (a) $\phi_{0.16}R_{30}$ and (b) $\phi_{0.16}R_5$ with $N_s = 32000$. Color code: LNPs (orange), SNPs (green), and solvent (blue). For clarity, only 5% of the solvent beads are visualized.

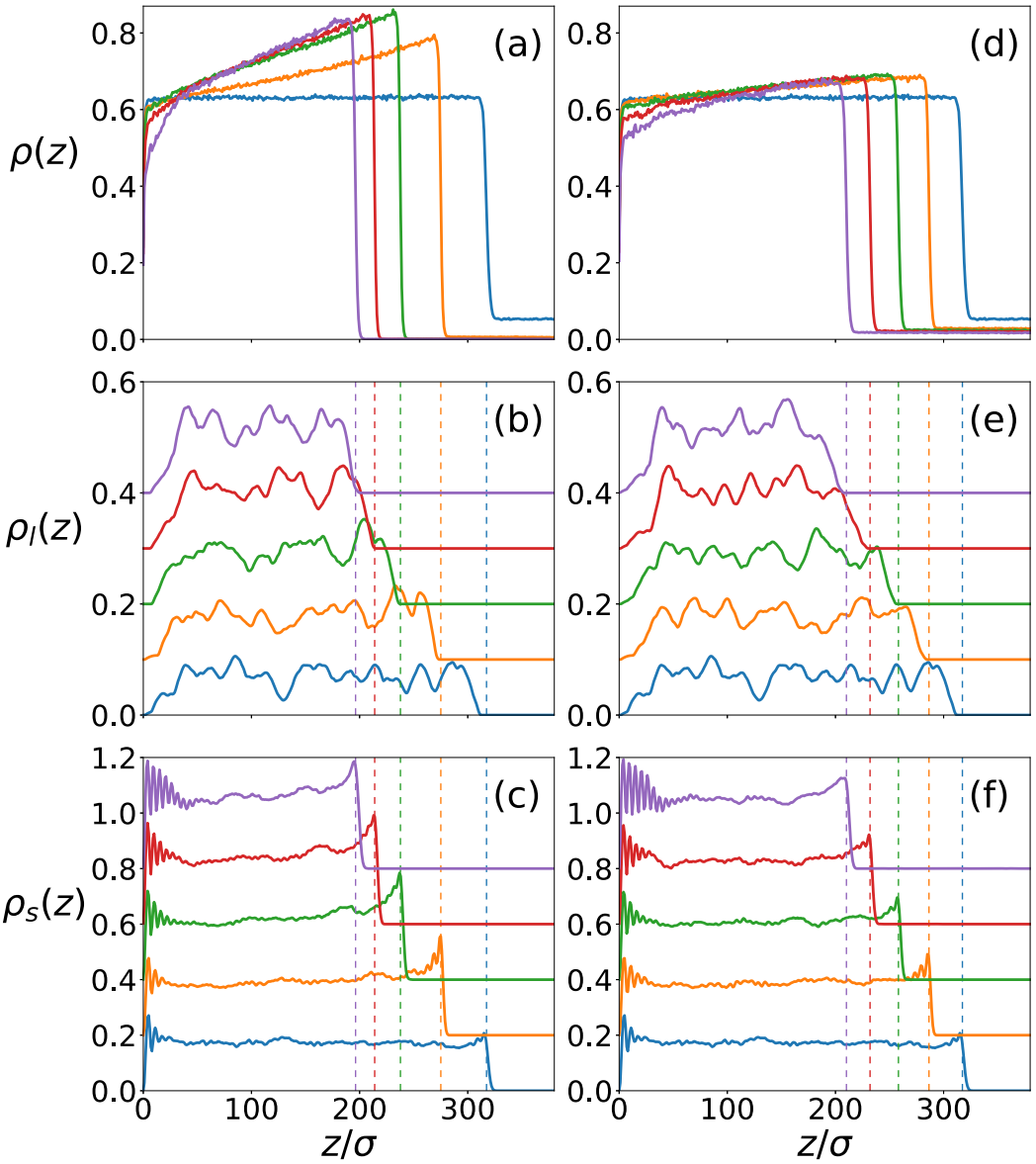

Figure A.14: Density profiles for $\phi_{0.16}R_{30}$ (left column) and $\phi_{0.16}R_5$ (right column): (a) and (d) solvent; (b) and (e) LNPs; (c) and (f) SNPs. The vertical dashed lines indicate the location of the liquid-vapor interface. For clarity, the density profiles for LNPs (SNPs) are shifted upward successively by $0.1m/\sigma^3$ ($0.2m/\sigma^3$).

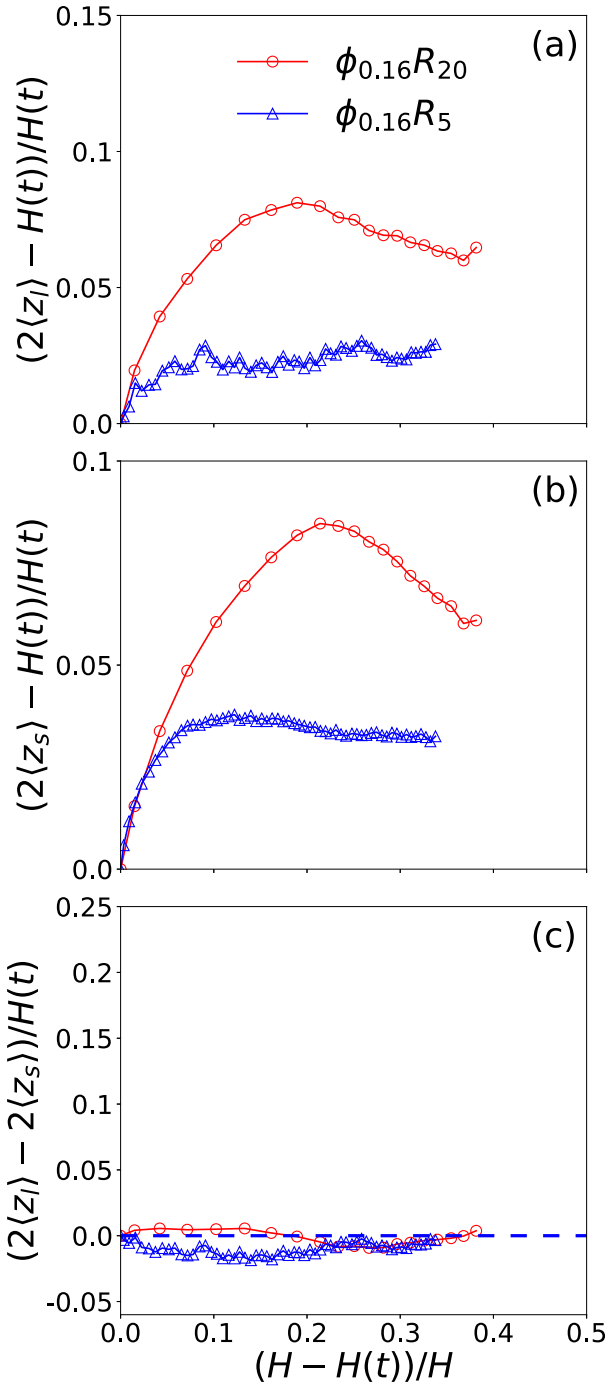

Figure A.15: Average position in the z direction relative to the center of the film, normalized by $H(t)/2$, is plotted against time $(H - H(t))/H$ for (a) LNPs and (b) SNPs. Panel (c) shows the average separation between LNPs and SNPs, normalized by $H(t)/2$, as a function of $(H - H(t))/H$. Data are for system $\phi_{0.16}R_{30}$ (red circles) and $\phi_{0.16}R_5$ (blue triangles).

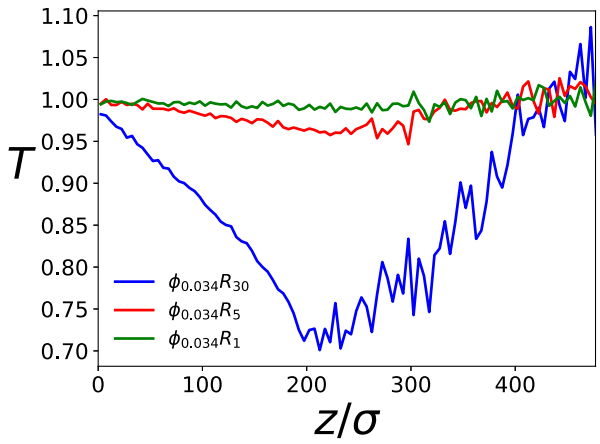

Figure A.16: The temperature profile along the z-direction at $t = 1 \times 10^5\tau$ for $\phi_{0.034}R_{30}$ (bottom blue line), $t = 3 \times 10^5\tau$ for $\phi_{0.034}R_5$ (middle red line), and $t = 4 \times 10^5\tau$ for $\phi_{0.034}R_1$ (top green line), respectively.

Appendix B

Thermophoresis of nanoparticles

To understand the thermophoresis of nanoparticles, we performed additional simulations for suspensions of only SNPs or only LNPs at volume fractions close to those in the suspension of the mixture of SNPs and LNPs. Each suspension was first equilibrated at $T = 1.0\epsilon/k_{\mathrm{B}}$. Then a thermal gradient was introduced into the system by thermalizing a top region of the liquid solvent and all the vapor at $T_H = 1.0\epsilon/k_{\mathrm{B}}$ while thermalizing a layer of the solvent adjacent to the bottom wall at T_L, as shown in Fig. B.1. Two values of T_L, $0.9\epsilon/k_{\mathrm{B}}$ and $0.7\epsilon/k_{\mathrm{B}}$, were used to generate a thermal gradient with different magnitudes in the direction perpendicular to the liquid-vapor interface. The average position of nanoparticles in each system was recorded as a function of time after the thermal gradient was imposed and the data are plotted in Fig. B.2. Since T_L is lower than the initial temperature of the equilibrium suspension, the liquid contracts and the liquid-vapor interface recedes when the thermal gradient is imposed. Our data show that for the nanoparticle-solvent interaction with $A_{ns} = 100\epsilon$, the SNPs first move toward the substrate because of the contraction of the liquid solvent. After this transient phase, the SNPs do not show any response to the imposed thermal gradient and their average position remains almost constant with time.

However, the LNPs show a clear thermophoretic response to the thermal gradient and drift toward the cooler region where the liquid density is higher. These independent simulations thus demonstrate that for the parameters used in this chapter, the LNPs exhibit strong thermophoresis while the SNPs exhibit none.

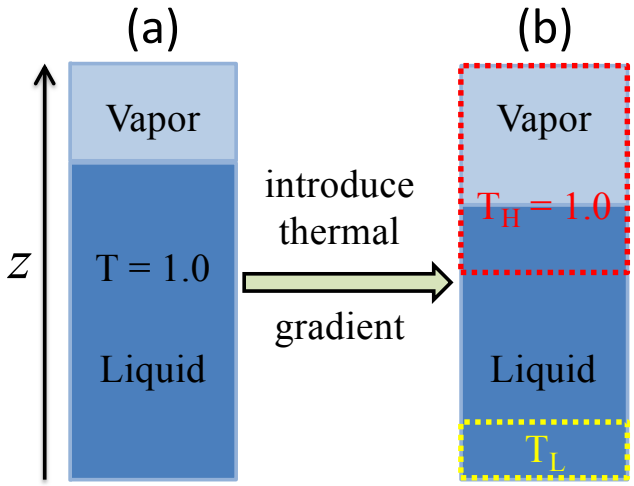

Figure B.1: The simulation set-up to study thermophoresis: (a) the entire solvent and vapor are thermalized at $T = 1.0\epsilon/k_{\mathrm{B}}$; (b) a top region of the liquid solvent and all the vapor are thermalized at $T_H = 1.0\epsilon/k_{\mathrm{B}}$ while a layer of the solvent adjacent to the bottom wall is thermalized at T_L. A positive thermal gradient is introduced into the system along the z-axis by using $T_L = T_H - 0.1\epsilon/k_{\mathrm{B}}$ or $T_L = T_H - 0.3\epsilon/k_{\mathrm{B}}$.

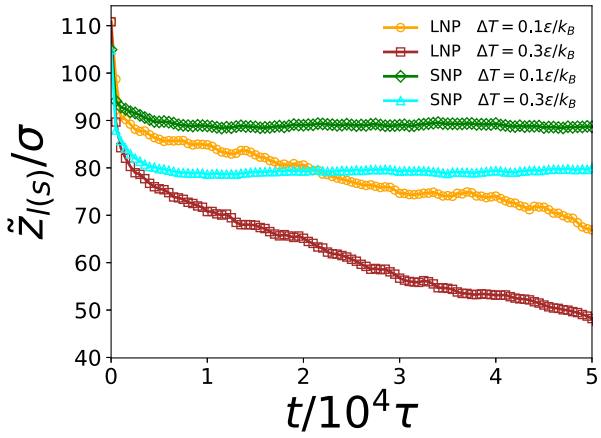

Figure B.2: Average positions of LNPs (orange circles and dark brown squares) and SNPs (green diamonds and cyan triangles) as a function of time after a positive thermal gradient along the z-axis is introduced into the system as described in Fig. B.1. The data are for $\Delta T \equiv T_H - T_L = 0.3\epsilon/k_{\mathrm{B}}$ (dark brown squares and cyan triangles) and $0.1\epsilon/k_{\mathrm{B}}$ (orange circles and green diamonds).

Appendix C

Diffusion coefficients of nanoparticles

The diffusion coefficients of the large nanoparticles (LNPs) and small nanoparticles (SNPs) were determined by an independent simulation. A suspension of LNPs and SNPs with the same volume fractions as in the initial suspension discussed in the main text, but without the vapor phase of the solvent, was prepared. The suspension has a cubic shape with edge length 101.3σ. Periodic boundary conditions were used in all three directions. The mean square displacements of both LNPs and SNPs as a function of time are shown in Fig. C.1. The data show a clear transition from ballistic regime at short times to diffusive regime at long times. The diffusion coefficients are $D_l = 1.76 \times 10^{-3}\sigma^2/\tau$ for LNPs and $D_s = 1.55 \times 10^{-2}\sigma^2/\tau$ for SNPs.

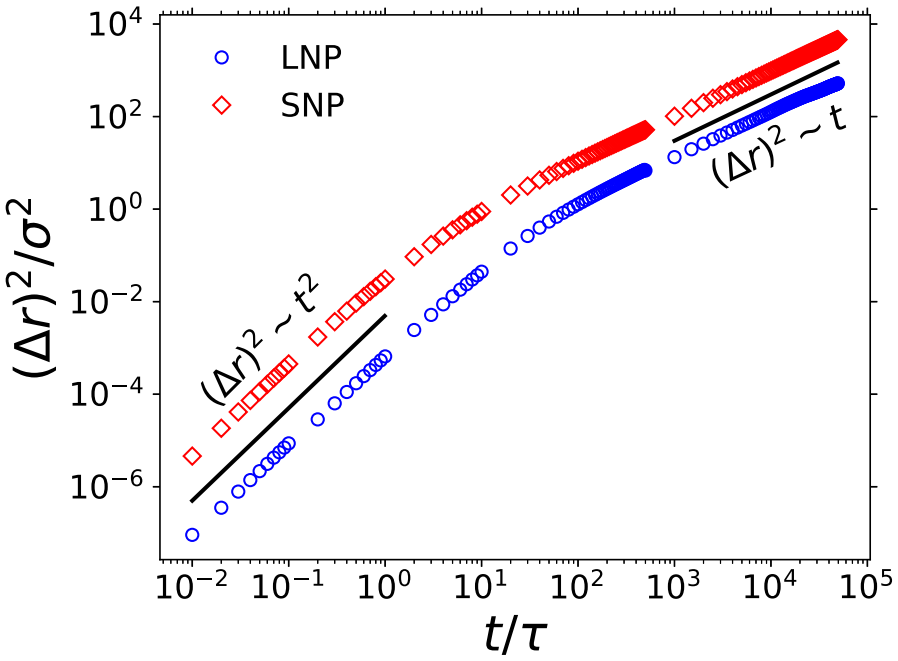

Figure C.1: Mean square displacement *vs* time for LNPs (blue circles) and SNPs (red diamonds).

Appendix D

Additional results for Chapter 3

We ran 5 additional simulations in which the systems were thermalized with Scheme C with $T_l = 1.0\epsilon/k_\mathrm{B}$ and $T_v = 1.1\epsilon/k_\mathrm{B}$, $1.05\epsilon/k_\mathrm{B}$, $0.9\epsilon/k_\mathrm{B}$, $0.85\epsilon/k_\mathrm{B}$, and $0.75\epsilon/k_\mathrm{B}$ at an evaporation rate set by $\zeta = 5$, as listed in Table 1 of the main text. Snapshots at various times during evaporation are shown in Fig. D.1 for $T^l_{1.0}T^v_{1.1}\zeta_5$, $T^l_{1.0}T^v_{1.05}\zeta_5$, and $T^l_{1.0}T^v_{0.75}\zeta_5$. The corresponding temperature and density profiles for these 3 systems are shown in Fig. D.2. The results for $T^l_{1.0}T^v_{0.85}\zeta_5$ and $T^l_{1.0}T^v_{0.9}\zeta_5$ are similar to those for $T^l_{1.0}T^v_{0.75}\zeta_5$.

Similar to $T^l_{1.0}T^v_{1.2}\zeta_5$, $T^l_{1.0}T^v_{1.1}\zeta_5$ exhibits "small-on-top" stratification, though it is difficult to see this behavior clearly from the snapshots in Fig. D.1(a). For this system, there is a weak positive thermal gradient in the evaporating suspension toward the liquid-vapor interface [Fig. D.2(a)]. Via the thermophoresis induced by this gradient, the LNPs are driven toward the substrate (i.e., toward the bottom of the liquid film) and depleted near the liquid-vapor interface. This depletion almost balances the accumulation of LNPs near the top of the film caused by the fast receding interface. As a result, the LNPs are almost uniformly distributed in the drying film, as shown in Figs. D.2(c) and D.3(a). The SNPs are essentially unaffected by the thermal gradient and accumulate below the interface since $\mathrm{Pe_s} > 1$ [see Figs. D.2(d)

and D.3(b)]. The net outcome is "small-on-top" stratification for $T^l_{1.0}T^v_{1.1}\zeta_5$, as shown by the order parameter of stratification plotted in Fig. D.3(c).

For $T^l_{1.0}T^v_{1.05}\zeta_5$, the evaporative cooling in the solvent is balanced by the heating from the vapor hermalized at $T_v = 1.05\epsilon/k_\mathrm{B}$. The temperature and solvent density are almost uniform in the evaporating suspension, as shown in Figs. D.2(e) and D.2(f). Both LNPs and SNPs accumulate below the receding interface as $\mathrm{Pe_l} > \mathrm{Pe_s} > 1$ [see Figs. D.2(g) and D.2(h) and Figs. D.3(a) and D.3(b)]. The distribution of nanoparticles in this system does not stratify in the early stage of drying, though there is a transition to weak "large-on-top" at late times, as shown by the corresponding order parameter of stratification in Fig. D.3(c).

$T^l_{1.0}T^v_{1.2}\zeta_5$ has been discussed in detail in the main text. Fig. D.3 shows the results of the average position of nanoparticles normal to the interface and the order parameter of stratification for $T^l_{1.0}T^v_{1.2}\zeta_5$, $T^l_{1.0}T^v_{1.1}\zeta_5$, and $T^l_{1.0}T^v_{1.05}\zeta_5$. This comparison clearly shows the transition from strong to weak "small-on-top" stratification and finally to almost no stratification or weak "large-on-top" when $T_v - T_l$ is reduced.

$T^l_{1.0}\zeta_5$ has a weak negative thermal gradient in the evaporating suspension because of evaporative cooling. Via the associated thermophoretic process, the LNPs are pushed toward the liquid-vapor interface where the solvent density is higher. Thermophoresis overpowers diffusiophoresis where the LNPs are pushed away from the interface by the concentration gradient of the SNPs. As a result, $T^l_{1.0}\zeta_5$ exhibits "large-on-top" stratification. Motivated by this observation, we ran $T^l_{1.0}T^v_{0.75}\zeta_5$ that has a large $|T_v - T_l|$. Our original goal was to induce a large negative thermal gradient in the evaporating suspension at a relatively small v_s such that the accompanying thermophoresis could generate strong "large-on-top" stratification in the drying suspension. However, as the initial vapor phase is at equilibrium with a liquid at $T_l = 1.0\epsilon/k_\mathrm{B}$, cooling the vapor down to $T_v = 0.75\epsilon/k_\mathrm{B}$ leads to droplet condensation in the vapor phase, as shown in Fig. D.1(c). Eventually, a liquid film of the solvent beads is

formed at the top of the simulation cell. Because of the condensation, the vapor density near the liquid-vapor interface decreases very quickly and as a result, the solvent evaporates at a rate much higher than for $\zeta = 5$. The actual evaporation rate in $T^l_{1.0}T^v_{0.75}\zeta_5$ is close to that in $T^l_{1.0}\zeta_{30}$. Increasing T_v to $0.85\epsilon/k_\mathrm{B}$ or $0.90\epsilon/k_\mathrm{B}$ yields similar droplet condensation in the vapor phase, though the extent of condensation decreases as T_v is increased. As a result, the receding speed of the liquid-vapor interface during evaporation decreases and becomes closer from above to the value set by $\zeta = 5$.

The average positions of LNPs and SNPs during drying are plotted in Fig. D.4 as a function of the extent of drying for the 5 systems discussed in the main text (see Table 1), as well as $T^l_{1.0}T^v_{0.75}\zeta_5$. It is clear that the LNPs have a large thermophoretic response while the SNPs only show changes in their average position in the late stage of drying, when the thermal gradient is varied. The behavior of SNPs is predominately affected by the receding speed of the liquid-vapor interface. The variation of their average positions in the late stage of drying under different thermal gradients is due to the change in the distribution of LNPs in the drying film. For example, when the LNPs are concentrated in a region, the SNPs are driven out of the same region because of crowding.

In Fig. D.5, the order parameter of stratification is plotted as a function of the extent of drying for $T^l_{1.0}\zeta_{30}$, $T^l_{1.0}\zeta_5$, and $T^l_{1.0}T^v_{0.75}\zeta_5$. $T^l_{1.0}T^v_{0.75}\zeta_5$ exhibits "large-on-top" stratification with an amplitude very close to that in $T^l_{1.0}\zeta_{30}$ for reasons discussed previously. The reason that $T^l_{1.0}\zeta_5$ shows even stronger "large-on-top" stratification than $T^l_{1.0}\zeta_{30}$ is discussed in the main text.

In Fig. D.6, we plot the average position of nanoparticles and the average separation between LNPs and SNPs for the 3 systems with $T_v < T_l$, i.e., $T^l_{1.0}T^v_{0.75}\zeta_5$, $T^l_{1.0}T^v_{0.85}\zeta_5$, and $T^l_{1.0}T^v_{0.9}\zeta_5$. While the SNPs show very little response to a thermal gradient, the distribution of LNPs is sensitive to the strength of the thermal gradient. When T_v approaches T_l from below,

the negative thermal gradient in the evaporating suspension becomes smaller in magnitude and the driving force for LNPs to migrate to the interfacial region decreases. However, the receding speed of the liquid-vapor interface also decreases as T_v is increased and gets closer to T_l from below, and the diffusiophoretic driving force that pushes LNPs way from the interfacial region thus decreases. The complicated interplay of these two factors makes "large-on-top" stratification stronger when T_v is increased as in $T^l_{1.0}T^v_{0.75}\zeta_5 \rightarrow T^l_{1.0}T^v_{0.85}\zeta_5 \rightarrow T^l_{1.0}T^v_{0.9}\zeta_5$ [see Fig. D.6(c)].

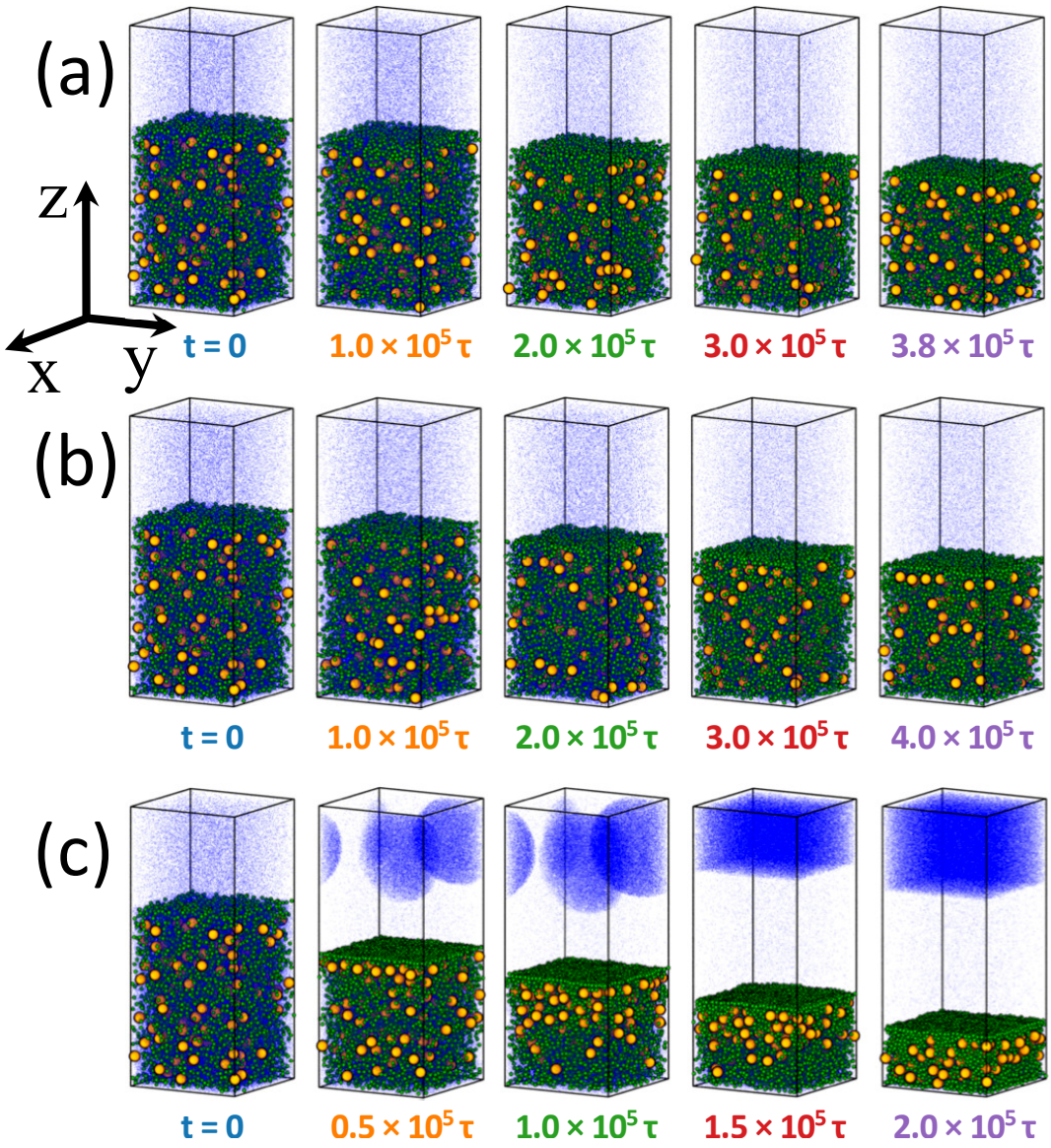

Figure D.1: Snapshots during solvent evaporation for (a) $T^l_{1.0}T^v_{1.1}\zeta_5$, (b) $T^l_{1.0}T^v_{1.05}\zeta_5$, and (c) $T^l_{1.0}T^v_{0.75}\zeta_5$. Elapsed time since evaporation was initiated at $t = 0$ is listed under each snapshot. Temperature and density profiles of the 5 systems are shown in Fig. D.2. Color code: SNPs (green), LNPs (orange), and solvent (blue). Only 5% of the solvent beads are visualized to improve clarity.

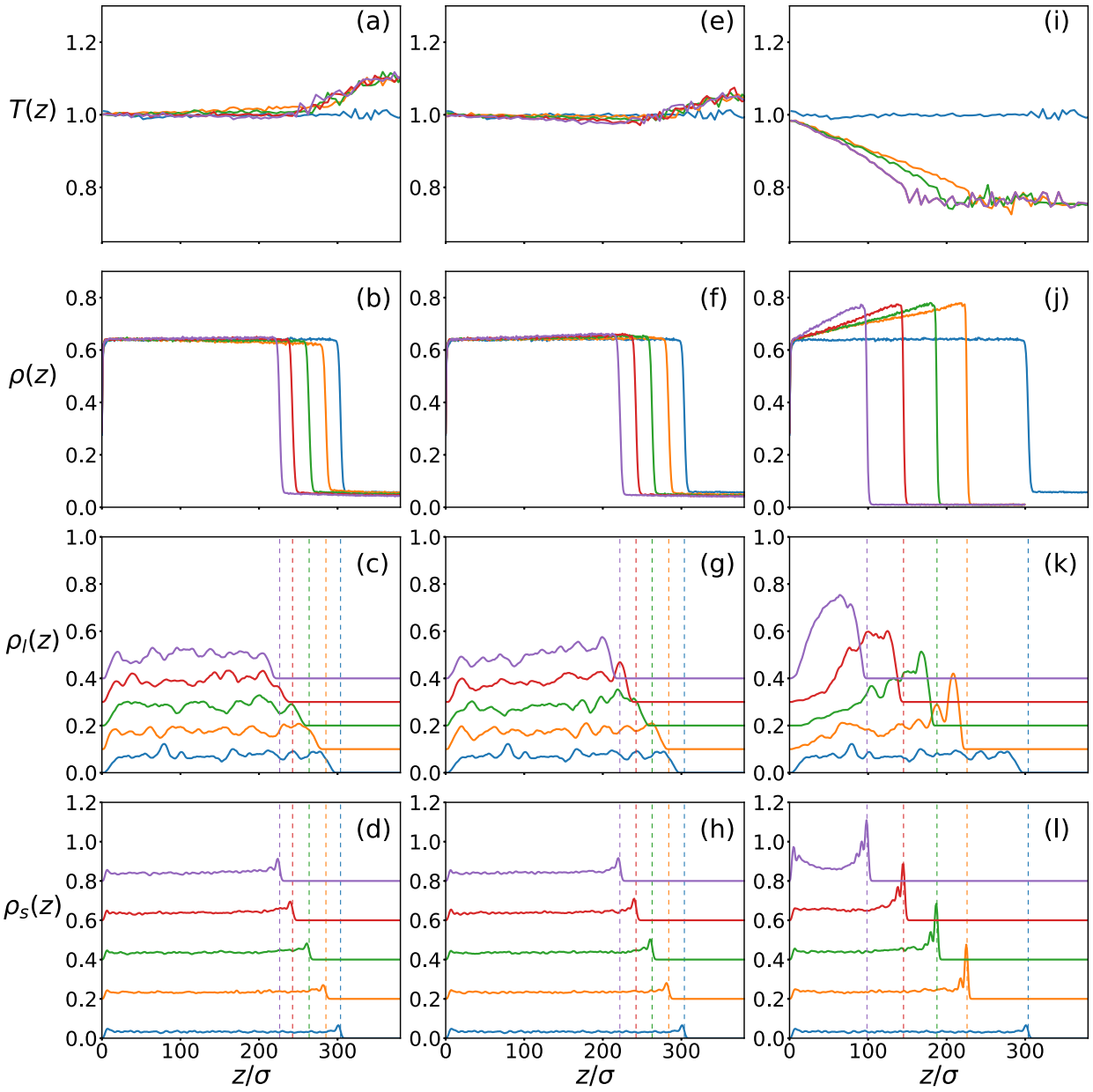

Figure D.2: Temperature profiles (top row) and density profiles for the solvent (second row), LNPs (third row), and SNPs (bottom row) for $T^l_{1.0}T^v_{1.1}\zeta_5$ (a-d), $T^l_{1.0}T^v_{1.05}\zeta_5$ (e-h), and $T^l_{1.0}T^v_{0.75}\zeta_5$ (i-l), respectively. The curves follow the same order as the snapshots shown in Fig. D.1. The vertical dashed lines indicate the location of the liquid-vapor interface. For clarity, the density profiles for LNPs (SNPs) are shifted upward by $0.1m/\sigma^3$ ($0.2m/\sigma^3$) successively.

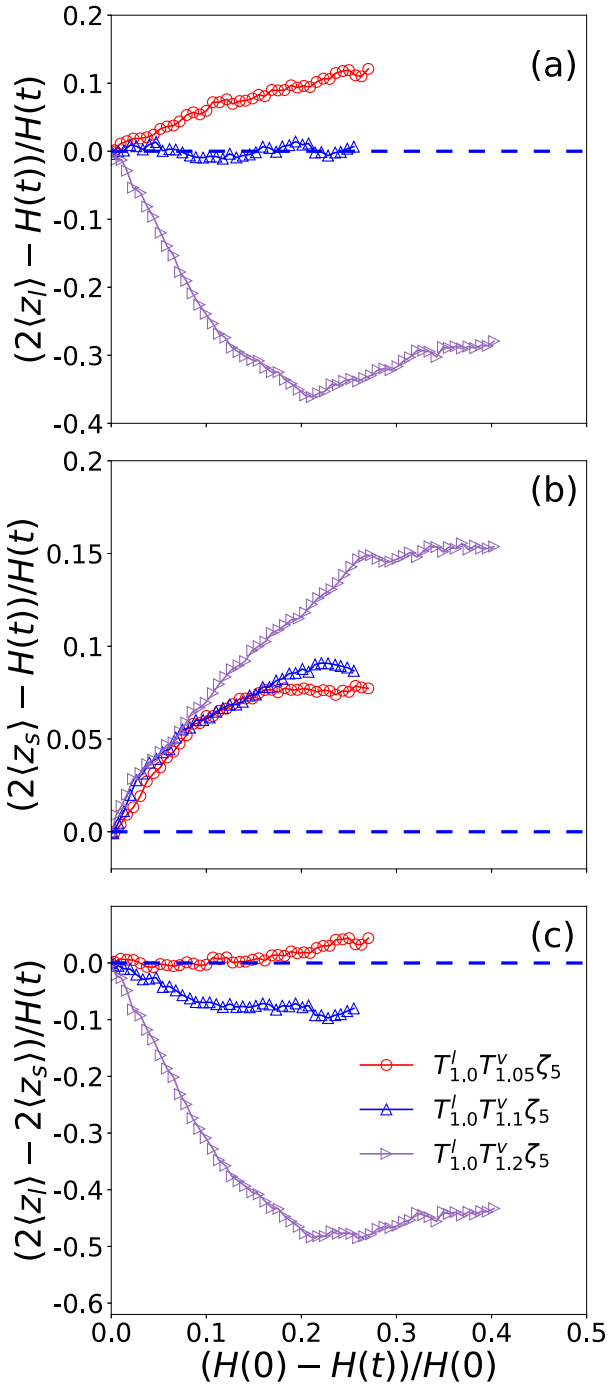

Figure D.3: Average position in the z direction relative to the center of the film, normalized by $H(t)/2$, is plotted against the extent of drying, quantified as $(H(0) - H(t))/H(0)$, for (a) LNPs and (b) SNPs. Panel (c) shows the average separation between LNPs and SNPs, normalized by $H(t)/2$, as a function of the extent of drying. Data are for $T^l_{1.0}T^v_{1.05}\zeta_5$ (red circles), $T^l_{1.0}T^v_{1.1}\zeta_5$ (blue triangles), and $T^l_{1.0}T^v_{1.2}\zeta_5$ (purple right-pointing triangles).

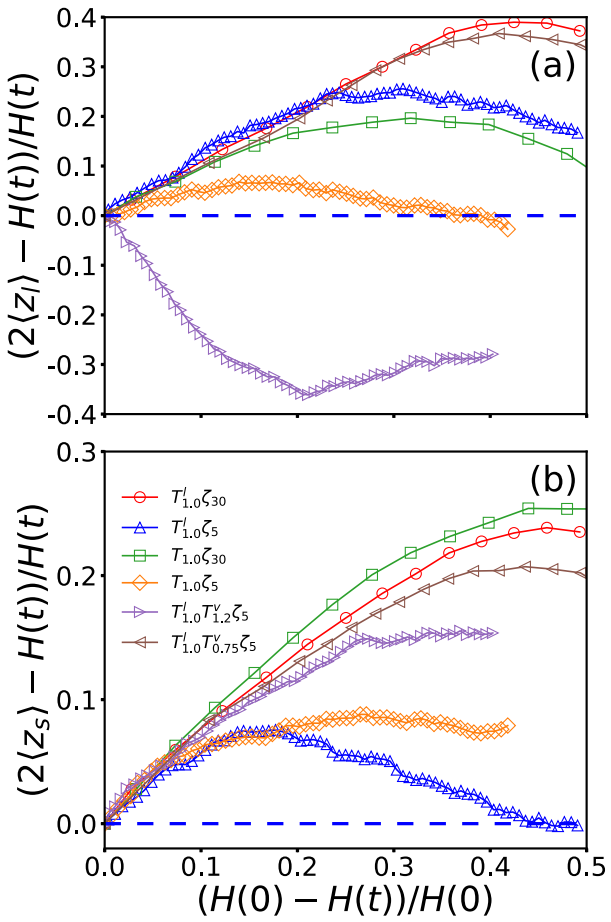

Figure D.4: Average position in the z direction relative to the center of the film, normalized by $H(t)/2$, is plotted against the extent of drying, quantified as $(H(0) - H(t))/H(0)$, for (a) LNPs and (b) SNPs. Data are for $T^l_{1.0}\zeta_{30}$ (red circles), $T^l_{1.0}\zeta_5$ (blue triangles), $T_{1.0}\zeta_{30}$ (green squares), $T_{1.0}\zeta_5$ (orange diamonds), $T^l_{1.0}T^v_{1.2}\zeta_5$ (purple right-pointing triangles), and $T^l_{1.0}T^v_{0.75}\zeta_5$ (brown left-pointing triangles).

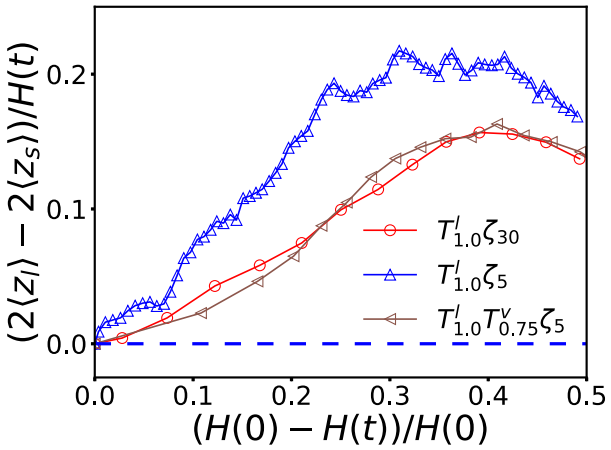

Figure D.5: Average position in the z direction relative to the center of the film, normalized by $H(t)/2$, is plotted against the extent of drying, quantified as $(H(0) - H(t))/H(0)$, for (a) LNPs and (b) SNPs. Panel (c) shows the average separation between LNPs and SNPs, normalized by $H(t)/2$, as a function of the extent of drying. Data are for $T^l_{1.0}\zeta_{30}$ (red circles), $T^l_{1.0}\zeta_5$ (blue triangles), and $T^l_{1.0}T^v_{0.75}\zeta_5$ (brown left-pointing triangles).

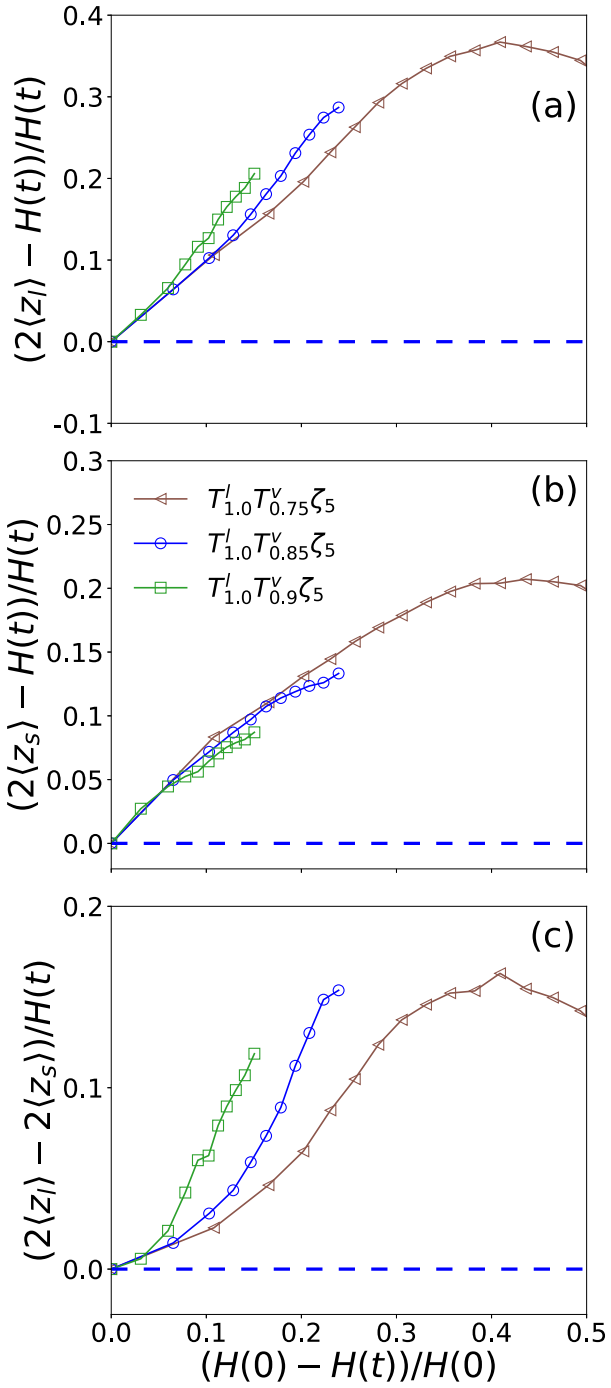

Figure D.6: Average position in the z direction relative to the center of the film, normalized by $H(t)/2$, is plotted against the extent of drying, quantified as $(H(0) - H(t))/H(0)$, for (a) LNPs and (b) SNPs. Panel (c) shows the average separation between LNPs and SNPs, normalized by $H(t)/2$, as a function of the extent of drying. Data are for $T^l_{1.0}T^v_{0.75}\zeta_5$ (brown left-pointing triangles), $T^l_{1.0}T^v_{0.85}\zeta_5$ (blue circles), and $T^l_{1.0}T^v_{0.9}\zeta_5$ (green squares).

Appendix E

Young-Laplace equation

E.1 Derivation of Young-Laplace equation

The profile of a meniscus is governed by Eq. (4.1), which has been discussed extensively for the geometry of sessile and pendant drops. Here we provide a simple derivation of this equation. The energy of a liquid bath bound by a cylindrical container and a meniscus on the outside of a cylinder at the center of the container (Fig. 4.1) is a sum of surface energy and gravitational terms, $G = \gamma S + \Delta p V + U_g$, where γ is the surface tension of the liquid, S is the surface area of the liquid-vapor interface, Δp is a Lagrange multiplier, V is the volume of the liquid bath which is fixed, and U_g is the potential energy of the liquid in the gravitational field. The meniscus profile can be found by minimizing G, which can be written in terms of the surface profile $z(r)$,

$$G = 2\pi\gamma \int_R^L r\sqrt{1+z'^2}\,\mathrm{d}r + 2\pi\Delta p \int_R^L rz\,\mathrm{d}r + \pi\Delta\rho g \int_R^L rz^2\,\mathrm{d}r. \tag{E.1}$$

We seek the surface profile that will make the energy function $G = \int f(z, z', r)\,\mathrm{d}r$ stationary, i.e., $\delta G = 0$. The resulting Euler-Lagrange equation is

$$\frac{\mathrm{d}}{\mathrm{d}r}\frac{\partial f}{\partial z'} - \frac{\partial f}{\partial z} = 0. \tag{E.2}$$

After some algebra, we obtain the following equation,

$$\gamma\Big[\frac{z''}{(1+z'^2)^{3/2}} + \frac{z'}{r(1+z'^2)^{1/2}}\Big] = \Delta p + \Delta\rho g z, \tag{E.3}$$

where the left hand side comes from the surface energy and the right hand side originates from the volume of the liquid bath being fixed and the gravitational potential energy, respectively. This equation is Eq. (4.1) in the main text.

E.2 Solution of zero-order

If the contact angle θ_1 on the cylinder in Fig. 4.1 is close to $\pi/2$, the resulting liquid-vapor interface is almost flat since the contact angle on the wall surface is fixed at $\pi/2$. In this case $z' = \tan\phi \ll 1$ and Eq. (4.1) can be approximated as

$$2\tilde{H} + \kappa^2 z = \frac{1}{r}\frac{\mathrm{d}}{\mathrm{d}r}\Big[\frac{rz'}{(1+z'^2)^{1/2}}\Big] \approx \frac{1}{r}\frac{\mathrm{d}}{\mathrm{d}r}\Big[rz'(1+\mathcal{O}(z'^2))\Big], \tag{E.4}$$

with the following boundary conditions,

$$\phi = \phi_1 \quad \text{at} \quad r = R, \tag{E.5a}$$

$$\phi = \phi_2 \quad \text{at} \quad r = L \quad \text{and} \quad z = 0, \tag{E.5b}$$

where $\phi_1 = \theta_1 + \pi/2$, $\phi_2 = \pi$. The solution of Eq. (E.4) which satisfies the boundary condition Eq. (E.5b) is,

$$z = \frac{2\tilde{H}}{\kappa^2}\Big[\frac{K_0(\kappa r)}{K_0(\kappa L)} - 1\Big], \tag{E.6}$$

and the angle ϕ is given by

$$\tan\phi = -\frac{2\tilde{H}}{\kappa}\frac{K_1(\kappa r)}{K_0(\kappa L)}, \tag{E.7}$$

where K_0 and K_1 are modified Bessel functions of second kind of order zero and one, respectively. The undetermined constant $\tilde{H}$ can be found using the other boundary condition Eq. (E.5a) and the result is

$$\tilde{H} = -\frac{\kappa}{2}\tan\phi_1\frac{K_0(\kappa L)}{K_1(\kappa R)}. \tag{E.8}$$

E.3 Expansion of elliptic integrals

Here we derive the series expansions of incomplete elliptic integrals $F(\phi, j)$ and $E(\phi, j)$ in the limit $j^2 \to -\infty$. To facilitate the discussion it is helpful to introduce a small parameter $\epsilon > 0$ and $j^2 = -\frac{1}{\epsilon^2}$; the limit $j^2 \to -\infty$ thus corresponds to $\epsilon \to 0$. Below we use the incomplete elliptic integral of second kind, $E(\phi, j)$, as an example. A similar expansion can

be performed for $F(\phi, j)$.

$$\begin{aligned} E(\phi, j) &= \int_0^{\phi} \sqrt{1 - j^2 \sin^2 t}\, \mathrm{d}t \quad (t \mapsto \sin t) \\ &= \frac{1}{\epsilon}\Big[\underbrace{\int_0^{\sqrt{\epsilon}} \sqrt{\epsilon^2 + t^2}\, \frac{\mathrm{d}t}{\sqrt{1 - t^2}}}_{t \mapsto \epsilon t} + \underbrace{\int_{\sqrt{\epsilon}}^{\sin\phi} \sqrt{\epsilon^2 + t^2}\, \frac{\mathrm{d}t}{\sqrt{1 - t^2}}}_{t \mapsto 1/t} \Big] \\ &= \frac{1}{\epsilon}\Big[\epsilon^2 \int_0^{1/\sqrt{\epsilon}} \sqrt{1 + t^2}\, \frac{\mathrm{d}t}{\sqrt{1 - \epsilon^2 t^2}} + \int_{1/\sin\phi}^{1/\sqrt{\epsilon}} \sqrt{1 + \epsilon^2 t^2}\, \frac{\mathrm{d}t}{t^2 \sqrt{t^2 - 1}} \Big] \\ &= \frac{1}{\epsilon}\,(1 - \cos\phi) + \epsilon \left(-\frac{\ln \epsilon}{2} + \ln 2 + \frac{1}{4} - \frac{1}{2} \ln \frac{1 + \cos\phi}{\sin\phi} \right) + \mathcal{O}(\epsilon^2). \end{aligned} \tag{E.9}$$

In this derivation we have employed the the following expansion,

$$\frac{1}{\sqrt{1 - \epsilon^2 t^2}} = 1 + \frac{1}{2}\epsilon^2 t^2 + \mathcal{O}(\epsilon^4 t^4)$$

and

$$\sqrt{1 + \epsilon^2 t^2} = 1 + \frac{1}{2}\epsilon^2 t^2 + \mathcal{O}(\epsilon^4 t^4)$$

, and assumed that $\sin\phi > \sqrt{\epsilon}$. The expansion of the incomplete elliptic integral of first kind, $F(\phi, j)$, can be obtained similarly and the result is

$$F(\phi, j) = \epsilon \left(-\ln \epsilon + 2 \ln 2 - \ln \frac{1 + \cos\phi}{\sin\phi} \right) + \mathcal{O}(\epsilon^2). \tag{E.10}$$

By substituting Eq. (E.9) and Eq. (E.10) into Eq. (4.18), we arrive at

$$\Delta h = R \cos\theta_1 \Big[\ln \frac{2L}{R(1 + \sin\theta_1)} - \frac{1}{2} \Big], \tag{E.11}$$

which is Eq. (4.19) in the main text. Here the relations $H = \frac{\sin\phi_1}{l^2 - 1} \approx \frac{\cos\theta_1}{l^2}$ and $\epsilon = \sqrt{-j^{-2}} = \sqrt{c}$ are used.

E.4 Relative error of Eq. (4.18) on predicting Δh

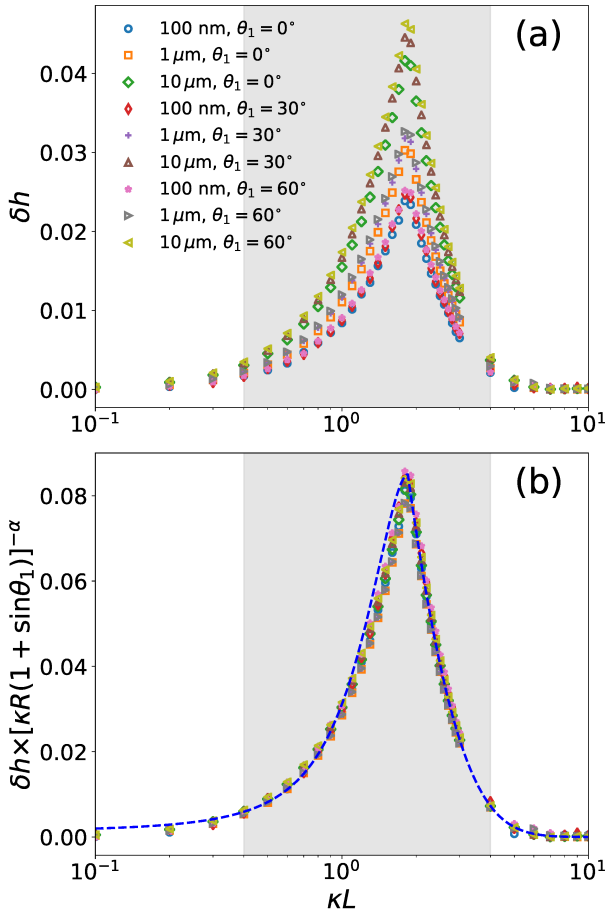

Figure E.1: (a) The relative error δh defined in Eq. (E.12) as a function of κL for various combinations of R and θ_1. (b) Data in (a) are collapsed onto a master curve when $\delta h \times [\kappa R(1+\sin\theta_1)]^{-0.12}$ is plotted against κL; the blue dashed line is the fit in Eq. (4.28). In both (a) and (b) the gray zone indicates the crossover region $0.4\kappa^{-1} \lesssim L \lesssim 4\kappa^{-1}$.

In order to obtain an even more accurate expression of the meniscus height that applies to $R \ll \kappa^{-1}$ and an arbitrary L, we denote the meniscus height predicted in Eq. (4.18) using elliptic integrals with the parameter l given in Eq. (4.26) as Δh(elliptic). The full numerical solution of Eq. (4.6) for an arbitrary L is denoted as Δh(actual). The relative error of using

Eq. (4.18) to predict the meniscus height is thus given by

$$\delta h = \frac{\Delta h(\text{elliptic}) - \Delta h(\text{actual})}{\Delta h(\text{elliptic})}. \tag{E.12}$$

In Fig. E.1(a), δh is shown as a function of L that is normalized by κ^{-1} for several combinations of the cylinder radius, R, and the contact angle on its surface, θ_1. As expected, the peak value of the relative error occurs at $\kappa L = 1.85$. We find that all the data collapse to a master curve if we plot $\delta h \times [\kappa R(1 + \sin\theta_1)]^{-0.12}$ against κL, as shown in Fig. E.1(b). The master curve can be fit with the kink function given in Eq. (4.28) [dashed blue line in Fig. E.1(b)]. With this universal fit to the collapsed data of relative error, we arrive at Eq. (4.27) in the main text that can be used to accurately predict the meniscus height for an arbitrary L.

Bibliography

[1] A. H. Persad and C. A. Ward, Chem. Rev. **116**, 7727 (2016).

[2] J.-T. Chen, M. Zhang, and T. P. Russell, Nano letters **7**, 183 (2007).

[3] K. Strawhecker, S. Kumar, J. Douglas, and A. Karim, Macromolecules **34**, 4669 (2001).

[4] J. M. Shin, Y. Kim, H. Yun, G.-R. Yi, and B. J. Kim, ACS Nano **11**, 2133 (2017).

[5] N. Jouault, D. Zhao, and S. K. Kumar, Macromolecules **47**, 5246 (2014).

[6] M. P. Arciniegas, A. Castelli, L. Ceseracciu, P. Bianchini, S. Marras, R. Brescia, and L. Manna, Nano Lett. **16**, 6154 (2016).

[7] T. P. Bigioni, X.-M. Lin, T. T. Nguyen, E. I. Corwin, T. A. Witten, and H. M. Jaeger, Nature Mater. **5**, 265 (2006).

[8] M. D. Dickey, E. A. Weiss, E. J. Smythe, R. C. Chiechi, F. Capasso, and G. M. Whitesides, ACS Nano **2**, 800 (2008).

[9] J. Chen, W.-S. Liao, X. Chen, T. Yang, S. E. Wark, D. H. Son, J. D. Batteas, and P. S. Cremer, ACS Nano **3**, 173 (2009).

[10] A. Utgenannt, R. Maspero, A. Fortini, R. Turner, M. Florescu, C. Jeynes, A. G. Kanaras, O. L. Muskens, R. P. Sear, and J. L. Keddie, ACS Nano **10**, 2232 (2016).

[11] W. F. Reinhart, A. W. Long, M. P. Howard, A. L. Ferguson, and A. Z. Panagiotopoulos, Soft Matter **13**, 4733 (2017).

[12] S. Cheng, M. J. Stevens, and G. S. Grest, J. Chem. Phys. **147**, 224901 (2017).

[13] A. F. Routh and W. B. Zimmerman, Chem. Eng. Sci. **59**, 2961 (2004).

[14] A. F. Routh, Rep. Prog. Phys. **76**, 046603 (2013).

[15] O. Cusola, S. Kivistö, S. Vierros, P. Batys, M. Ago, B. L. Tardy, L. G. Greca, M. B. Roncero, M. Sammalkorpi, and O. J. Rojas, Langmuir **34**, 5759 (2018).

[16] R. E. Trueman, E. Lago Domingues, S. N. Emmett, M. W. Murray, and A. F. Routh, J. Colloid Interface Sci. **377**, 207 (2012).

[17] R. E. Trueman, E. Lago Domingues, S. N. Emmett, M. W. Murray, J. L. Keddie, and A. F. Routh, Langmuir **28**, 3420 (2012).

[18] A. K. Atmuri, S. R. Bhatia, and A. F. Routh, Langmuir **28**, 2652 (2012).

[19] I. Nikiforow, J. Adams, A. M. König, A. Langhoff, K. Pohl, A. Turshatov, and D. Johannsmann, Langmuir **26**, 13162 (2010).

[20] A. Fortini, I. Martín-Fabiani, J. L. De La Haye, P.-Y. Dugas, M. Lansalot, F. D'Agosto, E. Bourgeat-Lami, J. L. Keddie, and R. P. Sear, Phys. Rev. Lett. **116**, 118301 (2016).

[21] A. Fortini and R. P. Sear, Langmuir **33**, 4796 (2017).

[22] H. Luo, C. M. Cardinal, L. E. Scriven, and L. F. Francis, Langmuir **24**, 5552 (2008).

[23] M. P. Howard, A. Nikoubashman, and A. Z. Panagiotopoulos, Langmuir **33**, 3685 (2017).

[24] J. Zhou, Y. Jiang, and M. Doi, Phys. Rev. Lett. **118**, 108002 (2017).

[25] D. K. Makepeace, A. Fortini, A. Markov, P. Locatelli, C. Lindsay, S. Moorhouse, R. Lind, R. P. Sear, and J. L. Keddie, Soft Matter **13**, 6969 (2017).

[26] X. Liu, W. Liu, A. J. Carr, D. S. Vazquez, D. Nykypanchuk, P. W. Majewski, A. F. Routh, and S. R. Bhatia, J. Colloid Interface Sci. **515**, 70 (2018).

[27] I. Martín-Fabiani, A. Fortini, J. Lesage de la Haye, M. L. Koh, S. E. Taylor, E. Bourgeat-Lami, M. Lansalot, F. D'Agosto, R. P. Sear, and J. L. Keddie, ACS Applied Materials & Interfaces **8**, 34755 (2016).

[28] S. Asakura and F. Oosawa, J. Chem. Phys. **22**, 1255 (1954).

[29] R. P. Sear and P. B. Warren, Phys. Rev. E **96**, 062602 (2017).

[30] R. P. Sear, J. Chem. Phys. **148**, 134909 (2018).

[31] T. Okuzono, K. Ozawa, and M. Doi, Phys. Rev. Lett. **97**, 136103 (2006).

[32] S. Cheng, J. B. Lechman, S. J. Plimpton, and G. S. Grest, J. Chem. Phys. **134**, 224704 (2011).

[33] J. F. Joanny and P. G. de Gennes, J. Chem. Phys. **81**, 552 (1984).

[34] Y. Tang, G. S. Grest, and S. Cheng, Langmuir **34**, 7161 (2018).

[35] S. Cheng and G. S. Grest, J. Chem. Phys. **138**, 064701 (2013).

[36] R. Everaers and M. R. Ejtehadi, Phys. Rev. E **67**, 041710 (2003).

[37] P. J. in 't Veld, S. J. Plimpton, and G. S. Grest, Comput. Phys. Commun. **179**, 320 (2008).

[38] P. J. in 't Veld, M. K. Petersen, and G. S. Grest, Phys. Rev. E **79**, 021401 (2009).

[39] G. S. Grest, Q. Wang, P. in 't Veld, and D. J. Keffer, J. Chem. Phys. **134**, 144902 (2011).

[40] S. Cheng and G. S. Grest, J. Chem. Phys. **136**, 214702 (2012).

[41] S. Plimpton, J. Comput. Phys. **117**, 1 (1995).

[42] M. Heinen, J. Vrabec, and J. Fischer, J. Chem. Phys. **145** (2016).

[43] H. Brenner, Physical Review E **84**, 066317 (2011).

[44] S. Cheng and G. S. Grest, ACS Macro Lett. **5**, 694 (2016).

[45] R. Piazza and A. Parola, J. Phys. Condens. Matter **20**, 153102 (2008).

[46] D. Beaglehole, J. Phys. Chem. **91**, 5091 (1987).

[47] V. Kuz, A. Garazo, and S. Fasano, J. Colloid Interface Sci. **133**, 511 (1989).

[48] Y. Tang and S. Cheng, J. Colloid Interface Sci. **533**, 401 (2019).

[49] P. Pieranski, Phys. Rev. Lett. **45**, 569 (1980).

[50] A. J. McElrone, B. Choat, G. A. Gambetta, and C. R. Brodersen, Nature Education Knowledge **4**, 6 (2013).

[51] D. J. Hornbaker, R. Albert, I. Albert, A.-L. Barabasi, and P. Schiffer, Nature **387**, 765 (1997).

[52] Y. Yuan and T. R. Lee, in *Surface Science Techniques*, edited by G. Bracco and B. Holst (Springer Berlin Heidelberg, Berlin, Heidelberg, 2013) pp. 3–34.

[53] S. H. Kang, N. Wu, A. Grinthal, and J. Aizenberg, Phys. Rev. Lett. **107**, 177802 (2011).

[54] R. D. Piner, J. Zhu, F. Xu, S. Hong, and C. A. Mirkin, Science **283**, 661 (1999).

[55] M. Ghosh, F. Fan, and K. J. Stebe, Langmuir **23**, 2180 (2007).

[56] A. R. Tao, J. Huang, and P. Yang, Accounts of Chemical Research **41**, 1662 (2008).

[57] L. J. Cote, F. Kim, and J. Huang, J. Am. Chem. Soc. **131**, 1043 (2009).

[58] M. Cavallaro, L. Botto, E. P. Lewandowski, M. Wang, and K. J. Stebe, Proc. Natl. Acad. Sci. **108**, 20923 (2011).

[59] M. He, B. Li, X. Cui, B. Jiang, Y. He, Y. Chen, D. O'Neil, P. Szymanski, M. A. EI-Sayed, J. Huang, and Z. Lin, Nature Commun. **8**, 16045 (2017).

[60] K. M. Takahashi, J. Colloid Interface Sci. **134**, 181 (1990).

[61] M. M. Yazdanpanah, M. Hosseini, S. Pabba, S. M. Berry, V. V. Dobrokhotov, A. Safir, R. S. Keynton, and R. W. Cohn, Langmuir **24**, 13753 (2008).

[62] P. G. de Gennes, F. Brochard-Wyart, and D. Quéré, *Capillarity and Wetting Phenomena: Drops, Bubbles, Pearls, Waves* (Springer, New York, USA, 2004).

[63] B. Derjaguin, Dokl. Akad. Nauk SSSR **51**, 517 (1946).

[64] D. A. White and J. A. Tallmadge, J. Fluid Mech. **23**, 325 (1965).

[65] C. Huh and L. Scriven, J. Colloid Interface Sci. **30**, 323 (1969).

[66] D. F. James, J. Fluid Mech. **63**, 657 (1974).

[67] L. L. Lo, J. Fluid Mech. **132**, 65 (1983).

[68] M. M. Alimov and K. G. Kornev, Proc. R. Soc. A Math. Phys. Eng. Sci. **470**, 20140113 (2014).

[69] J. Dupré de Baubigny, M. Benzaquen, L. Fabié, M. Delmas, J. P. Aimé, M. Legros, and T. Ondarçuhu, Langmuir **31**, 9790 (2015).

[70] F. Bashforth and J. C. Adams, *An Attempt to Test the Theories of Capillary Action* (Cambridge University Press, Cambridge, UK, 1883).

[71] P. Concus, J. Fluid Mech. **34**, 481 (1968).

[72] S. B. G. O'brien, J. Fluid Mech. **233**, 519 (1991).

[73] S. Srinivasan, G. H. McKinley, and R. E. Cohen, Langmuir **27**, 13582 (2011).

[74] D. N. Mazzone, G. I. Tardos, and R. Pfeffer, J. Colloid Interface Sci. **113**, 544 (1986).

[75] H. J. Butt and M. Kappl, Adv. Colloid Interface Sci. **146**, 48 (2009).

[76] F. M. Orr, L. E. Scriven, and A. P. Rivas, J. Fluid Mech. **67**, 723 (1975).

[77] N. P. Kruyt and O. Millet, J. Fluid Mech. **812**, 129 (2017).

[78] S. Cheng and M. O. Robbins, Phys. Rev. E **89**, 062402 (2014).

[79] S. Cheng and M. O. Robbins, Langmuir **32**, 7788 (2016).

[80] Y. Tang and S. Cheng, Phys. Rev. E **98**, 032802 (2018).

[81] W. H. Press, S. A. Teukolsky, W. T. Vetterling, and B. P. Flannery, *Numerical Recipes 3rd Edition: The Art of Scientific Computing*, 3rd ed. (Cambridge University Press, New York, USA, 2007).

[82] B. Y. Rubinstein and L. G. Fel, J. Colloid Interface Sci. **417**, 37 (2014).

[83] L. Landau and E. Lifshitz, *Fluid Mechanics* (Elsevier Science, 1987).

[84] B. M. Law, S. P. McBride, J. Y. Wang, H. S. Wi, G. Paneru, S. Betelu, B. Ushijima, Y. Takata, B. Flanders, F. Bresme, H. Matsubara, T. Takiue, and M. Aratono, Prog. Surf. Sci. **92**, 1 (2017).

[85] J. Zhou, X. Man, Y. Jiang, and M. Doi, Adv. Mater. **29**, 1703769 (2017).

[86] A. Statt, M. P. Howard, and A. Z. Panagiotopoulos, J. Chem. Phys. **149**, 024902 (2018).

[87] C. E. Colosqui, J. F. Morris, and J. Koplik, Phys. Rev. Lett. **111**, 028302 (2013).

[88] Y. Lin, H. Skaff, T. Emrick, A. D. Dinsmore, and T. P. Russell, Science **299**, 226 (2003).

[89] A. Dong, J. Chen, P. M. Vora, J. M. Kikkawa, and C. B. Murray, Nature **466**, 474 (2010).

[90] D. Ershov, J. Sprakel, J. Appel, M. A. Cohen Stuart, and J. van der Gucht, Proc. Nat. Acad. Sci. USA **110**, 9220 (2013).

[91] D. G. B., K. Timm, C. P. V., H. Jens, and B. Fernando, Adv. Mater. **26**, 6715 (2014).

[92] K. Stratford, R. Adhikari, I. Pagonabarraga, J.-C. Desplat, and M. E. Cates, Science **309**, 2198 (2005).

[93] D. S. Frost and L. L. Dai, Langmuir **27**, 11339 (2011).

[94] X.-C. Luu, J. Yu, and A. Striolo, Langmuir **29**, 7221 (2013).

[95] E. Sanz, K. A. White, P. S. Clegg, and M. E. Cates, Phys. Rev. Lett. **103**, 255502 (2009).

[96] X. Hua, M. A. Bevan, and J. Frechette, Langmuir **34**, 4830 (2018).

[97] A. D. Scheludko, B. V. Toshev, and D. T. Bojadjiev, J. Chem. Soc. Faraday Trans. 1: Phys. Chem. Condensed Phases **72**, 2815 (1976).

[98] N. Mitarai and F. Nori, Adv. Phys. **55**, 1 (2006).

[99] F. Bresme and M. Oettel, J. Phys.: Condensed Matter **19**, 413101 (2007).

[100] A. D. Scheludko and D. Nikolov, Colloid Polym. Sci. **253**, 396 (1975).

[101] A. V. Rapacchietta, A. W. Neumann, and S. N. Omenyi, J. Colloid Interface Sci. **59**, 541 (1977).

[102] A. V. Rapacchietta and A. W. Neumann, J. Colloid Interface Sci. **59**, 555 (1977).

[103] C. Huh and S. G. Mason, Can. J. Chem. **54**, 969 (1976).

[104] S. B. G. O'Brien, J. Colloid Interface Sci. **183**, 51 (1996).

[105] O. Pitois and X. Chateau, Langmuir **18**, 9751 (2002).

[106] X. Chateau and O. Pitois, J. Colloid Interface Sci. **259**, 346 (2003).

[107] V. Garbin, J. C. Crocker, and K. J. Stebe, Langmuir **28**, 1663 (2012).

[108] S. E. Anachkov, I. Lesov, M. Zanini, P. A. Kralchevsky, N. D. Denkov, and L. Isa, Soft Matter **12**, 7632 (2016).

[109] F. Dutka, Z. Rozynek, and M. Napiórkowski, Soft Matter **13**, 4698 (2017).

[110] M. Zanini, I. Lesov, E. Marini, C.-P. Hsu, C. Marschelke, A. Synytska, S. E. Anachkov, and L. Isa, Langmuir **34**, 4861 (2018).

[111] F. Schellenberger, P. Papadopoulos, M. Kappl, S. A. L. Weber, D. Vollmer, and H.-J. Butt, Phys. Rev. Lett. **121**, 048002 (2018).

[112] H. J. Butt, N. Gao, P. Papadopoulos, W. Steffen, M. Kappl, and R. Berger, Langmuir **33**, 107 (2016).

[113] G. D. Nadkarni and S. Garoff, Eur. Phys. Lett. **20**, 523 (1992).

[114] M. Preuss and H.-J. Butt, Langmuir **14**, 3164 (1998).

[115] R. Ettelaie and S. V. Lishchuk, Soft Matter **11**, 4251 (2015).

[116] S. V. Lishchuk and R. Ettelaie, Langmuir **32**, 13040 (2016).

[117] G. B. Davies, T. Krüger, P. V. Coveney, and J. Harting, J. Chem. Phys. **141**, 154902 (2014).

[118] D. Seveno and J. de Coninck, Langmuir **20**, 737 (2004).

[119] J. de Coninck and T. D. Blake, Annu. Rev. Mater. Res. **38**, 1 (2008).

[120] D. Seveno, T. D. Blake, and J. de Coninck, Phys. Rev. Lett. **111**, 096101 (2013).

[121] F. Bresme and N. Quirke, Phys. Rev. Lett. **80**, 3791 (1998).

[122] K. Kremer and G. S. Grest, J. Chem. Phys. **92**, 5057 (1990).

[123] J. G. Kirkwood and F. P. Buff, J. Chem. Phys. **17**, 338 (1949).

[124] J. Koplik and C. Maldarelli, Phys. Rev. Fluids **2**, 024303 (2017).

[125] D. Kashchiev, J. Chem. Phys. **118**, 9081 (2003).

[126] M. Schulz and J. L. Keddie, Soft Matter **14**, 6181 (2018).

[127] M. P. Howard, A. Nikoubashman, and A. Z. Panagiotopoulos, Langmuir **33**, 11390 (2017).

[128] R. Tatsumi, T. Iwao, O. Koike, Y. Yamaguchi, and Y. Tsuji, Appl. Phys. Lett. **112**, 053702 (2018).

[129] Y. Tang, G. S. Grest, and S. Cheng, (2018), arXiv:1810.01384 .

[130] Íbrahim Dinçer and C. Zamfirescu, *Drying Phenomena: Theory and Applications* (Wiley & Sons, Ltd., 2015).

[131] C. J. Brinker, MRS Bulletin **29**, 631 (2004).

[132] J. Keddie and A. F. Routh, *Fundamentals of Latex Film Formation: Processes and Properties* (Springer, Dordrecht, The Netherlands, 2010).

[133] J. L. Keddie, Mater. Sci. Engr. R: Reports **21**, 101 (1997).

[134] H. M. van der Kooij and J. Sprakel, Soft Matter **11**, 6353 (2015).

[135] S. Luo, V. Craciun, and E. Douglas, Langmuir **21**, 2881 (2005).

[136] J. M. Shin, Y. Kim, H. Yun, G.-R. Yi, and B. J. Kim, ACS Nano **11**, 2133 (2017).

[137] A. E. Imel and M. D. Dadmun, Polymer **75**, 134 (2015).

[138] S. K. Kumar, V. Ganesan, and R. A. Riggleman, J. Chem. Phys. **147**, 020901 (2017).

[139] M. P. Howard, W. F. Reinhart, T. Sanyal, M. S. Shell, A. Nikoubashman, and A. Z. Panagiotopoulos, J. Chem. Phys. **149**, 094901 (2018).

[140] W. F. Reinhart and A. Z. Panagiotopoulos, Soft Matter **14**, 6083 (2018).

[141] A. Statt, M. P. Howard, and A. Z. Panagiotopoulos, J. Chem. Phys. **147**, 184901 (2017).

[142] Y. Tang, G. S. Grest, and S. Cheng, (2018), arXiv:1810.05483 .

[143] R. D. Deegan, O. Bakajin, T. F. Dupont, G. Huber, S. R. Nagel, and T. A. Witten, Nature **389**, 827 (1997).

[144] Z. Mitov and E. Kumacheva, Phys. Rev. Lett. **81**, 3427 (1998).

[145] N. Bassou and Y. Rharbi, Langmuir **25**, 624 (2009).

[146] E. Lintingre, F. Lequeux, L. Talini, and N. Tsapis, Soft Matter **12**, 7435 (2016).

[147] E. Lintingre, G. Ducouret, F. Lequeux, L. Olanier, T. Périé, and L. Talini, Soft Matter **11**, 3660 (2015).

[148] H. M. Van Der Kooij, G. T. Van De Kerkhof, and J. Sprakel, Soft Matter **12**, 2858 (2016).

[149] L. S. Grundy, V. E. Lee, N. Li, C. Sosa, W. D. Mulhearn, R. Liu, R. A. Register, A. Nikoubashman, R. K. Prud'homme, A. Z. Panagiotopoulos, and R. D. Priestley, ACS Nano **12**, 4660 (2018).

[150] S. Nešić and J. Vodnik, Chemical Engineering Science **46**, 527 (1991).

[151] A. Lum, S. Mansouri, K. Hapgood, and M. W. Woo, Drying Technology **36**, 1802 (2018).

[152] B. K. Johnson and R. K. Prud'homme, AIChE J. **49**, 2264 (2003).

[153] B. K. Johnson and R. K. Prud'homme, Phys. Rev. Lett. **91**, 118302 (2003).

[154] A. Karma, D. A. Kessler, and H. Levine, Phys. Rev. Lett. **87**, 45501 (2001).

[155] A. J. Ladd and R. Verberg, J. Stat. Phys. **104**, 1191 (2001).

[156] N. I. Lebovka, Y. Y. Tarasevich, and N. V. Vygornitskii, Phys. Rev. E **97**, 1 (2018).

[157] D. C. Rapaport, Phys. Rev. Lett. **60**, 2480 (1988).

[158] H. Hu and R. G. Larson, J. Phys. Chem. B **106**, 1334 (2002).